

Thorsten Falk

# **From Voxels to Models**

## **Towards quantification in 3-D confocal microscopy**



Dissertation zur Erlangung des Doktorgrads  
der Technischen Fakultät  
der Albert-Ludwigs-Universität Freiburg im Breisgau

November 2015

Dekan: Prof. Dr. Georg Lausen

Prüfungskommission: Prof. Dr. Olaf Ronneberger  
Prof. Dr. Klaus Palme  
Prof. Dr. Rolf Backofen  
Prof. Dr. Matthias Teschner

Datum der Disputation: 15.01.2016

## Deutsche Zusammenfassung

Aktuelle mikroskopische Bildgebungsverfahren, die 3D-Aufnahmen biologischer Proben mit Auflösung im Submikrometerbereich (über die Zeit) ermöglichen, eröffnen völlig neue Wege Signalprozesse in lebenden Organismen zu untersuchen und zu verstehen. Obwohl diese Fortschritte in mikroskopischer Hardware theoretisch aufregende neue Studien ermöglichen, wird dieses Potential nur selten genutzt. Einer der Hauptgründe für diese “Verschwendung” ist ein Mangel an Werkzeugen um die Terabytes an aufgenommenen Bildern auf die wenigen Größen zu reduzieren, die zur Beantwortung einer biologischen Fragestellung benötigt werden. Die Datenmenge verhindert eine manuelle Auswertung, und viele Fragen, die durch mikroskopische Bilddaten beantwortet werden könnten, werden gar nicht erst gestellt.

Um mikroskopische Analysen im großen Maßstab zu ermöglichen, werden Algorithmen benötigt, die interessante Ereignisse detektieren, sie anatomischen Strukturen zuordnen und automatisch quantitative Messungen mit statistischen Sicherheiten ausgeben.<sup>1</sup> Auch wenn diese Beschreibung vage ist, enthält sie schon sehr wichtige Schlüsselwörter, nämlich “detektieren”: Wir benötigen allgemeingültige Detektoren, die mithilfe manuell annotierter Trainingsbeispiele, auf die Erkennung bestimmter Strukturen trainiert werden können; “zuordnen”: Wir müssen die Anatomie modellieren und Wege finden den Strukturen eindeutige anatomische Koordinaten zuzuordnen; “quantitativ”: Wir wollen unverfälschte Strukturparameter oder Verteilungen von Ereignissen messen; “Sicherheiten”: Wir müssen in der Lage sein die statistische Signifikanz dieser Messungen zu belegen.

In dieser Arbeit werden wir am Beispiel der Modellierung der Wurzelspitzenstammzellregion von *Arabidopsis thaliana* ein System beschreiben, das diese Spezifikation erfüllt. Wir werden eine vollständige Bildanalysepipeline präsentieren, die automatisch Lichtverluste in konfokalen Aufnahmen mit mehreren Ansichten korrigiert, Zellkerne mithilfe eines trainierbaren allgemeingültigen Detektors, der speziell für diese Aufgabe trainiert wurde, detektiert, detektierte Ereignisse in ein wurzelspezifisches Koordinatensystem abbildet und automatisch statistische Daten über Zellteilungsverteilungen verschiedener Mutantenpopulationen extrahiert.

Um diese Ziele zu erreichen, müssen verschiedene Techniken aus der Bildverarbeitung und dem maschinellen Lernen kombiniert werden.

Auf die gemessenen Bildintensitäten wenden wir eine auf Variationsrechnung basierende Energieminimierung an, um die den aufgenommen Bildern zugrundeliegende Fluorophorverteilung zu schätzen. Dafür haben wir ein auf Strahlenoptik basierendes physikalisch motiviertes Bildgebungsmodell entworfen, das in der Lage ist gewebeabhängige örtliche Signalabschwächung, Photobleichung und durch den Detektor hervorgerufenen Rauschen zu simulieren. Basierend auf einem Vergleich der gemessenen Intensitäten mit den durch dieses Modell vorhergesagten Intensitäten werden ein dichtes Abschwächungsfeld und die zugrundeliegenden wahren Intensitäten geschätzt. Zusätzliches Vorwissen kann problemlos in das Modell aufgenommen werden. Um das schlecht gestellte Rekonstruktionsproblem zu stabilisieren, haben wir verschiedene Glattheitsnebenbedingungen an

---

<sup>1</sup>Dieser Satz ist oft die vollständige Spezifikation, die ein Informatiker, der solch ein System entwickeln soll, von einem Biologieexperten bekommt.

das Abschwächungsfeld eingeführt, die auf synthetischen Daten zu ausgezeichneten und auf echten biologischen Proben zu sehr guten Rekonstruktionen führt.

In der Wurzelmodellierung wurden verschiedene Techniken kombiniert. Zunächst werden Zellkerne als anatomische Referenzstrukturen mit einem auf allgemeinen rotationsinvarianten Merkmalen basierenden Detektor erfasst. Dann wird die Wurzelachse mithilfe einer variationsbasierten Energieminimierung mit robustem Datenterm verfolgt und ihre örtlich variable Dicke bestimmt. Abschließend wird jeder erfasste Zellkern, mithilfe einer weiteren diskriminativen Klassifikation, einer Zellschicht zugeordnet.

Wir schließen die Arbeit mit einem statistischen Vergleich der Verteilungen von Zellteilungen in verschiedenen Arabidopsis Mutanten mit sehr subtilen Unterschieden im Phänotyp. Unser Modell ist in der Lage mit hoher statistischer Signifikanz bisher unbekannte Unterschiede in diesen Verteilungen zu finden, die bei Betrachtung einzelner Wurzeln der verschiedenen Populationen in der natürlichen Variabilität untergehen.

## Abstract

Current microscopic imaging techniques allow to record biological specimen with sub-micrometer resolution in 3-D (over time). They open completely new ways to observe and understand signaling in living organisms. Although these advances in microscopic hardware provide means to perform exciting new studies that have not been possible so far, their potential is rarely exploited due to a lack of tools for reducing the terabytes of recorded images to the small number of meaningful quantities required to answer an underlying biological question. The pure amount of data precludes manual analysis, and many questions, microscopic images could answer, will never be asked.

To allow large scale microscopic image analysis, algorithms are required that detect events of interest, relate them to the anatomical structure under investigation and automatically output quantitative measurements with statistical confidences.<sup>2</sup> Although vague, this description already contains very important key words, namely “detect”: we need general detectors that can be trained for specific structures using manually annotated sample data; “relate”: we have to model the surrounding anatomy and give means of uniquely assigning anatomically relevant coordinates to these structures; “quantitative”: we want to be able to get an unbiased quantification of structure parameters or event distributions; “confidence”: we must be able to measure statistical significance.

Within this thesis we will develop a system that fulfills this specification at the example of modeling the root apical meristem of *Arabidopsis thaliana*. We will present an end-to-end image analysis pipeline that is able to automatically correct light attenuation in confocal multiview recordings, detect nuclei using a trainable general-purpose detector specifically trained for that task, map detected events to a root specific coordinate system and automatically extract statistical data of mitosis distributions in different mutant populations.

To reach all these goals different techniques from image processing and machine learning have to be combined.

On the measured image intensities we apply a variational energy minimization to estimate their underlying fluorophore distribution. We designed a physically motivated image formation model based on ray optics which is able to simulate the effects of tissue dependent local signal attenuation, photo bleaching and noise introduced by the detector. Based on a comparison of the measurements to the intensities predicted by that model a dense attenuation field and the underlying intensities are estimated. Additional prior information can be easily included in the model. To stabilize the ill-posed reconstruction problem we introduced different smoothness priors on the attenuation field leading to excellent results on synthetic data and very good reconstructions on real biological samples.

For modeling the root, several techniques are combined. First nuclei as anatomical reference structures are detected using a trainable detector framework based on rotation-invariant general purpose features. Then a variational energy minimization with robust data term is employed to trace the root axis and give a spatially varying root thickness estimate. Finally cell layer labels are assigned to the detected nuclei using another supervised classification.

We conclude the thesis with a statistical comparison of mitosis distributions in different *Arabidopsis* mutants with very subtle phenotypic differences. Our model was able to find formerly unknown

---

<sup>2</sup>Often this sentence is the full specification an expert in biology gives to a computer scientist developing such a system.

differences in these distributions with high statistical significance that are hidden by natural variation when only considering single roots of each population.

## Acknowledgments

I want to thank the many people who helped me in several ways during my time as undergraduate and PhD student at the University of Freiburg finally leading to the publication of this thesis.

First of all I want to thank my parents for always supporting me in my decision of studying computer science and taking care of so many things during my time as undergraduate student. You allowed me to concentrate on my studies without being troubled of how to afford daily life.

I was in the very comfortable situation of profiting from the experience of three great senior researchers in one place during my time at the pattern recognition lab in Freiburg, namely my supervisor Prof. Olaf Ronneberger, Prof. Hans Burkhardt and Prof. Thomas Brox who all influenced my research by adding their specific expertise and ideas.

I want to thank Prof. Ronneberger for supervising me already during the student's research project, the diploma thesis and finally my PhD. Thank you for always bringing up great new ideas of how to successfully handle problems I might have called unsolvable in the first place. You always found motivating words when they were needed and pushed me in the right direction when required. It was a great time working for and together with you. You always gave me the feeling of being a valuable colleague, not a student that needs supervision.

I also want to thank Prof. Burkhardt, who introduced me to the world of invariant features. You believed in me when offering me my initial PhD position at the chair for pattern recognition in Freiburg. Thank you for allowing me to freely choose my direction of research and providing many valuable hints on how to reach my scientific goals.

Thank you, Prof. Brox for fascinating us for the field of variational energy minimization. I learned a lot for myself when supervising students in the new courses you offered and you managed to push us to the bleeding edge of research. Thank you for your open ear in scientific but also in administrative questions and the opportunity to continue working on biological image analysis while profiting from your basic research in computer vision.

I also want to acknowledge my many colleagues at the chair of pattern recognition and the botany department for many fruitful discussions. Thank you Alex Teynor and Lokesh Setia for offering me such a warm welcome in our office when I started my PhD and Maja Temerinac-Ott and Margret Keuper for another nice office clique. Especially the coffee breaks with you, Margret, were a great source of inspiration. You always had an open ear for my ideas and our invaluable discussions lead to many great works. You always backed me up when I thought I was stuck and encouraged me to get the final experiment done. I also want to thank Marco Reisert and Henrik Skibbe who provided me with the required background for invariant 3-D detection and Kun Liu for his appreciation of my work and the great extensions of the iRoCS Toolbox he provided. Then I want to thank Dominic and Robert for their tireless work on the many projects of our small image analysis group. You gave me the freedom to put some of the daily work aside to finally write up this thesis. I couldn't imagine a better team for keeping the image analysis lab in Freiburg running. I am looking forward to an exciting time with you.

Thanks to our system administration team, Stefan, Patrick and Felix for keeping our systems running. It was a pleasure working with you as interface between research and system administration

which added some extra-spice to my life as researcher.

I also want to thank Cynthia and Jasmin our secretaries for managing the many different projects and always providing good advice in the many administrative processes I faced during my work at the image analysis lab. Thank you for always having an open ear for our concerns.

Then I want to thank my friends who always back me up in stressful times and help me keeping balance between work and leisure time. I want to especially thank Jörg Fischer, for always reminding me of the right time for reaching the next milestone and his wife Martina Fischer for always having an open ear for any concern. I couldn't imagine better friends.

My greatest thanks, however, belong to my wife, Steffi. You always support any of my decisions and help me to not lose my way. With you, I feel like being able to manage everything. Thank you for doing uncountable small things and endure the stressful times when I work on the weekend or at night. Your support is invaluable and your belief in me cannot be rewarded enough. I love you.

# Contents

<b>1. Introduction</b>	<b>1</b>
1.1. Contributions . . . . .	2
1.2. Glossary . . . . .	6
<b>2. Variational attenuation correction</b>	<b>7</b>
2.1. Image Formation Model . . . . .	8
2.1.1. Photo bleaching . . . . .	10
2.2. Energy formulation . . . . .	12
2.2.1. MAP energy formulation . . . . .	12
2.2.2. Gaussian noise model: ViBE-Z two-view attenuation correction . . . . .	14
2.2.3. Zero order bleaching estimation . . . . .	16
2.2.4. Approximate Poisson noise model (Anscombe) . . . . .	18
2.2.5. Approximate Poisson-Gaussian noise model (Generalized Anscombe) . . . . .	19
2.2.6. Approximate Poisson-Gaussian noise model (Direct estimate) . . . . .	20
2.2.7. Wavelength dependent attenuation . . . . .	22
2.2.8. Structured Illumination . . . . .	24
2.2.9. Edge-preserving regularization . . . . .	27
2.2.10. Sparsity Prior . . . . .	28
2.3. Sample Data for Evaluation . . . . .	28
2.3.1. Synthetic Data for wavelength-independent absorption and zero order bleaching . . . . .	28
2.3.2. Synthetic Data for wavelength-dependent absorption and realistic bleaching . . . . .	30
2.3.3. Real world examples . . . . .	30
2.4. Implementation . . . . .	32
2.4.1. Discrete cone integration . . . . .	32
2.4.2. Discrete spatial derivatives of the attenuation field . . . . .	36
2.4.3. Optimization . . . . .	36
2.5. Results and Discussion . . . . .	40
2.5.1. Synthetic Data . . . . .	41
2.5.2. <i>Danio rerio</i> (Zebrafish) . . . . .	49
2.5.3. <i>Arabidopsis thaliana</i> (Thale cress) . . . . .	52
2.5.4. Limitations . . . . .	56
2.6. Conclusions . . . . .	56

---

<b>3. The intrinsic Root Coordinate System (iRoCS)</b>	<b>59</b>
3.1. The Arabidopsis root . . . . .	60
3.1.1. Developmental zones (longitudinal) . . . . .	61
3.1.2. Tissue types (transversal) . . . . .	63
3.1.3. Root growth control . . . . .	64
3.2. Detection and segmentation of cells and nuclei . . . . .	64
3.2.1. Nucleus detection . . . . .	65
3.2.2. Cell segmentation . . . . .	72
3.3. Continuous coordinate system fit . . . . .	75
3.3.1. Basic axis fit using Gaussian kernel smoothing . . . . .	75
3.3.2. Variational tube tracing using coupled curves on sparse surface points . . . . .	76
3.4. Layer label assignment . . . . .	88
3.4.1. Nucleus classification . . . . .	89
3.4.2. Cell classification . . . . .	90
3.5. The effect of <i>PIN2/4</i> knockout on proliferation in the Arabidopsis thaliana root tip . . . . .	91
3.6. Implementation: The iRoCS Toolbox . . . . .	94
<b>4. Summary</b>	<b>97</b>
<b>A. Variational attenuation correction</b>	<b>99</b>
A.1. Energy derivatives . . . . .	99
A.1.1. General framework . . . . .	99
A.1.2. Gâteaux derivatives of the basic simulation equation . . . . .	102
A.1.3. Explicit polynomial solution of the approximate Poisson noise model . . . . .	102
A.1.4. Regularization . . . . .	103
A.2. Numerical integration . . . . .	104
A.2.1. Integration along thin rays . . . . .	105
A.2.2. Interpolation along conic rays . . . . .	105
A.3. Numerical differentiation . . . . .	105
A.4. Data conditioning for direct L-BFGS-B optimization . . . . .	106
<b>B. Arabidopsis sample preparation</b>	<b>109</b>
B.1. Nucleus-based analysis . . . . .	109
B.2. Cell boundary-based analysis . . . . .	109
B.3. Pre-processing . . . . .	110

## Preface

... who doubtless will proceed in making and imparting more Observations, the better to evince the goodness of these his Glasses.

Dr. Regenerus de Graaf (1673) about Leewenhoeck's microscopes

Since the first stunning discoveries by Anton van Leewenhoeck (1632-1723) using his hand-crafted microscopes (Leewenhoeck and de Graaf, 1673), microscopy is an invaluable tool for the understanding of sub-cellular structure and interactions of and within biological specimen. The quality of Leewenhoeck's microscopes with up to 270× magnification was unreached for the following 200 years, till in the 1850s the physicist and optician Ernst Abbe laid the foundations for today's understanding of wave optics. In cooperation with the engineer Carl Zeiss and the glass manufacturer Otto Schott he substantially improved the image quality of microscopes based on his theoretical findings (Lummer and Reiche, 1910). In 1886 they produced the first apochromatic objectives without chromatic (color-dependent) aberrations and with substantially reduced spherical aberrations. The combination of these objectives with the illumination method developed by Köhler (1893) mark the current standard for trans-illumination microscopy.

Next to trans-illumination and incident light, fluorescence and auto-luminescence effects opened a new way of observing biological structures. Many biological samples exhibit natural auto-fluorescence, but the success of fluorescence microscopy stems from the possibility to selectively mark specific structures with appropriate fluorescent dyes. Fluorescence is very specific and allows clear distinction of marked structures from each other and the background. Prerequisites are a band-limited light source that is adjusted to the excitation spectrum of the fluorophore and an emission filter that is adjusted to the fluorophore's emission spectrum. Ideally, the spectra of the involved band-pass filters are disjoint which allows to only view the relevant emission.

The isolation and purification of the green fluorescent protein by Shimomura et al. (1962) allows in-vivo studies using fluorescence microscopy. Almost any protein can be augmented by the small GFP construct (and its variants with different excitation and emission light spectra), thus allowing to observe signaling processes on sub-cellular resolution in living specimen over time.

Another cornerstone was the development of the confocal point-scanning microscope which was first patented by Minsky (1957). The confocal principle increases the resolution especially along the optical axis by effectively suppressing out-of-focus light at two confocal pinholes. The confocal point spread function (PSF) tails off within few micrometers and can be well approximated by an anisotropic Gaussian function (Zhang et al., 2007; Cole et al., 2011). Confocal microscopy allows to image deep into thick tissues and record successive optical sections with varying depth which can be reconstituted into 3-D volumetric images of the specimen with high resolution along all dimensions. Davidovits and Egger (1969) replaced the classical full-spectral illumination by a Helium-Neon (He-Ne) laser that was rastered over the specimen. His vision were in-vivo studies using confocal microscopy, which till today are only possible in rare special cases.



# 1. Introduction

Modern microscopes equipped with digital capture devices produce huge amounts of 3-D(+t) data. Unbiased quantitative evaluation of these data requires automated image analysis techniques able to map the measured intensity distributions to physical quantities and to the anatomy of the imaged specimen. Several effects hinder the direct use of the measured intensities for quantification tasks. They include physically well-understood effects like light absorption, refraction and scatter and signal dispersion due to the point spread function (PSF) of the optical system. However, also random elements in the photon counting process leading to Poisson distributed intensity measurements superimposed by Gaussian read-out noise have to be considered when designing algorithms to process and analyze microscopic data.

Deconvolution techniques to estimate and reduce artifacts introduced by the point spread function are well established for microscopic 3-D data. They can be subdivided into approaches that assume knowledge of the point spread function and blind deconvolution approaches that simultaneously estimate the point spread function and the real signal (Sarder and Nehorai, 2006; Keuper et al., 2013). Both approaches implicitly assume that the effect of the point spread function is spatially invariant, *i.e.* the PSF shape is always the same independent of the recording position. Usually these approaches are iterative and non-linear to also reconstruct missing frequencies given appropriate prior knowledge. More sophisticated reconstruction algorithms drop the assumption of spatial invariance. They estimate local deconvolution kernels and blend the local reconstructions using appropriate interpolation functions. Especially for single plane illumination microscopy (SPIM) the imperfect light sheet geometry requires the assumption of locally varying signal degradation (Temerinac-Ott et al., 2012).

Although the confocal principle reduces the domain of the point spread function, the obtained resolution is anisotropic with high resolution within the image plane and lower resolution along the optical axis. Its effect can be well approximated by a convolution with an anisotropic Gaussian (Zhang et al., 2007; Cole et al., 2011).

In thick specimen spatial invariance of the point spread function is certainly violated since light refraction and scatter locally change its geometry. Imagine the simple case of one interface between two perfectly transparent media with different refractive indices perpendicular to the optical axis. Light hitting the surface in a  $90^\circ$  angle just changes its speed, but rays in the periphery of the illumination cone change their angle. With increasing depth the point spread function elongates accompanied by a focal shift. This effect is known as spherical aberration (Egner and Hell, 2006). Spherical aberrations are of specific interest, since they are one of the major sources of signal loss when the refractive indices of immersion and embedding media differ. Some microscope manufacturers solve this problem in hardware by adapting the focus with respect to imaging depth given the

known refractive indices, but if possible the media should be chosen to match each other and the specimen as well as possible.

Modeling of light scatter at interfaces within the specimen is harder because it depends on the specimen's geometry and the different media contained in its volume. For fixed samples clearing procedures that replace the liquid content of the specimen by liquids matching the refractive index of the embedding medium are most promising. Ideally all media are adjusted to the refractive index of the specimen's membranes.

Assuming we did all to reduce the discussed effects there is still the problem of light absorption which will be tackled in detail in chapter 2.

With the possibility to selectively knock-out specific genes, analyses of the downstream effects are required to understand their purpose. Knocking out a gene in coding DNA, can lead to drastic changes in phenotype that are easily observed by eye, others lead to very subtle differences that require averaging over populations to distinguish them from natural variation. In both cases the changes are described as deviations from the wild type, which itself shows natural variation. Instead of directly comparing individuals of a population with altered phenotype to individuals of the wild type population, comparison to an abstract atlas of the wild type is desired. Such atlases are well established for many model organisms in zoology like the mouse (*Mus*) (Lein et al., 2007; Dorr et al., 2008), fruit fly (*Drosophila*) (Fowlkes et al., 2008), nematode (*Caenorhabditis elegans*) (Long et al., 2009; Liu et al., 2009) and zebrafish (*Danio rerio*) (Ronneberger et al., 2012). But they are lacking for model organisms from botany, e.g. *Arabidopsis thaliana*. Laibach (1943) promoted *Arabidopsis* for genetic and proteomic studies. Its relatively small genome consists of 157 Mbp (Megabase pairs) grouped in ten Chromosomes which are fully sequenced. Its fast life cycle allows to quickly generate and cultivate genetically modified lines.

The plasticity of plants precludes the definition of whole plant atlases, but plants show recurring patterns in individual organs that can be well described. However, atlases on a single-cell scale can only be defined in very few exceptional cases. In chapter 3 we approach the goal of providing an *Arabidopsis* root tip atlas. The simple root geometry allows to map all measurements to a common bent cylinder coordinate system, which we refer to as **intrinsic Root Coordinate System (iRoCS)**. The resulting unified description of key events in iRoCS allows to analyze not only single recordings of roots, but to pool over plant populations and anatomically compare them among each other. We will show that pooling allows to find subtle differences which are normally masked by natural variation.

### 1.1. Contributions

We embedded the basic variational formulation of the attenuation estimation and correction developed for the **Virtual Brain Explorer in Zebrafish (ViBE-Z)** (Ronneberger et al., 2012) into a probabilistic maximum a-posteriori probability (MAP) framework based on an extended image formation model. The extended model includes wavelength-dependent attenuation, photo bleaching and a more realistic mixed Poisson-Gaussian noise assumption. We will show, that already a rough zero-order approximation to photo bleaching significantly improves the estimated attenuation fields and

the corresponding reconstructions of the intensities. Additionally we experimented with the prior assumption of piece-wise constant attenuation using total variation to allow for local discontinuities in the attenuation field, *e.g.* at the outer sample boundaries. Furthermore, introduction of a sparsity prior enforces zero attenuation in areas where an estimate is not supported by measurements. Finally, we present a way to obtain many different views of a sample using a standard confocal microscope and thereby better constrain the problem with additional measurements. This allows extensions to more general image formation models. We give preliminary results on synthetic data that show the general applicability of our idea.

Large parts of the presented extensions are published in Schmidt et al. (2013b,a).

The development of algorithms to fit the intrinsic root coordinate system to confocal microscopic 3-D images involves many small innovations ranging from image processing to abstract high level analysis using continuous models. Based on the spherical tensor filter framework of Reisert (2008), we developed a rotation-invariant trainable detector to detect cell nuclei in confocal recordings of the root tip (Skibbe et al., 2012). To register the bent cylinder coordinate system to pre-classified epidermis nuclei we developed a variational tube tracing algorithm (Schmidt et al., 2012) which is described in detail in section 3.3.2. In contrast to other tube tracing approaches, it requires only sparsely distributed surface points and is very robust to noise. A final classification extends the continuous cylinder coordinates by a discrete biologically meaningful dimension: the cell layer.

We published the full iRoCS toolbox in *The Plant Journal* (Schmidt et al., 2014). The also contained cell-boundary-based pipeline was developed by Kun Liu (Liu et al., 2013).

## List of publications

### Journal

- S. Lienkamp, A. Ganner, C. Boehlke, **T. Schmidt**, S. Arnold, T. Schäfer, D. Romaker, J. Schuler, S. Hoff, C. Powelske, A. Eifler, C. Krönig, A. Bullerkotte, R. Nitschke, E. Kuehn, E. Kim, H. Burkhardt, T. Brox, O. Ronneberger, J. Gloy and G. Walz. Inversin relays Frizzled-8 signals to promote proximal pronephros development. *Proceedings of the National Academy of Sciences*, **107(47)**, 2010, 20388–20393. doi:10.1073/pnas.1013070107.
- H. Skibbe, M. Reisert, **T. Schmidt**, T. Brox, O. Ronneberger and H. Burkhardt. Fast Rotation Invariant 3D Feature Computation utilizing Efficient Local Neighborhood Operators. *IEEE Transactions on Pattern Analysis and Machine Intelligence*, **34(8)**, 2012, 1563–1575. doi:10.1109/TPAMI.2011.263.
- O. Ronneberger, K. Liu, M. Rath, D. Rueß T. Mueller, H. Skibbe, B. Drayer, **T. Schmidt**, A. Filippi, R. Nitschke, T. Brox, H. Burkhardt and W. Driever. ViBE-Z: A Framework for 3D Virtual Colocalization Analysis in Zebrafish Larval Brains. *Nature Methods*, **9(7)**, 2012, 735–742. doi:10.1038/nmeth.2076.
- T. Schmidt**, J. Dürr, M. Keuper, T. Blein, K. Palme and O. Ronneberger. Variational attenuation correction in two-view confocal microscopy. *BMC Bioinformatics*, **14**, 2013a, 366. doi:10.1186/1471-2105-14-366.

- T. Schmidt**, T. Pasternak, K. Liu, T. Blein, D. Aubry-Hivet, A. Dovzhenko, J. Duerr, W. Teale, F. A. Ditengou, H. Burkhardt, O. Ronneberger and K. Palme. The iRoCS Toolbox – 3D analysis of the plant root apical meristem at cellular resolution. *The Plant Journal*, **77(5)**, 2014, 806–814. doi:10.1111/tpj.12429.
- K. Liu, H. Skibbe, **T. Schmidt**, T. Blein, K. Palme, T. Brox and O. Ronneberger. Rotation-Invariant HOG Descriptors using Fourier Analysis in Polar and Spherical Coordinates. *International Journal of Computer Vision*, **106(3)**, 2014, 342–364. doi:10.1007/s11263-013-0634-z.

## Conference

- J. Schulz, **T. Schmidt**, O. Ronneberger, H. Burkhardt, T. Pasternak, A. Dovzhenko and K. Palme. Fast Scalar and Vectorial Grayscale Based Invariant Features for 3D Cell Nuclei Localization and Classification. *Lecture Notes in Computer Science*, **4174/2006**, 2006, 182–191. doi:10.1007/11861898\_19.
- J. Fehr, O. Ronneberger, J. Schulz, **T. Schmidt**, M. Reisert and H. Burkhardt. Invariance via Group-Integration: A Feature Framework for 3D Biomedical Image Analysis. *Proceedings of Computer Graphics and Imaging*, 2008, 276–285.
- M. Keuper, **T. Schmidt**, J. Padeken, P. Heun, K. Palme, H. Burkhardt and O. Ronneberger. 3D Deformable Surfaces with Locally Self-Adjusting Parameters - A Robust Method to Determine Cell Nucleus Shapes. *IEEE International Conference on Pattern Recognition*, 2010, 2254–2257. doi:10.1109/ICPR.2010.552.
- D. Mai, **T. Schmidt** and H. Burkhardt. Robust Identification of Locally Planar Objects Represented by 2D Point Clouds under Affine Distortions. *Lecture Notes in Computer Science*, **6376**, 2010, 91–100. doi:10.1007/978-3-642-15986-2\_10.
- H. Skibbe, M. Reisert, **T. Schmidt**, K. Palme, O. Ronneberger and H. Burkhardt. 3D Object Detection Using a Fast Voxel-Wise Local Spherical Fourier Tensor Transformation. *Lecture Notes in Computer Science*, **6376**, 2010, 412–421. doi:10.1007/978-3-642-15986-2\_42.
- M. Keuper, **T. Schmidt**, M. Rodriguez-Franco, W. Schamel, T. Brox, H. Burkhardt and O. Ronneberger. Hierarchical Markov Random Fields for Mast Cell Segmentation in Electron Microscopic Recordings. *IEEE International Symposium on Biomedical Imaging*, 2011, 973–978. doi:10.5244/C.25.33.
- K. Liu, H. Skibbe, **T. Schmidt**, T. Blein, K. Palme and O. Ronneberger. 3D Rotation-Invariant Description from Tensor Operation on Spherical HOG Field. *British Machine Vision Conference*, 2011, 33.1–33-12. doi:10.5244/C.25.33.
- T. Schmidt**, M. Keuper, T. Pasternak, K. Palme and O. Ronneberger. Modeling of Sparsely Sampled Tubular Surfaces Using Coupled Curves. In *Pattern Recognition (Proc. DAGM)*. 2012, pp. 83–92. doi:10.1007/978-3-642-32717-9\_9.
- M. Keuper, **T. Schmidt**, M. Temerinac-Ott, J. Padeken, P. Heun, O. Ronneberger and T. Brox. Blind deconvolution of widefield fluorescence microscopic data by regularization of the optical transfer

function (OTF). In *IEEE Conference on Computer Vision and Pattern Recognition (CVPR)*. 2013, pp. 2179 – 2186. doi:10.1109/CVPR.2013.283.

K. Liu, **T. Schmidt**, T. Blein, J. Dürr, K. Palme and O. Ronneberger. Joint 3D Cell Segmentation and Classification in the Arabidopsis Root using Energy Minimization and Shape Priors. In *IEEE International Symposium on Biomedical Imaging (ISBI)*. 2013, pp. 422–425. doi:10.1109/ISBI.2013.6556502.

**T. Schmidt**, J. Dürr, M. Keuper, T. Blein, K. Palme and O. Ronneberger. Variational Attenuation Correction of Two-View Confocal Microscopic Recordings. In *IEEE International Symposium on Biomedical Imaging (ISBI)*. 2013, pp. 169–172. doi:10.1109/ISBI.2013.6556439.

## 1.2. Glossary

### Basic linear algebra

$i$	The imaginary unit ( $i^2 = -1$ )
$x \in \mathbb{R}, \mathbb{C}$	Scalar real or complex value
$\mathbf{x} \in \mathbb{R}^n, \mathbb{C}^n$	Column vector of real or complex values
$\mathbf{X} \in \mathbb{R}^{n \times m}, \mathbb{C}^{n \times m}$	Matrix of real or complex values
$\bar{x}, \bar{\mathbf{x}}, \bar{\mathbf{X}}$	Complex conjugate for scalars, vectors (element-wise) and matrices (element-wise)
$\mathbf{x}^\top, \mathbf{X}^\top$	Vector-, Matrix transpose
$\mathbf{X}^* := \bar{\mathbf{X}}^\top$	Adjoint of $\mathbf{X}$
$\langle \mathbf{x}, \mathbf{y} \rangle = \sum_i x_i \bar{y}_i$	The dot product of $\mathbf{x}$ and $\mathbf{y}$

### Tensorfields

$I \in [\mathbb{R}^d \rightarrow \mathbb{R}]$	Scalar field ( <i>e.g.</i> the image function)
$\mathbf{I} \in [\mathbb{R}^d \rightarrow \mathbb{R}^k]$	Vectorial field ( <i>e.g.</i> the image gradient or image features)
$\nabla I = \left( \frac{\partial I}{\partial x_1}, \dots, \frac{\partial I}{\partial x_d} \right)^\top \in [\mathbb{R}^d \rightarrow \mathbb{R}^d]$	Gradient of $I$
$\Delta I = \sum_{i=1}^d \frac{\partial^2 I}{\partial x_i^2} \in [\mathbb{R}^d \rightarrow \mathbb{R}]$	Laplacian of $I$
$I \cdot J$	Element-wise multiplication of two scalar fields
$I \cdot \mathbf{J}$	Element-wise multiplication of the scalar field $I$ with the vectorial field $\mathbf{J}$ (element-wise scalar multiplication)

### Biological notation

DAPI	4',6-diamidino-2-phenylindole (dye binding adenine-thymine bonds in DNA)
PI	Propidium iodide (dye marking cellulose in cell walls)
$PIN$ / $PIN$ / $pin$	The pinformed gene / protein / knock out mutant

## 2. Variational attenuation correction

Approaches for quantifying the amount of proteins or metabolites within a specimen are well established in western blots and mass spectrometry. They allow very accurate integrative molecule quantification but are not able to localize molecules in the specimen. For this task confocal microscopy is the state-of-the art. Its high spatial resolution allows 3-D sub-micron localization of fluorescently marked proteins. The measured intensities are not proportional to the amount of marked molecules, *i.e.* confocal microscopy allows binary decisions on the existence or absence of a fluorescent dye, but its direct quantification in thick samples is currently impossible.

Photon loss along the excitation and emission light paths by absorption or random scatter lead to attenuation of the recorded intensities. Both effects result in a multiplicative reduction of the number of collected photons by a local tissue specific factor, and can therefore be modeled by the Beer-Lambert's law. In this chapter, we will present efficient physically motivated algorithms to reconstruct the attenuation-free intensities leading to measurements which are closer to the underlying marker distributions.

Single view approaches try to estimate both, the unknown real intensity (proportional to the number of photons) and the attenuation coefficient for each recording position from one recording. This requires strong prior assumptions to constrain the solution space. Egner and Hell (2006) and Booth et al. (1998) assume an exponential signal decay with increasing depth. The resulting models can be used to correct images of samples with constant attenuation throughout the cubic recording volume. Spherical aberration induced attenuation and attenuation within homogeneous samples after proper preparation as *e.g.* cut tissue samples follow this assumption quite well (Guan et al., 2008). However, these models cannot resolve local attenuation changes in the recording volume. In contrast, Čapek et al. (2006) and Stanciu et al. (2010) estimate the attenuation from the per-slice intensity statistics. The overall intensity distribution is adapted towards a reference maximizing the overall coherence. These statistically motivated approaches can only globally adjust the intensity distribution of whole image slices but are not able to incorporate spatial context neither within nor across slices.

**Contributions:** We will first introduce a general image formation model for confocal microscopy with ideal point-spread function and pure absorption. We will briefly recall the variational two-view attenuation correction developed in Ronneberger et al. (2012) for the ViBE-Z zebrafish brain atlas. Then we will extend it in several directions, including more realistic noise statistics, photo bleaching, wavelength-dependent attenuation, and excitation light shaping. We will present a new prior assumption improving the reconstruction quality for sparse samples and analyze the effect of different loss functions in the smoothness prior. Finally, the effect of different numerical integration schemes on the approximation accuracy will be analyzed and alternative optimization schemes presented leading to lower energy solutions.

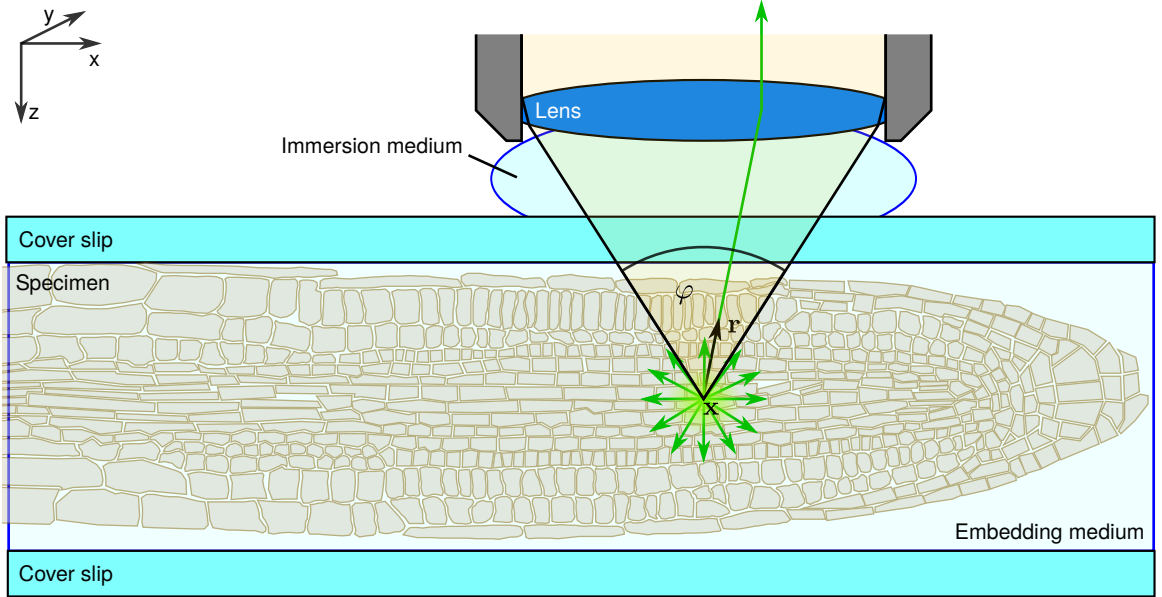


**Figure 2.1.:** Imaging setup. The specimen is embedded between two cover slips to allow recordings from both sides. Incident light in the aperture cone with opening angle  $\varphi$  focused at position  $\mathbf{x}$  leads to fluorescence emission (green). The light path for one sample emission ray with direction  $\mathbf{r}$  is shown.

Parts of the following extensions were presented at the International Symposium on Biomedical Imaging (ISBI 2013) (Schmidt et al., 2013b) and in BMC Bioinformatics (Schmidt et al., 2013a).

## 2.1. Image Formation Model

We use the simplified refraction-free discrete ray model described by Ronneberger et al. (2012) to simulate a confocal microscope.

According to Beer-Lambert's law the light transmission  $T^{[\alpha]} \in [0, 1]$  of a homogeneously absorbing medium for monochromatic light is given by

$$T^{[\alpha]} := \frac{I}{I_0} = e^{-\alpha L}$$

where  $I_0 \in \mathbb{R}^+$  is the initial intensity and  $I \in \mathbb{R}^+$  is the intensity after traveling a distance of  $L \in \mathbb{R}^+$  through a medium with absorption coefficient  $\alpha \in \mathbb{R}^+$ . The superscript  $[\alpha]$  indicates that the transmission depends on absorption coefficient  $\alpha$ . We will use this notation throughout to distinguish different models. In general, the absorption  $\alpha$  is a function of the light's wavelength  $\lambda \in \mathbb{R}^+$ . This will be discussed later.

In inhomogeneous media with space-variant attenuation  $\alpha : \mathbb{R}^3 \rightarrow \mathbb{R}^+$  we get the attenuation along the light ray originating in  $\mathbf{x}$  with direction  $\mathbf{r}$  as the integral over infinitesimally short homogeneous

absorption path segments

$$T_{\mathbf{r}}^{[\alpha]}(\mathbf{x}) := e^{-\int_0^\infty \alpha(\mathbf{x}+\ell \cdot \mathbf{r}) d\ell}.$$

Assume a point light source at position  $\mathbf{x}$  emitting light equally distributed in all directions. The fraction of light reaching the surface of the sphere centered at  $\mathbf{x}$  with radius  $R$  after space-variant absorption is then given by

$$C^{[\alpha,R]}(\mathbf{x}) = \int_S e^{-\int_0^R \alpha(\mathbf{x}+\ell \cdot \mathbf{r}) d\ell} d\mathbf{r} \quad (2.1)$$

where  $S$  is the unit sphere surface.

A microscope lens only captures light in a cone defined by the numerical aperture (NA) of the lens and the refractive indices of the media the light travels through. Assuming a medium with constant refractive index  $n$ , results in the opening angle  $\varphi$

$$\varphi = 2 \cdot \text{asin} \frac{\text{NA}}{n}$$

of the cone, as shown in Fig. 2.1

We model the aperture by a mask  $s : S \rightarrow \{0, 1\}$  on the unit sphere that is one for rays captured by the lens and zero otherwise. We assume that the object is small and the medium around the object is perfectly transparent. Therefore we can again integrate along infinite rays leading to the final cone transmission function

$$C^{[\alpha]}(\mathbf{x}) := \int_S s(\mathbf{r}) e^{-\int_0^\infty \alpha(\mathbf{x}+\ell \cdot \mathbf{r}) d\ell} d\mathbf{r}. \quad (2.2)$$

If light with intensity  $I_0$  was emitted at the focal point  $\mathbf{x}$  (and only there) we measure an intensity of

$$I(\mathbf{x}) = I_0(\mathbf{x}) \cdot \int_S s(\mathbf{r}) e^{-\int_0^\infty \alpha(\mathbf{x}+\ell \cdot \mathbf{r}) d\ell} d\mathbf{r}.$$

The aperture mask  $s(\mathbf{r})$  can also describe more complicated aperture geometries allowing to model structured illumination approaches without changing the general framework. We will employ this in section 2.2.8.

We will now follow a burst of photons on their way through a confocal microscope:

Assume a monochromatic point light source emitting  $I_0$  photons per second. The total number of photons emitted during excitation time  $\Delta t > 0$  is  $M_0 = I_0 \cdot \Delta t$ . Only the fraction given by the excitation cone transmission function  $C^{[\alpha_{\text{ex}}]}(\mathbf{x})$  reaches the focal point  $\mathbf{x}$ . At  $\mathbf{x}$  photons are absorbed with probability  $p^{\text{hit}} : \mathbb{R}^3 \rightarrow [0, 1]$  which is proportional to the spatio-temporally variant fluorophore concentration<sup>1</sup> and lower energy photons emitted in equally distributed directions. The ratio of emitted to absorbed photons is described by the quantum efficiency  $q \in [0, 1]$  of the fluorophore. Emitted photons get again absorbed on their way through the sample according to the emission transmission function  $C^{[\alpha_{\text{em}}]}(\mathbf{x})$ . The remaining photons reach the photo multiplier leading to a Poisson distributed read-out. The readout is linearly scaled by the detector gain  $a \in \mathbb{R}^+$  and the

<sup>1</sup>Even for fixed samples the fluorophore concentration changes with the absorbed photon dose due to bleaching.

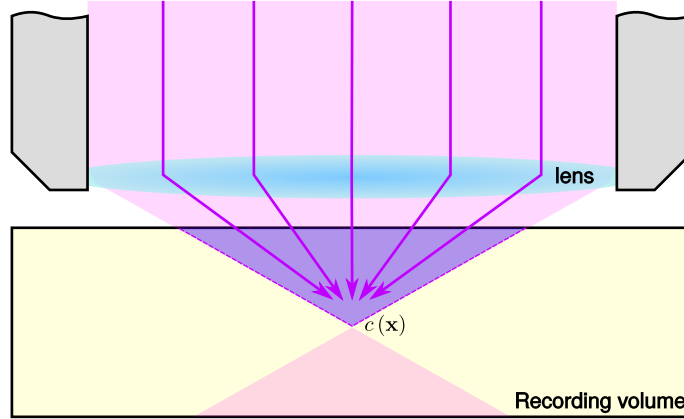


**Figure 2.2.:** 2D sketch of the bleaching regions. Excitation light focused in pink regions leads to bleaching at  $\mathbf{x}$ , or equivalently, excitation light focused at  $\mathbf{x}$  leads to bleaching in the purple area. Purple regions with dashed outline indicate positions altering  $p^{\text{hit}}(\mathbf{x})$  before it is scanned.

detector offset  $b \in \mathbb{R}$  to optimally use the dynamic range of the data type storing the measurements. Finally, thermal effects add Gaussian noise with standard deviation  $\sigma \in \mathbb{R}^+$ .

The Poisson mean  $\lambda_{\varphi}(\mathbf{x})$  is given by the expected number of photons reaching the detector for scan position  $\mathbf{x}$ , therefore

$$\lambda_{\varphi}(\mathbf{x}) = M_0 \cdot \underbrace{\int_S s^{\text{ex}}(\mathbf{r}) e^{-\int_0^{\infty} \alpha_{\text{ex}}(\mathbf{x}+\ell\mathbf{r}) d\ell} d\mathbf{r}}_{C^{[\alpha_{\text{ex}}]}(\mathbf{x})} \cdot p^{\text{hit}}(\mathbf{x}) \cdot q \cdot \underbrace{\int_S s^{\text{em}}(\mathbf{r}) e^{-\int_0^{\infty} \alpha_{\text{em}}(\mathbf{x}+\ell\mathbf{r}) d\ell} d\mathbf{r}}_{C^{[\alpha_{\text{em}}]}(\mathbf{x})}. \quad (2.3)$$

The image formation model is then given by

$$I(\mathbf{x}) = a \cdot \rho(\mathbf{x}) + \eta(\mathbf{x}) \quad (2.4)$$

$$\text{where } \rho(\mathbf{x}) \sim \mathcal{P}_{\lambda_{\varphi}(\mathbf{x})}(\xi) = \frac{(\lambda_{\varphi}(\mathbf{x}))^{\xi}}{\xi!} e^{-\lambda_{\varphi}(\mathbf{x})} \quad \text{and} \quad \eta(\mathbf{x}) \sim \mathcal{G}_{b,\sigma}(\xi) = \frac{1}{\sqrt{2\pi\sigma^2}} e^{-\frac{(\xi-b)^2}{2\sigma^2}}.$$

The detector offset  $b$  was included as mean of the Gaussian noise component  $\eta(\mathbf{x})$ . In practice, we remove  $b$  in a pre-processing step and will drop it in further derivations. For sparse samples  $b$  can be easily determined as the most frequent intensity occurring in the recordings. The Gaussian standard deviation  $\sigma \in \mathbb{R}^+$  is a free parameter that has to be adjusted to match the noise statistics for each recording setup.

### 2.1.1. Photo bleaching

Absorption of photons by fluorophores can already lead to out-of-focus fluorescence and irreversibly damage affected fluorophores, known as photo bleaching. We will ignore the out-of-focus emission

because its bulk is blocked by the collection pinhole, but bleaching steadily reduces  $p^{\text{hit}}(\mathbf{x})$  (and therefore the measured intensity) in regions exposed to excitation light (Fig. 2.2).

Let's assume a fluorophore gets destroyed by a hitting photon with probability  $p \ll 1$ . The probability  $p^{\text{hit}}(\mathbf{x})$  of hitting an intact fluorophore at position  $\mathbf{x}$  is steadily reduced during bleaching. The random process involved has the following urn equivalent: Assume a box containing  $N$  coins (possible photon paths) of which initially  $K(\mathbf{x})$  show heads (active fluorophores). The bleaching process corresponds to a random experiment in which for each photon a random coin is drawn from the box. If it shows tails, we just put it back into the box, but if it shows heads we turn it with probability  $p$  before putting it back. The probability of hitting an intact fluorophore after  $M(\mathbf{x})$  photons equals the proportion of coins showing heads after  $M(\mathbf{x})$  coin draws. This can be expressed as

$$p^{\text{hit}}(\mathbf{x}) = \sum_{k=0}^{K(\mathbf{x})} P(k|N, M(\mathbf{x}), p) \cdot \frac{k}{N}$$

$$P(k|N, M(\mathbf{x}), p) = \begin{cases} \delta(K(\mathbf{x}) - k) & \text{if } M(\mathbf{x}) = 0 \\ 0 & \text{if } k > K(\mathbf{x}) \\ P(k|N, M(\mathbf{x}) - 1, p) \left(1 - \frac{p}{N} \cdot k\right) \\ + P(k+1|N, M(\mathbf{x}) - 1, p) \cdot \frac{p}{N} \cdot (k+1) & \text{otherwise} \end{cases}$$

The marginalization over the number of fluorophores leads to the compound interest formula with interest rate  $\left(1 - \frac{p}{N}\right)$  over  $M(\mathbf{x})$  time intervals with given base value of  $p_0^{\text{hit}}(\mathbf{x}) := \frac{K(\mathbf{x})}{N}$

$$p^{\text{hit}}(\mathbf{x}) = p_0^{\text{hit}}(\mathbf{x}) \cdot \left(1 - \frac{p}{N}\right)^{M(\mathbf{x})} = \frac{K(\mathbf{x})}{N} \cdot \left(1 - \frac{p}{N}\right)^{M(\mathbf{x})}.$$

We are interested in the initial probabilities  $p_0^{\text{hit}} : \mathbb{R}^3 \rightarrow [0, 1]$  which are proportional to the initial fluorophore concentration. Given the known scanning order and excitation attenuation field, we can correct for bleaching even though all measurements (except measurements in the first plane) are distorted by prior out-of-focus exposure. When neglecting the boundary, the overall number of photons reaching  $\mathbf{x} = (x, y, z)$  linearly increases with depth  $z$ . When recording voxel  $\mathbf{x}$ , it has been already bleached by approx.  $M(\mathbf{x}) := (z-1) \cdot M_0 \cdot C^{\text{ex}}(\mathbf{x})$  photons, reducing the fluorescence probability to

$$p^{\text{hit}}(\mathbf{x}) = p_0^{\text{hit}}(\mathbf{x}) \cdot \left(1 - \frac{p}{N}\right)^{M(\mathbf{x})} = p_0^{\text{hit}}(\mathbf{x}) \cdot \left(1 - \frac{p}{N}\right)^{(z-1) \cdot M_0 \cdot C^{\text{ex}}(\mathbf{x})}.$$

Plugging this into equation 2.3 we get the final average number of detected photons

$$\lambda_{\varphi}(\mathbf{x}) = M_0 \cdot C^{\text{[ex]}}(\mathbf{x}) \cdot p_0^{\text{hit}}(\mathbf{x}) \cdot \left(1 - \frac{p}{N}\right)^{(z-1) \cdot M_0 \cdot C^{\text{[ex]}}(\mathbf{x})} \cdot q \cdot C^{\text{[em]}}(\mathbf{x}). \quad (2.5)$$

In the upcoming sections we will present several simplifications of the general model that allow efficient and accurate estimation of the attenuation fields and the “real intensities” we would have measured without the modeled signal degradation. We will give explicit schemes to solve the problem given discrete measurements and show the efficacy of the approach on synthetic and real biological data.

## 2.2. Energy formulation

Within this section we derive energy functionals to estimate the local attenuation in multiple microscopic recordings of biological specimen. We will employ the calculus of variations to obtain the energy derivatives needed to solve the attenuation estimation problem using gradient-based numerical solvers. Where easily possible we also give analytic solutions to sub-problems or second derivatives to be able to also employ approaches using higher order derivative information to speed up the computations using *e.g.* Newton's method.

### 2.2.1. MAP energy formulation

Let  $\hat{I} : \Omega \rightarrow \mathbb{R}^+$ ,  $\hat{I}(\mathbf{x}) := a \cdot M_0 \cdot p^{\text{hit}}(\mathbf{x}) \cdot q$  be an estimate of the “real” attenuation-free intensities, where  $\Omega \subset \mathbb{R}^3$  is the recording volume. Further, let  $\alpha_{\text{ex}} : \Omega \rightarrow \mathbb{R}^+$  be the attenuation coefficients for the excitation wavelength,  $\alpha_{\text{em}} : \mathbb{R}^3 \rightarrow \mathbb{R}^+$  the attenuation coefficients for the emission wavelength, and  $\theta \in \mathbb{R}^n$  a set of scalar parameters we want to estimate. Our goal is to maximize the posterior probability  $P(\hat{I}, \alpha_{\text{ex}}, \alpha_{\text{em}}, \theta | I_1, \dots, I_k)$  given  $k$  independent microscopic recordings  $I_i : \Omega \rightarrow \mathbb{R}$ ,  $i = 1, \dots, k$  of the sample.

We assume that the noise is independent for every voxel. Within this thesis we restrict ourselves to Gaussian statistics with per-voxel mean  $\mu_i(\mathbf{x}) := f(F_i(\mathbf{x}))$  and standard deviation  $\sigma(\mathbf{x}) := g(F_i(\mathbf{x}))$ , where we define  $F_i : \Omega \rightarrow \mathbb{R}^+$ ,  $i = 1, \dots, k$  to be simulated intensities according to a specific simplification of the general image formation model.  $f : \mathbb{R} \rightarrow \mathbb{R}$  and  $g : \mathbb{R} \rightarrow \mathbb{R}^+$  are arbitrary intensity transformations. The dependency of both functions on  $F_i$  allows to also approximately model non-Gaussian noise statistics, as will be seen in the concrete models.

With the Gaussian noise assumption we can formulate the probability of the measurements given the underlying model parameters and obtain

$$P(I_1, \dots, I_k | \alpha_{\text{ex}}, \alpha_{\text{em}}, \hat{I}, \theta) = \prod_{i=1}^k \prod_{\mathbf{x} \in \Omega'} \frac{1}{\sqrt{2\pi (g(F_i(\mathbf{x})))^2}} e^{-\frac{(f(I_i(\mathbf{x})) - f(F_i(\mathbf{x})))^2}{2(g(F_i(\mathbf{x})))^2}} \quad (2.6)$$

where  $\Omega'$  is the discrete image domain.

To obtain the posterior probability for our model parameters, we apply Bayes' rule

$$P(\alpha_{\text{ex}}, \alpha_{\text{em}}, \hat{I}, \theta | I_1, \dots, I_k) = \frac{P(I_1, \dots, I_k | \alpha_{\text{ex}}, \alpha_{\text{em}}, \hat{I}, \theta) P(\alpha_{\text{ex}}, \alpha_{\text{em}}, \hat{I}, \theta)}{P(I_1, \dots, I_k)}. \quad (2.7)$$

We want to find the parameter set maximizing the posterior probability

$$\arg \max_{\alpha_{\text{ex}}, \alpha_{\text{em}}, \hat{I}, \theta} P(\alpha_{\text{ex}}, \alpha_{\text{em}}, \hat{I}, \theta | I_1, \dots, I_k) = \arg \max_{\alpha_{\text{ex}}, \alpha_{\text{em}}, \hat{I}, \theta} P(I_1, \dots, I_k | \alpha_{\text{ex}}, \alpha_{\text{em}}, \hat{I}, \theta) P(\alpha_{\text{ex}}, \alpha_{\text{em}}, \hat{I}, \theta).$$

Therefore the prior probability of the measurements  $P(I_1, \dots, I_k)$ , that are independent of the optimization variables, could be dropped.  $P(\alpha_{\text{ex}}, \alpha_{\text{em}}, \hat{I}, \theta)$  allows to add any prior information that

may guide the optimization. For the moment we will just leave it as a place-holder and give specific priors in the corresponding concrete models.

Instead of maximizing the posterior we minimize its negative logarithm, leading to the general (continuous) energy minimization problem

$$\begin{aligned} \arg \min_{\alpha_{\text{ex}}, \alpha_{\text{em}}, \hat{I}, \theta} E(\alpha_{\text{ex}}, \alpha_{\text{em}}, \hat{I}, \theta) &= \sum_{i=1}^k \int_{\Omega} \left( \frac{f(I_i(\mathbf{x})) - f(F_i(\mathbf{x}))}{g(F_i(\mathbf{x}))} \right)^2 + \ln(g(F_i(\mathbf{x}))) \, d\mathbf{x} + E_{\text{prior}} \\ \text{subject to} \quad \forall \mathbf{x} \in \Omega &: \alpha_{\text{ex}}(\mathbf{x}) \geq 0 \wedge \alpha_{\text{em}}(\mathbf{x}) \geq 0 \end{aligned} \quad (2.8)$$

where constant terms were removed and  $E_{\text{prior}} = -\ln P(\alpha_{\text{ex}}, \alpha_{\text{em}}, \hat{I}, \theta)$ .

We will use gradient-based optimization to minimize the energy. In sloppy notation we obtain the derivative w.r.t. an arbitrary parameter  $\theta \in \{\alpha_{\text{ex}}(\mathbf{x}), \alpha_{\text{em}}(\mathbf{x}), \hat{I}(\mathbf{x}), \theta_1, \dots, \theta_n\}$

$$\frac{\partial E(\alpha_{\text{ex}}, \alpha_{\text{em}}, \hat{I}, \theta)}{\partial \theta} = - \sum_{i=1}^k \int_{\Omega} \frac{2D_i(\mathbf{x}) f'(F_i(\mathbf{x})) + (2D_i^2(\mathbf{x}) - 1) g'(F_i(\mathbf{x}))}{g(F_i(\mathbf{x}))} \cdot \frac{\partial F_i(\mathbf{x})}{\partial \theta} \, d\mathbf{x} + \frac{\partial E_{\text{prior}}}{\partial \theta} \quad (2.9)$$

where  $D_i(\mathbf{x}) := \frac{f(I_i(\mathbf{x})) - f(F_i(\mathbf{x}))}{g(F_i(\mathbf{x}))}$ ,  $f'(F_i(\mathbf{x})) = \frac{\partial f(F_i(\mathbf{x}))}{\partial F_i(\mathbf{x})}$  and  $g'(F_i(\mathbf{x})) = \frac{\partial g(F_i(\mathbf{x}))}{\partial F_i(\mathbf{x})}$ . We also compute the second derivative

$$\begin{aligned} \frac{\partial^2 E(\alpha_{\text{ex}}, \alpha_{\text{em}}, \hat{I}, \theta)}{\partial \theta^2} &= \sum_{i=1}^k \int_{\Omega} \left( \frac{2(f'(F_i(\mathbf{x})) + 2D_i(\mathbf{x}) g'(F_i(\mathbf{x})))^2 - (2D_i^2(\mathbf{x}) + 1) g'^2(F_i(\mathbf{x}))}{g^2(F_i(\mathbf{x}))} \right. \\ &\quad \left. - \frac{2D_i(\mathbf{x}) f''(F_i(\mathbf{x})) + (2D_i^2(\mathbf{x}) - 1) g''(F_i(\mathbf{x}))}{g(F_i(\mathbf{x}))} \right) \left( \frac{\partial F_i(\mathbf{x})}{\partial \theta} \right)^2 \\ &\quad - \frac{2D_i(\mathbf{x}) f'(F_i(\mathbf{x})) + (2D_i^2(\mathbf{x}) - 1) g'(F_i(\mathbf{x}))}{g(F_i(\mathbf{x}))} \frac{\partial^2 F_i(\mathbf{x})}{\partial \theta^2} \, d\mathbf{x} + \frac{\partial^2 E_{\text{prior}}}{\partial \theta^2}. \end{aligned} \quad (2.10)$$

Detailed step-by-step derivations are given in Appendix A.1.1.

The specific energy minimization problems presented in the following sections are fully specified by the microscope simulation  $F_i$  and the gray value transformations  $f$  and  $g$  modeling different noise statistics. In practice we only employ terms which are linear in  $F_i$  for second order optimization. Therefore, terms involving the second derivative  $\frac{\partial^2 F_i}{\partial \theta^2}$  are never evaluated. The pre-factors of the first derivative

$$\begin{aligned} \mathcal{D}_i^{[f, g, F_i]}(\mathbf{x}) &:= \frac{2D_i(\mathbf{x}) f'(F_i(\mathbf{x})) + (2D_i^2(\mathbf{x}) - 1) g'(F_i(\mathbf{x}))}{g(F_i(\mathbf{x}))} \\ \mathcal{D}_i^{[f, g, F_i]'}(\mathbf{x}) &:= \frac{2(f'(F_i(\mathbf{x})) + 2D_i(\mathbf{x}) g'(F_i(\mathbf{x})))^2 - (2D_i^2(\mathbf{x}) + 1) g'^2(F_i(\mathbf{x}))}{g^2(F_i(\mathbf{x}))} \\ &\quad - \frac{2D_i(\mathbf{x}) f''(F_i(\mathbf{x})) + (2D_i^2(\mathbf{x}) - 1) g''(F_i(\mathbf{x}))}{g(F_i(\mathbf{x}))} \end{aligned}$$

and the derivative  $\frac{\partial F_i(\mathbf{x})}{\partial \theta}$  of the simulation equation fully characterize the derivatives needed in the different practical implementations we will describe in the following.

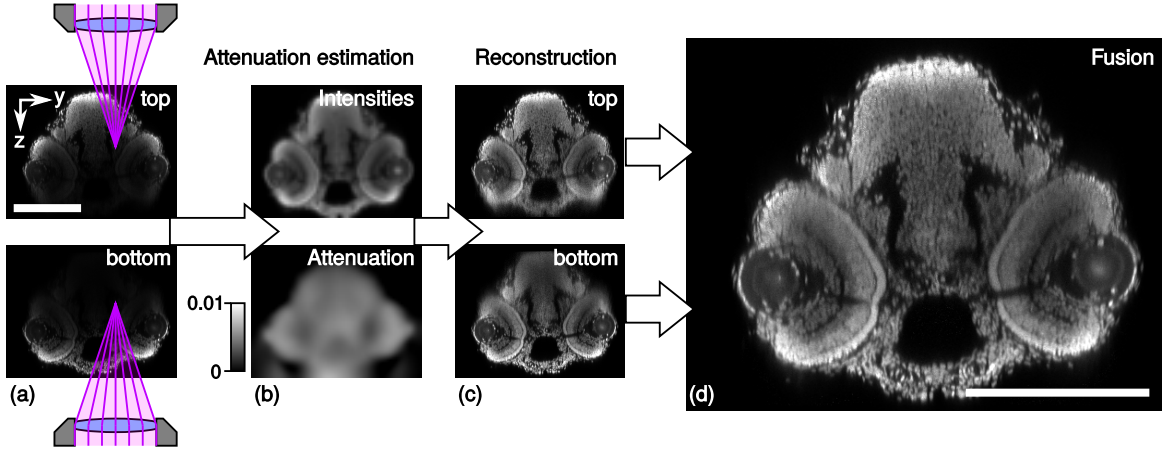


**Figure 2.3.:** The attenuation correction work flow. (a)  $zy$ -sections of raw confocal stacks from two views (top/bottom). (b) Estimated real intensities and attenuation coefficients in low processing resolution. (c) Independently reconstructed intensities (high resolution) of the top- and bottom-views. (d) Final result after fusion of the reconstructed views. Scale bars:  $200\mu\text{m}$ . Shown intensities are clipped to the  $[0, 500]$  range.

### 2.2.2. Gaussian noise model: ViBE-Z two-view attenuation correction

As introduction, we will briefly describe the first variational approach developed and implemented by Ronneberger et al. (2012) to recover the attenuation-free intensities given two spatially registered recordings of the same sample from opposite sides (Fig. 2.3).

#### Assumptions:

**Wavelength independent attenuation** ( $\alpha := \alpha_{\text{ex}} = \alpha_{\text{em}}$ ) Only one attenuation field needs to be estimated. Besides other effects, this implies that absorption of excitation light at the fluorophores is ignored, which is approximately true for small fluorophore concentrations.

**Equal excitation and emission cone geometries** ( $s := s_{\text{ex}} = s_{\text{em}}$ ) Given also wavelength independent attenuations, we obtain identical cone transmission functions in both light paths ( $C := C^{[\alpha_{\text{ex}}]} = C^{[\alpha_{\text{em}}]}$ ).

**No bleaching** ( $p = 0$ ) The distribution of active fluorophores is constant over time.

**Pure Gaussian noise** The measured intensities are only affected by additive Gaussian noise with fixed standard deviation. The Poissonian part of the noise statistics is not modeled.

The corresponding simplified image formation model is

$$I(\mathbf{x}) \approx \hat{I}(\mathbf{x}) \left( \int_S s(\mathbf{r}) \cdot e^{-\int_0^\infty \alpha(\mathbf{x}+\ell\mathbf{r}) d\ell} d\mathbf{r} \right)^2 + n(\mathbf{x}) . \quad (2.11)$$

To solve for attenuation coefficients  $\alpha(\mathbf{x})$  and true intensities  $\hat{I}(\mathbf{x})$  two independent and noise-free measurements per recording position are required. To get these two independent measurements

the sample volume is recorded twice, once from top giving  $I_1(\mathbf{x})$  and the second time after a  $180^\circ$  rotation giving  $I_2(\mathbf{x})$ .

Can et al. (2003) already exploited the idea of two-view recordings to increase the signal to noise ratio (SNR) of intensities in the reconstructed volume. They directly relate the absorption to the observed fluorophore distribution. This model is applicable for perfectly transparent samples absorbing excitation light only during the fluorescence process. Absorption not related to fluorescence is ignored. We go the opposite way and assume that fluorescence-induced attenuation is negligible compared to the overall absorption in the tissue. The confocal image formation allows to recover attenuation in not fluorescently marked areas as long as they cast “shadows” through the sample along the excitation and emission cones of the different views (Visser et al., 1991; Ronneberger et al., 2012). Only in regions where the light hits no fluorophores at all or in the case of full absorption an estimation is impossible.

Both recordings have to be accurately registered to a common coordinate system. When turning the sample holder, specimen may deform in liquid media. Due to these deformations, rigid registration may be insufficient to align the different views. We therefore use an elastic registration to refine the initial euclidean transformation and warp  $I_2$  according to the deformation field to the coordinate system of  $I_1$ . The overall transformation is still very close to a pure  $180^\circ$  rotation. Plugged into our image formation model we obtain the simulation equations

$$F_i^{[\alpha, \hat{I}]}(\mathbf{x}) := \hat{I}(\mathbf{x}) \cdot \left( \int_S s_i(\mathbf{r}) \cdot e^{-\int_0^\infty \alpha(\mathbf{x} + \ell \mathbf{r}) d\ell} d\mathbf{r} \right)^2 = \left( \hat{I} \cdot C_i^{[\alpha]^2} \right)(\mathbf{x}), \quad (2.12)$$

where  $i = 1$  for the top and  $i = 2$  for the bottom recording.  $s_2(\mathbf{r})$  is simply rotated by  $180^\circ$  relative to  $s_1(\mathbf{r})$ .  $F_i^{[\alpha, \hat{I}]}(\mathbf{x})$  are the expected noise-free intensity measurements at  $\mathbf{x}$ . Their variations w.r.t.  $\alpha$  and  $\hat{I}$  are given by

$$\begin{aligned} \left. \frac{d}{d\epsilon} F_i^{[\alpha + \epsilon h, \hat{I}]}(\mathbf{x}) \right|_{\epsilon=0} &= -2 \int_S s_i(\mathbf{r}) \int_0^\infty \left( \hat{I} \cdot C_i^{[\alpha]} \cdot T_{\mathbf{r}}^{[\alpha]} \right)(\mathbf{x}) \cdot h(\mathbf{x} + \ell \mathbf{r}) d\ell d\mathbf{r} \\ \left. \frac{d}{d\epsilon} F_i^{[\alpha, \hat{I} + \epsilon h]}(\mathbf{x}) \right|_{\epsilon=0} &= C_i^{[\alpha]^2}(\mathbf{x}) \cdot h(\mathbf{x}). \end{aligned}$$

We have to add prior knowledge to also solve the ill-posed problem with noisy measurements. Our prior assumption is a smooth attenuation field w.r.t. the  $L_2$ -norm of its gradient (Tikhonov, 1963) leading to the prior probability

$$P(\alpha, \hat{I}) \sim e^{-\frac{\lambda}{2} \int_\Omega \|\nabla \alpha(\mathbf{x})\|_2^2 d\mathbf{x}}.$$

The constant normalization factor only depending on  $\lambda$  and the number of measurements was omitted since it does not alter the optimum.

The negative logarithm of the full MAP problem is given by

$$\begin{aligned} E^{[\mathcal{G}]}(\alpha, \hat{I}) &= \sum_{i=1}^2 \int_\Omega \left( I_i(\mathbf{x}) - F_i^{[\alpha, \hat{I}]}(\mathbf{x}) \right)^2 d\mathbf{x} + \frac{\lambda}{2} \int_\Omega \|\nabla \alpha(\mathbf{x})\|_2^2 d\mathbf{x} \\ \text{with } &\forall \mathbf{x} \in \Omega : \alpha(\mathbf{x}) \geq 0 \end{aligned} \quad (2.13)$$

## 2. Variational attenuation correction

---

where the constant term  $+\ln(\sigma)$  was omitted, because it only affects the magnitude of the energy.

To model pure Gaussian noise we can choose the gray value transformations  $f^{[\mathcal{G}]}(s) := \text{id}(s) = s$  and  $g^{[\mathcal{G}]}(s) := \sigma$ . Scaling the energy does not change the position of the optimum, therefore, we remove the dependency on  $\sigma$  and set  $g^{[\mathcal{G}]}(s) := 1$  instead. The corresponding factors  $\mathcal{D}^{[\text{id}, 1, F_i^{[\alpha, \hat{I}]}]}$  and  $\mathcal{D}^{[\text{id}, 1, F_i^{[\alpha, \hat{I}]}]}'$  simplify to

$$\mathcal{D}_i^{[\text{id}, 1, F_i^{[\alpha, \hat{I}]}]}(\mathbf{x}) = 2 \left( I_i(\mathbf{x}) - F_i^{[\alpha, \hat{I}]}(\mathbf{x}) \right) \quad \text{and} \quad \mathcal{D}_i^{[\text{id}, 1, F_i^{[\alpha, \hat{I}]}]}'(\mathbf{x}) = 2. \quad (2.14)$$

We plug  $\mathcal{D}^{[\text{id}, 1, F_i^{[\alpha, \hat{I}]}]}$  and the variations of  $F_i^{[\alpha, \hat{I}]}$  into (2.9) and get the functional derivatives of the energy w.r.t.  $\alpha$  and  $\hat{I}$

$$\begin{aligned} \frac{\delta E^{[\mathcal{G}]}(\alpha, \hat{I})}{\delta \alpha(\mathbf{x})} &= 2 \sum_{i=1}^2 \int_S s_i(\mathbf{r}) \int_0^\infty \left( \mathcal{D}_i^{[\text{id}, 1, F_i^{[\alpha, \hat{I}]}]} \cdot \hat{I} \cdot C_i^{[\alpha]} \cdot T_{\mathbf{r}}^{[\alpha]} \right) (\mathbf{x} - \ell \mathbf{r}) \, d\ell \, d\mathbf{r} - \lambda \cdot \Delta \alpha(\mathbf{x}) \\ \frac{\delta E^{[\mathcal{G}]}(\alpha, \hat{I})}{\delta \hat{I}(\mathbf{x})} &= - \sum_{i=1}^2 \left( \mathcal{D}_i^{[\text{id}, 1, F_i^{[\alpha, \hat{I}]}]} \cdot C_i^{[\alpha]^2}(\mathbf{x}) \right) \end{aligned}$$

where  $\Delta$  is the Laplacian operator.

The required Gâteaux derivatives of the simulation are given in Appendix A.1.2. In the derivatives w.r.t. the attenuations we additionally change  $h(\mathbf{x} + \ell \mathbf{r})$  to  $h(\mathbf{y})$  using the substitution  $\mathbf{y} := \mathbf{x} + \ell \mathbf{r}$ . Afterwards we rename  $\mathbf{y}$  to  $\mathbf{x}$  to get the final functional derivative. This is possible due to the integration over infinitely long rays. In practice we always integrate until we reach the image border and assume zero attenuation outside the image domain.

Given an estimate of  $\alpha$  we can analytically find the optimal  $\hat{I}$  for that estimate by solving  $\frac{\delta E^{[\mathcal{G}]}(\alpha, \hat{I})}{\delta \hat{I}(\mathbf{x})} = 0$  which has the unique solution

$$\hat{I}(\mathbf{x}) = \frac{\sum_{i=1}^2 \left( I_i \cdot C_i^{[\alpha]^2} \right) (\mathbf{x})}{\sum_{i=1}^2 C_i^{[\alpha]^4}(\mathbf{x})}. \quad (2.15)$$

Ronneberger et al. (2012) exploit this explicit intensity update to significantly improve the convergence speed of the optimization in the final implementation.

### 2.2.3. Zero order bleaching estimation

The described model ignores bleaching effects. In the following extensions we want to at least account for it in a zero order approximation, in which we assume that the intensities of the second recording are globally lower than the intensities of the first recording. We model this as constant factors  $\beta_i \in (0, 1]$  which are applied to the simulated intensities

$$F_i^{[\alpha, \hat{I}, \beta_i]} := \beta_i \cdot F_i^{[\alpha, \hat{I}]} = \beta_i \cdot \hat{I}(\mathbf{x}) \cdot \left( \int_S s_i(\mathbf{r}) \cdot e^{-\int_0^\infty \alpha(\mathbf{x} + \ell \mathbf{r}) \, d\ell} \, d\mathbf{r} \right)^2 \quad (2.16)$$

before comparing them to the measured intensities  $I_i$ . We set the intensity scaling  $\beta_1 := 1$  for the first recording.

For the model of Ronneberger et al. (2012) bleaching slightly changes the energy to

$$E^{[\mathcal{G}]}(\alpha, \hat{I}, \beta_2) = \sum_{i=1}^2 \int_{\Omega} \left( I_i(\mathbf{x}) - F_i^{[\alpha, \hat{I}, \beta_i]}(\mathbf{x}) \right)^2 d\mathbf{x} + \frac{\lambda}{2} \int_{\Omega} \|\nabla \alpha(\mathbf{x})\|_2^2 d\mathbf{x}$$

with  $\beta_1 = 1 \quad \wedge \quad \beta_2 \in (0, 1] \quad \wedge \quad \forall \mathbf{x} \in \Omega : \alpha(\mathbf{x}) \geq 0$  (2.17)

where  $\beta_2$  has to be optimized alongside with  $\alpha$  and  $\hat{I}$ . The characteristic pre-factors

$$\mathcal{D}_i^{[\text{id}, 1, F_i^{[\alpha, \hat{I}, \beta_i]}]}(\mathbf{x}) = 2 \left( I_i(\mathbf{x}) - F_i^{[\alpha, \hat{I}, \beta_i]}(\mathbf{x}) \right) \quad \text{and} \quad \mathcal{D}_i^{[\mathcal{G}, \alpha, \hat{I}, \beta_i]'}(\mathbf{x}) = 2$$

are identical to (2.14), only the simulations have been replaced by the ones including  $\beta_i$ . The variations of the simulation are simply scaled by the new factor. Also including the additional partial derivative w.r.t.  $\beta_i$  we obtain

$$\begin{aligned} \left. \frac{d}{d\epsilon} F_i^{[\alpha + \epsilon h, \hat{I}, \beta_i]}(\mathbf{x}) \right|_{\epsilon=0} &= -2\beta_i \int_S s_i(\mathbf{r}) \int_0^\infty \left( \hat{I} \cdot C_i^{[\alpha]} \cdot T_{\mathbf{r}}^{[\alpha]} \right)(\mathbf{x} - \ell \mathbf{r}) \cdot h(\mathbf{x} + \ell \mathbf{r}) d\ell d\mathbf{r} \\ \left. \frac{d}{d\epsilon} F_i^{[\alpha, \hat{I} + \epsilon h, \beta_i]}(\mathbf{x}) \right|_{\epsilon=0} &= \beta_i C_i^{[\alpha]^2}(\mathbf{x}) \cdot h(\mathbf{x}) \\ \frac{\partial}{\partial \beta_i} F_i^{[\alpha, \hat{I}, \beta_i]}(\mathbf{x}) &= \left( \hat{I} \cdot C_i^{[\alpha]^2} \right)(\mathbf{x}). \end{aligned} \quad (2.18)$$

Plugging  $\mathcal{D}_i^{[\text{id}, 1, F_i^{[\alpha, \hat{I}, \beta_i]}]}$  and the variations/partial derivatives of  $F_i^{[\alpha, \hat{I}, \beta_i]}$  into (2.9) gives the new set of functional/partial derivatives

$$\begin{aligned} \frac{\delta E^{[\mathcal{G}]}(\alpha, \hat{I}, \beta_2)}{\delta \alpha(\mathbf{x})} &= 2 \sum_{i=1}^2 \beta_i \int_S s_i(\mathbf{r}) \int_0^\infty \left( \mathcal{D}_i^{[\text{id}, 1, F_i^{[\alpha, \hat{I}, \beta_i]}]} \cdot \hat{I} \cdot C_i^{[\alpha]} \cdot T_{\mathbf{r}}^{[\alpha]} \right)(\mathbf{x} - \ell \mathbf{r}) d\ell d\mathbf{r} - \lambda \cdot \Delta \alpha(\mathbf{x}) \\ \frac{\delta E^{[\mathcal{G}]}(\alpha, \hat{I}, \beta_2)}{\delta \hat{I}(\mathbf{x})} &= - \sum_{i=1}^2 \beta_i \left( \mathcal{D}_i^{[\text{id}, 1, F_i^{[\alpha, \hat{I}, \beta_i]}]} \cdot C_i^{[\alpha]^2} \right)(\mathbf{x}) \\ \frac{\partial E^{[\mathcal{G}]}(\alpha, \hat{I}, \beta_2)}{\partial \beta_2} &= - \int_{\Omega} \left( \mathcal{D}_2^{[\text{id}, 1, F_2^{[\alpha, \hat{I}, \beta_2]}]} \cdot \hat{I} \cdot C_2^{[\alpha]^2} \right)(\mathbf{x}) d\mathbf{x}. \end{aligned} \quad (2.19)$$

We can speed up the optimization with a coordinate descent on the sub-space spanned by  $\hat{I}$  and  $\beta_2$  using Newton's method in an inner iteration. The required second derivatives are

$$\begin{aligned} \frac{\delta^2 E^{[\mathcal{G}]}(\alpha, \hat{I}, \beta_2)}{\delta \hat{I}(\mathbf{x})^2} &= \sum_{i=1}^2 \beta_i^2 \left( \mathcal{D}_i^{[\text{id}, 1, F_i^{[\alpha, \hat{I}, \beta_i]}]'} \cdot C_i^{[\alpha]^4} \right)(\mathbf{x}) \\ \frac{\partial^2 E^{[\mathcal{G}]}(\alpha, \hat{I}, \beta_2)}{\partial \beta_2^2} &= \int_{\Omega} \left( \mathcal{D}_2^{[\text{id}, 1, F_2^{[\alpha, \hat{I}, \beta_2]}]} \cdot \left( \hat{I} \cdot C_2^{[\alpha]^2} \right)^2 \right)(\mathbf{x}) d\mathbf{x}. \end{aligned} \quad (2.20)$$

In this specific case  $\hat{I}$  and  $\beta_2$  can even be optimized analytically in an alternating inner iteration given an estimate for  $\alpha$ . This requires to solve the linear equations

$$\hat{I}(\mathbf{x}) = \frac{\sum_{i=1}^2 \beta_i \left( I_i \cdot C_i^{[\alpha]^2} \right) (\mathbf{x})}{\sum_{i=1}^2 \beta_i^2 C_i^{[\alpha]^4} (\mathbf{x})} \quad \text{and} \quad \beta_2 = \frac{\int_{\Omega} \left( I_2 \cdot \hat{I} \cdot C_2^{[\alpha]^2} \right) (\mathbf{x}) \, d\mathbf{x}}{\int_{\Omega} \left( \hat{I} \cdot C_2^{[\alpha]^2} \right)^2 (\mathbf{x}) \, d\mathbf{x}}.$$

Equations (2.18) – (2.20) hold for all noise models using the simulation  $F_i^{[\alpha, \hat{I}, \beta_i]}$  when inserting their specific characteristic factors  $\mathcal{D}_i^{[f, g, F_i^{[\alpha, \hat{I}, \beta_i]}]}$  and  $\mathcal{D}_i^{[f, g, F_i^{[\alpha, \hat{I}, \beta_i]}]}'$ . Therefore, we will often refer to these equations instead of writing them down, to avoid redundancy.

#### 2.2.4. Approximate Poisson noise model (Anscombe)

If the noise statistics is dominated by the Poisson distributed photon counting process, the Gaussian noise model is not appropriate. We therefore present an alternative model approximating pure Poisson noise using Anscombe transformed data and simulations. As shown by Anscombe (1948) Poissonian statistics are well approximated by Gaussian statistics of the square root of the continuity corrected random variables. The Anscombe transform is defined as

$$\mathcal{A}(x) := \begin{cases} 2 \sqrt{x + \frac{3}{8}} & x > -\frac{3}{8} \\ 0 & \text{otherwise} \end{cases}$$

approximating the discrete Poisson distributed random variable  $x \geq 4$  by the Gaussian random variable  $\mathcal{A}(x)$  with approximate unit variance. We exploit this idea in Schmidt et al. (2013b), where we input gamma corrected input images ( $\gamma = 2$ ) and gamma correct the simulations accordingly for comparing measurements and simulations in the data term. Here, we slightly extend the model also incorporating the continuity correction constant  $\frac{3}{8}$  which has the nice side-effect of stabilizing the solutions compared to the “pure” gamma correction.

The Anscombe transform allows to transfer the Poisson model to the Gaussian framework by minimizing the energy

$$E^{\mathcal{A}}(\alpha, \hat{I}, \beta_2) = \sum_{i=1}^2 \int_{\Omega} \left( \mathcal{A}(I_i(\mathbf{x})) - \mathcal{A}\left(F_i^{[\alpha, \hat{I}, \beta_i]}(\mathbf{x})\right) \right)^2 d\mathbf{x} + \frac{\lambda}{2} \int_{\Omega} \|\nabla \alpha(\mathbf{x})\|_2^2 d\mathbf{x} \\ \text{with} \quad \beta_2 \in (0, 1] \quad \wedge \quad \forall \mathbf{x} \in \Omega : \alpha(\mathbf{x}) \geq 0 \quad (2.21)$$

Put into the general framework we now apply the gray value transformation  $f^{\mathcal{A}}(s) := \mathcal{A}(s)$  with derivative  $f^{\mathcal{A}'}(s) = \frac{2}{\mathcal{A}(s)}$ , and second derivative  $f^{\mathcal{A}''}(s) = -\frac{4}{\mathcal{A}^3(s)}$ . The standard deviation is again constant  $g^{\mathcal{A}}(s) := 1$ .

The pre-factors  $\mathcal{D}_i^{[\mathcal{A}, 1, F_i^{[\alpha, \hat{I}, \beta_i]}]}$  and  $\mathcal{D}_i^{[\mathcal{A}, 1, F_i^{[\alpha, \hat{I}, \beta_i]}]}'$  are given by

$$\mathcal{D}_i^{[\mathcal{A}, 1, F_i^{[\alpha, \hat{I}, \beta_i]}]}(\mathbf{x}) = 4 \left( \frac{\mathcal{A}(I_i(\mathbf{x}))}{\mathcal{A}\left(F_i^{[\alpha, \hat{I}, \beta_i]}(\mathbf{x})\right)} - 1 \right) \quad \text{and} \quad \mathcal{D}_i^{[\mathcal{A}, 1, F_i^{[\alpha, \hat{I}, \beta_i]}]}'(\mathbf{x}) = 8 \frac{\mathcal{A}(I_i(\mathbf{x}))}{\mathcal{A}^3\left(F_i^{[\alpha, \hat{I}, \beta_i]}(\mathbf{x})\right)}.$$

To obtain the final energy derivatives, we simply replace  $\mathcal{D}^{[\text{id}, 1, F_i^{[\alpha, \hat{I}, \beta_i]}]}$  by  $\mathcal{D}^{[\mathcal{A}, 1, F_i^{[\alpha, \hat{I}, \beta_i]}]}$  in (2.19) and (2.20).

As before it is possible to analytically solve for  $\hat{I}$  given an estimate for  $\alpha$  and  $\beta_2$ . However, instead of a linear equation, now the roots of a polynomial of degree four have to be determined. The corresponding derivation is given in Appendix A.1.3. An analytic solution for  $\beta_2$  cannot be given any more.

In practice an inner fixed-point iteration alternating between iteratively computing  $\hat{I}$  and iteratively computing  $\beta_2$  for fixed  $\alpha$  using Newton's method proved to be very stable. In most cases it converges within less than ten iterations to an accuracy of seven significant digits. To also capture more complicated cases we set the maximum number of iterations to twenty, although an exact solution is not required to continue the outer optimization.

### 2.2.5. Approximate Poisson-Gaussian noise model (Generalized Anscombe)

Starck et al. (1998) present an extension of the classical Anscombe transform to also approximate the sum of a scaled Poisson random variable and a Gaussian random variable. This generalized Anscombe transform

$$\mathcal{A}_{\mathcal{P}\mathcal{G}}(x) := \begin{cases} \frac{2}{a} \sqrt{ax + \frac{3}{8}a^2 + \sigma^2 - ab} & x > -\frac{3}{8}a - \frac{\sigma^2}{a} + b \\ 0 & \text{otherwise} \end{cases}$$

approximates the Poisson-Gaussian random variable  $x = a\rho + \eta$  where  $a \in \mathbb{R}^+$ ,  $\rho \sim \mathcal{P}^{[\lambda]}$  and  $\eta \sim \mathcal{G}^{[b, \sigma]}$  by the Gaussian random variable  $\mathcal{A}_{\mathcal{P}\mathcal{G}}(x)$  with approximate unit variance.

In accordance with Mäkitalo and Foi (2013) we apply the affine transforms  $\tilde{x} = \frac{x-b}{a}$  and  $\tilde{\sigma} = \frac{\sigma}{a}$  to obtain the simplified formulation

$$\mathcal{A}_{\mathcal{P}\mathcal{G}}(\tilde{x}) := \begin{cases} 2 \sqrt{\tilde{x} + \frac{3}{8} + \tilde{\sigma}^2} & \tilde{x} > -\frac{3}{8} - \tilde{\sigma}^2 \\ 0 & \text{otherwise} \end{cases}.$$

The energy for this model can be written as

$$E^{\mathcal{A}_{\mathcal{P}\mathcal{G}}}(\alpha, \hat{I}, \beta_2) = \sum_{i=1}^2 \int_{\Omega} \left( \mathcal{A}_{\mathcal{P}\mathcal{G}}\left(\frac{I_i(\mathbf{x})}{a}\right) - \mathcal{A}_{\mathcal{P}\mathcal{G}}\left(\frac{F_i^{[\alpha, \hat{I}, \beta_i]}(\mathbf{x})}{a}\right) \right)^2 d\mathbf{x} + \frac{\lambda}{2} \int_{\Omega} \|\nabla \alpha(\mathbf{x})\|_2^2 d\mathbf{x}$$

with  $\beta_2 \in (0, 1] \quad \wedge \quad \forall \mathbf{x} \in \Omega : \alpha(\mathbf{x}) \geq 0$  (2.22)

Note the identity of the generalized Anscombe model with the pure Poissonian Anscombe model from the previous section when setting  $a := 1$  and  $\sigma := 0$ .

Besides the division by the detector gain the derivations strictly follow the basic Anscombe model s.t.

$$\mathcal{D}_i^{[\mathcal{A}\mathcal{P}\mathcal{G}, 1, F_i^{[\alpha, \hat{I}, \hat{\beta}_i]}]}(\mathbf{x}) = \frac{4}{a} \left( \frac{\mathcal{A}\mathcal{P}\mathcal{G} \left( \frac{I_i(\mathbf{x})}{a} \right)}{\mathcal{A}\mathcal{P}\mathcal{G} \left( \frac{F_i^{[\alpha, \hat{I}, \hat{\beta}_i]}(\mathbf{x})}{a} \right)} - 1 \right) \text{ and } \mathcal{D}_i^{[\mathcal{A}\mathcal{P}\mathcal{G}, 1, F_i^{[\alpha, \hat{I}, \hat{\beta}_i]}]'}(\mathbf{x}) = \frac{8}{a^2} \frac{\mathcal{A}\mathcal{P}\mathcal{G} \left( \frac{I_i(\mathbf{x})}{a} \right)}{\mathcal{A}\mathcal{P}\mathcal{G}^3 \left( \frac{F_i^{[\alpha, \hat{I}, \hat{\beta}_i]}(\mathbf{x})}{a} \right)}. \quad (2.23)$$

The final derivatives are obtained by replacing  $\mathcal{D}^{[\text{id}, 1, F_i^{[\alpha, \hat{I}, \hat{\beta}_i]}]}$  by  $\mathcal{D}^{[\mathcal{A}\mathcal{P}\mathcal{G}, 1, F_i^{[\alpha, \hat{I}, \hat{\beta}_i]}]}$  in (2.19) and (2.20) as before.

### 2.2.6. Approximate Poisson-Gaussian noise model (Direct estimate)

In this section we recapitulate our findings published in Schmidt et al. (2013a).

As already discussed, the measured image intensities are dominated by the Poisson distributed photon counting process but they also contain additive Gaussian distributed read-out noise. The resulting noise model is the convolution of a scaled Poisson distribution with a zero-mean Gaussian distribution (assuming the offset is subtracted beforehand) with standard deviation  $\sigma \in \mathbb{R}^+$ . To allow practical computation, we approximate the Poisson distribution by a Gaussian distribution with variance proportional to its mean (which is a quite good approximation for Poisson mean  $> 20$ ). With this simplification we can exploit the linearity of the Gaussian distribution approximating the Poisson distribution and simply scale its mean and variance by detector gain  $a$ . We further assume, that the measured intensities are close to the scaled Poisson mean value and directly use them as variance estimate. The convolution of the two Gaussian distributions results in the combined Gaussian distribution

$$\begin{aligned} P(I_i(\mathbf{x}) | \alpha, \hat{I}, \hat{\beta}_i, \sigma) &\approx \frac{1}{\sqrt{2\pi I_i(\mathbf{x})}} e^{-\frac{(I_i(\mathbf{x}) - F_i^{[\alpha, \hat{I}, \hat{\beta}_i]}(\mathbf{x}))^2}{2I_i(\mathbf{x})}} * \frac{1}{\sqrt{2\pi\sigma^2}} e^{-\frac{(I_i(\mathbf{x}) - F_i^{[\alpha, \hat{I}, \hat{\beta}_i]}(\mathbf{x}))^2}{2\sigma^2}} \\ &= \frac{1}{\sqrt{2\pi (I_i(\mathbf{x}) + \sigma^2)}} e^{-\frac{(I_i(\mathbf{x}) - F_i^{[\alpha, \hat{I}, \hat{\beta}_i]}(\mathbf{x}))^2}{2(I_i(\mathbf{x}) + \sigma^2)}}. \end{aligned}$$

In Schmidt et al. (2013a) we also introduced a Poisson standard deviation scaling factor  $m \in \mathbb{R}^+$  which allows to weight the noise components against each other

$$P(I_i(\mathbf{x}) | \alpha, \hat{I}, \hat{\beta}_i, m, \sigma) \approx \frac{1}{\sqrt{2\pi (m^2 I_i(\mathbf{x}) + \sigma^2)}} e^{-\frac{(I_i(\mathbf{x}) - F_i^{[\alpha, \hat{I}, \hat{\beta}_i]}(\mathbf{x}))^2}{2(m^2 I_i(\mathbf{x}) + \sigma^2)}}. \quad (2.24)$$

For  $m = 0$  and  $\sigma = 1$  the Poisson-Gaussian model coincides with the pure Gaussian model presented in section 2.2.3.

The actual values for  $m$  and  $\sigma$  have to be determined in a microscope calibration phase. If unknown one of them can be fixed to an arbitrary value (we always fixed  $\sigma = 1$ ), and the other one adjusted to qualitatively obtain the optimum result. If additional sample information is available, *e.g.* the recordings consist of large homogeneous regions of different intensities, one can also try to estimate the parameters from the images themselves as done by Foi et al. (2008) for photographs. However, for sparsely marked biological samples this is rarely the case.

The final energy formulation is again obtained by replacing the maximization of the posterior probability by a minimization of its negative logarithm resulting in

$$E^{[\mathcal{P}\mathcal{G}]}(\alpha, \hat{I}, \beta_2) = \sum_{i=1}^2 \int_{\Omega} \left( \frac{I_i(\mathbf{x}) - F_i^{[\alpha, \hat{I}, \beta_i]}(\mathbf{x})}{\sqrt{m^2 I_i(\mathbf{x}) + \sigma^2}} \right)^2 d\mathbf{x} + \frac{\lambda}{2} \int_{\Omega} \|\nabla \alpha(\mathbf{x})\|_2^2 d\mathbf{x}$$

with  $\beta_2 \in (0, 1] \quad \wedge \quad \forall \mathbf{x} \in \Omega : \alpha(\mathbf{x}) \geq 0$  (2.25)

The assumption that the measured intensities are a good estimate of the Poisson mean make the denominator  $g^{[\mathcal{P}\mathcal{G}]}(F_i^{[\alpha, \hat{I}, \beta_i]}(\mathbf{x})) := \sqrt{m^2 I_i(\mathbf{x}) + \sigma^2}$  independent of the optimization variables. For each voxel it is only a scalar weighting factor making the derivatives particularly easy to compute. The factor is proportional to the measured intensity, giving the contribution of differences in high intensity regions a lower weight compared to low intensity regions in the energy. This is intuitive, since higher intensities carry higher uncertainty. As in the Gaussian case the intensities are not transformed s.t.  $f^{[\mathcal{P}\mathcal{G}]}(s) := \text{id}(s) = s$ .

The characteristic factors  $\mathcal{D}_i^{[\text{id}, \sqrt{m^2 I_i + \sigma^2}, F_i^{[\alpha, \hat{I}, \beta_i]}]}$  and  $\mathcal{D}_i^{[\text{id}, \sqrt{m^2 I_i + \sigma^2}, F_i^{[\alpha, \hat{I}, \beta_i]}]}'$  are very similar to the pure Gaussian case and given by

$$\mathcal{D}_i^{[\text{id}, \sqrt{m^2 I_i + \sigma^2}, F_i^{[\alpha, \hat{I}, \beta_i]}]}(\mathbf{x}) = 2 \frac{I_i(\mathbf{x}) - F_i^{[\alpha, \hat{I}, \beta_i]}(\mathbf{x})}{m^2 I_i(\mathbf{x}) + \sigma^2} \quad \text{and} \quad \mathcal{D}_i^{[\text{id}, \sqrt{m^2 I_i + \sigma^2}, F_i^{[\alpha, \hat{I}, \beta_i]}]}'(\mathbf{x}) = \frac{2}{m^2 I_i(\mathbf{x}) + \sigma^2}$$

which are plugged into (2.19) and (2.20) to get the final derivatives.

Given an estimate of  $\alpha$  and  $\beta_2$  the intensities can be optimized analytically, likewise given  $\alpha$  and  $\hat{I}$ ,  $\beta_2$  can be optimized analytically using the linear equations

$$\hat{I} = \frac{\sum_{i=1}^2 \beta_i \frac{(I_i \cdot C_i^{[\alpha]^2})(\mathbf{x})}{m^2 I_i(\mathbf{x}) + \sigma^2}}{\sum_{i=1}^2 \frac{\beta_i^2 C_i^{[\alpha]^4}(\mathbf{x})}{m^2 I_i(\mathbf{x}) + \sigma^2}} \quad \text{and} \quad \beta_2 = \frac{\int_{\Omega} \frac{(I_2 \cdot \hat{I} \cdot C_2^{[\alpha]^2})(\mathbf{x})}{m^2 I_2(\mathbf{x}) + \sigma^2} d\mathbf{x}}{\int_{\Omega} \frac{(\hat{I} \cdot C_2^{[\alpha]^2})^2(\mathbf{x})}{m^2 I_2(\mathbf{x}) + \sigma^2} d\mathbf{x}}$$

which will be exploited to solve these sub-problems in an inner fixed-point iteration as before.

### Dynamic mean adjustment

What if the measured intensities are no good estimator for the mean of the Poisson-Gaussian distributions? In low-intensity areas this assumption is quite accurate, but in high-intensity areas with

linearly increasing Poisson variance the error can become large. An alternative is to base the noise variance estimate on the simulated (noise-free) intensities  $F_i^{[\alpha, \hat{I}, \beta_i]}$ . The resulting formulation becomes slightly more complicated since the weights now dependent on the optimization parameters. The probability of measuring intensity  $I_i(\mathbf{x})$  (without priors) becomes

$$P(I_i(\mathbf{x})|\alpha, \hat{I}, \beta_i, m, \sigma) \approx \frac{1}{\sqrt{2\pi (m^2 F_i^{[\alpha, \hat{I}, \beta_i]}(\mathbf{x}) + \sigma^2)}} e^{-\frac{(I_i(\mathbf{x}) - F_i^{[\alpha, \hat{I}, \beta_i]}(\mathbf{x}))^2}{2(m^2 F_i^{[\alpha, \hat{I}, \beta_i]}(\mathbf{x}) + \sigma^2)}}.$$

The Gaussian normalization factor now changes with the intensity estimate, and has to be considered in the energy

$$\begin{aligned} E^{\mathcal{P}\mathcal{G}_2}(\alpha, \hat{I}, \beta_2) &= \sum_{i=1}^2 \int_{\Omega} \left( \frac{I_i(\mathbf{x}) - F_i^{[\alpha, \hat{I}, \beta_i]}(\mathbf{x})}{\sqrt{m^2 \cdot F_i^{[\alpha, \hat{I}, \beta_i]}(\mathbf{x}) + \sigma^2}} \right)^2 + \ln \left( \sqrt{m^2 F_i^{[\alpha, \hat{I}, \beta_i]}(\mathbf{x}) + \sigma^2} \right) d\mathbf{x} \\ &\quad + \lambda \int_{\Omega} \|\nabla \alpha(\mathbf{x})\|_2^2 d\mathbf{x} \\ \text{with } \beta_2 &\in (0, 1] \quad \wedge \quad \forall \mathbf{x} \in \Omega : \alpha(\mathbf{x}) \geq 0. \end{aligned} \quad (2.26)$$

As in the previous simplified variant of the Poisson-Gaussian model, this model reduces to the pure Gaussian model when setting  $m = 0$  and  $\sigma = 1$ .

As before  $f^{[\mathcal{P}\mathcal{G}_2]}(s) := \text{id}(s) = s$ , but the standard deviation  $g^{[\mathcal{P}\mathcal{G}_2]}(F_i^{[\alpha, \hat{I}, \beta_i]}) := \sqrt{m^2 F_i^{[\alpha, \hat{I}, \beta_i]} + \sigma^2}$  now depends on the simulated intensity making the characteristic factors  $\mathcal{D}_i^{[\text{id}, g^{[\mathcal{P}\mathcal{G}_2]}, F_i^{[\alpha, \hat{I}, \beta_i]}]}$  and  $\mathcal{D}_i^{[\text{id}, g^{[\mathcal{P}\mathcal{G}_2]}, F_i^{[\alpha, \hat{I}, \beta_i]}]}'$  a little more complicated

$$\begin{aligned} \mathcal{D}_i^{[\text{id}, g^{[\mathcal{P}\mathcal{G}_2]}, F_i^{[\alpha, \hat{I}, \beta_i]}]}(\mathbf{x}) &= \frac{2 \left( I_i(\mathbf{x}) - F_i^{[\alpha, \hat{I}, \beta_i]}(\mathbf{x}) \right) + m^2 \left( \frac{(I_i(\mathbf{x}) - F_i^{[\alpha, \hat{I}, \beta_i]}(\mathbf{x}))^2}{m^2 F_i^{[\alpha, \hat{I}, \beta_i]}(\mathbf{x}) + \sigma^2} - \frac{1}{2} \right)}{m^2 F_i^{[\alpha, \hat{I}, \beta_i]}(\mathbf{x}) + \sigma^2} \\ \mathcal{D}_i^{[\text{id}, g^{[\mathcal{P}\mathcal{G}_2]}, F_i^{[\alpha, \hat{I}, \beta_i]}]}'(\mathbf{x}) &= \frac{2 \left( 1 + m^2 \frac{(I_i - F_i^{[\alpha, \hat{I}, \beta_i]})(\mathbf{x})}{m^2 F_i^{[\alpha, \hat{I}, \beta_i]}(\mathbf{x}) + \sigma^2} \right)^2 - \frac{m^4}{2(m^2 F_i^{[\alpha, \hat{I}, \beta_i]}(\mathbf{x}) + \sigma^2)}}{m^2 F_i^{[\alpha, \hat{I}, \beta_i]}(\mathbf{x}) + \sigma^2} \end{aligned} \quad (2.27)$$

which, when plugged into (2.19) and (2.20), yield the final derivatives.

### 2.2.7. Wavelength dependent attenuation

Up to now our model only allowed for wavelength-independent attenuation. When dropping this assumption, different attenuation coefficients for excitation and emission wavelength have to be estimated at each recording position. With two recordings this generalized problem cannot be solved.

The generalization however allows us to model absorption of excitation light in fluorophores. In this special case we know the sites of additional attenuation along the excitation path, which are just the measured emission sites and we know that the attenuation at these sites is proportional to their expected intensity. This can be modeled as a wavelength-independent absorption  $\alpha$  as before which is modified in the excitation path by adding the intensity estimate scaled with a constant  $\gamma \in \mathbb{R}$ , s.t.  $\alpha_{\text{ex}}(\mathbf{x}) := \alpha(\mathbf{x}) + \gamma \hat{I}(\mathbf{x})$ .

The simulation of the noise-free intensities therefore changes to

$$F_i^{[\alpha, \hat{I}, \beta_i, \gamma]}(\mathbf{x}) := \beta_i \hat{I}(\mathbf{x}) \cdot \underbrace{\int_S s_i(\mathbf{r}) \cdot e^{-\int_0^\infty (\alpha + \gamma \hat{I})(\mathbf{x} + \ell \mathbf{r}) d\ell} d\mathbf{r}}_{=: C_i^{[\alpha, \hat{I}, \gamma]}(\mathbf{x})} \cdot \underbrace{\int_S s_i(\mathbf{r}) \cdot e^{-\int_0^\infty \alpha(\mathbf{x} + \ell \mathbf{r}) d\ell} d\mathbf{r}}_{=: C_i^{[\alpha]}(\mathbf{x})}$$

with Gâteaux/partial derivatives

$$\left. \frac{d}{d\epsilon} F_i^{[\alpha + \epsilon \hat{I}, \hat{I}, \beta_i, \gamma]}(\mathbf{x}) \right|_{\epsilon=0} = -\beta_i \int_S s_i(\mathbf{r}) \int_0^\infty \left( \hat{I} \cdot \left( T_{\mathbf{r}}^{[\alpha, \hat{I}, \gamma]} \cdot C_i^{[\alpha]} + C_i^{[\alpha, \hat{I}, \gamma]} \cdot T_{\mathbf{r}}^{[\alpha]} \right) \right) (\mathbf{x}) \cdot h(\mathbf{x} + \ell \mathbf{r}) d\ell d\mathbf{r}$$

$$\begin{aligned} \left. \frac{d}{d\epsilon} F_i^{[\alpha, \hat{I} + \epsilon h, \beta_i, \gamma]}(\mathbf{x}) \right|_{\epsilon=0} &= \beta_i \left( C_i^{[\alpha, \hat{I}, \gamma]} \cdot C_i^{[\alpha]} \right) (\mathbf{x}) \cdot h(\mathbf{x}) \\ &\quad - \gamma \beta_i \int_S s_i(\mathbf{r}) \left( \hat{I} \cdot T_{\mathbf{r}}^{[\alpha, \hat{I}, \gamma]} \cdot C_i^{[\alpha]} \right) (\mathbf{x}) \int_0^\infty h(\mathbf{x} + \ell \mathbf{r}) d\ell d\mathbf{r} \end{aligned}$$

$$\frac{\partial}{\partial \beta_i} F_i^{[\alpha, \hat{I}, \beta_i, \gamma]}(\mathbf{x}) = \left( \hat{I} \cdot C_i^{[\alpha, \hat{I}, \gamma]} \cdot C_i^{[\alpha]} \right) (\mathbf{x})$$

$$\frac{\partial}{\partial \gamma} F_i^{[\alpha, \hat{I}, \beta_i, \gamma]}(\mathbf{x}) = -\beta_i \left( \hat{I} \cdot C_i^{[\alpha]} \right) (\mathbf{x}) \cdot \int_S s_i(\mathbf{r}) T_{\mathbf{r}}^{[\alpha, \hat{I}, \gamma]}(\mathbf{x}) \int_0^\infty \hat{I}(\mathbf{x} + \ell \mathbf{r}) d\ell d\mathbf{r}.$$

We again use the Poisson-Gaussian noise approximation leading to the almost unchanged energy

$$\begin{aligned} E^{\mathcal{P}\mathcal{G}_2}(\alpha, \hat{I}, \beta_2, \gamma) &= \sum_{i=1}^2 \int_{\Omega} \frac{\left( I_i(\mathbf{x}) - F_i^{[\alpha, \hat{I}, \beta_i, \gamma]}(\mathbf{x}) \right)^2}{m^2 F_i^{[\alpha, \hat{I}, \beta_i, \gamma]}(\mathbf{x}) + \sigma^2} + \ln \left( \sqrt{m^2 F_i^{[\alpha, \hat{I}, \beta_i, \gamma]}(\mathbf{x}) + \sigma^2} \right) d\mathbf{x} \\ &\quad + \frac{\lambda}{2} \int_{\Omega} \|\nabla \alpha(\mathbf{x})\|_2^2 d\mathbf{x} \\ \text{with } &\beta_2 \in (0, 1] \quad \wedge \quad \gamma \in \mathbb{R}^+ \quad \wedge \quad \forall \mathbf{x} \in \Omega : \alpha(\mathbf{x}) \geq 0. \end{aligned} \quad (2.28)$$

Plugging the variations/partial derivatives of the simulation equation into (2.9) we obtain the functional/partial derivatives

$$\begin{aligned} \frac{\delta E^{\mathcal{P}\mathcal{G}_2}(\alpha, \hat{I}, \beta_2, \gamma)}{\delta \alpha(\mathbf{x})} &= \sum_{i=1}^2 \beta_i \int_S s_i(\mathbf{r}) \cdot \int_0^\infty \left( \mathcal{D}_i^{\left[ \text{id}, \mathcal{P}\mathcal{G}_2, F_i^{[\alpha, \hat{I}, \beta_i, \gamma]} \right]} \cdot \hat{I} \right. \\ &\quad \left. \cdot \left( T_{\mathbf{r}}^{[\alpha, \hat{I}, \gamma]} \cdot C_i^{[\alpha]} + C_i^{[\alpha, \hat{I}, \gamma]} \cdot T_{\mathbf{r}}^{[\alpha]} \right) \right) (\mathbf{x} - \ell \mathbf{r}) d\ell d\mathbf{r} - \lambda \Delta \alpha(\mathbf{x}) \end{aligned}$$

$$\begin{aligned}
\frac{\delta E_{\text{data}}^{\mathcal{P}\mathcal{G}_2, \gamma}(\alpha, \hat{I}, \beta_2, \gamma)}{\delta \hat{I}(\mathbf{x})} &= - \sum_{i=1}^2 \beta_i \left( \mathcal{D}_i^{\left[ \text{id}, g^{\mathcal{P}\mathcal{G}_2}, F^{\left[ \alpha, \hat{I}, \beta_i, \gamma \right]} \right]} \cdot C_i^{\left[ \alpha, \hat{I}, \gamma \right]} \cdot C_i^{\left[ \alpha \right]} \right) (\mathbf{x}) \\
&\quad + \gamma \sum_{i=1}^2 \beta_i \int_S s_i(\mathbf{r}) \int_0^\infty \left( \mathcal{D}_i^{\left[ \text{id}, g^{\mathcal{P}\mathcal{G}_2}, F^{\left[ \alpha, \hat{I}, \beta_i, \gamma \right]} \right]} \cdot \hat{I} \right. \\
&\quad \left. \cdot T_{\mathbf{r}}^{\left[ \alpha, \hat{I}, \gamma \right]} \cdot C_i^{\left[ \alpha \right]} \right) (\mathbf{x} - \ell \mathbf{r}) \, d\ell \, d\mathbf{r} \\
\frac{\partial E_{\text{data}}^{\mathcal{P}\mathcal{G}_2, \gamma}(\alpha, \hat{I}, \beta_2, \gamma)}{\partial \beta_2} &= - \int_{\Omega} \left( \mathcal{D}_2^{\left[ \text{id}, g^{\mathcal{P}\mathcal{G}_2}, F^{\left[ \alpha, \hat{I}, \beta_2, \gamma \right]} \right]} \cdot \hat{I} \cdot C_2^{\left[ \alpha, \hat{I}, \gamma \right]} \cdot C_2^{\left[ \alpha \right]} \right) (\mathbf{x}) \, d\mathbf{x} \\
\frac{\partial E_{\text{data}}^{\mathcal{P}\mathcal{G}_2, \gamma}(\alpha, \hat{I}, \beta_2, \gamma)}{\partial \gamma} &= \sum_{i=1}^2 \beta_i \int_{\Omega} \left( \mathcal{D}_i^{\left[ \text{id}, g^{\mathcal{P}\mathcal{G}_2}, F^{\left[ \alpha, \hat{I}, \beta_i, \gamma \right]} \right]} \cdot \hat{I} \cdot C_i^{\left[ \alpha \right]} \right) (\mathbf{x}) \\
&\quad \cdot \int_S s_i(\mathbf{r}) T_{\mathbf{r}}^{\left[ \alpha, \hat{I}, \gamma \right]}(\mathbf{x}) \int_0^\infty \hat{I}(\mathbf{x} + \ell \mathbf{r}) \, d\ell \, d\mathbf{r} \, d\mathbf{x}.
\end{aligned}$$

where the pre-factors  $\mathcal{D}_i^{\left[ \text{id}, g^{\mathcal{P}\mathcal{G}_2}, F^{\left[ \alpha, \hat{I}, \beta_i, \gamma \right]} \right]}$  for this noise model are the same as (2.27) when replacing the cone and ray transmissions accordingly. When inserting the pre-factors (2.23) instead, the generalized Anscombe model is obtained.

The per voxel intensity derivatives are not independent any more, therefore the up-to-now employed explicit coordinate descent in the sub-space spanned by  $\hat{I}$  cannot be easily applied. In our current implementation we solve the whole problem using L-BFGS-B making the optimization quite slow and the approach hardly applicable in practice.

### 2.2.8. Structured Illumination

To generalize the model to arbitrary wavelength dependent attenuation fields not only modeling absorption at the fluorophores we need to estimate three quantities per voxel, the expected intensity, and the attenuation fields for excitation and emission wavelengths. To solve this problem, at least three independent measurements for each voxel are required. One possibility to obtain arbitrarily many recordings is to change the sample holder geometry allowing recordings from arbitrary angles as done in single plane illumination microscopy (SPIM, Keller and Stelzer (2006)). However, the required specialized hardware is not yet available in standard laboratory environments. The preparation effort is quite high compared to slide-based microscopy and sample storing for later re-recording is hardly possible. The required registration of the different recordings to one common coordinate system further complicates the processing.

Instead we propose an approach that allows to employ conventional slide-based sample preparation. To obtain the required additional recordings we modify the excitation light geometry by changing the properties of the excitation aperture diaphragm. One easily applicable change is to narrow the aperture cone of the excitation light. This can be easily achieved in any standard confocal microscope by closing the aperture diaphragm to a specified area fraction of the open aperture. In

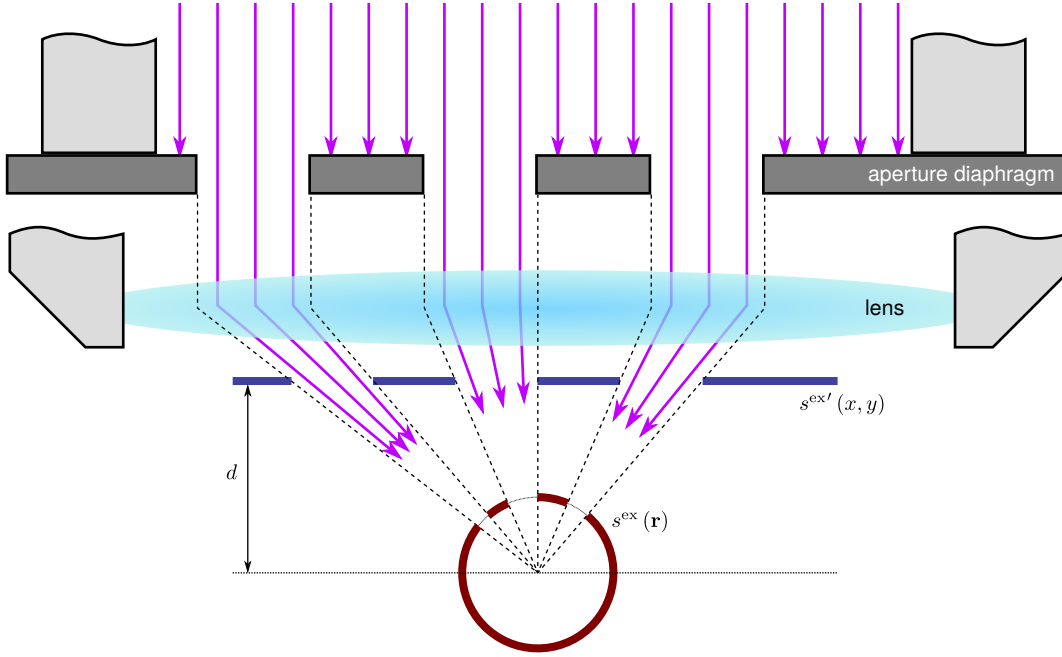


**Figure 2.4.:** 2D sketch of the excitation light path using an arbitrarily patterned aperture diaphragm. The diaphragm is inserted in the Fourier plane, where rays are parallel. When passing the lens the pattern becomes proportionally smaller till the rays converge at the focal point.  $s^{ex'} : \mathbb{R}^2 \rightarrow \{0, 1\}$  is the planar mask at distance  $d \in \mathbb{R}$  from the focal point. Both, mask and distance, are inputs to the simulation. The ray mask  $s^{ex} : S \rightarrow \{0, 1\}$  is the corresponding mask projected to the unit sphere surface which is used in the optimization. Purple arrows indicate sample excitation light rays.

many cases one can replace the diaphragm and insert a structured aperture mask instead. Both cases can be modeled when modifying the aperture mask functions  $s_i^{ex}(\mathbf{x})$  accordingly as shown in Fig. 2.4.

Theoretically, shaping the excitation cone even allows to estimate the attenuations and reconstruct the real intensities using recordings from one side only. However, in practice this requires very precise approximations of the integrations over the masked light cones. The disadvantage of additional recordings is increased recording time and loss of light due to the aperture mask leading to decreased signal to noise ratio. With our zero-order bleaching approximation we now estimate factors  $\beta_i$  for all recordings  $i = 2 \dots k$  (we again set  $\beta_1 := 1$  for the first recording).

The simulation equation for recording  $i$  changes to

$$F_i^{[\alpha_{ex}, \alpha_{em}, \hat{I}, \beta_i]}(\mathbf{x}) := \beta_i \hat{I}(\mathbf{x}) \cdot \underbrace{\int_S s_i^{ex}(\mathbf{r}) e^{-\int_0^\infty \alpha_{ex}(\mathbf{x} + \ell \mathbf{r}) d\ell} d\mathbf{r}}_{=: C_i^{[\alpha_{ex}]}(\mathbf{x})} \cdot \underbrace{\int_S s_i^{em}(\mathbf{r}) e^{-\int_0^\infty \alpha_{em}(\mathbf{x} + \ell \mathbf{r}) d\ell} d\mathbf{r}}_{=: C_i^{[\alpha_{em}]}(\mathbf{x})}$$

## 2. Variational attenuation correction

with Gâteaux/partial derivatives

$$\begin{aligned} \left. \frac{d}{d\epsilon} F_i^{[\alpha_{\text{ex}} + \epsilon h, \alpha_{\text{em}}, \hat{I}, \beta_i]}(\mathbf{x}) \right|_{\epsilon=0} &= -2\beta_i \int_S s_i^{\text{ex}} \int_0^\infty \left( \hat{I} \cdot T_{\mathbf{r}}^{[\alpha_{\text{ex}}]} \cdot C_i^{[\alpha_{\text{em}}]} \right)(\mathbf{x}) \cdot h(\mathbf{x} + \ell \mathbf{r}) \, d\ell \, d\mathbf{r} \\ \left. \frac{d}{d\epsilon} F_i^{[\alpha_{\text{ex}}, \alpha_{\text{em}} + \epsilon h, \hat{I}, \beta_i]}(\mathbf{x}) \right|_{\epsilon=0} &= -2\beta_i \int_S s_i^{\text{em}} \int_0^\infty \left( \hat{I} \cdot C_i^{[\alpha_{\text{ex}}]} \cdot T_{\mathbf{r}}^{[\alpha_{\text{em}}]} \right)(\mathbf{x}) \cdot h(\mathbf{x} + \ell \mathbf{r}) \, d\ell \, d\mathbf{r} \\ \left. \frac{d}{d\epsilon} F_i^{[\alpha_{\text{ex}}, \alpha_{\text{em}}, \hat{I} + \epsilon h, \beta_i]}(\mathbf{x}) \right|_{\epsilon=0} &= \beta_i \left( C_i^{[\alpha_{\text{ex}}]} \cdot C_i^{[\alpha_{\text{em}}]} \right)(\mathbf{x}) \cdot h(\mathbf{x}) \\ \frac{\partial}{\partial \beta_i} F_i^{[\alpha_{\text{ex}}, \alpha_{\text{em}}, \hat{I}, \beta_i]}(\mathbf{x}) &= \left( \hat{I} \cdot C_i^{[\alpha_{\text{ex}}]} \cdot C_i^{[\alpha_{\text{em}}]} \right)(\mathbf{x}). \end{aligned}$$

Any of the presented approaches can be easily extended to multiple views with different light geometries by plugging the new image formation model and the appropriate noise functions  $f$  and  $g$  into (2.9) and (2.10). We exemplarily give the corresponding equations for the direct MAP Poisson-Gaussian approximation.

The energy formulation for the MAP model becomes

$$\begin{aligned} E^{\mathcal{P}\mathcal{G}_2}(\alpha_{\text{ex}}, \alpha_{\text{em}}, \hat{I}, \boldsymbol{\beta}) &= \sum_{i=1}^k \int_{\Omega} \frac{\left( I_i(\mathbf{x}) - F_i^{[\alpha_{\text{ex}}, \alpha_{\text{em}}, \hat{I}, \beta_i]}(\mathbf{x}) \right)^2}{m^2 F_i^{[\alpha_{\text{ex}}, \alpha_{\text{em}}, \hat{I}, \beta_i]}(\mathbf{x}) + \sigma^2} + \ln \left( \sqrt{m^2 F_i^{[\alpha_{\text{ex}}, \alpha_{\text{em}}, \hat{I}, \beta_i]}(\mathbf{x}) + \sigma^2} \right) \, d\mathbf{x} \\ &\quad + \frac{\lambda}{2} \int_{\Omega} \left\| \nabla \alpha^{\text{ex}}(\mathbf{x}) \right\|_2^2 + \left\| \nabla \alpha^{\text{em}}(\mathbf{x}) \right\|_2^2 \, d\mathbf{x} \quad (2.29) \\ \text{with } \beta_i &\in (0, 1], \, i = 1, \dots, k \quad \wedge \quad \forall \mathbf{x} \in \Omega : \alpha_{\text{ex}}(\mathbf{x}) \geq 0 \wedge \alpha_{\text{em}}(\mathbf{x}) \geq 0. \end{aligned}$$

The corresponding functional/partial derivatives are given by

$$\begin{aligned} \frac{\delta E^{\mathcal{P}\mathcal{G}_2}(\alpha_{\text{ex}}, \alpha_{\text{em}}, \hat{I}, \boldsymbol{\beta})}{\delta \alpha_{\text{ex}}(\mathbf{x})} &= 2 \sum_{i=1}^k \beta_i \int_S s_i^{\text{ex}} \int_0^\infty \left( \mathcal{D}_i^{[\text{id}, g^{\mathcal{P}\mathcal{G}_2}, F_i^{[\alpha_{\text{ex}}, \alpha_{\text{em}}, \hat{I}, \beta_i]}]} \cdot \hat{I} \cdot T_{\mathbf{r}}^{[\alpha_{\text{ex}}]} \cdot C_i^{[\alpha_{\text{em}}]} \right)(\mathbf{x} - \ell \mathbf{r}) \, d\ell \, d\mathbf{r} - \lambda \Delta \alpha_{\text{ex}}(\mathbf{x}) \\ \frac{\delta E^{\mathcal{P}\mathcal{G}_2}(\alpha_{\text{ex}}, \alpha_{\text{em}}, \hat{I}, \boldsymbol{\beta})}{\delta \alpha_{\text{em}}(\mathbf{x})} &= 2 \sum_{i=1}^k \beta_i \int_S s_i^{\text{em}} \int_0^\infty \left( \mathcal{D}_i^{[\text{id}, g^{\mathcal{P}\mathcal{G}_2}, F_i^{[\alpha_{\text{ex}}, \alpha_{\text{em}}, \hat{I}, \beta_i]}]} \cdot \hat{I} \cdot C_i^{[\alpha_{\text{ex}}]} \cdot T_{\mathbf{r}}^{[\alpha_{\text{em}}]} \right)(\mathbf{x} - \ell \mathbf{r}) \, d\ell \, d\mathbf{r} - \lambda \Delta \alpha_{\text{em}}(\mathbf{x}) \\ \frac{\delta E^{\mathcal{P}\mathcal{G}_2}(\alpha_{\text{ex}}, \alpha_{\text{em}}, \hat{I}, \boldsymbol{\beta})}{\delta \hat{I}(\mathbf{x})} &= - \sum_{i=1}^k \beta_i \left( \mathcal{D}_i^{[\text{id}, g^{\mathcal{P}\mathcal{G}_2}, F_i^{[\alpha_{\text{ex}}, \alpha_{\text{em}}, \hat{I}, \beta_i]}]} \cdot C_i^{[\alpha_{\text{ex}}]} \cdot C_i^{[\alpha_{\text{em}}]} \right)(\mathbf{x}) \\ \frac{\delta E^{\mathcal{P}\mathcal{G}_2}(\alpha_{\text{ex}}, \alpha_{\text{em}}, \hat{I}, \boldsymbol{\beta})}{\partial \beta_i} &= - \sum_{i=1}^k \int_{\Omega} \left( \mathcal{D}_i^{[\text{id}, g^{\mathcal{P}\mathcal{G}_2}, F_i^{[\alpha_{\text{ex}}, \alpha_{\text{em}}, \hat{I}, \beta_i]}]} \cdot \hat{I} \cdot C_i^{[\alpha_{\text{ex}}]} \cdot C_i^{[\alpha_{\text{em}}]} \right)(\mathbf{x}) \, d\mathbf{x}, \end{aligned}$$

and

$$\begin{aligned}\frac{\delta^2 E^{\mathcal{P}\mathcal{G}_2}(\alpha, \hat{I}, \beta_2, \beta)}{\delta \hat{I}(\mathbf{x})^2} &= \sum_{i=1}^k \beta_i^2 \left( \mathcal{D}_i^{\left[ \text{id}, g^{\mathcal{P}\mathcal{G}_2}, F_i^{\left[ \alpha_{\text{ex}}, \alpha_{\text{em}}, \hat{I}, \beta_i \right]} \right]'} \cdot C_i^{\left[ \alpha_{\text{ex}} \right]^2} \cdot C_i^{\left[ \alpha_{\text{em}} \right]^2} \right) (\mathbf{x}) \\ \frac{\partial^2 E^{\mathcal{P}\mathcal{G}_2}(\alpha, \hat{I}, \beta)}{\partial \beta_i^2} &= \int_{\Omega} \left( \mathcal{D}_i^{\left[ \text{id}, g^{\mathcal{P}\mathcal{G}_2}, F_i^{\left[ \alpha_{\text{ex}}, \alpha_{\text{em}}, \hat{I}, \beta_i \right]} \right]'} \cdot \hat{I} \cdot C_i^{\left[ \alpha_{\text{ex}} \right]^2} \cdot C_i^{\left[ \alpha_{\text{em}} \right]^2} \right) (\mathbf{x}) \, d\mathbf{x}.\end{aligned}$$

### 2.2.9. Edge-preserving regularization

The assumption of smooth attenuation fields enforced by the quadratic penalizer on the gradient of the attenuation field effectively avoids noisy solutions. However, sharp edges between tissue boundaries or at the outer specimen boundary violate the smoothness assumption and cannot be recovered with strong regularization which is required to suppress noise amplification. In variational image denoising, edge-preserving techniques replace the quadratic Tikhonov regularizer (loss:  $\psi_{\text{TM}}(s^2) = s^2$ ) by the total variation (loss:  $\psi_{\text{TV}}(s^2) = \sqrt{s^2} = |s|$ ) leading to piece-wise constant regions with sharp boundaries. The strict TV regularization is not differentiable at 0, therefore we slightly relax it to  $\psi'_{\text{TV}}(s^2) = \sqrt{s^2 + \epsilon_{\text{TV}}^2}$ , with a small constant  $\epsilon_{\text{TV}} \in \mathbb{R}_+$ . Charbonnier et al. (1997) introduced this relaxed TV loss function and showed its edge preservation properties on simulated tomography data.

To allow for different loss function we generalize the formulation of the smoothness term to

$$E_{\text{smooth}}(\alpha) := \int_{\Omega} \psi(\|\nabla \alpha(\mathbf{x})\|^2) \, d\mathbf{x}$$

where the choice of loss function  $\psi$  decides for the smoothness properties of the result.

The corresponding generalized functional derivative is then given by

$$\frac{\delta E_{\text{smooth}}(\alpha)}{\delta \alpha(\mathbf{x})} = 2 \cdot \text{div}(\psi'(\|\nabla \alpha(\mathbf{x})\|^2) \nabla \alpha(\mathbf{x}))$$

which simplifies for Tikhonov regularization to the up-to-now used Laplacian term

$$\frac{\delta E_{\text{TM}}(\alpha)}{\delta \alpha(\mathbf{x})} = 2 \cdot \Delta \alpha(\mathbf{x})$$

and for the relaxed total variation to

$$\frac{\delta E_{\text{TV}}(\alpha)}{\delta \alpha(\mathbf{x})} = \text{div} \left( \frac{\nabla \alpha(\mathbf{x})}{\sqrt{\|\nabla \alpha(\mathbf{x})\|^2 + \epsilon_{\text{TV}}^2}} \right).$$

The functional derivatives are derived in appendix A.1.4.

### 2.2.10. Sparsity Prior

In confocal microscopy we only have sparse measurements where fluorophores accumulate. Therefore, the dense attenuation field and the real intensities have to be estimated given only few cues. For some positions no measurements might be available and any attenuation estimate would perfectly explain the measured signal. Estimated attenuations in those regions are only defined by image noise, leading to arbitrarily high and unrealistic attenuations. To avoid such outliers we introduce the sparsity prior

$$E_{\text{sparse}}(\alpha) := \int_{\Omega} \sqrt{\alpha^2(\mathbf{x}) + \epsilon_{\text{sp}}^2} \, d\mathbf{x}$$

where  $\epsilon_{\text{sp}} \in \mathbb{R}^+$  is again a small constant to stabilize its derivative

$$\frac{\delta E_{\text{sparse}}(\alpha)}{\delta \alpha(\mathbf{x})} = \frac{\alpha(\mathbf{x})}{\sqrt{\alpha^2(\mathbf{x}) + \epsilon_{\text{sp}}^2}}.$$

This prior enforces the attenuations to be as small as possible while still explaining the measured signal leading to zero attenuation estimates in regions, where no measurements are available for a reconstruction. Additionally the influence of artifacts introduced by the simplified image formation model is reduced and only affects small local areas.

## 2.3. Sample Data for Evaluation

### 2.3.1. Synthetic Data for wavelength-independent absorption and zero order bleaching

To quantitatively evaluate the presented methods for attenuation correction, we generated two different synthetic datasets. The first consists of a solid sphere with constant absorption coefficients of 0.006 per voxel. The interior 60% of the sphere were set to an intensity value of 4094. We added a smooth random texture with a variance of approximately 30% of the maximum of the corresponding quantity. This corresponds to the “well-posed” case when intensity and absorption information is available in the whole domain. The second dataset is the well-known Shepp-Logan phantom (Shepp and Logan, 1974) consisting of a set of overlapping ellipsoids with homogeneous intensities. We assigned absorption coefficients to the different regions avoiding direct correlation with the intensities. Some regions were assigned equal attenuations independent of their intensity difference. In the simulation we applied an anisotropic Gaussian smoothing to model the band-limiting effect of the microscope’s point spread function and ensure Nyquist sampling. For both datasets two recordings  $I_1$  and  $I_2$  from opposite sides were simulated using equation (2.16) modeling absorption and photo bleaching ( $\beta_1 := 1.0, \beta_2 := 0.8$ , meaning 20% signal loss between the recordings). Then Poisson noise with scaling  $m = 0.05$  (Detector gain  $a \approx 4.5$ ) and Gaussian noise with mean  $\mu = 0$  and standard deviation  $\sigma = 10$  were applied. The datasets are shown in Fig. 2.5.

For these simulations the cone integrations were normalized so that zero attenuation coefficients lead to unit cone transmission given a fixed numerical aperture as in Ronneberger et al. (2012); Schmidt et al. (2013b,a).

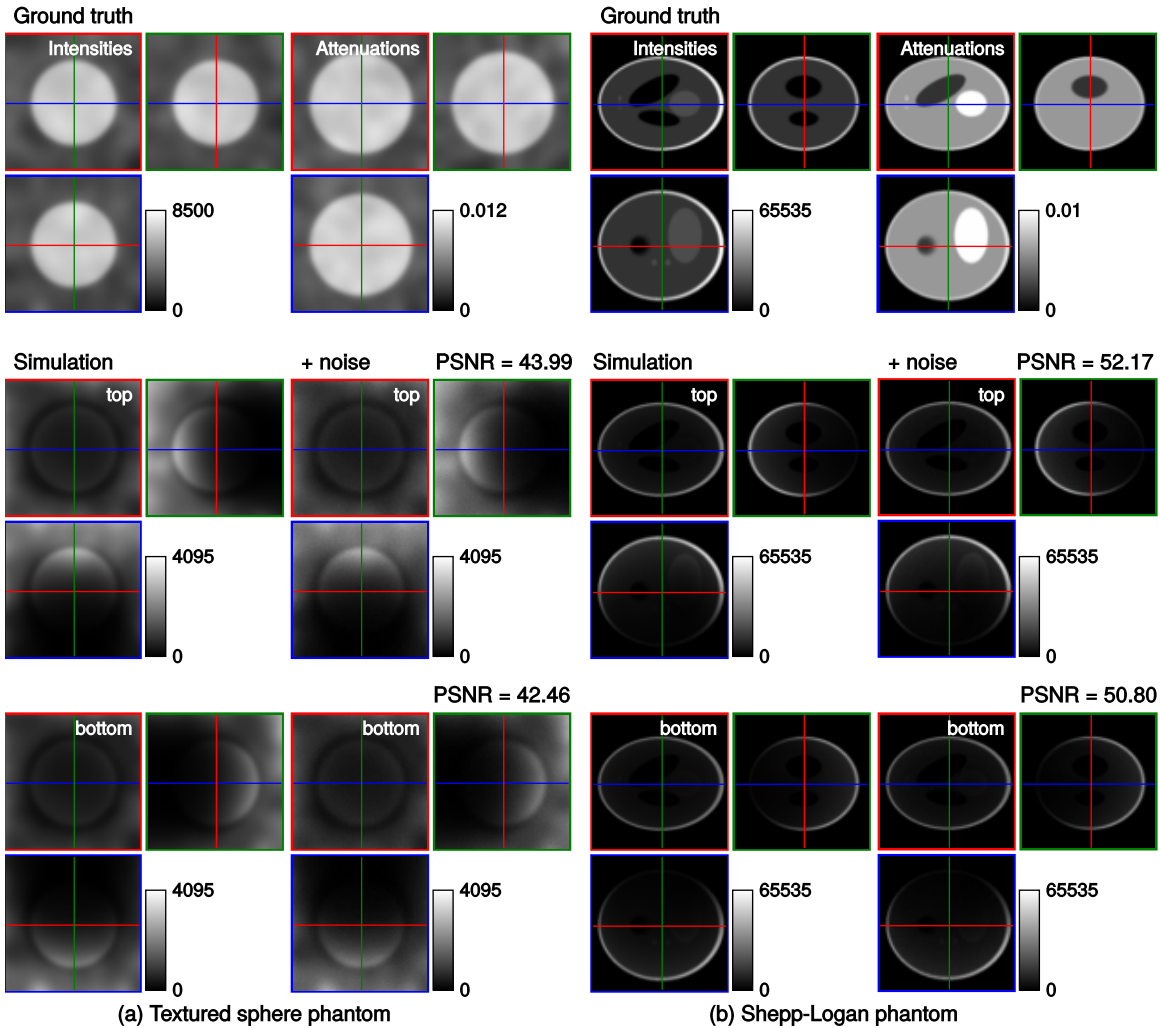


**Figure 2.5.:** Synthetic ground truth and top/bottom simulations using the simplified simulation equation (2.16) with constant bleaching factor. (a) dense data with smooth random texture added to attenuations and intensities (well-posed reconstruction problem); (b) sparse phantom with large constant areas (ill-posed reconstruction problem). All views show orthographic slices through the corresponding 3D volumes. First row: ground truth intensities  $I$  (left) and absorption coefficients  $\alpha$  (right). Second and third row: Confocal simulations from top/bottom without noise (left) and with applied Poisson-Gaussian noise with  $m = 0.05$  and  $\sigma = 10$  (right). PSNR: peak signal to noise ratio compared to the noise free simulation.

### 2.3.2. Synthetic Data for wavelength-dependent absorption and realistic bleaching

To also evaluate how well the zero-order approximation copes with more realistic bleaching and wavelength-dependent absorption, we generated different synthetic attenuation coefficient fields for excitation and emission wavelengths. Using these fields, two top and two bottom views were simulated using the general image formation equation (2.5) (Fig. 2.6). Sim 1 and Sim 2 were simulated with the full aperture cone given by the combination of lens ( $NA = 0.8$ ) and immersion medium ( $n_{\text{immersion}} = 1.4729$ ). For Sim 3 and Sim 4 the aperture was partially closed giving a net lens numerical aperture of  $NA_{\text{closed}} = 0.4$ . This allows to also test the multi-view case that poses no further assumptions on the attenuations in the excitation and emission light paths. We again applied Poisson-Gaussian noise to the simulated recordings with parameters:  $M_0 = 10^9$ ,  $N = 10^5$ ,  $p = 10^{-6}$ ,  $q = 0.25$ ,  $a = 3$ ,  $b = 0$  and  $\sigma = 10$  using dense rays. The number of fluorophores per voxel  $K : \Omega \rightarrow \mathbb{N}$  is in the  $[0, 1000]$  range, the attenuation range is  $[0, 0.013]$  at a voxel size of  $4 \times 4 \times 4 \mu\text{m}$  with a final volume of  $300 \times 300 \times 300 \mu\text{m}$  ( $= 75 \times 75 \times 75 \text{vx}$ ).

To allow for variable cone geometries we changed the normalization of the cone integrations to match the point light source setting described in section 2.1. Within that model the aperture itself already leads to a strong base signal attenuation which is proportional to the fraction of the surface of the sphere segment captured by the (masked) aperture to the full sphere surface. The real intensity estimate is increased by the product of these surface fractions for excitation and emission cones. As seen in Fig. 2.6, this scaling results in different dynamic ranges of ground truth intensities and simulations.

### 2.3.3. Real world examples

#### ***Danio rerio* (Zebrafish)**

To show that the approach also copes well with real world data, we tested it on samples of the ViBE-Z database consisting of confocal recordings of whole zebrafish embryos, which were fixed 72h after fertilization (Fig. 2.7). Sample preparation, recording setup and image pre-processing are described in detail by Ronneberger et al. (2012). The datasets contain two channels, a reference channel with marked nuclei and a second channel containing a gene expression pattern for which the attenuation correction should yield quasi-quantitative reconstructions. Processing was performed on sub-sampled data with isotropic voxel extents of  $8 \mu\text{m}$ .

#### ***Arabidopsis thaliana* (Thale cress)**

Finally we tested the approach on two-channel recordings of the root tip of the model plant *Arabidopsis thaliana* (Fig. 2.8). The first channel shows cell membranes marked using an Alexa488 antibody stain. The second channel shows DAPI stained nuclei. The samples were fixed 96h after germination. They were embedded in SlowFade Gold Antifade (Invitrogen) ( $n_{\text{embedding}} = 1.42$ ) and

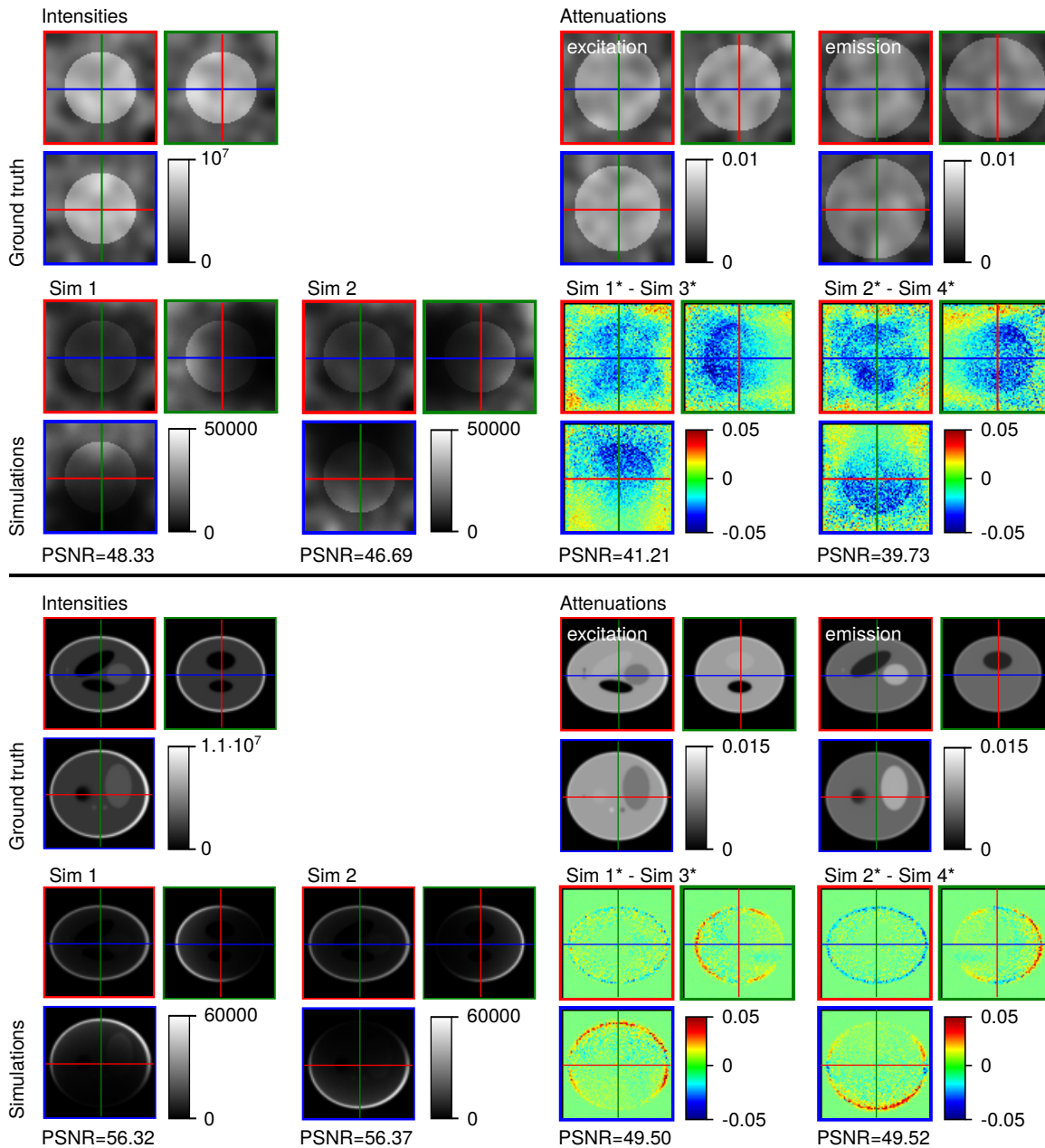


**Figure 2.6.:** Orthographic views of synthetic ground truth and top/bottom simulations using the general simulation equation (2.5). Top panel: textured sphere, bottom panel: Shepp-Logan phantom. Top row (left to right): Intensities without attenuation; attenuation fields for excitation and emission wavelengths. Bottom row: Simulated confocal recordings; Sim 1: from top, open aperture; Sim 2: from bottom, open aperture; Sim 1\* - Sim 3\*: difference of  $[0, 1]$  normalized simulations with open and 50% closed aperture (Sim 3); Sim 2\* - Sim 4\*: from bottom, difference of  $[0, 1]$  normalized simulations with open and 50% closed aperture (Sim 4). Intensity and attenuation ranges are indicated. PSNR is the peak signal to noise ratio of the corresponding simulation compared to a noise free simulation. Colored lines indicate positions of the slices shown in the correspondingly colored boxes.

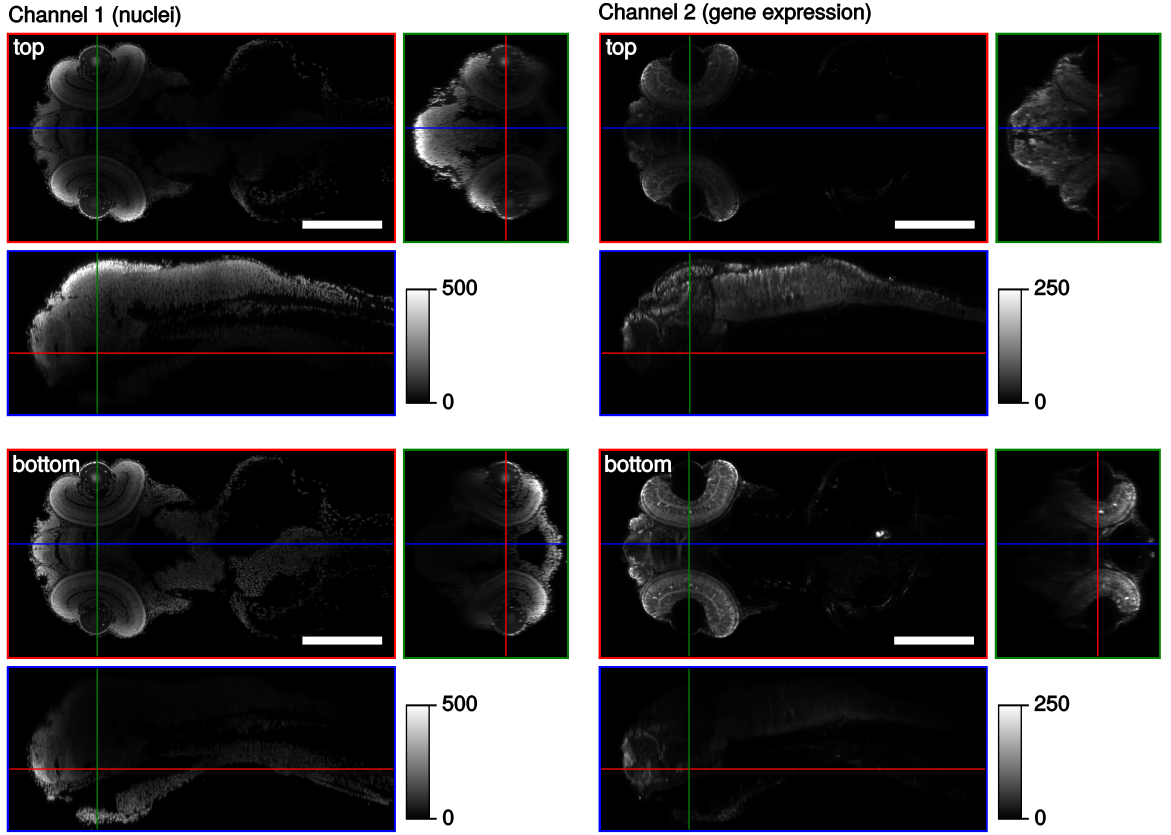


**Figure 2.7.:** Orthographic views of a sample zebrafish recording from the ViBE-Z database. Left: Reference nucleus stain; right: Gene expression pattern. Top row: Dorsal recording direction; bottom row: Ventral recording direction. Colored lines indicate positions of the slices shown in the correspondingly colored boxes. Scale bars:  $200\mu\text{m}$ .

recorded from top and bottom using a confocal microscope equipped with a  $25\times$  Glycerol immersion objective (NA 0.8,  $n_{\text{immersion}} = 1.4716$ ). We registered the bottom view to the top view using thin-plate spline interpolation on point correspondences obtained through local normalized cross correlation. Finally we performed a background subtraction prior to applying the attenuation correction. The attenuation correction was performed on sub-sampled data with isotropic voxel extents of  $2\mu\text{m}$ .

## 2.4. Implementation

### 2.4.1. Discrete cone integration

For the cone transmission functions  $C_i^{[\alpha_{\text{ex/em}}]}(\mathbf{x})$  and in the data term derivatives we need to compute integrals over all excitation and emission light rays. We approximate them as the sum over a

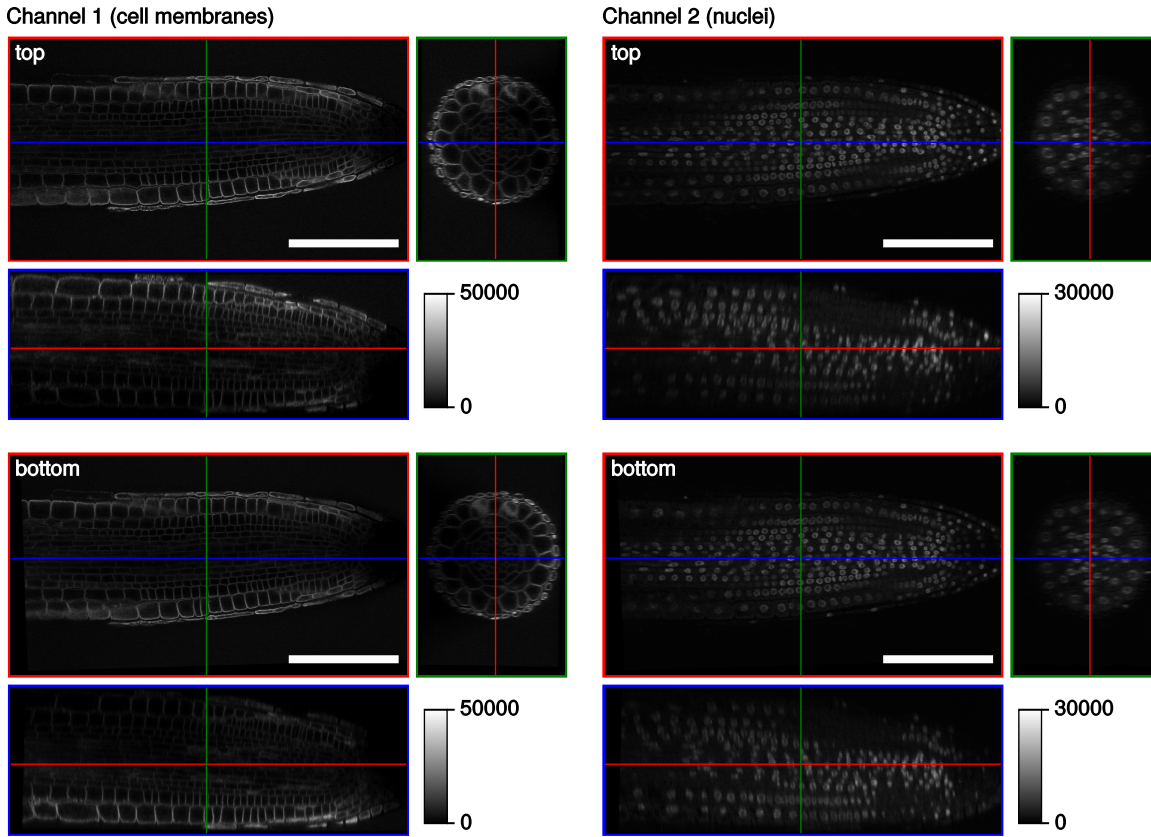


**Figure 2.8.:** Orthographic views of a sample *Arabidopsis* root tip recording. Left: Cell membrane antibody stain; right: DAPI (nucleus stain). Top row: Recorded from top direction; bottom row: Recorded from bottom. Colored lines indicate positions of the slices shown in the correspondingly colored boxes. Scale bars:  $100\mu\text{m}$ .

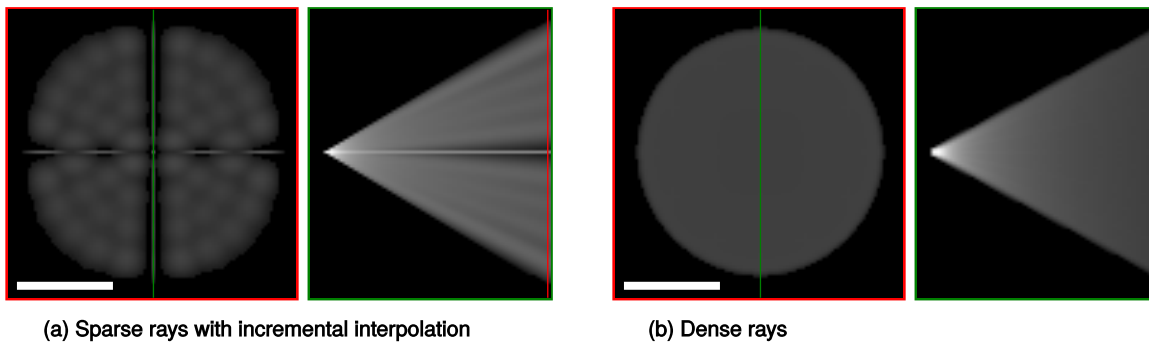


**Figure 2.9.:** Cone sampling with incrementally widening rays using bilinear interpolation (a) compared to densely sampled thin rays (b). Both panels show x-y and z-y sections through the simulated emission cone of a point light source. The intensities shown are gamma corrected ( $\gamma = 5$ ) to allow visualization of the quadratically decreasing intensities over a large depth range. Simulation parameters: voxel shape:  $0.6\mu\text{m} \times 0.6\mu\text{m} \times 1\mu\text{m}$ ,  $\text{NA} = 0.8$ ,  $n_{\text{immersion}} = 1.4729$ , (a) ray spacing =  $6^\circ$ . Scale bars:  $20\mu\text{m}$ .

discrete subset of rays in a fixed angular grid and divide the sum by the number of rays (approximately the fraction of the cone volume each ray describes). The integral along each ray is again discretized matching the plane-spacing. In-plane sub-pixel positions are interpolated using bilinear interpolation in the incremental scheme described in Appendix A.2.2. With this scheme “rays” get wider with increasing distance from the focal point, which can be regarded as a model for positional uncertainty with increasing distance to the focal point. As desirable side-effect every voxel in the (masked) cone contributes to the integral given only a small number of rays. The widening is angle dependent leading to not perfectly homogeneous cone sampling as shown in Fig. 2.9. This is most prominent where the rays always exactly hit the image voxels, leading to no ray widening.

We also did experiments with an alternative ray integration scheme that uses thin rays instead of the widening conic rays of Ronneberger et al. (2012). To still capture all positions within the cone the ray spacing was reduced to get a dense sampling at the largest cone diameter with respect to the volume grid (Fig. 2.9b). To obtain thin rays, we first shear the attenuation field so that the integration direction is the z-direction. We only interpolate twice: once in the shearing transform and once to get the sub-pixel accurate cone origin in the sheared volume. This alternative dense integration scheme with thin rays is still an approximation but should yield better reconstructions. However, the required additional integration directions make it infeasible in practice.

For all experiments we initialized the optimization variables with

$$\begin{aligned} \forall \mathbf{x} \in \Omega : \hat{I}^{\text{init}}(\mathbf{x}) &:= \min \{I_1(\mathbf{x}), I_2(\mathbf{x})\} \\ \forall \mathbf{x} \in \Omega : \alpha_{\text{ex}}^{\text{init}}(\mathbf{x}) &:= \alpha_{\text{em}}^{\text{init}}(\mathbf{x}) := 0 \\ \forall i = 1, \dots, k : \beta_i^{\text{init}} &:= 1. \end{aligned}$$

In Fig. 2.10 we compare reconstructions using sparse widening rays to dense thin rays on a noise-free dataset. In the simulation we used dense ray integration to compute the cone transmissions from the ground-truth attenuations. As baseline we used exactly the same dense integration scheme for the reconstruction which is shown in the leftmost column of Fig. 2.10. Even in this ideal case stripe artifacts in the attenuations are visible and a peak signal to noise ratio (PSNR) of 38.99 for the intensities and 23.10 for the attenuation field was measured. The fast approximation using incremental interpolations further reduces the PSNR. The reconstruction of the attenuation field shows cross-shaped artifacts and elongation of structures along the optical axis. Imposing a sparsity prior improves the reconstruction dramatically in both cases (Figure 2.10 3rd and 4th column).

Fig 2.11 shows the course of the energy, the norm of the gradients projected to the feasible direction, and the root mean squared errors (rms) of intensities and attenuations using a quasi Newton solver (L-BFGS-B) for the  $\alpha$  update and an analytic coordinate descent in  $\hat{I}$  direction (Details follow). The dense ray model did not converge within 1000 iterations. The rms of intensities and attenuations, however, changed only marginally after 200 iterations. The sparsity prior yields higher energies that reach the same energy plateau after only 50 iterations for both integration schemes. The strong changes in the rms of both intensities and attenuations up to the 150th iteration show that a large range of possible solutions lead to similar energies, which underlines the ill-posedness of the inverse problem.

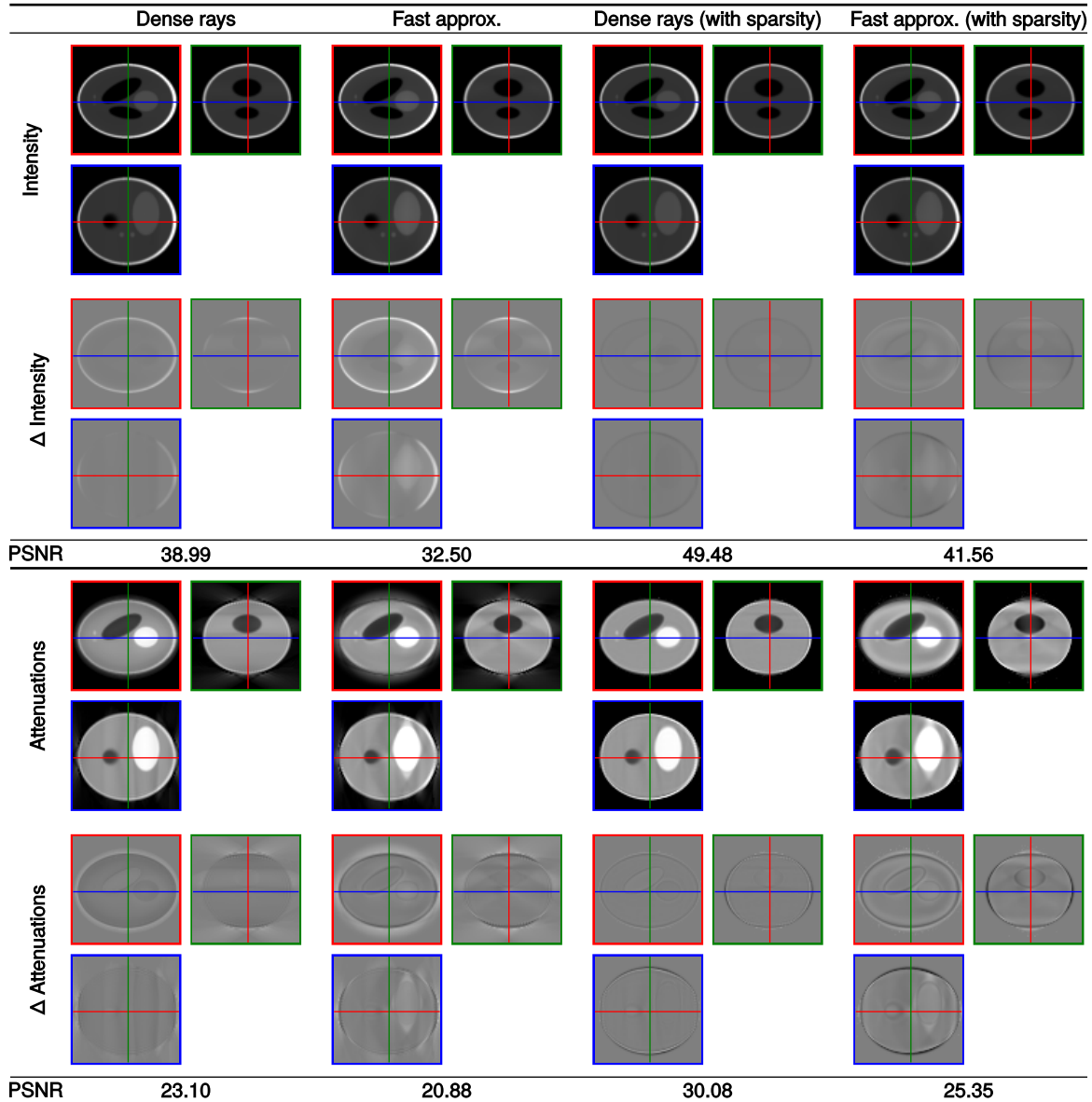


**Figure 2.10.:** Effects of the integration scheme on the reconstruction of intensities and attenuations. Each column corresponds to one optimization setup, consisting of the indicated integration strategy. “Dense Rays”: Accurate cone integration using densely sampled thin rays; “Fast Approx”: The proposed fast approximation using sparse sampling with conic rays. “sparse”: ( $\mu = 10^6$ ). PSNR: peak signal to noise ratio compared to the ground-truth intensities/attenuation fields. Intensities: [0, 65535], intensity differences: [-20000, 20000], attenuations: [0, 0.01], attenuation differences: [-0.01, 0.01].

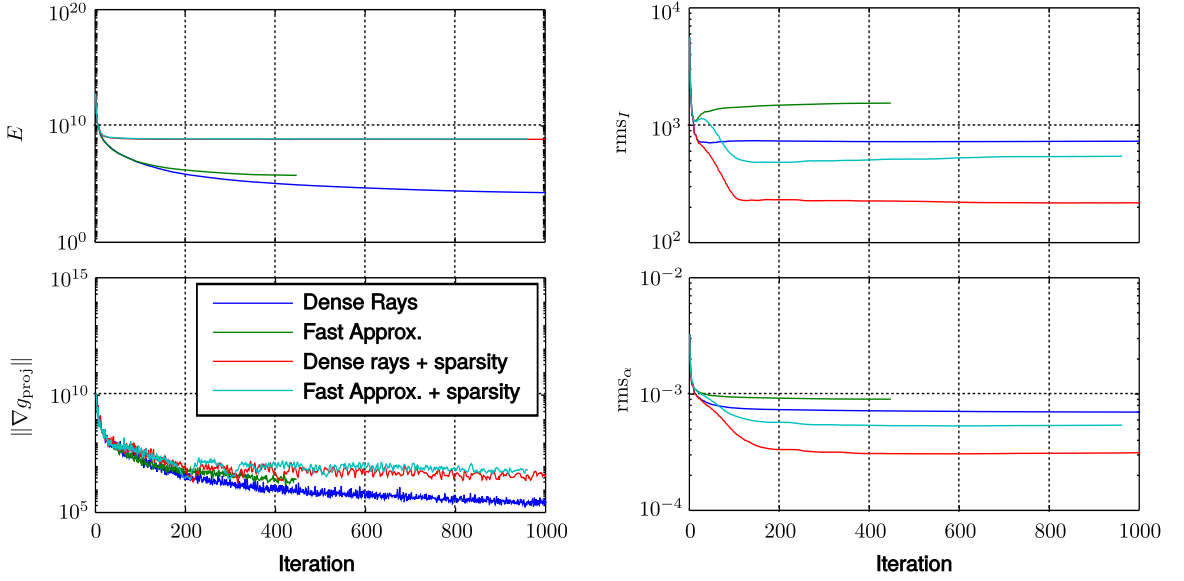


**Figure 2.11.:** Effects of the integration scheme on (a) energy, (b) norm of the energy gradient projected on the closest feasible direction, (c) root mean squared error (rms) of reconstructed intensities, and (d) of reconstructed attenuations. “Dense Rays”: Accurate cone integration using densely sampled thin rays; “Fast Approx.”: The proposed fast approximation using sparse sampling with cone-shaped rays; “sparsity”:  $\mu = 10^6$ .

## 2.4.2. Discrete spatial derivatives of the attenuation field

For Tikhonov-Miller regularization we approximated the gradient of the attenuation field using first order forward differences  $\frac{\partial \alpha(\mathbf{x})}{\partial x_d} \approx \frac{\alpha(\mathbf{x}+\mathbf{e}_d) - \alpha(\mathbf{x})}{h_d}$  and the Laplacian as the sum of second order differences  $\Delta \alpha(\mathbf{x}) \approx \sum_{d=1}^D \frac{-\alpha(\mathbf{x}-\mathbf{e}_d) + 2\alpha(\mathbf{x}) - \alpha(\mathbf{x}+\mathbf{e}_d)}{h_d^2}$ .

For total variation regularization we approximated the gradient of the attenuation field using first order central differences  $\frac{\partial \alpha(\mathbf{x})}{\partial x_d} \approx \frac{\alpha(\mathbf{x}+\mathbf{e}_d) - \alpha(\mathbf{x}-\mathbf{e}_d)}{2h_d}$ . The discrete numerical approximation to the divergence is an extension of the scheme used by Brox (2005) to 3-D and is given in Appendix A.3.

## 2.4.3. Optimization

### Low memory Broyden-Fletcher-Goldfarb-Shanno (L-BFGS)

Ronneberger et al. (2012) employ the low memory Broyden-Fletcher-Goldfarb-Shanno (L-BFGS) quasi Newton optimizer contained in the GNU scientific library<sup>2</sup> to minimize the energy. They iteratively optimize the attenuations  $\alpha$  only. At each iteration the corresponding  $\hat{I}$  is explicitly computed using (2.15). Negative attenuations are re-projected to the positive half-space of valid solutions in each iteration.

<sup>2</sup><http://www.gnu.org/software/gsl>

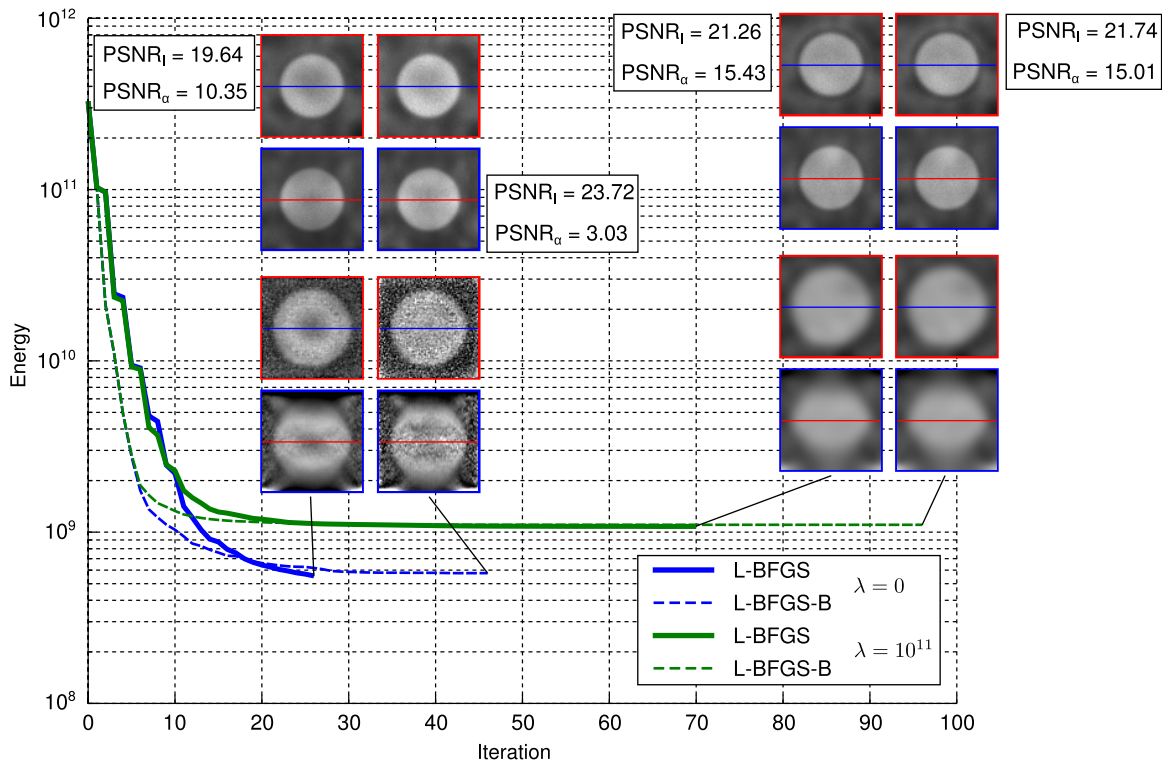


**Figure 2.12.:** Comparison of reconstruction results on the textured sphere phantom at convergence of L-BFGS and L-BFGS-B without regularization ( $\lambda = 0$ ) and with strong regularization ( $\lambda = 10^{11}$ ). x-y and x-z sections through the reconstructed intensities (upper rows), and attenuations (lower rows) at convergence are shown.  $\text{PSNR}_{I/\alpha}$ : peak signal to noise ratio compared to the real intensities/attenuations.

### L-BFGS with box constraints on the variables (L-BFGS-B)

The re-projections can be avoided when using a variant of L-BFGS that internally maintains box constraints on the optimization variables. They can then already be considered for suppressing strong gradients pointing out of the positive half-space during the approximate Hessian update. With L-BFGS-B, Zhu et al. (1997) provide a FORTRAN implementation of the L-BFGS solver including this extension. When managing the constraints within the optimizer, the energy drops quicker in the beginning of the optimization but tails off more slowly to finally reach a very similar energy as with explicit subspace projections (see Fig. 2.12).

Looking at the reconstructions without regularization ( $\lambda = 0$ ), strong noise amplification with increasing iteration count becomes visible. With high regularization this effect can be reduced leading to convincing reconstructions. This small example already shows that even in this comparably well-posed inverse problem low noise levels require strong priors to reach good reconstruction results.

If not explicitly written, we use L-BFGS-B for all optimizations of  $\alpha$ . Linear sub-problems are solved analytically resulting in an alternating coordinate descent approach. If analytic solutions require to find polynomial roots we however found that it is more efficient to iteratively solve the

sub-problem using Newton’s method directly on the derivative instead of computing the polynomial coefficients and then run a polynomial root solver.

In theory all optimization strategies yield the same optimal solution. However, in practice the resulting reconstructions can differ quite a lot. An extreme case is a full optimization of attenuations and intensities using L-BFGS-B. Without proper pre-conditioning of the optimization variables the numerical optimization will not even find an approximate solution to the problem while running virtually forever. If only the optimization of the attenuations is given to the L-BFGS-B optimizer in an alternating coordinate descent scheme all variables of each sub-problem are in the same order of magnitude and the energy minimum is quickly found especially if sub-problems can be solved analytically or with quadratic convergence order using Newton’s method.

The corresponding algorithm with explicit coordinate descent in the sub-space spanned by  $\hat{I}$  and  $\beta$  using Newton’s method is given in Alg. 1.

We analyzed the optimization times of the direct Poisson-Gaussian approximation approach using L-BFGS-B to optimize the attenuation coefficients and iterative intensity and  $\beta$  update using inner Newton iterations. We ran the optimization on an Intel Xeon E5-2680 (2.7GHz) Dual-Processor system with Ubuntu 12.04 operating system. One iteration for data sub-sampled to  $75 \times 75 \times 75$  voxels needed on average 1.8 seconds, so a full reconstruction can be computed in the range of a few minutes. The complexity scales linearly with the number of voxels to process within each iteration (Fig. 2.13). The memory complexity also scales linearly with the raw data volume (not shown). Both quantities can be limited by sub-sampling the high resolution raw data. This has two advantages: First, less computational resources are needed and second, the weighted averaging during the sub-sampling already considerably reduces image noise. The cone transmission is computed in parallel for all ray directions leading to a significant speed-up of the confocal microscope simulation if multiple CPU cores are available. Depending on the random computation order introduced by the scheduling, the results can slightly deviate from the numbers reported in section 2.5. For real-world data we observed deviations of the estimated intensities of up to 3% after convergence of the algorithm. However, these differences are visually not recognizable.

We did not try to compute the polynomial roots analytically, because the computation of the coefficients of the quartic function requires already more operations than twenty times computing first and second derivatives which are required for the numerical solution using Newton’s method. The same argument also disqualifies the iterative root solving strategy. We assume (without proof) that Newton’s method is numerically more accurate compared to direct polynomial root computation, because the numerical range spanned by the coefficients is huge leading to large round-off errors in practical computations.

### Parameter setup

We want all terms in the energy to have approximately the same influence on the optimization process. This leads to rough rules of thumb for the selection of  $\lambda$  and  $\mu$  for the different approaches. For all models the choice is independent of the number of voxels because all terms in the energy integrate over the whole image domain.

---

```

Input :  $I_1, \dots, I_k, \lambda, \mu, m / a, \sigma$ 
Output :  $\alpha_{\text{ex}}^*, \alpha_{\text{em}}^*, \hat{I}^*, \beta^*$ 
 $\hat{I} \leftarrow \min \{I_1, \dots, I_k\}, \alpha \leftarrow 0, \forall i = 1, \dots, k : \beta_i \leftarrow 1, \epsilon \leftarrow 10^{-14};$ 
while  $\neg \text{converged}$  do
    Compute  $E(\alpha_{\text{ex}}, \alpha_{\text{em}}, \hat{I}, \beta)$  and  $\frac{\delta E(\alpha_{\text{ex}}, \alpha_{\text{em}}, \hat{I}, \beta)}{\delta \alpha(\mathbf{x})}$ ;
    Do L-BFGS-B step; // Updates  $\alpha_{\text{ex}}$  and  $\alpha_{\text{em}}$ 
    // Coordinate descent in  $\hat{I}$  and  $\beta$  directions
     $i \leftarrow 0;$ 
    repeat
         $E_{\text{old}} \leftarrow E(\alpha_{\text{ex}}, \alpha_{\text{em}}, \hat{I}, \beta);$ 
        foreach  $\mathbf{x} \in \Omega$  do
            // Iteratively compute  $\hat{I}(\mathbf{x})$  using Newton's method
             $j \leftarrow 0;$ 
            repeat
                 $\delta \leftarrow \frac{\frac{\delta}{\delta \hat{I}(\mathbf{x})} E(\alpha_{\text{ex}}, \alpha_{\text{em}}, \hat{I}, \beta)}{\frac{\delta^2}{\delta \hat{I}(\mathbf{x})^2} E(\alpha_{\text{ex}}, \alpha_{\text{em}}, \hat{I}, \beta)};$ 
                 $\hat{I}(\mathbf{x}) \leftarrow \hat{I}(\mathbf{x}) - \delta;$ 
                 $j \leftarrow j + 1;$ 
            until  $j = 20 \vee |\delta| < \epsilon \cdot |\hat{I}(\mathbf{x})|;$ 
        end
        for  $\ell \leftarrow 1$  to  $k$  do
            // Iteratively compute  $\beta_\ell$  using Newton's method
             $j \leftarrow 0;$ 
            repeat
                 $\delta \leftarrow \frac{\frac{\partial}{\partial \beta_\ell} E(\alpha_{\text{ex}}, \alpha_{\text{em}}, \hat{I}, \beta)}{\frac{\partial^2}{\partial \beta_\ell^2} E(\alpha_{\text{ex}}, \alpha_{\text{em}}, \hat{I}, \beta)};$ 
                 $\beta_\ell \leftarrow \beta_\ell - \delta;$ 
                 $j \leftarrow j + 1;$ 
            until  $j = 20 \vee |\delta| < \epsilon \cdot |\beta_\ell|;$ 
        end
         $E_{\text{new}} \leftarrow E(\alpha_{\text{ex}}, \alpha_{\text{em}}, \hat{I}, \beta);$ 
         $i \leftarrow i + 1;$ 
    until  $i = 10 \vee |E_{\text{old}} - E_{\text{new}}| < \epsilon \cdot |E_{\text{new}}|;$ 
end

```

**Algorithm 1** : Variational attenuation correction with coordinate descent in  $\hat{I}$  and  $\beta_2$  directions using Newton's method.

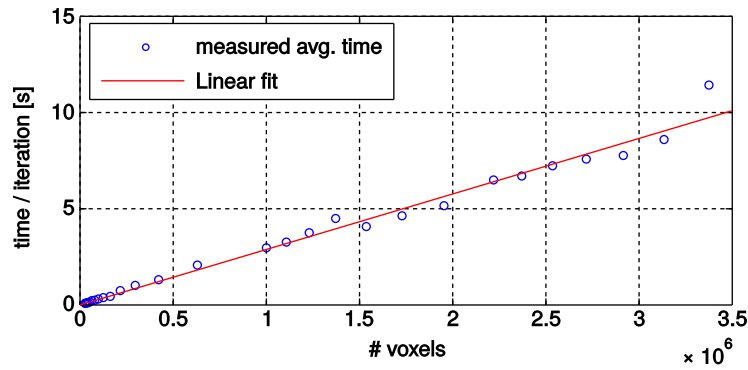


**Figure 2.13.:** The effect of increasing volume sizes on the running time of the algorithm using the fast approximate cone integration scheme. Measurements (blue circles) were performed on a workstation equipped with two Intel Xeon E5-2680 CPUs. The linear fit (red line) confirms the theoretical linear complexity of the algorithm in practice.

The Tikhonov Miller (TM) smoothness term contributes the sum of squared gradient magnitudes of the attenuation field to the energy. On our synthetic datasets the average attenuation gradient magnitude is approximately ten times smaller than the average attenuation. Using the factor ten as rule of thumb a choice of  $\lambda \approx 100\mu$  leads to similar contributions of both terms to the overall energy. For TV regularization, with absolute gradient magnitude contribution in the smoothness term, the corresponding choice is  $\lambda \approx 10\mu$ .

We know how to choose  $\lambda$  given  $\mu$ , but we still need to determine a rough estimate for  $\mu$ . Its choice depends on the image formation model, but for all models it is the expected residual noise variance multiplied by the number of recordings  $k$  divided by the expected mean attenuation.

For the Poisson-Gaussian model with Poisson weighting  $m$  the energy contribution of the data term is in the order of the squared expected intensity differences between recording and simulation divided by the Poisson weights. E.g. for intensity data with an expected residual intensity difference of 5 (the standard deviation of the residual noise) and pure Gaussian noise with expected attenuation coefficients of 0.005 and gradient magnitudes of 0.0005 initial choices of  $\lambda = \frac{5^2}{0.0005^2} = 4 \cdot 10^8$  and  $\mu = \frac{5^2}{0.005} = 5000$  (TM), resp.  $\lambda = \frac{5^2}{0.0005} = 5 \cdot 10^4$  and  $\mu = 5000$  (TV) are appropriate. The approximate estimates for the expected attenuations and their gradients were empirically confirmed on real world samples. For higher Poisson weighting  $m$  the factors have to be decreased accordingly. The optimal values depend on the image content and should be optimized for specific types of data.

## 2.5. Results and Discussion

We first apply all two-view attenuation correction approaches to the synthetic phantoms shown in Fig. 2.5 generated using the simplified image formation model (2.16) which were already used in Schmidt et al. (2013a). For all approaches we show the result for the combination of parameters  $\lambda$ ,  $\mu$ ,  $a/m$  and  $\sigma$  maximizing the sum of the peak signal to noise ratios (PSNR) of intensities and atten-

uations. The parameters were empirically determined with an exponential grid search over the parameters  $\lambda \in \{0, 10^0, \dots, 10^{14}\}$  and  $\mu \in \{0, 10^0, \dots, 10^7\}$ ,  $a/m \in \{0, 0.02, 0.05, 0.07, 0.1, 0.5, 1.0\}$  and  $\sigma \in \{0, 1\}$ . For the real world samples we used a conservative parameter set of  $\lambda = 10^7$ ,  $\mu = 0$  and  $m = 0.1$  (Arabidopsis) or  $\lambda = 10^8$ ,  $\mu = 10^4$  and  $m = 0$  (zebrafish) for all experiments with TM regularization. For the zebrafish experiments with TV regularization we set  $\lambda = 5 \cdot 10^4$ ,  $\mu = 0$ , and  $m = 0$ . For the real world samples we stopped the iterative process when the visually optimal reconstruction of the intensities was reached, which was after between 3 to 20 iterations. All results reported for the synthetic datasets were reached at convergence of the algorithm.

Fig. 2.14 summarizes the influence of the different extensions to the original model of Ronneberger et al. (2012). If no prior knowledge about the attenuations is introduced, the approach is already able to reasonably reconstruct the original intensities (Fig. 2.14c). However, the attenuation field is coarse and cannot be applied to the reconstruction of secondary channels. With regularization (Fig. 2.14d and e) the attenuation field is much smoother, but especially with Tikhonov Miller regularization strong spurious attenuations outside the sample are estimated. Application of the sparsity term reduces these attenuation estimates (Fig. 2.14f and g). The residual apparent “bleeding” of the attenuation coefficients below the sample are the effect of different mean intensities in the top and bottom recordings, as *e.g.* introduced by photo bleaching. When additionally estimating  $\beta_2$  during the optimization, the lower boundary becomes much clearer.

## 2.5.1. Synthetic Data

### Simplified image formation model

As a first baseline measure we computed the best possible outcome of the optimal “one-factor-per-slice method” using the ground truth intensities of the synthetically generated phantoms. *I.e.* no method that assumes that the correction factors are a function of the z-position in the recorded volume can perform better. The optimal correction factor for each slice was computed by minimizing the root mean squared error (rmse) of the estimated intensities compared to the true intensities. The reconstruction error for slice  $\Omega_z \subset \Omega$  is given by

$$E_z(c_1, c_2) := \sum_{i=1}^2 \sum_{\mathbf{x} \in \Omega_z} (c_i \cdot I_i(\mathbf{x}) - \hat{I}(\mathbf{x}))^2, \quad (2.30)$$

where the  $c_i \in \mathbb{R}$  are the correction factors for the top- and bottom-view and  $\hat{I}$  are the true intensities. The corresponding optimal correction factors  $c_1$  and  $c_2$  can be computed analytically to

$$c_i = \frac{\sum_{\mathbf{x} \in \Omega_z} \hat{I}(\mathbf{x}) I_i(\mathbf{x})}{\sum_{\mathbf{x} \in \Omega_z} I_i^2(\mathbf{x})}. \quad (2.31)$$

The reconstructions are shown in the second column of table 2.1 and 2.3. In both cases the one-factor-per-slice model was not able to reconstruct the interior intensities even though the true intensities were given.

## 2. Variational attenuation correction

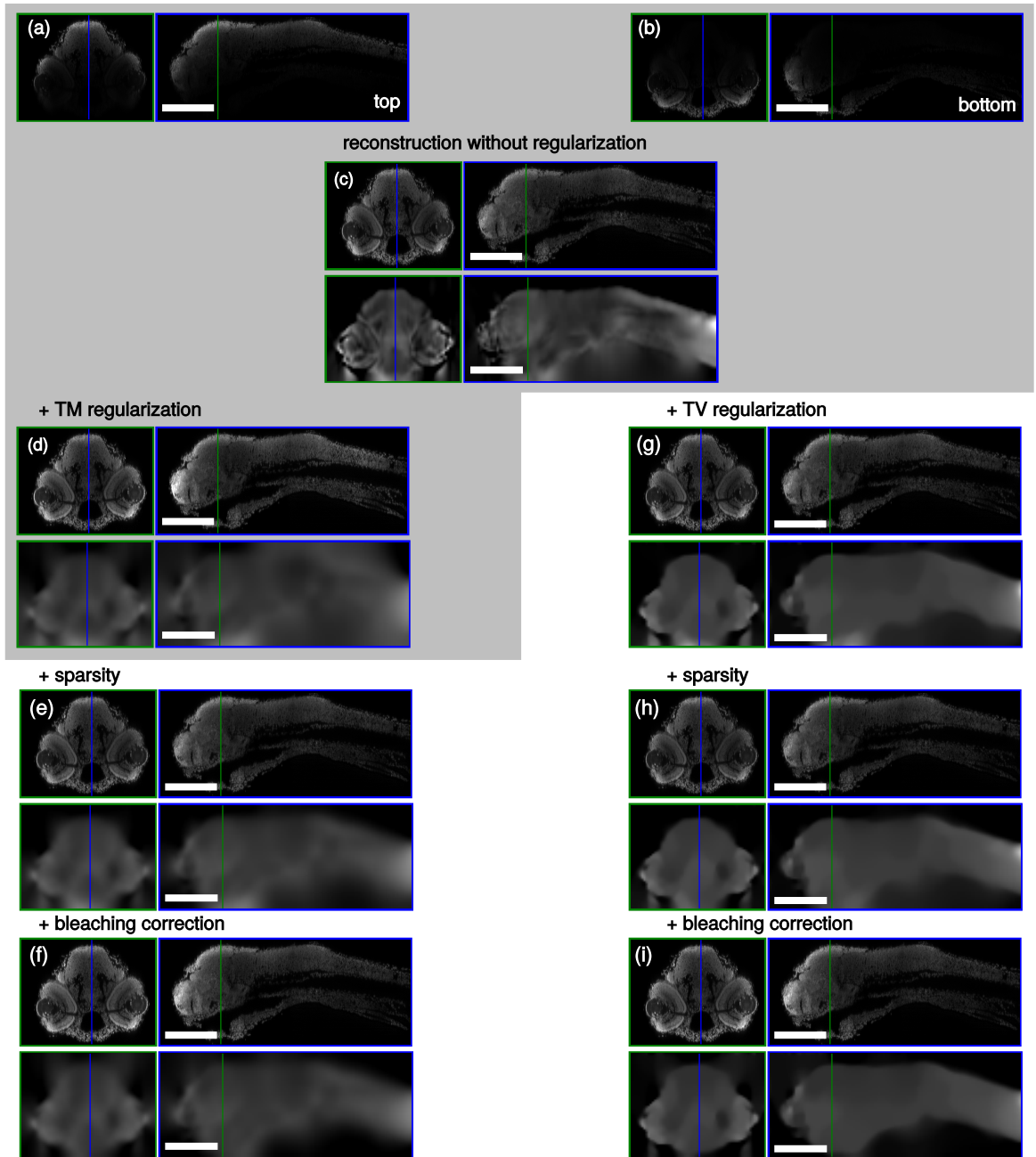
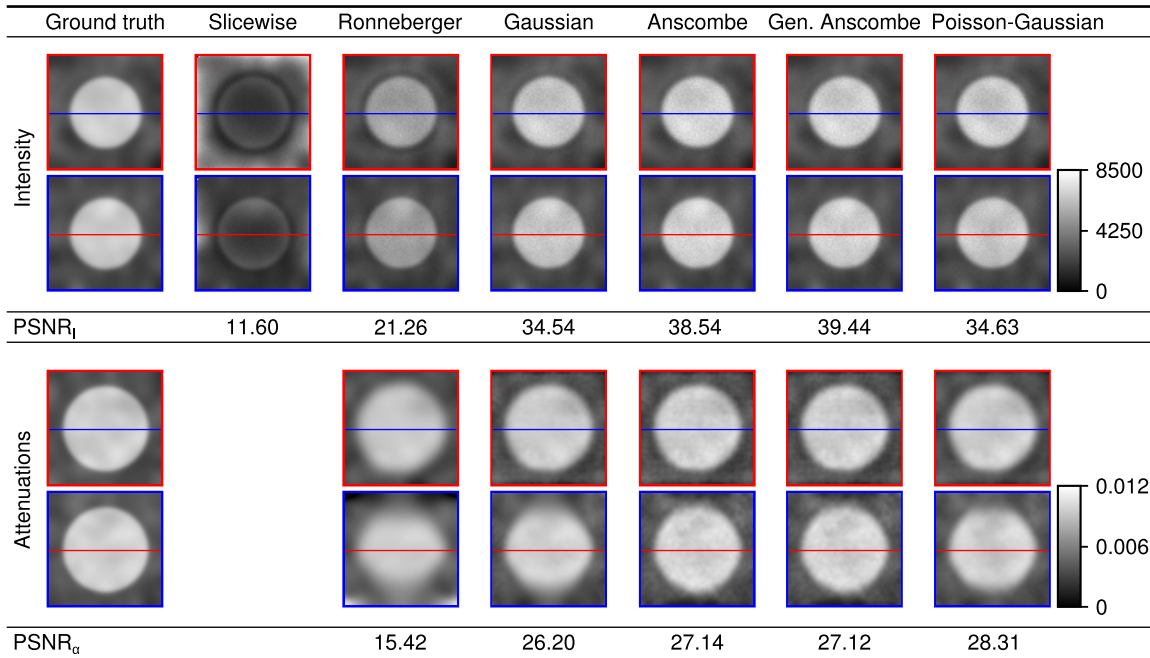


**Figure 2.14.:** Overview over the extensions to Ronneberger et al. (2012) given two views. (a-b) zy- and xz-sections of raw confocal stacks (top/bottom); (c) optimal reconstruction without regularization; left: (d) with Tikhonov Miller regularization ( $\lambda = 10^7$ ); (e) with sparsity ( $\mu = 1000$ ); (f) with bleaching correction (est.  $\beta = 0.64$ ); right: (g) with total variation regularization ( $\lambda = 10^4$ ); (h) with sparsity ( $\mu = 1000$ ); (i) with bleaching correction (est.  $\beta = 0.63$ ). Parts shaded in gray are already implemented in Ronneberger et al. (2012). Scale bars:  $200\mu\text{m}$ .

**Table 2.1.:** Reconstruction quality after variational attenuation correction on the textured sphere phantom generated using the simplified image formation assuming constant bleaching-induced intensity reduction. Best results over all parameter sets. PSNR = Peak signal to noise ratio compared to the ground truth.

Method	Reg.	m	a	$\sigma$	$\lambda$	$\mu$	#iter	$\beta_2$	PSNR <sub>I</sub>	PSNR <sub><math>\alpha</math></sub>
Ronneberger et al. (2012)	TM	0	1	$10^{11}$	0		72	1.0	21.26	15.42
Gaussian (2.2.3)	TM	0	1	$10^{10}$	$10^4$		115	0.80	34.54	26.20
Anscombe (2.2.4)	TM	1	0	$10^7$	$10^2$		78	0.80	38.54	27.14
Gen. Anscombe (2.2.5)	TM	1	1	$10^7$	$10^2$		70	0.80	<b>39.44</b>	27.12
Poisson-Gaussian (2.2.6)	TM	0.07	1	$10^9$	$10^3$		78	0.80	33.54	27.91
Poisson-Gaussian dyn. (2.2.6)	TM	0.5	1	$10^8$	$10^2$		61	0.80	34.63	<b>28.31</b>



As second baseline we applied the attenuation correction of Ronneberger et al. (2012) to all datasets and empirically determined the best regularization parameter  $\lambda$  for each of them using the same parameter range.

The peak signal to noise ratios and corresponding estimated intensities and attenuations of the best reconstructions for each approach are given in tables 2.1 and 2.3.

Using L-BFGS-B for the optimization in combination with the zero-order bleaching estimation that perfectly matches the used simplified image formation model clearly outperforms the baseline of Ronneberger et al. (2012). The models among each other perform very similar with slight preference for models including Poisson noise statistics. However, the small remaining differences might be introduced by the parameter sampling. The reconstructions look equally convincing for the Gaussian

## 2. Variational attenuation correction

**Table 2.2.:** Reconstruction quality after variational attenuation correction on the textured sphere phantom generated using the simplified image formation assuming constant bleaching-induced intensity reduction. Best results with partial parameter fixation using the generalized Anscombe model. PSNR = Peak signal to noise ratio compared to the ground truth.

Method	Reg.	m / a	$\sigma$	$\lambda$	$\mu$	#iter	$\beta_2$	PSNR <sub>I</sub>	PSNR <sub><math>\alpha</math></sub>
Ronneberger et al. (2012)	TM	0	1	$10^{11}$	0	72	1.0	21.26	15.42
Anscombe (2.2.4)	TM	1	0	$10^8$	0	64	1.0	28.79	15.14
Gen. Anscombe (2.2.5)	TM	1	1	$10^8$	0	58	1.0	28.80	15.16
Anscombe (2.2.4)	TM	1	0	$10^7$	0	98	0.80	28.43	27.85
Gen. Anscombe (2.2.5)	TM	1	1	$10^7$	0	77	0.80	29.05	<b>28.02</b>
Gen. Anscombe (2.2.5)	TM	0.5	1	$10^7$	0	72	0.80	32.20	26.89
Anscombe (2.2.4)	TM	1	0	$10^7$	100	78	0.80	38.54	27.14
Gen. Anscombe (2.2.5)	TM	1	1	$10^7$	100	70	0.80	<b>39.44</b>	27.12
Anscombe (2.2.4)	TV	1	0	0	0	36	1.0	27.84	3.28
Gen. Anscombe (2.2.5)	TV	1	1	$5 \cdot 10^4$	0	590	1.0	18.90	13.65
Gen. Anscombe (2.2.5)	TV	0.1	1	$10^4$	0	32	1.0	25.56	12.09
Gen. Anscombe (2.2.5)	TV	1	0	$5 \cdot 10^4$	10	321	1.0	18.76	14.40
Gen. Anscombe (2.2.5)	TV	0.1	1	$10^4$	0	32	1.0	25.60	12.09
Anscombe (2.2.4)	TV	1	0	$10^3$	0	201	0.80	32.40	20.78
Gen. Anscombe (2.2.5)	TV	1	1	500	0	20	0.80	32.02	21.23
Gen. Anscombe (2.2.5)	TV	0.5	1	500	0	40	0.80	37.31	21.03
Gen. Anscombe (2.2.5)	TV	1	0	$10^3$	100	198	0.80	38.96	20.62
Gen. Anscombe (2.2.5)	TV	0.5	1	500	10	33	0.80	38.41	21.31

the Poisson and the Poisson-Gaussian noise models using appropriate parameters.

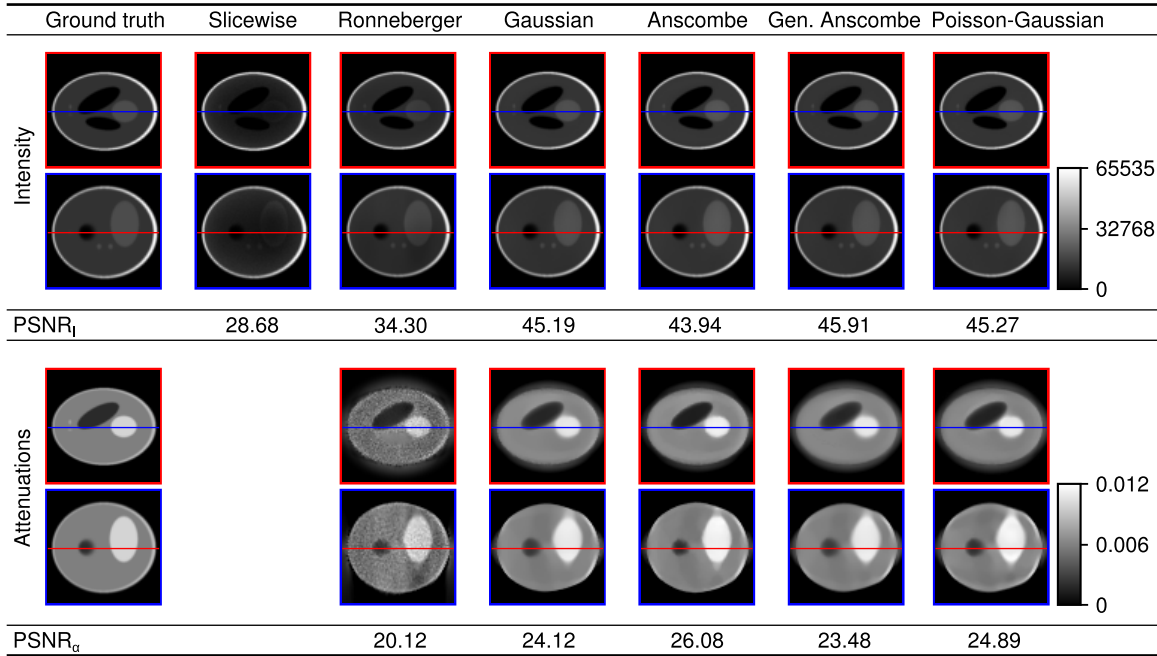
Including Poisson statistics in the model slightly improves the reconstructions but does not explain the big gap between the reconstructions obtained using the baseline approach of Ronneberger et al. (2012) and the proposed extensions. To further investigate the reasons, we systematically enabled only parts of the extensions. The corresponding results for the generalized Anscombe noise model are shown in table 2.2 and 2.4.

For both synthetic datasets bleaching estimation significantly increases the PSNR of the estimated attenuation field. This is obvious, because, if not modeled explicitly, bleaching must be explained by (at least locally) increased absorption.

Sparsity increases the PSNR of the estimated intensities. We explain this due to the preference for lower absolute attenuation which suppresses extreme over-estimates in the attenuation field and therefore stops the optimization if noise amplification becomes too strong. The effect is stronger for the Shepp-Logan phantom in which background attenuation estimates are actively suppressed. Therefore, large sparsity factors  $\mu$  give the best results. The choice of the loss function in the smoothness prior is not as important as expected. However, L2 smoothness leads to the best reconstructions of the smoothly varying attenuation field of the textured sphere phantom, whereas TV regulariza-

**Table 2.3.:** Reconstruction quality after variational attenuation correction on the Shepp-Logan phantom generated using the simplified image formation model assuming constant bleaching-induced intensity reduction. PSNR = Peak signal to noise ratio compared to the ground truth.

Method	Reg.	$m$	$a$	$\sigma$	$\lambda$	$\mu$	#iter	$\beta_2$	PSNR <sub>I</sub>	PSNR <sub><math>\alpha</math></sub>
Ronneberger et al. (2012)	TM	0	1	$10^9$	0		386	1.0	34.30	20.12
Gaussian (2.2.3)	TV	0	1	$10^7$	$10^7$		371	0.80	45.19	24.12
Anscombe (2.2.4)	TV	1	0	$10^3$	$10^3$		424	0.80	43.94	<b>26.08</b>
Gen. Anscombe (2.2.5)	TV	0.5	1	$10^4$	$10^4$		359	0.80	<b>45.91</b>	23.48
Poisson-Gaussian (2.2.6)	TV	0.5	1	$10^4$	$10^4$		231	0.80	45.86	24.42
Poisson-Gaussian dyn. (2.2.6)	TV	0.5	1	$10^4$	$10^4$		312	0.80	45.27	24.89



tion is well-suited for reconstructing the piecewise constant attenuation fields of the Shepp-Logan phantom.

We evaluated the reconstruction quality with respect to the three parameters  $\lambda$ ,  $\mu$ , and  $m$  (TM: Fig. 2.15a and b, TV: Fig. 2.16a and b). As quality measure we used the root mean squared error (rmse) of the estimated intensities. We found that the results are stable over a wide range of parameters. The parameter having the highest impact on the result is the smoothness weight  $\lambda$ , followed by the sparsity weight  $\mu$  and finally the Poisson scaling factor  $m$ . We also evaluated the evolution of the rmse during the optimization process for different choices of the parameters (TM: Fig. 2.15c and d, TV: Fig. 2.16c and d). For all parameter choices the rmse first decreases rapidly reaching a very good reconstruction after 30 to 60 iterations (From practical observations we found that for

## 2. Variational attenuation correction

**Table 2.4.:** Reconstruction quality after variational attenuation correction on the Shepp-Logan phantom using the simplified image formation model assuming constant bleaching-induced intensity reduction. Best results with partial parameter fixation using the generalized Anscombe model. PSNR = Peak signal to noise ratio compared to the ground truth.

Method	Reg.	m	a	$\sigma$	$\lambda$	$\mu$	#iter	$\beta_2$	PSNR <sub>I</sub>	PSNR <sub><math>\alpha</math></sub>
Ronneberger et al. (2012)	TM	0	1		$10^9$	0	386	1.0	34.30	20.12
Anscombe (2.2.4)	TM	1	0		$10^6$	0	417	1.0	32.69	17.05
Gen. Anscombe (2.2.5)	TM	1	1		$10^6$	0	368	1.0	32.02	17.82
Gen. Anscombe (2.2.5)	TM	0.02	1		$10^9$	0	17	1.0	38.83	17.81
Anscombe (2.2.4)	TM	1	0		$10^8$	$10^4$	246	1.0	40.63	19.49
Gen. Anscombe (2.2.5)	TM	1	1		$10^8$	$10^4$	252	1.0	40.65	19.49
Gen. Anscombe (2.2.5)	TM	0.1	1		10	$10^4$	24	1.0	42.87	19.23
Gen. Anscombe (2.2.5)	TM	1	0		$10^6$	0	292	0.82	33.84	22.21
Gen. Anscombe (2.2.5)	TM	1	0		$10^6$	$10^3$	256	0.80	42.94	<b>26.32</b>
Gen. Anscombe (2.2.5)	TM	0.5	1		$10^7$	$10^4$	41	0.80	<b>45.95</b>	23.41
Gen. Anscombe (2.2.5)	TV	1	0		$5 \cdot 10^4$	0	2764	1.0	38.38	17.93
Gen. Anscombe (2.2.5)	TV	1	1		$5 \cdot 10^4$	0	818	1.0	38.82	18.03
Gen. Anscombe (2.2.5)	TV	1	0		$5 \cdot 10^3$	$10^3$	171	1.0	43.24	19.58
Gen. Anscombe (2.2.5)	TV	0.5	1		$10^4$	$10^4$	97	1.0	44.34	20.50
Gen. Anscombe (2.2.5)	TV	1	0		100	0	269	0.81	36.28	24.05
Gen. Anscombe (2.2.5)	TV	1	0		$10^3$	$10^3$	424	0.80	43.94	26.08

real world data the optimum is reached earlier). Beyond that point image noise amplification and boundary effects lead to an increase in the rmse for TM regularization. For high TV regularization the attenuations are well localized within the sample volume and therefore no significant attenuations are estimated at the boundaries. This results in monotonically decreasing rmses with small local fluctuations.

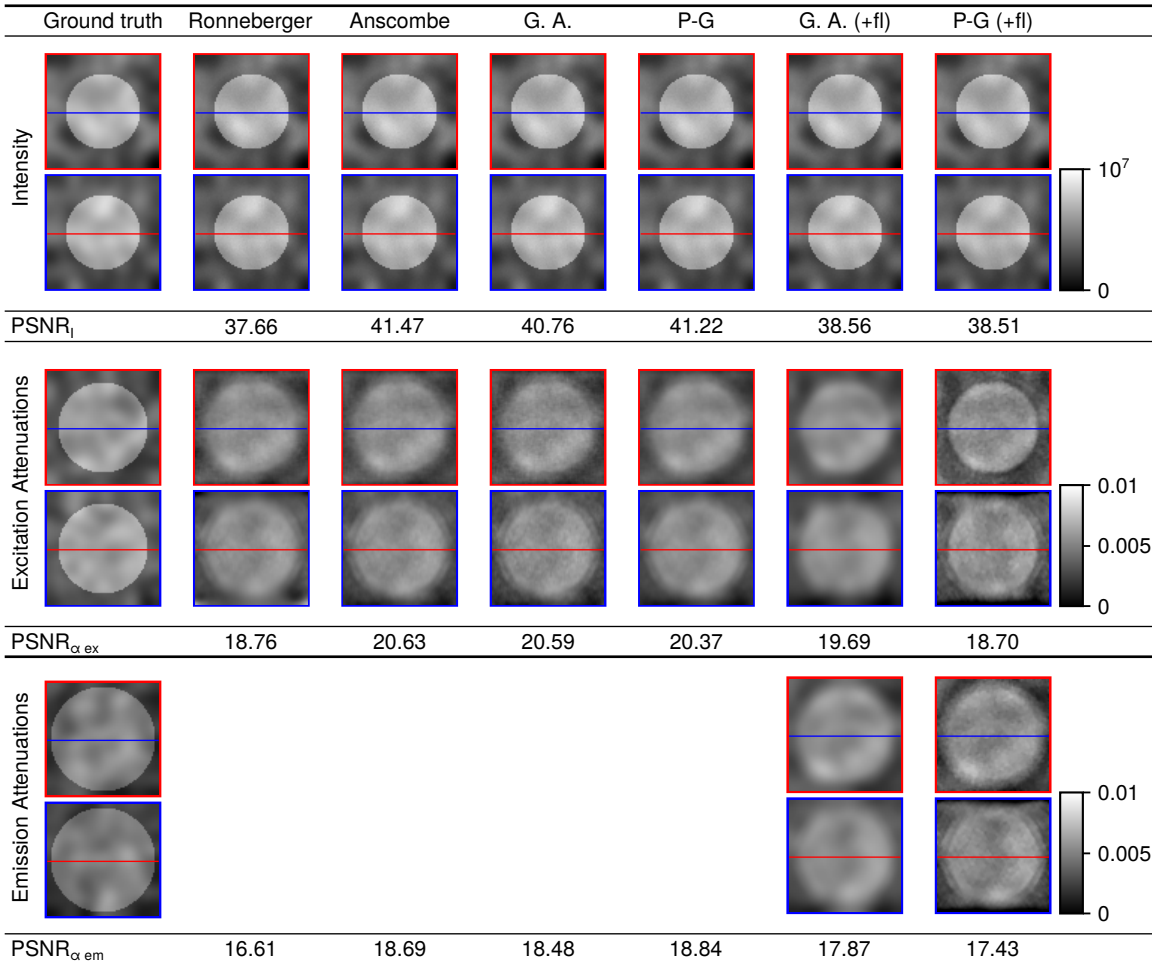
### Full image formation model

We applied all approaches (besides the one-factor-per-slice model) to the phantoms that were generated using the full image formation model with different attenuation fields for excitation and emission wavelength and more realistic bleaching. The best results from the grid-search are shown in table 2.5 and 2.6. Again, modeling of Poisson noise statistics slightly improves the reconstructions. The overall difference to the baseline is not as big, though, because the modeled bleaching is comparably mild with an average intensity reduction of only 5%.

With the full model we simulated two recordings from both sides, therefore we could also apply the multi-view approach with structured illumination. We expected an improvement especially in the reconstruction of the attenuation fields which was confirmed in the reconstructions of the Shepp-Logan phantom. However, the overall reconstructions of the intensities are slightly worse compared

**Table 2.5.:** Reconstruction quality after variational attenuation correction on the textured sphere phantom generated using the full image formation model. PSNR = Peak signal to noise ratio compared to the ground truth; G. A.: Generalized Anscombe; P-G: Poisson-Gaussian; +fl: structured illumination approach estimating two independent attenuation fields.

Method	Reg.	m / a	$\sigma$	$\lambda$	$\mu$	#iter	$\beta_2$	PSNR <sub>I</sub>	PSNR <sub><math>\alpha_{ex}</math></sub>	PSNR <sub><math>\alpha_{em}</math></sub>
Ronneberger et al. (2012)	TM	0	1	$10^{12}$	0	78	1.0	37.66	18.76	16.61
Gaussian (2.2.3)	TM	0	1	$10^{11}$	$10^6$	131	0.93	40.75	19.64	17.63
Anscombe (2.2.4)	TM	1	0	$10^8$	$10^3$	67	0.94	<b>41.47</b>	<b>20.63</b>	18.69
Gen. Anscombe (2.2.5)	TM	5	10	$10^7$	100	75	0.94	40.76	20.59	18.48
Poisson-Gaussian (2.2.6)	TM	5	10	$10^7$	100	62	0.94	41.28	20.38	<b>18.84</b>
Poisson-Gaussian dyn. (2.2.6)	TM	5	10	$10^7$	100	55	0.94	41.22	20.37	<b>18.84</b>
Gen. Anscombe (2.2.8)	TM	1	0	$10^9$	$10^4$	59	0.94	38.56	19.69	17.87
Poisson-Gaussian dyn. (2.2.8)	TV	5	10	10	100	24	0.94	38.51	18.70	17.43



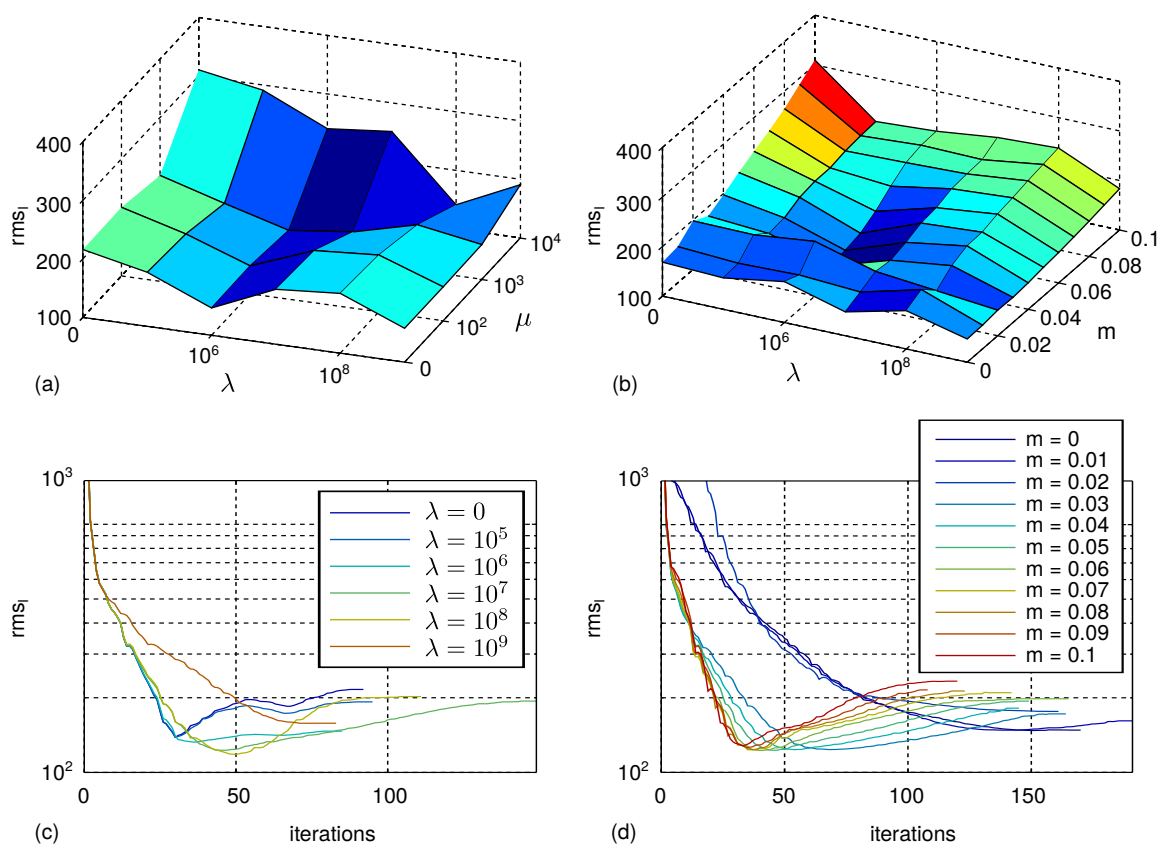
## 2. Variational attenuation correction

**Table 2.6.:** Reconstruction quality after variational attenuation correction on the Shepp-Logan phantom generated using the full image formation model. PSNR = Peak signal to noise ratio compared to the ground truth; G. A.: Generalized Anscombe; P-G: Poisson-Gaussian; +fl: structured illumination approach estimating two independent attenuation fields.

Method	Reg.	m	a	$\sigma$	$\lambda$	$\mu$	#iter	$\beta_2$	PSNR <sub>I</sub>	PSNR <sub><math>\alpha_{ex}</math></sub>	PSNR <sub><math>\alpha_{em}</math></sub>
Ronneberger et al. (2012)	TM	0	1	$10^{10}$	0		283	1.0	41.69	18.55	18.27
Gaussian (2.2.3)	TM	0	1	$10^{10}$	$10^6$		200	0.96	45.27	20.91	18.97
Anscombe (2.2.4)	TV	1	0	$10^3$	100		100	0.96	47.19	20.71	19.17
Gen. Anscombe (2.2.5)	TM	5	10	$10^6$	100		109	0.95	45.70	21.34	19.37
Poisson-Gaussian (2.2.6)	TV	5	10	50	10		629	0.94	45.56	21.47	19.37
Poisson-Gaussian dyn. (2.2.6)	TV	5	10	50	1		366	0.96	<b>47.58</b>	21.00	19.31
Gen. Anscombe (2.2.8)	TV	1	0	$10^3$	$10^3$		400	0.94	46.28	22.25	19.75
Poisson-Gaussian dyn. (2.2.8)	TV	5	10	50	10		725	0.95	42.86	<b>22.84</b>	<b>20.09</b>

	Ground truth	Ronneberger	Anscombe	G. A.	P-G	G. A. (+fl)	P-G (+fl)
Intensity							
PSNR <sub>I</sub>		41.69	47.19	45.70	47.58	46.28	42.86
Excitation Attenuations							
PSNR <sub><math>\alpha_{ex}</math></sub>		18.55	20.71	21.34	21.00	22.25	22.84
Emission Attenuations							
PSNR <sub><math>\alpha_{em}</math></sub>		18.27	19.17	19.37	19.31	19.75	20.09



**Figure 2.15.:** Effects of different choices for  $\lambda$ ,  $\mu$ , and  $m$  on the rmse of the reconstructed intensities of the textured sphere using TM regularization. (a) Effect of different combinations of  $\lambda$  and  $\mu$  on the reconstruction. Residual parameters:  $m = 0.05$ ,  $nIter = 50$ . (b) Effect of different combinations of  $\lambda$  and  $m$  on the rmse of the reconstruction. Residual parameters:  $\mu = 0$ ,  $nIter = 50$ . (c) Evolution of the rmse of the intensities during the iterative process for different choices of  $\lambda$ . Residual parameters:  $\mu = 0$ ,  $m = 0.05$ . (d) Evolution of the rmse of the intensities during the iterative process for different choices of  $m$ . Residual parameters:  $\lambda = 10^7$ ,  $\mu = 0$ .

to the two-view approaches, which only assume one wavelength-independent attenuation field. For the textured sphere neither the results for intensities nor attenuation fields could be improved. One explanation is, that the added measurements with partially closed aperture contain redundant information and they are much noisier compared to the primary recordings with fully opened aperture diaphragm. Additionally, changing the aperture geometry requires very fine cone sampling. We decreased the angular spacing to two degrees and used thin rays for the reconstructions. Dense sampling would further improve the results but is, as already discussed, infeasible in practice.

### 2.5.2. *Danio rerio* (Zebrafish)

Additionally to the result shown in Fig. 2.3, we applied our method to other zebrafish samples with varying staining quality. The reconstructions with Tikhonov Miller regularization are shown in

## 2. Variational attenuation correction

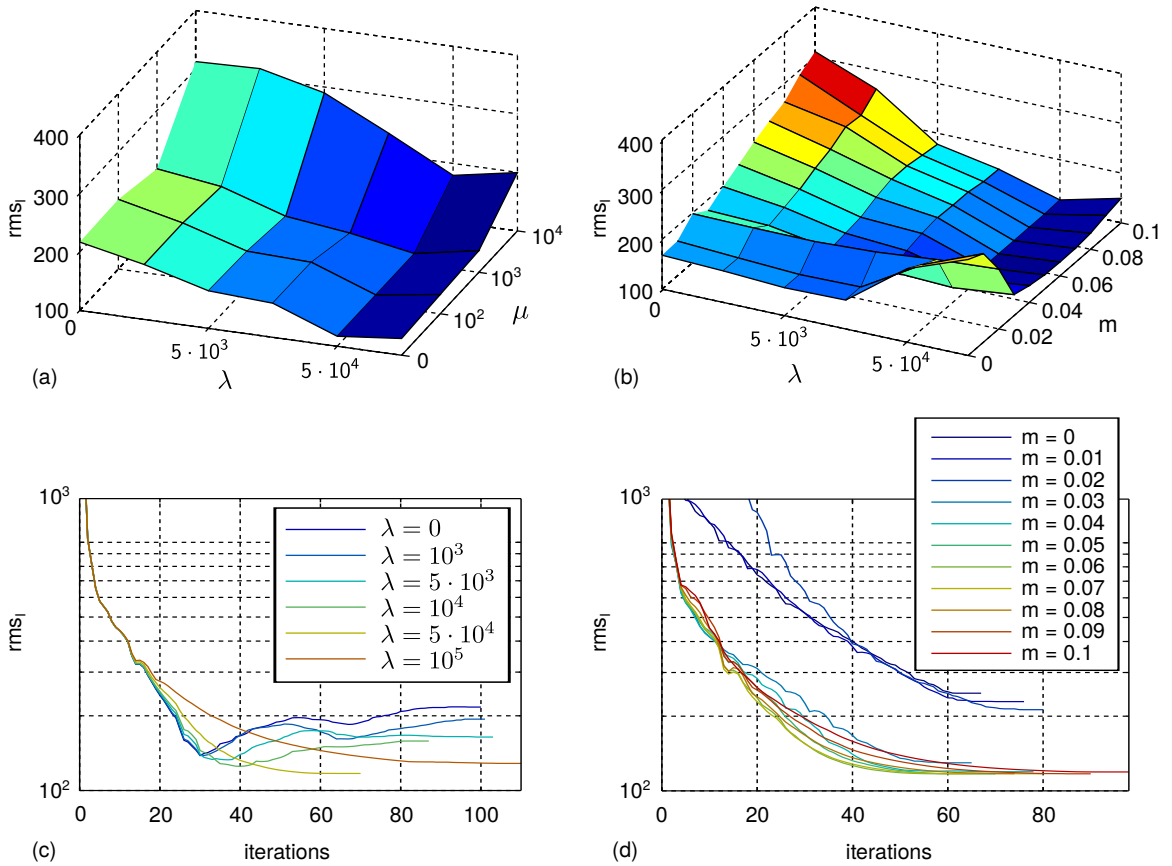


**Figure 2.16.:** Effects of different choices for  $\lambda$ ,  $\mu$ , and  $m$  on the rmse of the reconstructed intensities of the textured sphere phantom using TV regularization. (a) Effect of different combinations of  $\lambda$  and  $\mu$  on the reconstruction. Residual parameters:  $m = 0.05$ , run to convergence. (b) Effect of different combinations of  $\lambda$  and  $m$  on the reconstruction. Residual parameters:  $\mu = 0$ , run to convergence. (c) Evolution of the rmse of the intensities during the iterative process for different choices of  $\lambda$ . Residual parameters:  $\mu = 0$ ,  $m = 0.05$ . (d) Evolution of the rmse of the intensities during the iterative process for different choices of  $m$ . Residual parameters:  $\lambda = 5 \cdot 10^4$ ,  $\mu = 0$ .

Fig. 2.17 and for total variation regularization in Fig. 2.18. The estimated attenuation coefficients clearly resemble the shapes of the embryos. The bright spots in the eyes stem from strong refraction in the eyes' lenses showing the modeling limitations of the presented approach. However, due to the imposed priors the artifact is localized in a small region and affects the surrounding reconstruction only marginally.

Fig. 2.19 shows a comparison of the proposed direct Poisson-Gaussian approach to the one-factor-per-slice model and the baseline approach of Ronneberger et al. (2012) for one fish. For the baseline of Ronneberger et al. (2012) we set  $\lambda = 10^7$ , for the proposed approach we used  $\lambda = 10^7$ ,  $\mu = 10^3$  and  $m = 0$ . The one-factor-per-slice model is not able to recover the intensity spectrum since it cannot change the ratio between the boundary and interior intensities. In the brain region of the fish the

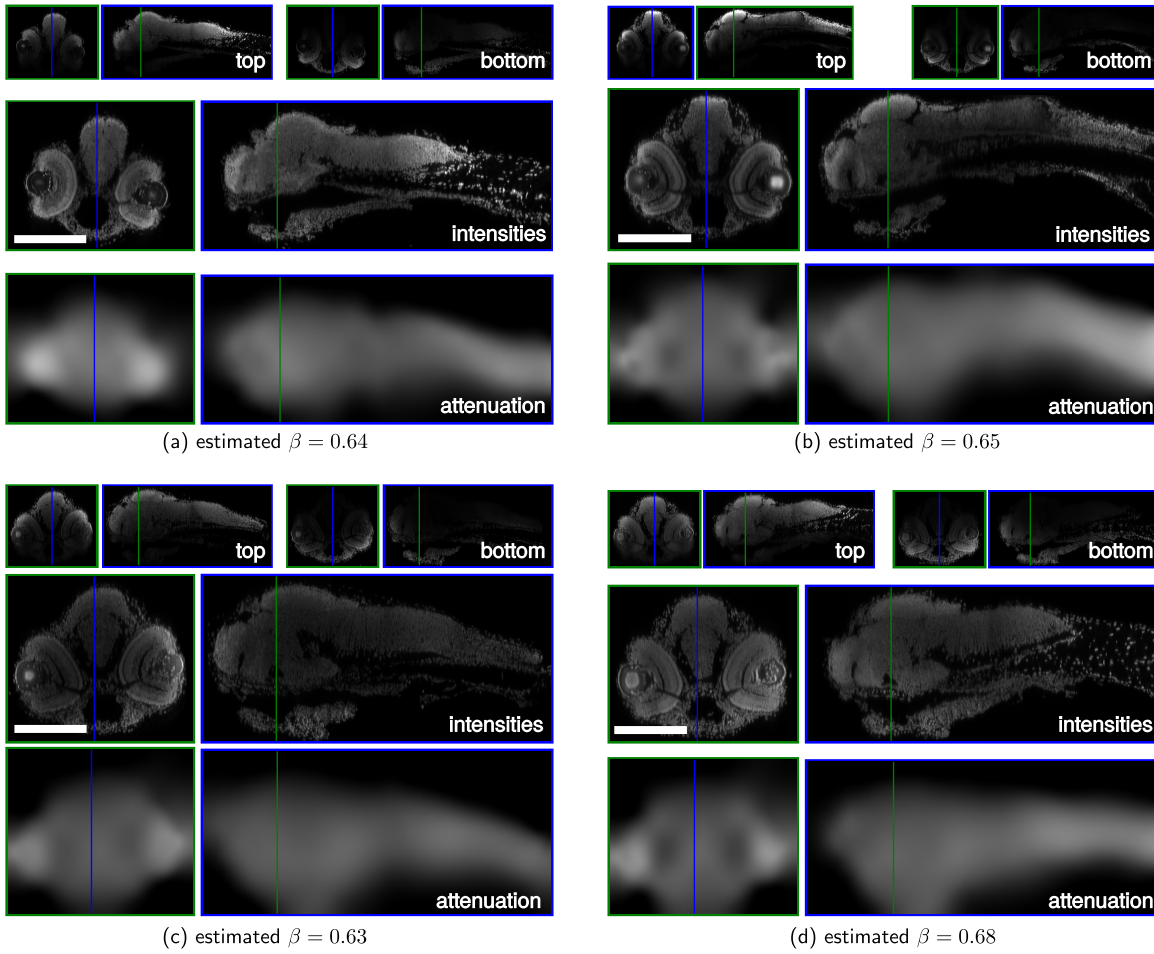


**Figure 2.17.:** Result of the application of the proposed method to four challenging samples of the ViBE-Z database (TM regularized,  $\lambda = 10^8$ ,  $\mu = 10^4$ ,  $m = 0$ ). Each panel shows: top: yz- and xz-cuts through zebrafish recordings from top and bottom; middle: Reconstructed intensities; bottom: Estimated attenuation coefficients. Colored lines indicate cut positions of the corresponding views. Scale bars:  $200\mu\text{m}$ .

baseline and the proposed approach estimate the same intensities, whereas the proposed approach emphasizes the tissue layers in the zebrafish eyes stronger. The proposed approach shows slightly smaller intensity overshoots at the eyes' surfaces and around the nose but overall both reconstructions are convincing. The apparent ventral "bleeding" of the attenuation coefficients is reduced. The stair-casing artifacts along the back of the fish in the baseline approach which were introduced with the orthogonal subspace projections are effectively removed.

## 2. Variational attenuation correction

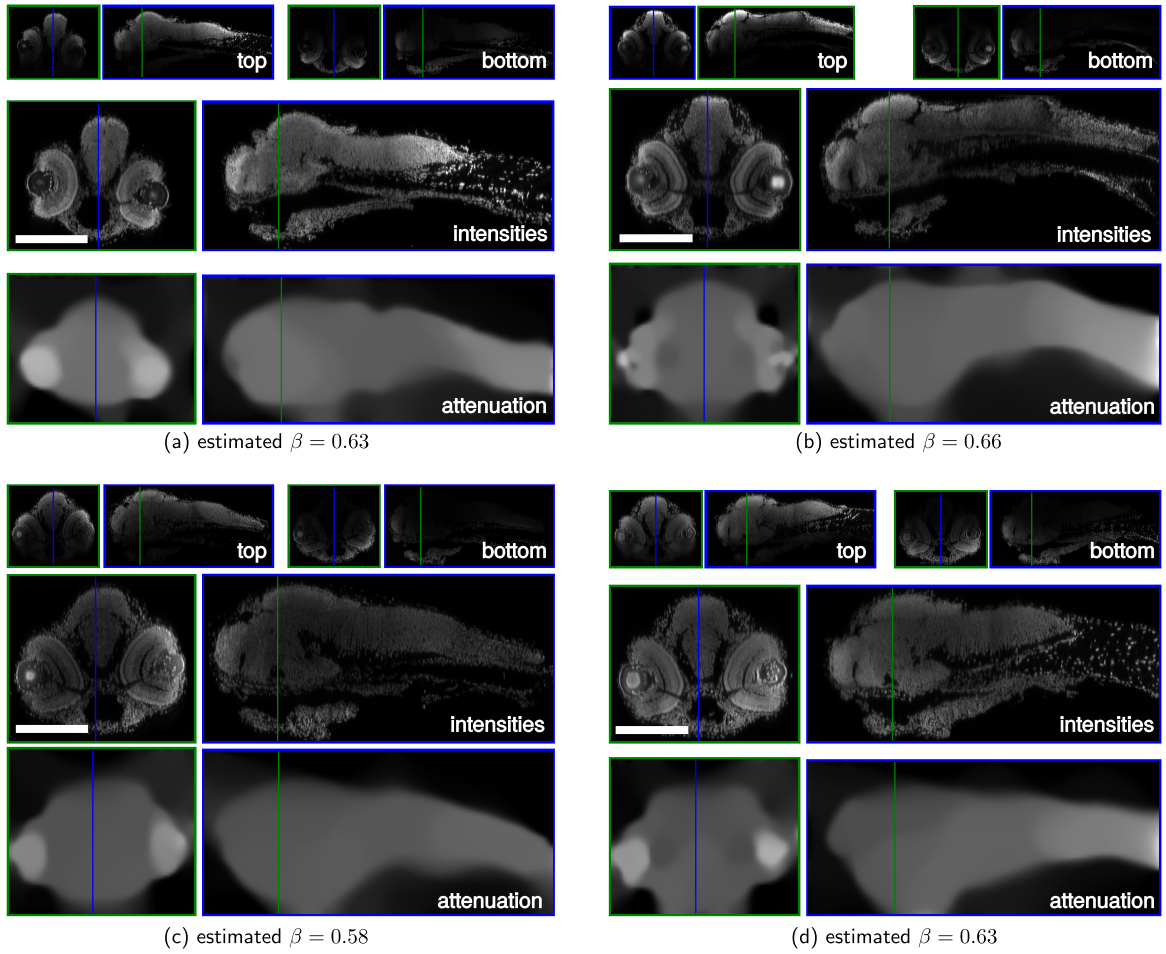
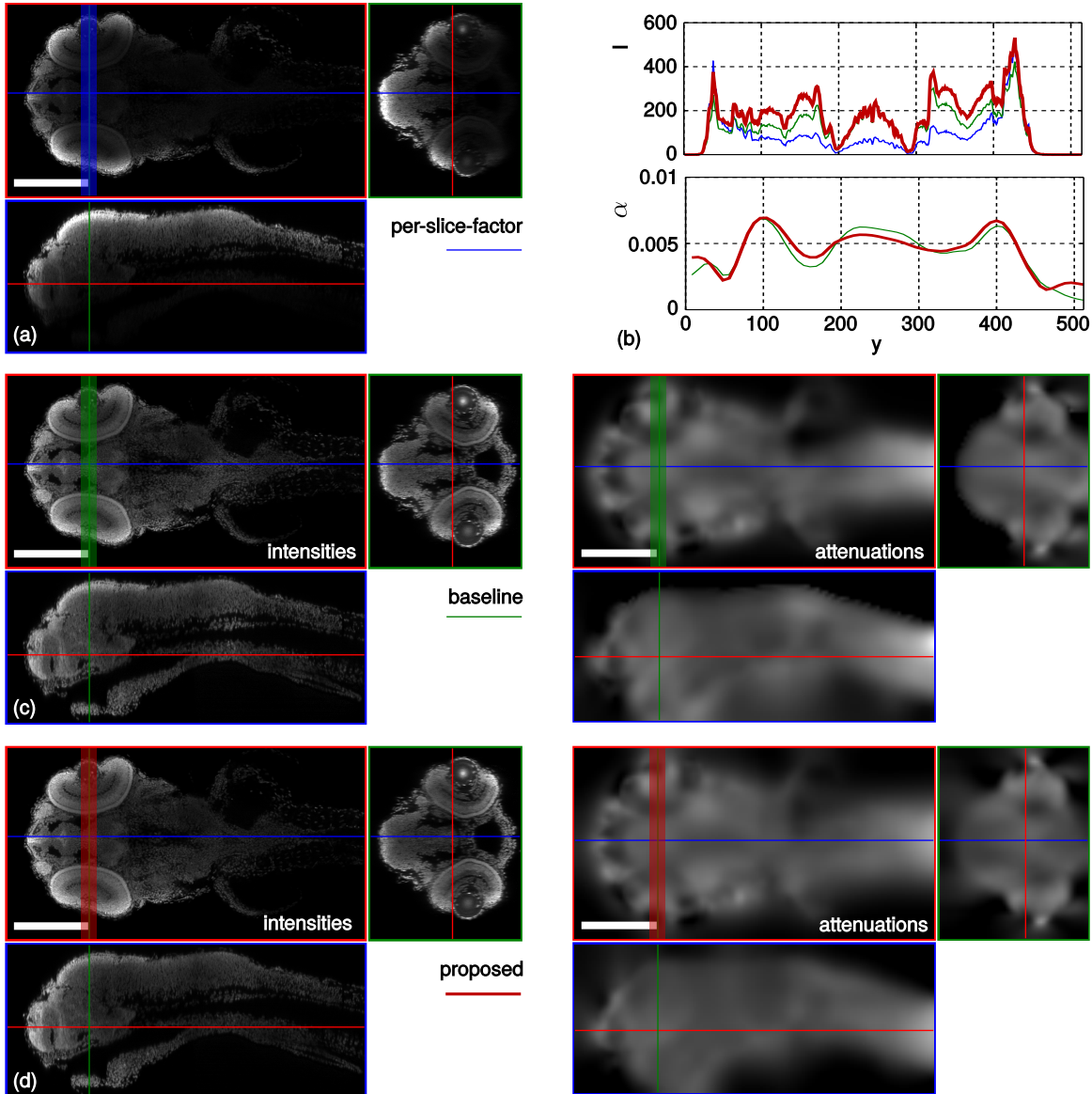


**Figure 2.18.:** Result of the application of the proposed method to four challenging samples of the ViBE-Z database (TV regularized,  $\lambda = 5 \cdot 10^4$ ,  $\mu = 0$ ,  $m = 0$ ). Each panel shows: top: yz- and xz-cuts through zebrafish recordings from top and bottom; middle: Reconstructed intensities; bottom: Estimated attenuation coefficients. Colored lines indicate cut positions of the corresponding views. Scale bars: 200 μm.

### 2.5.3. *Arabidopsis thaliana* (Thale cress)

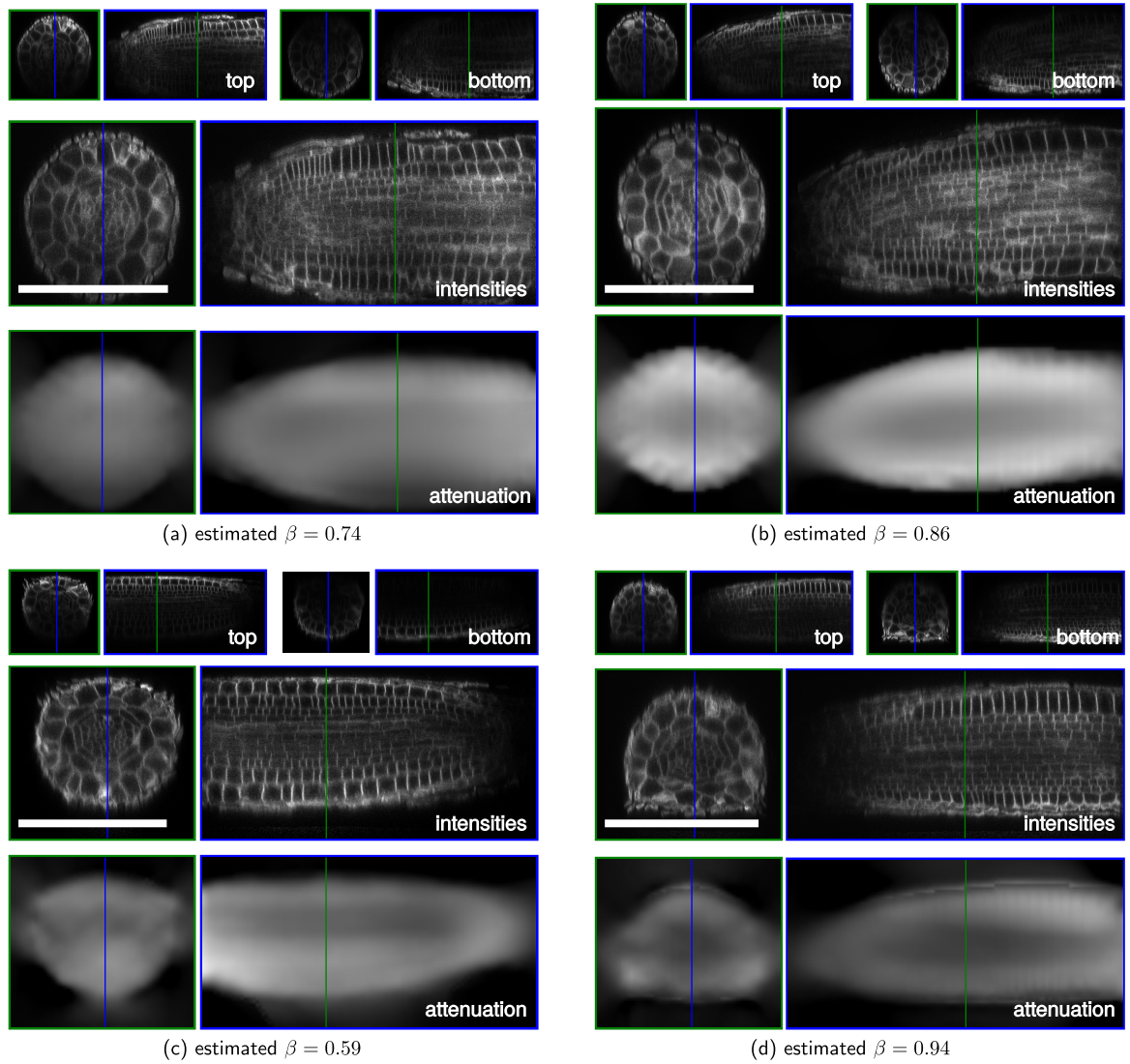
The mismatch in refractive indices of immersion and embedding media in the *Arabidopsis* sample preparation leads to an aberration induced signal loss, that is not modeled in the presented approach. However, Fig. 2.20 shows that our method still accurately reconstructs the intensities of the root tip datasets.

Fig. 2.21 shows a comparison of the proposed approach to the one-factor-per-slice model and the baseline approach of Ronneberger et al. (2012) for one root tip. Again the one-factor-per slice model cannot reconstruct the interior intensities. Both, the approach of Ronneberger et al. (2012) and the proposed direct Poisson-Gaussian model significantly enhance the root-internal contrast. However, an intensity gradient towards the root center remains visible. We assume, that it is induced



**Figure 2.19.:** Comparison of the proposed direct Poisson-Gaussian estimate with Ronneberger et al. (2012) and the one-factor-per-slice model on one zebrafish dataset. Each panel shows xy-, xz- and zy-cuts through the volume. The cut positions are indicated by colored lines. (a) Raw recording with scaled intensities to match the intensities of the reconstruction on the eye surface. (b) Averaged intensity and attenuation profiles along the y-direction of the xy cuts. Cut positions and averaging width are indicated by colored bars. (c) Baseline reconstruction Ronneberger et al. (2012). (d) Proposed method. Scale bars: 200µm.

## 2. Variational attenuation correction



**Figure 2.20.:** Attenuation Correction on *Arabidopsis thaliana* images. Result of the application of the proposed direct Poisson-Gaussian model to four *Arabidopsis* root tip samples (TM regularized,  $\lambda = 10^7$ ,  $\mu = 0$ ,  $m = 0.1$ ). Each panel shows: top: yz- and xz-cuts through *Arabidopsis* root tip recordings from top and bottom; middle: Reconstructed intensities; bottom: Estimated attenuation coefficients. Colored lines indicate cut positions in the corresponding views. Scale bars:  $100\mu\text{m}$ .

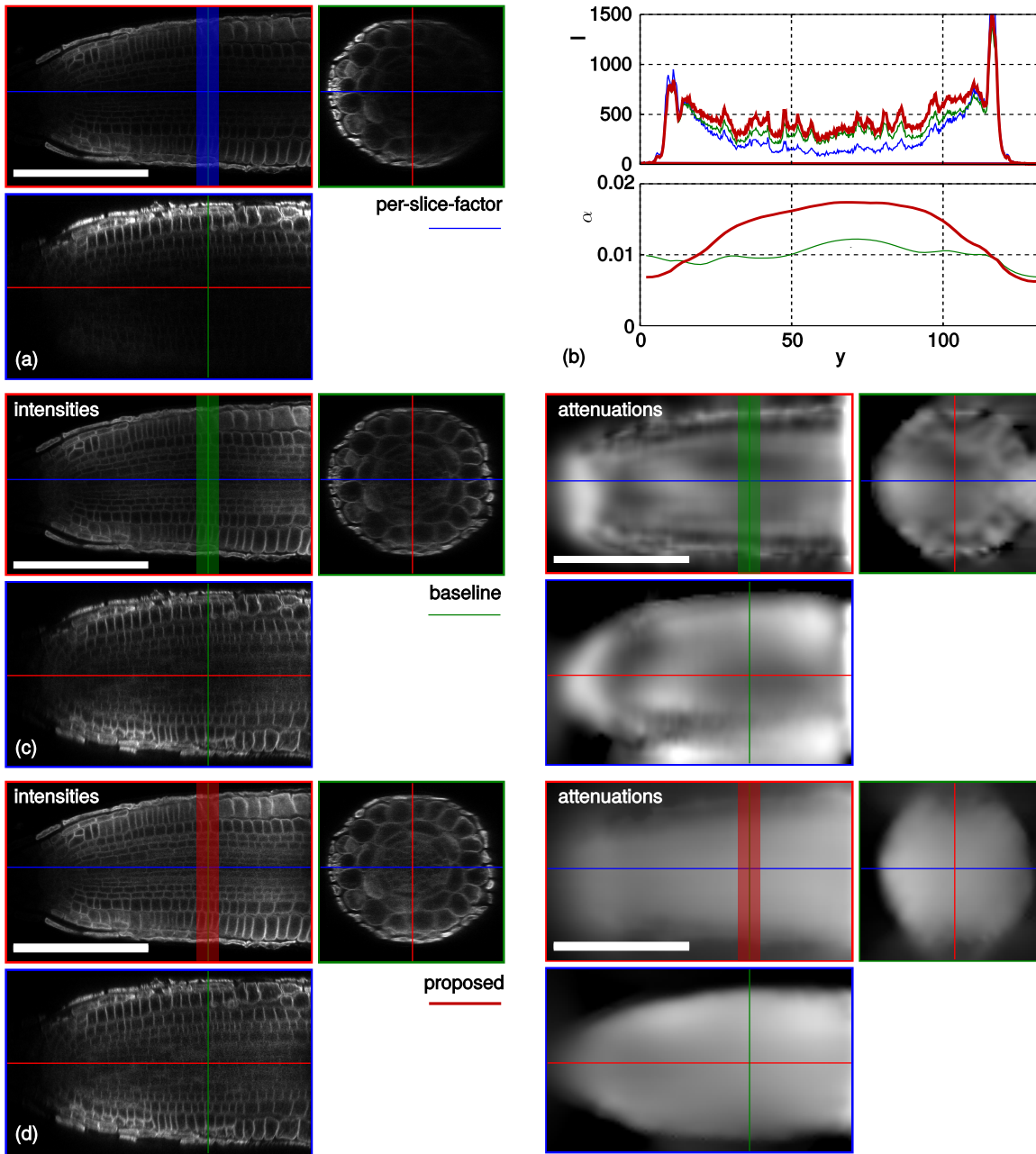


**Figure 2.21.:** Comparison of the direct Poisson-Gaussian model with Ronneberger et al. (2012) and the one-factor-per-slice model on one Arabidopsis root tip dataset. Each panel shows xy-, xz- and zy-cuts through the volume. The cut positions are indicated by colored lines. (a) Raw recording with scaled intensities to match the intensities of the reconstructions at the root boundary. (b) Averaged intensity profiles along the y-direction of the xy cuts. Cut positions and averaging widths are indicated by colored bars. (c) Baseline reconstruction Ronneberger et al. (2012). (d) Proposed method. Scale bars:  $100\mu\text{m}$ .

by imperfect marker distributions due to incomplete tissue penetration and the properties of the inner cell membranes. The estimated attenuation field closely resembles the root's shape and is homogeneous compared to the baseline approach. The baseline approach shows strong variation within the root and additionally estimates strong attenuation outside the root volume to cope with bleaching effects. Such erroneous attenuation estimates may lead to reasonable reconstructions of the intensities of the channel they were estimated on, but they will fail in reconstructing secondary channels containing the markers to quantify like protein patterns.

### 2.5.4. Limitations

The exponential decay model along a ray is only strictly valid for pure absorption. In most cases local random light scatter can also be described by this model. However, in areas with clearly structured refraction, as *e.g.* in the eyes of the zebrafish, where the light is actively bundled, the model is violated and localized errors in the attenuation estimates are introduced. We minimize the influence of these errors with high regularization, however, a better modeling of refraction would be a desirable – though practically very challenging – extension.

Another source of error is the limited recording volume. Samples exceeding this volume introduce the problem of sensibly guessing the outside attenuations the rays pass before entering the recording volume. Boundary effects can lead to solutions with low energies which are qualitatively far away from the optimum, especially when performing many iterations. In our image formation model we assume zero outside attenuations (natural boundary conditions), while for the regularization we assume Neumann boundary conditions. If possible, the recording volume should be increased to contain more background in cases of boundary problems. If this is not possible TV regularization with its sharp boundaries is to prefer over TM regularization. Additionally a high weight on the sparsity term alleviates effects that lead to extreme attenuation estimates. This can be the case when outside attenuations are explained by a thin highly absorbing region at the image boundary. An alternative, that leads to visually good, but energetically suboptimal results, is to restrict the number of iterations (less than ten iterations usually lead to qualitatively good results). This has the additional advantage of very low computation times.

## 2.6. Conclusions

We could significantly improve the results of the variational attenuation correction of Ronneberger et al. (2012) by additionally modeling photo bleaching in a zero-order approximation. The modeled Poisson-Gaussian noise statistics had only minor impact on the reconstructions. While in the phantoms a small quality increase is still measurable in practice the Gaussian model leads to equally plausible results. The choice of the loss function in the smoothness term allows to choose between smoothly varying (TM) or piece-wise constant (TV) attenuation fields. The appropriate choice is application dependent. In our case both regularization strategies lead to equally plausible results in the rather inhomogeneous biological samples analyzed. TV regularization is more stable in practice because the attenuation is much better localized, and therefore less boundary artifacts – that

may lead to convergence to undesired solutions – are introduced. For both regularization strategies the sparsity term also actively avoids boundary errors, by keeping the attenuation field compact. However, high sparsity weights lead to an underestimation of the attenuation volume and should be avoided.

As we could observe in Fig. 2.15 lower energy results do not guarantee good reconstructions. The energy first rapidly drops while properly estimating attenuations and intensities. In these first iterations the model is accurate enough to point the optimization in the right direction. Later in the optimization imperfections of the model and numerical inaccuracies may dominate, leading to convergence to undesired solutions. Therefore limiting the number of iterations often leads to better reconstructions. Similar behavior can be observed for other inverse problems as well (*e.g.* Keuper et al. (2013) in image deconvolution). For the presented synthetic data fifty iterations were a good compromise to reach high PSNR results, whereas, for our real world examples reconstructions after less than ten iterations were visually most convincing.

We showed the efficacy of the presented method on highly complex real world examples, where it was able to significantly increase the homogeneity of the measured signal and attenuation fields. This is crucial if the attenuation field is used to correct secondary channels containing sparse structures within the anatomy. Based on these findings, we conclude that the presented attenuation correction approach is an important step towards the quantification of confocal microscopic data.



### 3. The intrinsic Root Coordinate System (iRoCS)

Most current approaches for the analysis of the Arabidopsis root architecture and development are restricted to the central longitudinal 2-D root slice (Santuari et al., 2011; Federici et al., 2012). For many analyses this is sufficient, assuming perfect rotational root symmetry. Even with slight imperfections many valid conclusions can be drawn from analyzing one plane only. However, obtaining an image of the central root slice without imaging the whole 3-D root geometry is a challenge in itself. Very careful preparation is required to mechanically fix the root perpendicular to the optical axis without pressing it. To circumvent the mechanical fixation problem, Santuari et al. (2011) recorded full 3-D stacks of roots, then manually fitted a B-spline surface to the central longitudinal plane of each of them and rendered 2-D images of those planes for further analysis. Although all data for a full 3-D analysis were available 90% of the recorded data were not analyzed due to a lack of tools to perform such 3-D analyses. Besides this waste of valuable data, manual choice of the plane may introduce an experimental bias, *e.g.* when analyzing the distribution of cell divisions in the root tip, sections containing many divisions are selected. When analyzing the whole root volume instead, all events are captured, and especially in the case of rare events, like mitoses, statistical conclusions drawn are of much higher significance given the same number of root samples.

In this chapter we will present our approach to the automatic analysis of confocal 3-D image stacks of the Arabidopsis root tip to quantify key events in the root context. For this we describe the root geometry in the **intrinsic Root Coordinate System (iRoCS)** which maps any Euclidean recording position  $\mathbf{p} = (p_1, p_2, p_3) \in \Omega$  to a unique anatomic coordinate  $(z, r, \varphi, \text{layer}, \text{file}) \in \mathbb{R} \times \mathbb{R}^+ \times [0, 2\pi) \times \mathbb{N} \times \mathbb{N}$ , where  $z$  is the signed distance to the quiescent center along the root axis,  $r$  is the radial distance perpendicular to the axis,  $\varphi$  is the angle around the axis, layer is the cell layer index and file is the cell file index (Fig. 3.1). The model enables pooling of detected key events in individual roots of different plant populations and compare those populations to each other. We developed automated image processing pipelines to compute this mapping (except for cell file classification) based on different anatomical reference structures: cell nuclei and cell boundaries (walls/membranes) (Fig. 3.2).

#### Outline

In section 3.1 we give a brief description of the Arabidopsis root tip anatomy and of the signaling process we analyze in section 3.5. We will compare different approaches to detect nuclei in 3D images of fixed, DAPI-stained root samples in section 3.2 and present a general approach allowing to adapt the detector to different tasks by supervised training. There we also briefly introduce the

### 3. The *intrinsic Root Coordinate System (iRoCS)*

---

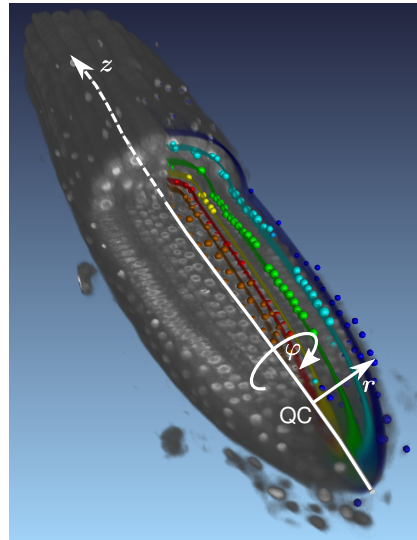


**Figure 3.1.:** The **intrinsic Root Coordinate System (iRoCS)**. Gray: 3D rendering of a DAPI stained root tip cut along a bent longitudinal plane; Colored spheres: Sample nuclei; Colored Shells: Cell layers; White annotations: The bent cylinder coordinate system fitted to the root.

cellular segmentation which is the first step in the cell boundary based pipeline that was developed by Kun Liu. Then, in section 3.3.2 we will describe a variational approach to fit a bent cylinder with varying thickness to measured sparse and noisy surface points. This fit, in conjunction with the manually given quiescent center position, form the continuous coordinate axes of iRoCS. A description of the root in cylinder coordinates was already introduced by Sena et al. (2011), who analyzed nuclear motion in *Arabidopsis* root tips. Based on appearance cues and its normalized position in the root, the discrete dimension “cell layer” is finally assigned to each cell. Additional manual annotations are possible which allow to further distinguish cell files and if required even single cells.

#### 3.1. The *Arabidopsis* root

The root tip architecture is depicted in Fig. 3.3. The segmentation and layer labels in Fig. 3.3b-c result from applying the iRoCS pipeline to a propidium iodide (PI) stained root. Classification errors (less than 10% of all cells) were manually corrected and cell sub-types (initial cells, columella/lateral root cap, T/AT cells and the different cell types in vasculature) were labeled manually.

The used terminology and definition of the *Arabidopsis* root architecture in the upcoming sections mainly follow Scheres et al. (2002); Cederholm et al. (2012).

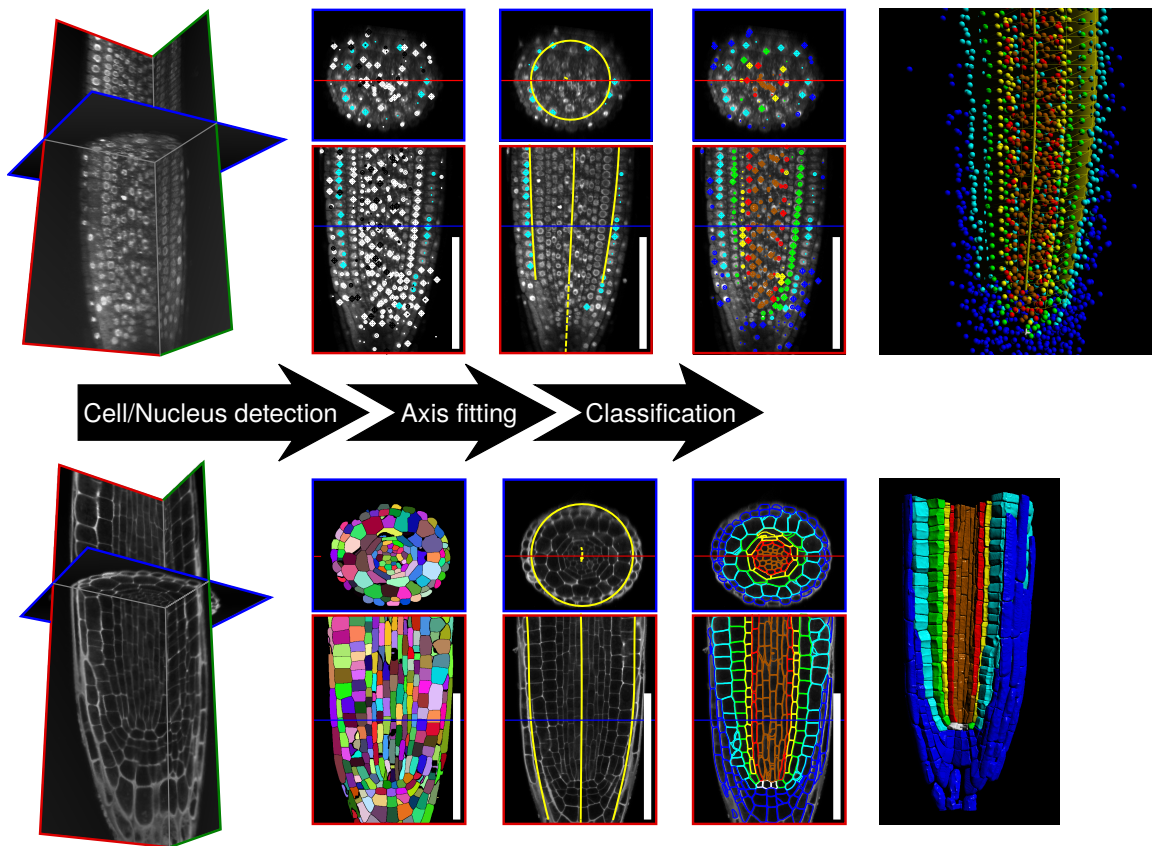


**Figure 3.2.:** The iRoCS pipelines. Top: Nucleus-based pipeline; bottom: cell-boundary based pipeline. Both pipelines consist of three steps: Structure detection/segmentation; registration of a bent cylinder coordinate system; assignment of discrete layer labels to the individual cells/nuclei. The only required input is the position of the root's quiescent center, marking the coordinate origin of iRoCS.

### 3.1.1. Developmental zones (longitudinal)

The origin of all root cells is the quiescent center (QC) consisting of four rarely dividing initial cells (short: initials) at the apex of the root apical meristem. In the further course of this these all measures will be given relative to the QC position.

The main root can be subdivided into different longitudinal zones. Starting from QC, these are the root apical meristem (MZ or RAM) ( $\approx 350\mu\text{m}$ ), a transition zone (TZ), the elongation zone (EZ), the differentiation zone (DZ) and the mature root.

**MZ (Meristematic zone (RAM))** The meristematic zone consists of a few thousand short undifferentiated cells. Within the RAM new cells are produced via patterned cell divisions. Nuclei within the RAM can be visually clearly distinguished from nuclei of differentiated cells. Their

### 3. The *intrinsic* Root Coordinate System (iRoCS)

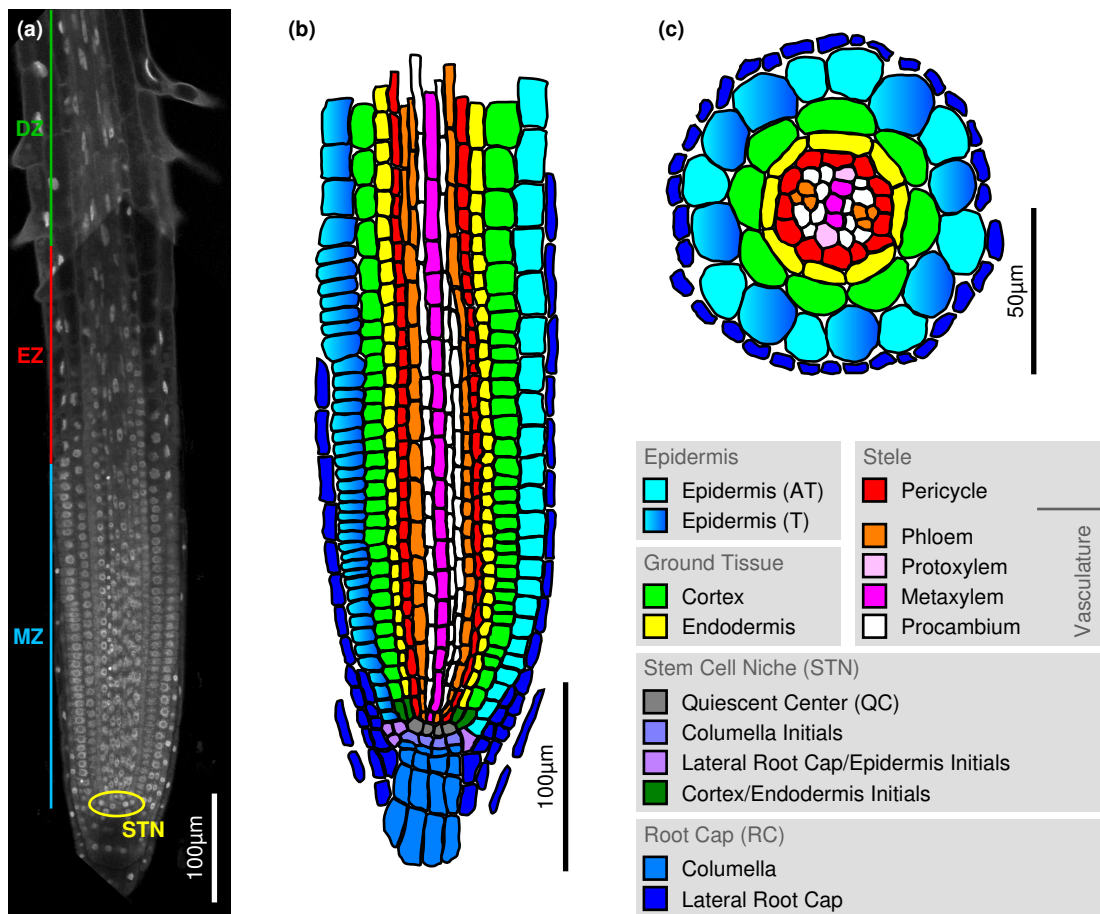


**Figure 3.3.:** The *Arabidopsis thaliana* root architecture. (a) Longitudinal section through a DAPI stained *Arabidopsis* root tip. The developmental zones are marked with colored bars. MZ = meristematic zone, EZ = elongation zone, DZ = differentiation zone, STN = Stem cell niche. (b) Sketch of a longitudinal section showing the different cell types. (c) Sketch of a transversal section. Black lines indicate cell membranes. Epidermis is subdivided into cells that potentially produce root hairs (Trichoblasts T) and cells that cease this possibility (Atrichoblasts AT).

chromosomes are almost completely unfolded into a homogeneous distribution of chromatin within the nuclear volume. Besides the chromatin they contain, with few exceptions, one big nucleolus, which is roughly centered in the nucleus. With DNA stain this gives the nuclei a characteristic appearance of bright roughly ellipsoidal shells containing a centered dark sphere, the nucleolus. Especially towards the root center the nuclear appearance changes slightly. Nuclei become elongated and in few cases multiple nucleoli can be observed.

**EZ (Elongation zone)** Rapid longitudinal elongation of cells in the elongation zone is the main factor of root growth. Within EZ no further cellular divisions can be observed and the cells start to take on their final fate. DNA is still copied in many cells, leading to polyploid nuclei, which lose their ability to divide. Cells elongate from initial lengths of 10 to 15  $\mu\text{m}$  up to 100  $\mu\text{m}$  and more upon maturation.

**DZ (Differentiation zone)** Within the differentiation zone cells change their architecture to fulfill their final purposes, which are anchorage of the plant in soil, water and nutrient uptake and transport towards the shoot, and sugar and photosynthesis product transport towards the root tip. For this, several different cell types are produced which are detailed in the following subsection. Visually the starting point of the DZ can be clearly determined by the outgrowth of root hairs. During maturation, cells do not reproduce any more. Only parts of the DNA need to be read-out, therefore mature nuclei contain compact chromosomes and unfolded DNA (chromatine), giving the nuclei an inhomogeneous appearance. The nucleoli become very small. Sometimes their size drops below the resolution limit of optical imaging methods and therefore they seem to disappear completely. Only few cells in the DZ are still potent to divide for the purpose of secondary lateral root formation. Lateral roots – once their stem cell niche is established – show the same architecture as the primary root. All experiments within this thesis were performed on the primary root.

### 3.1.2. Tissue types (transversal)

The root cap consists of two parts, the columella distal from QC and the lateral root cap which acts as a protecting shell around the RAM. Adjacent to the four QC cells are the initial cells for the inner root tissues and the root cap. One can distinguish three types of initial cells, the columella initials apical to the QC, the root cap/epidermis initials, forming the outer cell layers and the cortex/endodermis initials, forming the inner cell layers, the so-called ground tissue. Root cap/epidermis and cortex/endodermis initials first perform an anticlinal cell division resulting in two adjacent cell layers, namely lateral root cap and epidermis, resp. cortex and endodermis. All subsequent divisions are periclinal and produce two daughter cells in longitudinal direction. This stereotypic division pattern leads to single strings of cells originating from the same initial cell. These strings, during the rest of the thesis called files, make up the cell layers which fulfill different tasks upon differentiation. As already enumerated layers are the lateral root cap, epidermis, cortex, endodermis, and pericycle. The residual interior cells are the (pro-)vasculature. The lateral root cap peels off at a distance of approximately 350 $\mu$ m from QC, marking the transition zone.

A closer look at the epidermis allows to further refine the model and distinguish two groups of cells. In the mature root some of the files produce root hairs (trichoblasts), and the others do not. Cells potentially producing trichoblasts are called trichoblast cells (T) the others atrichoblast cells (AT). The higher cell density in T cell files compared to AT cell files allows to distinguish them already in the RAM prior to root hair formation. Trichoblasts fulfill two purposes, first they anchor the plant in soil, and secondly they lead nutrients and water into the root. Overall the epidermis consists of around 20 cell files, eight of them having the potential to produce trichoblasts. The signaling pathways leading to these distinct fates are not fully understood, but T cells always attach to cortex cells of two cell files, whereas AT cells only attach to one.

In the wild type, the cortex cell layer is made up of eight cell files. It consists of very large cells, allowing to easily distinguish this layer from others in transversal root sections.

The endodermis also consists of eight cell files. In DAPI stained root tips this layer sometimes pops out due to strong cytoplasmic fluorescence emission. Whether this signal increase is a result

### 3. The *intrinsic Root Coordinate System (iRoCS)*

---

of higher cell organelle density, of which some have their own DNA content, or an effect of lower rinsing efficiency due to lower permeability of the membranes, is not clear. The latter assumption is strengthened by the fact that the root-internal flux is inverted at the inner membrane of this layer. More details on the flux within the root apical meristem will be given in section 3.1.3.

The pericycle cell layer consists of approximately 15 cell files of comparably small cells. In contrast to the other cell layers some cells of this layer keep their stem cell property even in the MZ. This is important for root branching, since differentiated cells cease their ability to divide.

The number of cell files in the inner root tissue, the vasculature, is variable. However, it shows a clear two-fold symmetry. A small number of vasculature files produce the medial xylem sheet dividing the vasculature into two halves. In the RAM they pop out because of their large cell and nucleus size compared to the surrounding procambial cells. During maturation they elongate to thin tubules which are responsible for rapid water and nutrient transport towards the shoot. At the vascular poles perpendicular to the xylem sheet are the phloem files, which upon differentiation lead photosynthetic products like sugars, RNA, proteins and others towards the root tip. Before maturation phloem cells are small with very condensed nuclei with tiny nucleoli, which allows to easily distinguish them from the surrounding cell files.

#### **3.1.3. Root growth control**

Root growth requires first, production of new cells via cell division in the RAM and secondly, cellular elongation in the EZ. Whether a cell is dividing or elongating is controlled by different factors of which only some are known. One very important factor is the plant hormone auxin (mostly Indole-3-acetic acid (IAA)) forming a longitudinal concentration gradient in the Arabidopsis root tip. This gradient is maintained by auxin influx and efflux carriers which are membrane-bound proteins regulating cell-to-cell auxin flux in the RAM. The maximum auxin concentration is found apical to QC in the columella initials where the influx from stele is redirected (inverted) to the ground tissue. One known auxin influx carrier is AUX1 which carries auxin directly from the shoot towards the root through the vascular parenchyma. Known auxin efflux carriers are the family of pinformed proteins (PINs) of which eight types can be found in Arabidopsis at different locations in the root tip. Four PINs, 1, 3, 4 and 7, are located in the stele and act redundantly (Friml et al., 2002; Teale et al., 2006), whereas another, PIN2, mediates the epidermal flow of auxin away from the root tip to influence the root's gravitropic response (Müller et al., 1998).

## **3.2. Detection and segmentation of cells and nuclei**

One important task in the analysis of biological image data is the detection of structures of interest. These may be simple geometric structures like planes, plane intersections or spots, but also more abstract ones like cell outlines, nuclei or organelles. The kind of detector to apply depends on the type of structure to extract. The quality of the results mainly depends on the proficiency of the expert in selecting the right pre-processing steps and detector. Often this choice is not straight forward and requires some creativity to cope with the different visual appearances of high-level structures.

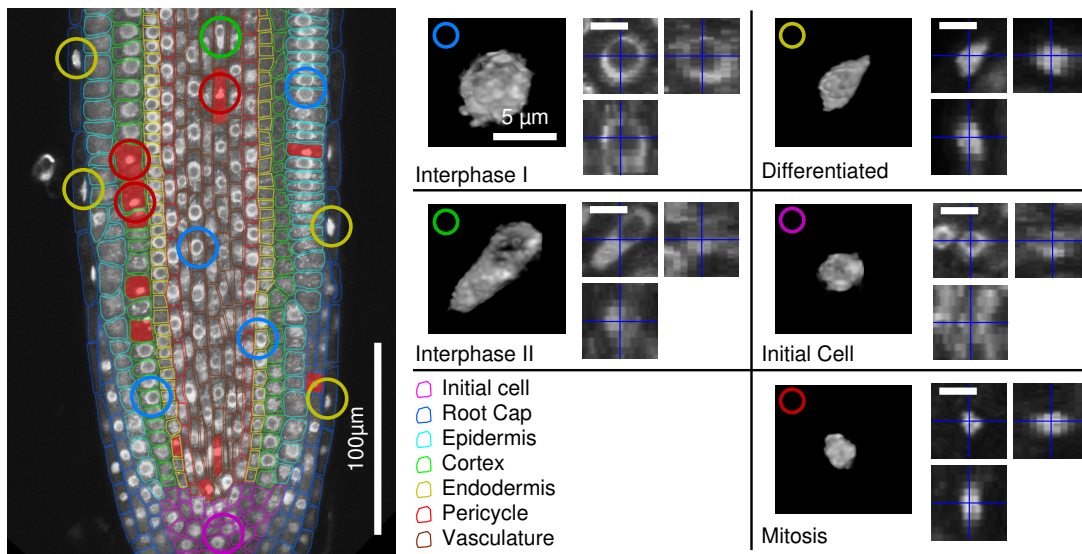


**Figure 3.4.:** Cross-section through a DAPI stained Arabidopsis root tip after colchicine treatment (left), and examples of nuclear morphologies (right). Cell boundaries are manually annotated. There are five prominent classes of nuclear appearance. Each panel shows one volume rendering and three orthographic views of a typical nucleus.

### 3.2.1. Nucleus detection

Nuclear morphology varies depending on the cell’s developmental state and final fate. This is already visible in the RAM and becomes clearer with cell differentiation. Therefore giving a uniform description of how a cell nucleus looks like is not straight forward. Figure 3.4 gives an impression of this variation restricted to the RAM which is of special interest for developmental studies.

If not indicated otherwise, results reported within this thesis were obtained on fixed root tip samples recorded using confocal microscopy. To make the nuclei emit fluorescent light under UV excitation they were marked with 4’,6-diamidino-2-phenylindole (DAPI) (Kapusinski, 1995). DAPI directly binds to DNA and targets regions with high adenine-thymine (A-T) bond density. For undifferentiated nuclei within the RAM this leads to the characteristic appearance of bright spherical structures enclosing a dark roughly concentric dark sphere – the nucleolus. An exception are dividing cells that can have very different nuclear appearances depending on their mitotic state. In section 3.5 we will use iRoCS to compare mitosis distributions. To allow such a comparison with comparably few roots we treated the plants with colchicine one hour before fixation. Colchicine inhibits the chromosome separation in anaphase by degrading the microtubules responsible for proper chromosome transport. This has two nice effects for the analysis. First, mitoses become trapped in metaphase and accumulate over the incubation period leading to many more samples for the statistical analysis, and secondly the dense unorganized “chromosome balls” that are formed can be easily distinguished from surrounding stem cells. Only differentiated root cap nuclei show similar appearance and can be confused with mitoses in regions with low signal to noise ratio. Compared to the entire duration of the cell cycle (approx. 24h) the incubation period was chosen very short to avoid side-effects.

The almost perfectly spherical nucleolus of interphase nuclei in stem cells seems to be a very robust feature for nucleus detection and there exist several detectors that are able to robustly recognize spheres in dense gray value data. In this section we will introduce two specific approaches explicitly designed for the detection of spherical structures. First, a matched filter approach is examined, namely the Laplacian of Gaussian (LoG) blob detector as *e.g.* used by Lowe (2004) in the popular SIFT detector. Secondly, 1-point vectorial invariants which are specifically designed to detect concentric spheres with two strong intensity changes (Schulz et al., 2006) are evaluated. Finally we will present a more general filtering approach, that can be adapted to the detection of arbitrary structures after supervised training.

#### Matched filter-based nucleus detection

To obtain the nuclear positions one can try to optimally fit a nuclear model to the observed gray values. A very simple model for a dark sphere on light background is the isotropic second derivative of a Gaussian function (Laplacian of Gaussian)

$$\text{LoG}_\sigma(\mathbf{x}) := \sum_{d=1}^D \frac{\partial^2}{\partial x_d^2} \mathcal{N}_\sigma(x) \quad (3.1)$$

where  $D$  is the dimensionality (*e.g.* 3 for a sphere detector) and  $\mathcal{N}_\sigma : \mathbb{R}^D \rightarrow \mathbb{R}$  is the mean-free  $D$ -dimensional normal distribution with isotropic standard deviation  $\sigma \in \mathbb{R}^+$ . The LoG is the trace of the Hessian matrix of a normal distribution. In the literature the normal distribution is often replaced by a Gaussian function without unit integral normalization. Blob-like structures of matching radius lead to local maxima in the filtering result. Variation of the standard deviation allows to adapt the filter to structures with different radii. Alternatively,  $\sigma$  can be fixed and the filter applied to scaled images. Lowe (2004) employ this in their well-known difference of Gaussian (DoG) approximation to the multi-scale LoG. Instead of explicitly computing the LoG filters, they simply apply Gaussian filters with increasing standard deviation to the input image, leading to a Gaussian scale-space. Then, they approximate the LoG by the difference of subsequent image scales. To increase performance they gradually reduce the image size which is possible without loss of significant information after applying a Gaussian filter with sufficiently high standard deviation.

The LoG filter is the sum of axis-aligned second derivatives of a Gaussian, therefore the structure radius can be given analytically as the distance of the zero-crossing of the linear combination of the corresponding degree two Hermite polynomials to the origin.

The (scale-normalized) Hermite polynomials are recursively defined as

$$\begin{aligned} \tilde{H}_0(x) &:= 1 \\ \tilde{H}_1(x) &:= \frac{1}{\sigma^2} x \\ \tilde{H}_{n+1}(x) &:= \frac{1}{\sigma^2} (x \tilde{H}_n(x) - n \tilde{H}_{n-1}(x)) . \end{aligned}$$

The  $n$ 'th Gaussian derivative is the  $n$ 'th Hermite polynomial weighted by a Gaussian envelope with alternating sign:

$$\frac{d^n}{dx^n} \mathcal{N}_\sigma(x) = \frac{d^n}{dx^n} \frac{1}{\sqrt{2\pi}\sigma} e^{-\frac{x^2}{2\sigma^2}} = (-1)^n \tilde{H}_n(x) \cdot \mathcal{N}_\sigma(x). \quad (3.2)$$

Since the envelope does not change the zero-crossing position, we can disregard it in the following calculations. We also exploit the rotational symmetry of the *LoG* and restrict our search for the zero-crossing to the direction of the first unit vector. With these simplifications the problem becomes

$$\sum_{d=1}^D \frac{1}{\sigma^2} \left( \frac{1}{\sigma^2} x_d^2 - 1 \right) \stackrel{\forall i \neq 1: x_i := 0}{=} \frac{1}{\sigma^4} x_1^2 - \frac{D}{\sigma^2} = 0. \quad (3.3)$$

$r := x_1 = \sqrt{D}\sigma$  fully defines the zero level set of the function and corresponds to the structure radius leading to maximum filter response.

To make the ‘‘Laplacian of Gaussian’’ functions comparable among different scales their responses are scale-normalized by multiplying the variance of the underlying Gaussian.

### Vectorial invariants

In Schulz et al. (2006) we developed features directly adapted to nucleus detection in confocal recordings of DAPI stained tissue. They are based on haar features that are invariant against rotations by integrating over the rotation group  $O_3$  which is represented by rotation matrices  $\mathbf{R} \in \mathbb{R}^{3 \times 3}$ . The vectorial invariant  $F(I, \mathbf{x}_0, \mathbf{r}) \in \mathbb{R}$  at position  $\mathbf{x}_0$  for structure radius  $\|\mathbf{r}\| \in \mathbb{R}^+$  in the recorded intensity image  $I$  is computed as

$$F(I, \mathbf{x}_0, \mathbf{r}) := \int_{O_3} \mathbf{R}^{-1} \frac{(\nabla I)(\mathbf{R}\mathbf{r} - \mathbf{x}_0)}{\|(\nabla I)(\mathbf{R}\mathbf{r} - \mathbf{x}_0)\|} \cdot \frac{\mathbf{r}}{\|\mathbf{r}\|} d\mathbf{R}.$$

Due to the integration over  $O_3$  the direction of  $\mathbf{r}$  is irrelevant and we always choose  $\mathbf{r} := (\|\mathbf{r}\|, 0, 0)^\top$ . Large feature magnitudes indicate that the majority of gradients on the sphere surface with radius  $\|\mathbf{r}\|$  around position  $\mathbf{x}_0$  point in radial direction away or towards  $\mathbf{x}_0$ . If pointing towards  $\mathbf{x}_0$  feature values are negative and when pointing away from  $\mathbf{x}_0$  they are positive. Starting from the nucleolus center, DAPI stained stem cell nuclei contain a dark-to-bright transition from nucleolus to chromatine and a bright-to-dark transition from chromatine to cytoplasm. We exploit this structural knowledge by computing the minimum and maximum feature values  $F^-$ ,  $F^+$  and corresponding radii  $R^-$ ,  $R^+$  for a fixed set of search radii  $\|\mathbf{r}\| \in \{0.5, 1.0, \dots, 6.0\} \mu\text{m}$

$$\begin{aligned} F^-(I, \mathbf{x}_0) &:= \min_{\|\mathbf{r}\|} F(I, \mathbf{x}_0, \mathbf{r}) \\ R^-(I, \mathbf{x}_0) &:= \arg \min_{\|\mathbf{r}\|} F(I, \mathbf{x}_0, \mathbf{r}) \\ F^+(I, \mathbf{x}_0) &:= \max_{\|\mathbf{r}\|} F(I, \mathbf{x}_0, \mathbf{r}) \\ R^+(I, \mathbf{x}_0) &:= \arg \max_{\|\mathbf{r}\|} F(I, \mathbf{x}_0, \mathbf{r}). \end{aligned} \quad (3.4)$$

### 3. The *intrinsic Root Coordinate System (iRoCS)*

---

In the concrete implementation, we approximate the image gradients with central differences after application of a Gaussian filter with standard deviation  $\sigma = 0.5\mu\text{m}$  for noise suppression.

The described invariants are closely related to the generalized Hough transform for spheres (Ballard, 1981). However, the gradient-based voting allows much faster computation and is very memory efficient due to the lower-dimensional hough space. We could show that these features are able to successfully detect many nuclei. Besides nuclear localization,  $R^+(I, \mathbf{x}_0)$  also gives a rough estimate of the radius of a nucleolus located at  $\mathbf{x}_0$ . Schulz et al. (2006) interpreted  $F^-$  and  $F^+$  as independent probabilities. The joint probability of both voting directions leads to high precision and recall for stem cell nuclei, however for differentiated nuclei and in vasculature the detection rate drops quickly (Fig. 3.5, blue line).

#### **Trainable filters for nucleus detection**

Both introduced approaches to nucleus detection allow to detect a majority of nuclei in the RAM, however they only allow to successfully detect roundish nuclei. They perform bad in the detection of elongated nuclei, *e.g.* in provascular tissue or the lateral root cap.

We therefore developed a trainable approach that learns nuclear morphologies from manually annotated roots, resulting in an optimally adapted filter for nucleus detection in the Arabidopsis RAM. The basic idea is to extract a set of invariant features for positive and negative samples and then train a discriminative classifier that is applied to all voxels of a dataset. For classification we use a soft-margin support vector machine (SVM) with RBF kernel (Vapnik, 1998; Schölkopf and Smola, 1998). We map the SVM decision values to probabilities according to Platt (2000) and perform a non-maximum suppression with  $3\mu\text{m}$  radius on the resulting probability map.

Positive samples are provided by manual annotation of nuclei in few sample roots, while negative samples are randomly sampled from the same root images with a pre-defined distance (we used  $3\mu\text{m}$ ) from the annotated nucleus center positions. This approach has the drawback that all nuclei of the training roots must be annotated to avoid inclusion of positive nucleus samples in the background class. Since full manual root annotation is tedious we restricted ourselves to two training roots giving approximately 12000 positive nucleus annotations. The positions of 100.000 background samples were drawn from a uniform distribution over the respective image domain and another 100.000 from a Gaussian distribution with parameters estimated from the expert annotations.

To get a rich feature set we employ Gauß-Laguerre features (Skibbe et al., 2012; Liu et al., 2014) which are based on the spherical harmonic transform (SHT, Edmonds (1957)).

The SHT transforms a spherical function to frequency space, similar to the Fourier transform for Euclidean coordinates. To apply the SHT, Euclidean positions  $\mathbf{r} = (x, y, z)^\top$  are transformed to spherical coordinates  $(\theta, \varphi, r)$ , where

$$\begin{aligned}\theta &= \arccos\left(\frac{z}{\|\mathbf{r}\|}\right) \\ \varphi &= \text{atan2}(y, x) \\ r &= \|\mathbf{r}\|.\end{aligned}$$

For one fixed radius  $r$  the spherical function  $f : S_2 \rightarrow \mathbb{R}$  defined by the gray values on the corresponding spherical shell is then mapped onto the Schmidt semi-normalized orthogonal spherical harmonic basis functions  $Y_m^\ell : S_2 \rightarrow \mathbb{C}$

$$Y_m^\ell(\theta, \varphi) := \sqrt{\frac{(\ell - m)!}{(\ell + m)!}} P_m^\ell(\cos \theta) e^{im\varphi}$$

where  $P_m^\ell : \mathbb{R} \rightarrow \mathbb{R}$  denotes the associated Legendre polynomial with band  $\ell \in \mathbb{N}_0$  and order  $m \in \mathbb{Z}$ ,  $-\ell \leq m \leq \ell$  and  $i$  denotes the imaginary unit.

With this normalization the SHT is defined as

$$f(\theta, \varphi) = \sum_{\ell=0}^{\infty} \sum_{m=-\ell}^{\ell} \tilde{f}_m^\ell \overline{Y_m^\ell}(\theta, \varphi) = \sum_{\ell=0}^{\infty} \langle \tilde{\mathbf{f}}^\ell, \mathbf{Y}^\ell(\theta, \varphi) \rangle$$

where  $\tilde{\mathbf{f}}^\ell := (\tilde{f}_{-\ell}^\ell, \dots, \tilde{f}_\ell^\ell)^T \in \mathbb{C}^{2\ell+1}$  is the SHT coefficient vector and  $\mathbf{Y}^\ell := (Y_{-\ell}^\ell, \dots, Y_\ell^\ell)^T \in S_2 \rightarrow \mathbb{C}^{2\ell+1}$  is the vector of spherical harmonic basis functions of band  $\ell$ .  $\overline{Y}$  indicates the complex conjugate of  $Y$ .

The coefficients can be computed by means of dot products of the spherical function with the basis functions

$$\tilde{\mathbf{f}}^\ell = \frac{2\ell + 1}{4\pi} \langle f, \overline{\mathbf{Y}^\ell} \rangle.$$

The coefficient vectors are co-variant with respect to rotations, *i.e.* for any rotation of the original spherical function exists an isomorphic matrix operation that can be applied to the coefficients. Therefore, the coefficients form a set of spherical tensors (one for each band of corresponding rank  $\ell$ ). The representations of rotations in the Euclidean and the SH domain differ though. While a rotation  $g \in \text{SO}(3)$  in 3D Euclidean space is represented by an orthonormal rotation matrix  $\mathbf{R}_g \in \mathbb{R}^{3 \times 3}$  acting on the domain of the function, the dual representation in the SH domain is given by band-specific Wigner-D matrices  $\mathbf{D}_g^\ell \in \mathbb{C}^{(2\ell+1) \times (2\ell+1)}$  acting directly on the SH coefficients. Let  $\mathbf{r}' := \mathbf{R}_g \mathbf{r}$  be the rotated Euclidean position with spherical representation  $(\theta', \varphi', r)$ , then

$$f(\theta', \varphi') = \sum_{\ell=0}^{\infty} \langle \mathbf{D}_g^\ell \tilde{\mathbf{f}}^\ell, \mathbf{Y}^\ell(\theta, \varphi) \rangle.$$

The spherical harmonics can be extended to solid harmonics for the transformation of 3D volumes by additionally introducing radial functions. We employ Gaussian-weighted Laguerre polynomials leading to the Laguerre Gaussian-type functions (Chiu and Moharerrzadeh, 1999)

$$\mathcal{L}_{n,m}^\ell(\mathbf{r}) e^{-\frac{r^2}{2\sigma^2}} := L_n^{\ell-n+\frac{1}{2}}\left(\frac{r^2}{2\sigma^2}\right) e^{-\frac{r^2}{2\sigma^2}} r^{\ell-n} Y_m^{\ell-n}(\theta, \varphi)$$

where  $n \in \mathbb{N}_0$ ,  $n \leq \ell$ .  $L_n^\alpha : \mathbb{R} \rightarrow \mathbb{R}$  denotes the Laguerre polynomial of order  $n$  associated with  $\alpha \in \mathbb{R}_{\geq 0}$ . The standard deviation of the Gaussian function is given by  $\sigma \in \mathbb{R}$ .

### 3. The *intrinsic Root Coordinate System (iRoCS)*

---

Let  $I : \mathbb{R}^3 \rightarrow \mathbb{R}$  be a tensor field of rank 0. The solid harmonic coefficients  $a_{n,m}^\ell(\mathbf{x}) \in \mathbb{C}$  for band  $\ell$ , Laguerre order  $n$  and harmonic order  $m$  around the center of expansion  $\mathbf{x} \in \mathbb{R}^3$  are given by

$$a_{n,m}^\ell(\mathbf{x}) := \int_{\mathbf{r} \in \mathbb{R}^3} I(\mathbf{r} + \mathbf{x}) \overline{\mathcal{L}_{n,m}^\ell(\mathbf{r})} e^{-\frac{\|\mathbf{r}\|^2}{2\sigma^2}} d\mathbf{r}.$$

Each  $(\ell, n)$ -combination yields a spherical coefficient tensor  $\mathbf{a}_n^\ell := (a_{n,-(\ell-n)}^\ell, \dots, a_{n,\ell-n}^\ell)^T \in \mathbb{C}^{2(\ell-n)+1}$ . Similar to the energy of the Fourier transform coefficients, the L2-norms of these tensors are rotation invariant. So each choice of  $\ell$  and  $n$  provides one independent invariant feature describing different aspects of the local gray value distribution around the rotation center. By varying the parameter  $\sigma$ , the size of the neighborhood can be adjusted, to capture either fine local details or coarser geometric cues.

We compute the solid harmonic coefficients for each voxel position within the 3D image. This can be done very efficiently using local spherical derivative filters within a Gaussian scale-space (Skibbe et al., 2012).

As features we use the L2-norms of all coefficient tensors up to  $\ell + n = 5$

$$\{\|\tilde{\mathbf{a}}_0^0\|, \|\tilde{\mathbf{a}}_0^1\|, \|\tilde{\mathbf{a}}_0^2\|, \|\tilde{\mathbf{a}}_0^3\|, \|\tilde{\mathbf{a}}_0^4\|, \|\tilde{\mathbf{a}}_0^5\|, \|\tilde{\mathbf{a}}_1^1\|, \|\tilde{\mathbf{a}}_1^2\|, \|\tilde{\mathbf{a}}_1^3\|, \|\tilde{\mathbf{a}}_1^4\|, \|\tilde{\mathbf{a}}_1^5\|, \|\tilde{\mathbf{a}}_2^2\|, \|\tilde{\mathbf{a}}_2^3\|\}$$

on eight exponentially increasing scales ( $\sigma \in \{0.5, 1.0, 2.0, 4.0, 8.0, 16.0, 32.0, 64.0\} \mu\text{m}$ ).

Overall this leads to 96 invariant features.

We augment this base feature set by appending  $F^-$ ,  $F^+$ ,  $R^-$  and  $R^+$  (3.4) of Schulz et al. (2006). This finally leads to 100-dimensional feature vectors for each voxel that are used for training and classification. The dynamic ranges of the Gauß-Laguerre features are image intensity dependent and their magnitudes drop quickly with increasing band, whereas the vectorial invariants are very robust to intensity changes. Redundancy among the features is very low by construction, and mainly stems from oversampling at very small scales. However, to maximize classification performance the individual features should be weighted according to their discriminative power.

Assume, that during image stack recording, the microscope is setup to optimally use the available dynamic range (12 bit,  $[0, 4096]$ ). We first map this range to the  $[0, 1]$  interval prior to feature computation. After this global normalization, the nucleus detection algorithm still needs to be robust with respect to local illumination changes which are unavoidable when imaging thick tissues via optical sectioning. For reasons of flexibility, we do not assume attenuation corrected image data. To achieve robustness against global intensity variations we first normalize the Gauß-Laguerre feature vectors to unit norm and then normalize each individual feature (including the vectorial invariants) to zero mean and unit standard deviation during training. The found normalization parameters are stored alongside with the SVM models and applied to new features prior to classification.

## Results

A comparison of the discussed approaches for nucleus detection is given in figure 3.5. The proposed learned detector clearly outperforms the simple filter-based detectors as expected. The LoG blob

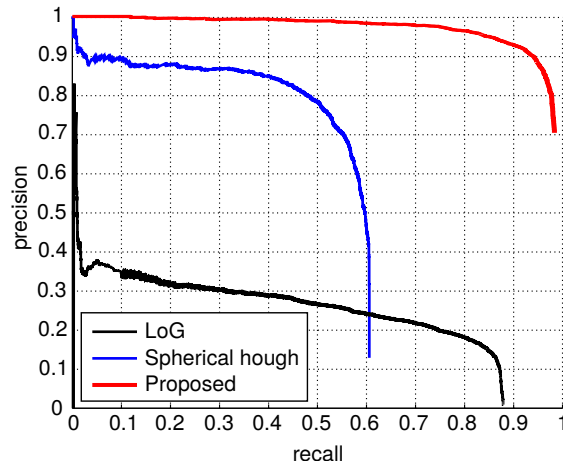


**Figure 3.5.:** Precision-Recall graph of nucleus detection performance of the proposed trained detector, the Laplacian of Gaussian blob detector (LoG) and vectorial 1-point invariants (Spherical hough). LoG and Hough: Responses for bright and dark blobs/spheres on 12 scales ( $0.5\mu\text{m}$  to  $6.0\mu\text{m}$  with  $0.5\mu\text{m}$  step) were multiplied making up the final detection score to exploit the nuclear appearance consisting of the dark nucleolus surrounded by bright chromatine.

detector has pretty high recall when taking into account many detections, but its precision is bad. The top-ranked detection is already a false positive and with decreasing filter response approximately one out of three to four detections is a true positive. False positives with high filter response mostly stem from dark areas between the nuclei which also fulfill the blob property of being homogeneously dark regions surrounded by bright regions.

The spherical hough transform shows different behavior. Round nuclei making up approximately 60% of nuclei in the root tip are very well detected with very good precision, but as soon as all of them are found the precision rapidly drops and only very few further nuclei are detected.

For detector training we determined good parameters (kernel width  $\gamma$  and outlier cost  $C$ ) for the RBF kernel in a cross-validation experiment in which one wild type root with expert annotations was used for training and another for testing. We applied the resulting detector to a set of 6 further wild type roots for which the detection result was manually corrected. The augmented set containing eight roots was then used to train the final detector.

An example of a probability map obtained through voxelwise classification of a root tip recording using the described feature set and classifier is given in Fig. 3.6a. Fig. 3.6b shows the precision and recall of the final detector on that root. Using a threshold of 50% (curve endpoints) we could achieve an overall recall of over 99% at a precision of approximately 70% (black curve). The precision-recall curves for the individual layers assume that nuclei of other layers are false positive detections, therefore the reduced performance. From the plots one can see that first epidermis and cortex nuclei are detected, then root cap and the inner tissues follow. The small gap to 100% recall is almost only due to missing detections in the provascular tissue containing very hard cases of elongated nuclei. For many provascular nuclei the nucleolus partitions the chromatine into two disjoint parts,

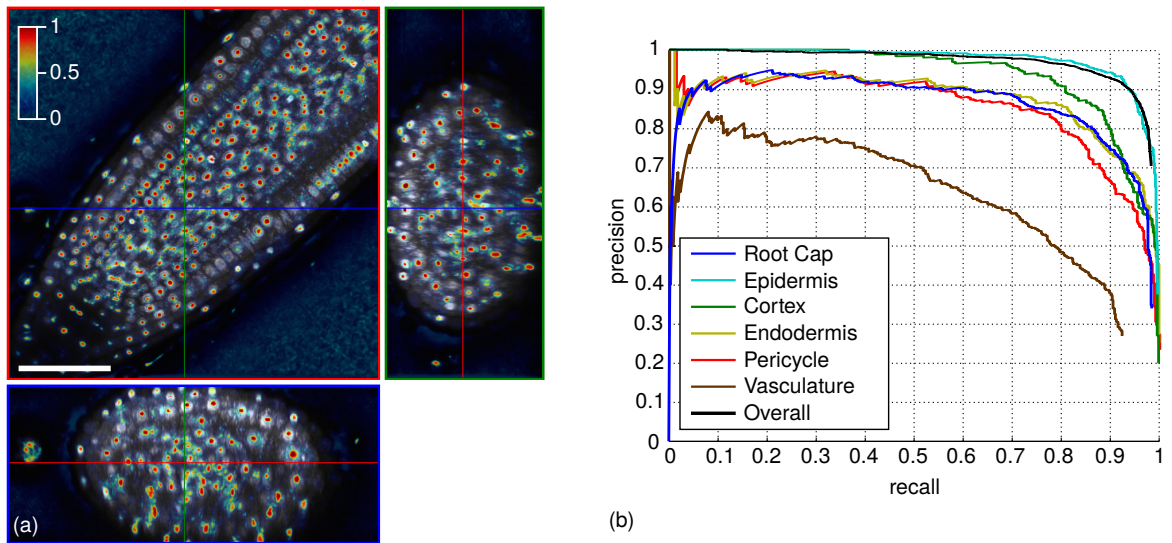


**Figure 3.6.:** Nucleus detection performance with a detector trained on annotated sample roots using Gauß-Laguerre features and 1-point vectorial invariants. (a) per-voxel nucleus center probability normalized to the  $[0, 1]$  range for one sample dataset; (b) the corresponding precision-recall curve (probability threshold: 1 - 0.5). Scale bar:  $100\mu\text{m}$ .

of which each shows very similar appearance to differentiated root cap nuclei. Therefore instead of one central detection in the nucleolus two very confident detections in each of the chromatine segments were generated which suppress the true positive detection in the center.

For a comparison of the trainable filter approach using other state of the art feature sets we refer to (Skibbe et al., 2012).

### 3.2.2. Cell segmentation

Cell boundaries are a very interesting alternative anatomical reference structure that allow to uniquely relate measured events to the cell they originate from. Instead of detecting sparse point positions as in the nucleus detection described earlier, we want to obtain a cellular segmentation of the root that partitions the input 3-D image into segments that represent cells or background. Each segment is identified by a unique label, where background is labeled as zero and cells are labeled with successive numbers starting from two. The label one is reserved for root-internal voxels which cannot be uniquely assigned to a cell, *i.e.* one indicates cell boundaries.

The cell segmentation approach presented in this section was developed by Kun Liu. I recapitulate it briefly to give the complete picture of the iRoCS toolbox.

#### Implementation

To alleviate attenuation and irregular staining effects a local intensity variance normalization is performed using a Gaussian kernel with standard deviation  $20\mu\text{m}$  for mean and variance computation.

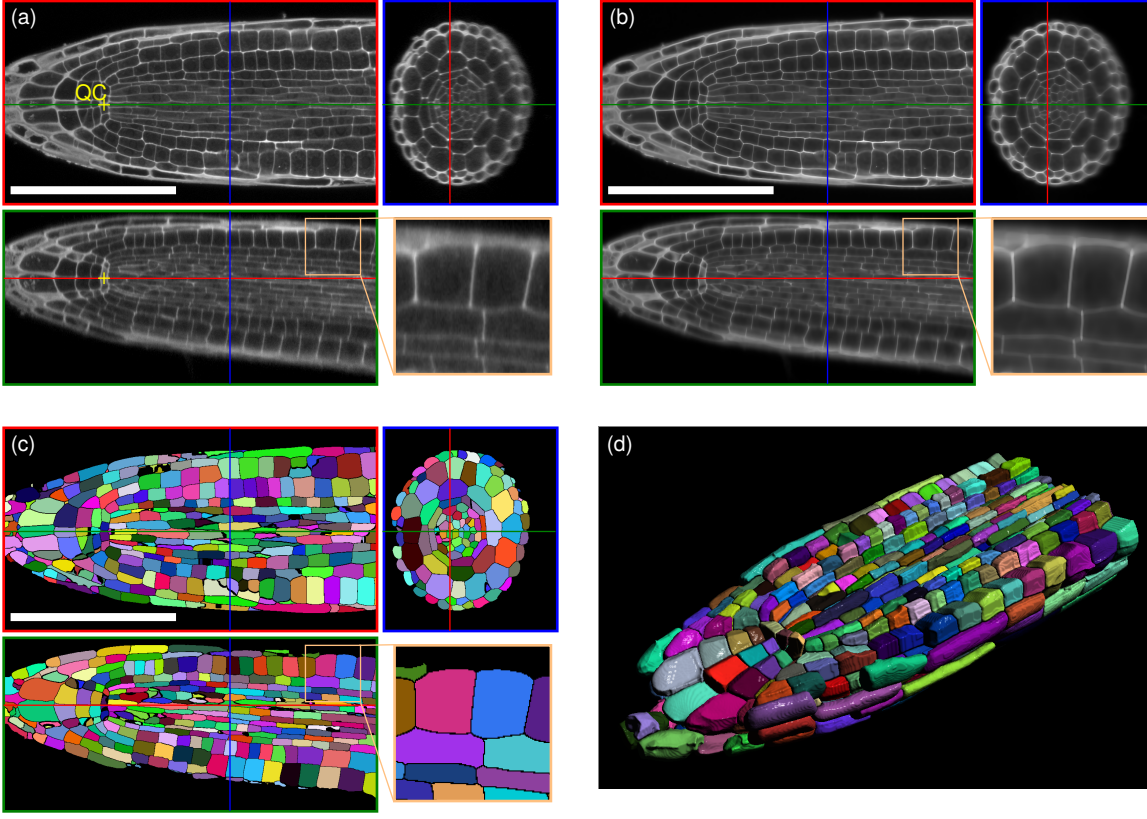


**Figure 3.7.:** Result of an automatic cell wall-based segmentation. (a) Raw data, (b) enhanced image after anisotropic diffusion, (c) Segmented cells with random color coding. (d) Surface rendering of cells of half of the root cut along an axial plane. Colored lines indicate orthoview cut planes. Scale bars:  $100\mu\text{m}$ .

To stabilize the variance of the apparent Poisson noise a gamma correction with  $\gamma = 2$  is performed (Anscombe, 1948). Residual detector spikes are removed using a small median filter (edge length = 3 voxels).

Finally planar structures are enhanced using coherence-enhancing anisotropic diffusion (Weickert, 1998). The general diffusion equation is given by

$$\frac{\partial I(\mathbf{x})}{\partial t} = \text{div}(D(\mathbf{x})\nabla I(\mathbf{x})) \quad (3.5)$$

where  $I : \Omega \rightarrow \mathbb{R}$  is the image/volume the diffusion is applied to.  $\nabla$  and  $\text{div}$  indicate the gradient and divergence operators respectively. Diffusion is controlled by the diffusion tensor  $D$  and the result for diffusion time  $t$  is computed by explicit time integration. To obtain optimal plane enhancing behavior we base the diffusion tensor on the second derivatives of the image intensities. Let  $\lambda_1 > \lambda_2 > \lambda_3$  be the eigenvalues of the local Hessian matrix with corresponding eigenvectors  $\mathbf{v}_1, \mathbf{v}_2, \mathbf{v}_3$ , then we construct the diffusion tensor as

$$D = e^{-(\min(\lambda_1,0)/\kappa)^2} \mathbf{v}_1 \mathbf{v}_1^T + e^{-(\min(\lambda_2,0)/\kappa)^2} \mathbf{v}_2 \mathbf{v}_2^T + e^{-(\min(\lambda_3,0)/\kappa)^2} \mathbf{v}_3 \mathbf{v}_3^T. \quad (3.6)$$

### 3. The *intrinsic Root Coordinate System (iRoCS)*

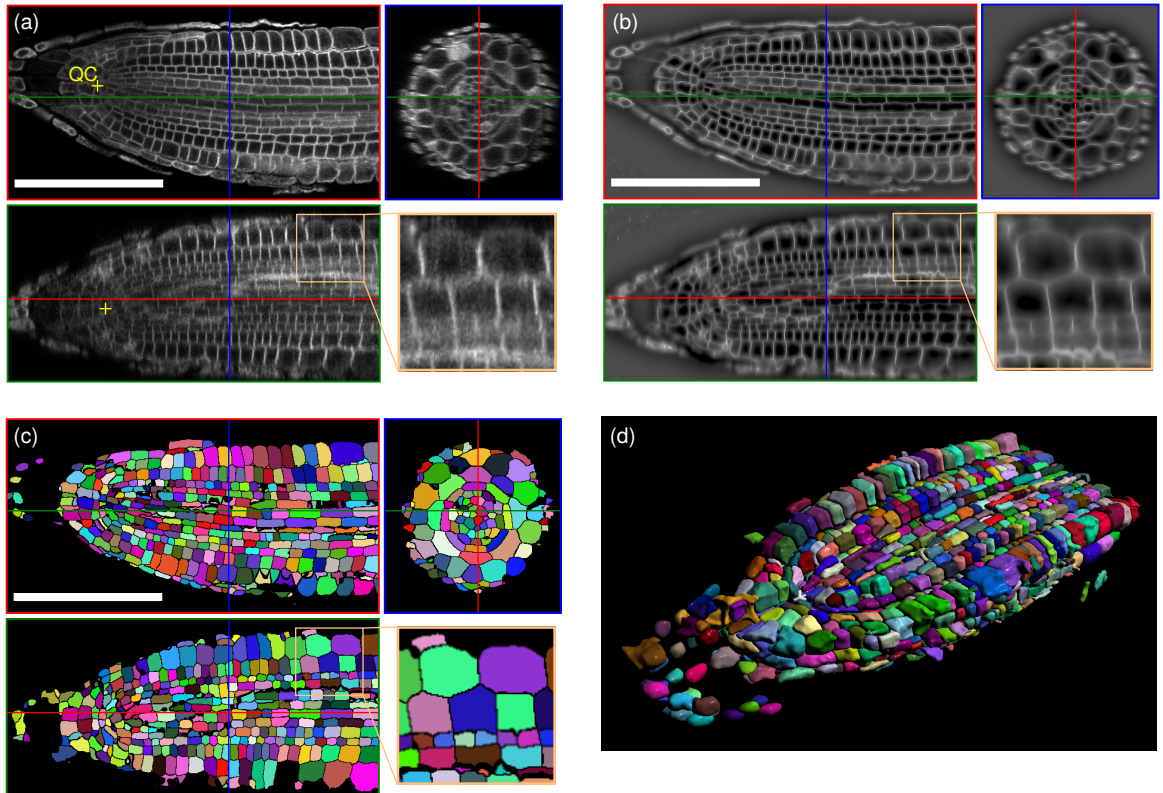


**Figure 3.8.:** Automatic cell membrane-based segmentation. (a) Raw data; (b) enhanced image after anisotropic diffusion; (c) Segmented cells with random color coding. (d) Surface rendering of cells of half of the root virtually cut along an axial plane. Colored lines indicate orthoview cut planes. Scale bars:  $100\mu\text{m}$ .

The parameter  $\kappa$  is chosen s.t. weak edges are still emphasized and determined experimentally to 0.3. The minimum operation in the exponential ensures that the diffusion tensor stays in the  $[0, 1]$  range, while actively enhancing bright structures only. This choice leads to strong diffusion along bright structures, while diffusion across those structures is suppressed. In dark areas we obtain isotropic diffusion. Therefore edges are enhanced, noise along bright structures and in areas of low contrast is reduced and the overall structural coherence is significantly increased which can be seen in Fig. 3.7b and 3.8b. To extract the cell boundaries we use the inverse of the third eigenvalue  $-\lambda_3$ . After choosing an appropriate threshold (We used  $-0.2$ ) the cell walls are separated from cell bodies and background. Finally a standard watershed algorithm is applied (Meyer, 1994) to the thresholded edge image twice. After the first watershed segmentation pass very small fragments are removed. To fill the gaps from segment removal the watershed is applied again using the new smaller set of seed regions.

A majority of cell fragments can thereby be correctly assigned to their “mother cell”, however for large fragments, *e.g.* a cell is split in two equally sized parts, this approach fails. Liu et al. (2013) propose an energy minimization approach to automatically fix this kind of over-segmentation and

also slight under-segmentation using prior knowledge on the distribution of cell shapes in Arabidopsis root tips. Remaining over-segmentations can be easily corrected in a manual post-processing step by simply marking the segments to merge and re-running the watershed algorithm. Manual correction of under-segmentations requires to annotate missing cell boundaries in 3D, which is very time consuming and error prone. In practice under-segmented cells should be removed from the segmentation to not harm the later analysis.

If possible, the segmentation parameters should be adjusted to get a slight over-segmentation if no perfect segmentation can be achieved by any parameter setup.

### 3.3. Continuous coordinate system fit

Parallel line structures or tubes in 3D are of high importance in detection and classification tasks. Their accurate tracing and segmentation is required to solve problems coming from medicine, biology, robotics, or aerial and satellite image analysis. Especially for biological and medical applications, with their wide spectrum of imaging methods, geometric modeling is an important step towards data abstraction and quantification.

In this section we introduce the heart-piece of iRoCS, the continuous bent cylinder coordinate system that is fitted to the detected nucleus positions. In section 3.3.1 we first introduce a basic model of which parts will be used to initialize and validate the variational coupled curves model which is described in section 3.3.2. The variational coupled curve fitting was presented at the German conference on pattern recognition in Schmidt et al. (2012).

#### 3.3.1. Basic axis fit using Gaussian kernel smoothing

Given straight roots and a perfect detector, all detections could be used for the task of fitting the axis to the distribution of nucleus positions by just computing the covariance matrix of the point distribution and choosing the main axis of this distribution. Although roots are never perfectly straight in practice, their rigidity does not allow arbitrary bending. In most cases it is possible to find a functional relationship between the bent root axis and the straight main axis of the point distribution. This functional relationship allows to convolve the residual coordinates orthogonal to the main axis with a Gaussian kernel to estimate the real bent axis.

Let  $X = \{\mathbf{x}_1, \dots, \mathbf{x}_n\}$ , where  $\mathbf{x}_i \in \mathbb{R}^3$  be the point set obtained from the detector. We estimate the mean and covariance matrix of  $X$  as

$$\begin{aligned}\boldsymbol{\mu}_X &:= \frac{1}{n} \sum_{i=1}^n \mathbf{x}_i \\ \mathbf{C}_X &:= \frac{1}{n} \sum_{i=1}^n (\mathbf{x}_i - \boldsymbol{\mu}_X) (\mathbf{x}_i - \boldsymbol{\mu}_X)^\top.\end{aligned}$$

### 3. The *intrinsic Root Coordinate System (iRoCS)*

---

Using its eigenvalue decomposition  $\mathbf{C}_X = \mathbf{U}\mathbf{\Lambda}\mathbf{U}^\top$  we obtain the transformation matrix  $\mathbf{U}$  that rotates the main axes of the point distribution to the canonical Euclidean coordinate axes. Applying  $\mathbf{U}$  and  $\boldsymbol{\mu}_X$  to the points gives their normalized positions

$$\hat{\mathbf{x}}_i := \mathbf{U} (\mathbf{x}_i - \boldsymbol{\mu}_X) .$$

*W.l.o.g.* let the main axis of the transformed point distribution be  $\mathbf{e}_1 = (1, 0, 0)^\top$  (this can be easily fulfilled by sorting eigenvalues and eigenvectors s.t. the largest eigenvalue is  $\lambda_1$ ). The bent axis of the normalized points can then be approximated by locally averaging their remaining dimensions with a sufficiently wide Gaussian kernel  $\mathcal{G}_\sigma$

$$\hat{\mathbf{a}}(u) := \begin{pmatrix} u \\ \frac{\sum_{i=1}^n \mathcal{G}_\sigma(u - \hat{x}_{i,1}) * \hat{x}_{i,2}}{\sum_{i=1}^n \mathcal{G}_\sigma(u - \hat{x}_{i,1})} \\ \frac{\sum_{i=1}^n \mathcal{G}_\sigma(u - \hat{x}_{i,1}) * \hat{x}_{i,3}}{\sum_{i=1}^n \mathcal{G}_\sigma(u - \hat{x}_{i,1})} \end{pmatrix} .$$

We will refer to this approach as point-based kernel smoothing (PKS) in the following.

The PKS approach requires very good detection results to give proper axis estimates. However, signal loss and the resulting lower signal to noise ratio in the part of the root distal to the microscope objective can result in many false positive detections and missed nuclei. To overcome this problem and to also allow for strong bending we developed an alternative robust variational model that estimates the root axis from detected epidermis nuclei only. To distinguish nuclei of different cell layers we manually labeled all detections in the 8 training roots as root cap, epidermis, cortex, endodermis, pericycle vasculature or background. We additionally distinguished nuclei in interphase from nuclei of dividing cells and trained a multi-class support vector machine for the resulting 13 classes. A typical classification result is given in table 3.1. We choose epidermis for the axis estimation task due to its good detection performance and its availability over the whole root length. Additionally it contains a large fraction of the roots nuclei with comparably high cell density.

For the epidermis detection task we are not interested in the fine distinction of tissues or mitotic states, therefore we can combine classifications for root cap, cortex, endodermis, pericycle and vasculature to a common ‘‘other nucleus’’ class resulting in the simplified confusion table 3.2.

#### 3.3.2. Variational tube tracing using coupled curves on sparse surface points

The detected epidermis nuclei are sparse and noisy samples from the tube formed by the epidermal tissue layer. Starting from this basic observation we will now develop a general tube tracing approach that is not restricted to iRoCS. Our variational tube tracing can model any simple (no branching, circular profile) and smooth tubular structure with thickness variations given sufficiently dense surface points.

The model consists of a vector-valued tube axis function  $\mathbf{a} : \mathbb{R} \rightarrow \mathbb{R}^D$  ( $D \in \{2, 3\}$ ) and a scalar tube thickness function  $t : \mathbb{R} \rightarrow \mathbb{R}^+$ . Both functions are coupled by a common curve parametrization into a combined tubular model which is fit to surface points in a robust variational energy minimization

**Table 3.1.:** Classification accuracy of the layer assignment based on invariant gray-value features on one sample root tip. The confusion matrix shows the number of nucleus candidates classified as either root cap, epidermis, cortex, endodermis, pericycle, vasculature (in interphase or mitosis) or background. Rows indicate the real label (manually annotated), columns show the label predicted by a soft-margin SVM with RBF kernel. The overall precision excluding the background class is given in the lower right corner.

		True label													$\Sigma$	Precision [%]
		Background	Root Cap	Epidermis	Cortex	Endodermis	Pericycle	Vasculature	Root Cap (M)	Epidermis (M)	Cortex (M)	Endodermis (M)	Pericycle (M)	Vasculature (M)		
Classified as	Background	2055	89	58	16	19	21	161	2	1		1		1	2424	84.8
	Root Cap	98	1370	23	6	7	4	6	7	5	3	1	1	3	1534	89.3
	Epidermis	142	21	1410	56	12	6								1647	85.6
	Cortex	45	9	96	563	263	59	25							1060	53.1
	Endodermis	114	103	97	44	436	264	36		3					1097	39.7
	Pericycle	84	15	46	24	120	424	158			1		2		874	48.5
	Vasculature	658	21	16	13	69	122	735	1				2	4	1641	44.8
	Root Cap (M)								1		1				2	50.0
	Epidermis (M)	2	9							13	13	4	4	1	46	28.3
	Cortex (M)		1						1	1		1		1	5	0.0
	Endodermis (M)	2	5						2	9	4	5	4	3	34	14.7
	Pericycle (M)	11	3					10		4	3	5	6	13	55	10.9
	Vasculature (M)	4	1						1	1	2	4	3	8	24	33.3
	$\Sigma$		3215	1647	1746	722	926	900	1131	15	37	27	21	22	34	
Recall [%]		63.9	83.2	80.8	78.0	47.1	47.1	65.0	6.7	35.1	0.0	23.8	27.3	23.5		62.0

**Table 3.2.:** Classification accuracy of epidermis labeling on a sample root tip. The confusion matrix shows the number of nucleus candidates classified as epidermis, other nucleus or background. Rows indicate the real label (manually annotated), columns show the label predicted by a soft-margin SVM with RBF kernel. The overall accuracy excluding the background class is given in the lower right corner.

		True label			$\Sigma$	Precision [%]
		Background	Epidermis	Other		
Classified as	Background	2055	58	311	2424	84.8
	Epidermis	142	1410	95	1647	85.6
	Other	1018	286	5025	6329	79.4
$\Sigma$		3215	1746	5431		
Recall [%]		63.9	80.8	92.5		80.7

### 3. The *intrinsic Root Coordinate System (iRoCS)*

---

scheme. The model is designed to work solely on the sparse point positions, without the need for surface normal estimation. We will show that it leads to very accurate fits even in the case of high noise and missing surface points.

A key benefit of the proposed model is that it “grows” into arbitrarily long tubular structures from a very small local initialization, *i.e.* it solves the tracing and accurate fitting problem within a single energy minimization.

#### **Related Work**

In medical applications various approaches exist to analyze images of vascular and neuronal networks based on different imaging methods ranging from low resolution CT and MRT, through light microscopy down to electron microscopy (Kirbas and Quek, 2004; Meijering et al., 2004; Friman et al., 2010). Independent of the actual source of data, all approaches have in common that they rely on densely imaged interfaces between the structures of interest and mainly depend on the gray values and their derivatives to guide the model fitting. One possibility of robustly finding the axis of a tubular structure is a symmetry analysis around the potential axis (Pock et al., 2005). Morphology-driven approaches try to find the axis by structure thinning leading to a skeletonization. Filter based approaches first try to emphasize the structures using filter banks or steerable filters and apply thresholding and thinning afterwards.

In the field of robotics, approaches to fit parametric tubular structures to point cloud data recorded using laser range scanners are of high interest (Bauer and Polthier, 2009). Most existing approaches exploit the scanned dense mesh structure to estimate local surface normals guiding the model fitting process. These approaches have to cope with noisy data and therefore estimate the normals for each surface position from relatively large neighborhoods. Others try to detect shapes using Hough-like voting based approaches (Schnabel et al., 2007). These are especially suited to detect man-made rigid objects, but don’t perform well on deformable objects as they are common in biological and medical applications.

In Laptev et al. (2000) the coupling of two evolving splines describing the center-lines and thicknesses of roads and rivers in aerial and satellite images was introduced. Although the noise level in images of that kind is very high, the gradients are still a valuable piece of information to guide the snake evolution. A different approach using two coupled splines to describe the outlines of the biologically highly interesting model organism *C-Elegans* was introduced in Q.Wang et al. (2009).

In Lee (2000) a non-self-intersecting 1-D line from unstructured and noisy 3D point data was reconstructed using moving least-squares interpolation. For homogeneously distributed tube-surface data around its circumference this approach is also applicable to solve the tube axis fitting task, although it does not determine the tube thickness.

Our setting is different from the above-mentioned, since our approach has to perform the task of simultaneously estimating the axis and variable thickness of a tubular structure based on sparse surface points only. The low point density and high data noise preclude the extraction of reliable surface normals. We formulate the task of fitting the model to a point cloud as one closed energy minimization problem, which incorporates all available points and a set of tubular models to which on demand new models can be added.

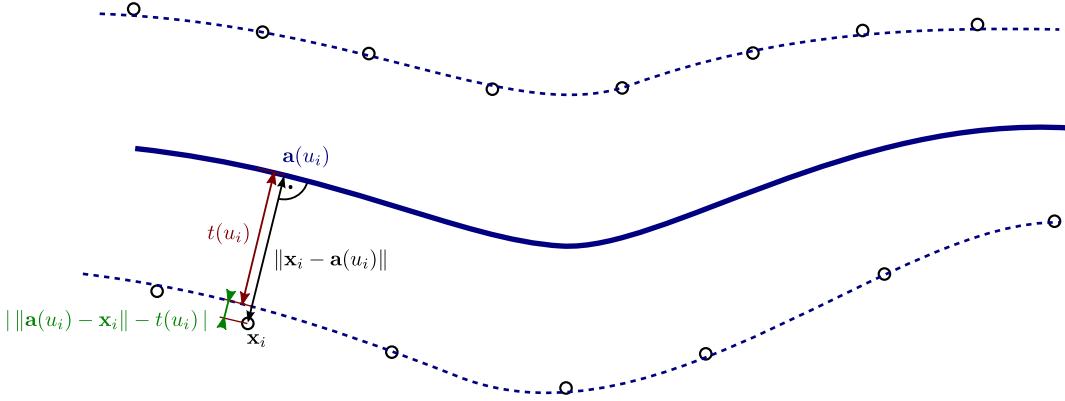


**Figure 3.9.:** A 2-D sketch of the tube model fit to a point set depicted as black circles. Bold blue line: Axis; stippled blue lines: estimated tube surface; red: tube thickness at curve parameter  $u_i$ ; green: distance minimized during optimization.

### Variational formulation

We define a tube as a function mapping a curve parameter  $u \in \mathbb{R}$  to the  $(D + 1)$ -dimensional vector  $(\mathbf{a}^\top(u), t(u))^\top$ , where  $\mathbf{a} : \mathbb{R} \rightarrow \mathbb{R}^D$  is the tube axis function and  $t : \mathbb{R} \rightarrow \mathbb{R}$  is the corresponding tube thickness function. Fig. 3.9 sketches the tube model. To optimally map the model to a set of tube surface points  $X = \{\mathbf{x}_1, \dots, \mathbf{x}_n\}$ ,  $\mathbf{x}_i \in \mathbb{R}^D$  we minimize the energy

$$E_{\text{data}}(\mathbf{a}, t) := \sum_{i=1}^n \psi(\left| \|\mathbf{a}(u_i) - \mathbf{x}_i\| - t(u_i) \right|^2) \quad (3.7)$$

where  $u_i := \arg \min_u \|\mathbf{x}_i - \mathbf{a}(u)\|$  is the curve parameter projection of  $\mathbf{x}_i$  and  $\psi(\rho^2)$  is a robust distance measure.

To cope with sparse surface points and high data noise, we additionally introduce smoothness terms penalizing axis curvature and tube thickness variations

$$E_a(\mathbf{a}) = \int_{-\infty}^{\infty} \left\| \frac{d^2}{du^2} \mathbf{a}(u) \right\|^2 du \quad \text{and} \quad E_t(t) = \int_{-\infty}^{\infty} \left( \frac{d}{du} t(u) \right)^2 du. \quad (3.8)$$

The full energy minimization problem is then given by

$$\begin{aligned} (\mathbf{a}^{*\top}, t^*)^\top &= \arg \min_{\mathbf{a}, t} \sum_{i=1}^n \psi(\left| \|\mathbf{a}(u_i) - \mathbf{x}_i\| - t(u_i) \right|^2) + \int_{-\infty}^{\infty} \lambda \left\| \frac{d^2}{du^2} \mathbf{a}(u) \right\|^2 + \mu \left( \frac{d}{du} t(u) \right)^2 du \\ \text{where } u_i &= \arg \min_u \|\mathbf{x}_i - \mathbf{a}(u)\| \end{aligned} \quad (3.9)$$

where  $\lambda, \mu \in \mathbb{R}^+$  weight the influence of the smoothness terms.

### Parametrization Using B-Splines

We approximate the curves with open B-Splines of degree  $p$ , therefore the nodes at the spline end-points are repeated  $p+1$  times. In the theoretic derivation we will *w.l.o.g.* restrict the spline parameter  $u$  to the  $[0, 1]$ -range. In practice the curve length in micrometers is used. We obtain the B-Spline approximation of the general axis and thickness functionals

$$\mathbf{a}(u) := \sum_{j=0}^{m-1} \mathbf{c}_j^a b_{j,p,\mathbf{s}}(u) \quad \text{and} \quad t(u) := \sum_{j=0}^{m-1} c_j^t b_{j,p,\mathbf{s}}(u) \quad (3.10)$$

where  $C^a = \{\mathbf{c}_0^a, \dots, \mathbf{c}_{m-1}^a\}$  and  $C^t = \{c_0^t, \dots, c_{m-1}^t\}$  are the spline control points, and  $b_{j,p,\mathbf{s}}$  are the recursively defined basis functions

$$b_{j,p,\mathbf{s}}(u) := \begin{cases} 1 & p = 0 \wedge u \in [s_i, s_{i+1}[ \\ 0 & p = 0 \wedge u \notin [s_i, s_{i+1}[ \\ \frac{u-s_j}{s_{j+p}-s_j} b_{j,p-1,\mathbf{s}}(u) + \frac{s_{j+p+1}-u}{s_{j+p+1}-s_{j+1}} b_{j+1,p-1,\mathbf{s}}(u) & \text{otherwise} \end{cases}$$

with node-vector  $\mathbf{s} = (s_0, \dots, s_{m+p})^\top$ .

**Lemma 1** (B-Spline derivative (de Boor, 1978)). *Let  $f(u) := \sum_{j=0}^{m-1} c_j b_{j,p,\mathbf{s}}(u)$  be a B-Spline of degree  $p \in \mathbb{N}_0$ , with control points  $c_j$ ,  $j = 0, \dots, m-1$  defined over the knot vector  $\mathbf{s} = (s_0, \dots, s_{m+p})^\top$ . Then the derivative*

$$f'(u) = \frac{d}{du} f(u) = \sum_{j=0}^{m-2} c'_j b_{j,p-1,\mathbf{s}'}(u)$$

*is another B-Spline of degree  $p-1$  defined over the knot vector  $\mathbf{s}' = (s_1, \dots, s_{m+p-1})$  with control points  $c'_j = \frac{p}{s_{j+p+1}-s_{j+1}} (c_{j+1} - c_j)$ .*

For the proof we refer to de Boor (1978).

The general energy from (3.9) changes to

$$\begin{aligned} E_{\text{data}}(\mathbf{a}, t) &= \sum_{i=1}^n \psi(\|\mathbf{a}(u_i) - \mathbf{x}_i\| - t(u_i))^2 \\ &+ \lambda \cdot \sum_{d=1}^D \int_0^1 \left( \sum_{j=0}^{m-3} c_{j,d}''^a b_{j,p-2,\mathbf{s}''}(u) \right)^2 du + \mu \cdot \int_0^1 \left( \sum_{j=0}^{m-2} c_j''^t b_{j,p-1,\mathbf{s}'}(u) \right)^2 du. \end{aligned} \quad (3.11)$$

where  $u_i = \arg \min_u \|\mathbf{x}_i - \mathbf{a}(u)\|$

The primed variables are obtained by applying Lemma 1 (twice for the axis) to the original splines.

To minimize the energy using gradient descent we need to compute the partial derivatives with respect to the control points  $\mathbf{c}_j^a$  and  $c_j^t$

$$\begin{aligned} \frac{\partial}{\partial c_{j,d}^a} E(\mathbf{a}, t) &= 2 \sum_{i=1}^n \psi'(\|\mathbf{a}(u_i) - \mathbf{x}_i\| - t(u_i))^2 \left(1 - \frac{t(u_i)}{\|\mathbf{a}(u_i) - \mathbf{x}_i\|}\right) (a_d(u_i) - x_{i,d}) b_{j,p,s}(u_i) \\ &\quad + 2\lambda \sum_{j'=0}^{m-1} c_{j',d}^a \int_0^1 \frac{d^2}{du^2} b_{j',p,s}(u) \frac{d^2}{du^2} b_{j,p,s}(u) du \end{aligned} \quad (3.12)$$

$$\begin{aligned} \frac{\partial}{\partial c_j^t} E(\mathbf{a}, t) &= -2 \sum_{i=1}^n \psi'(\|\mathbf{a}(u_i) - \mathbf{x}_i\| - t(u_i))^2 (\|\mathbf{a}(u_i) - \mathbf{x}_i\| - t(u_i)) b_{j,p,s}(u_i) \\ &\quad + 2\mu \sum_{j'=0}^{m-1} c_{j'}^t \int_0^1 \frac{d}{du} b_{j',p,s}(u) \frac{d}{du} b_{j,p,s}(u) du, \end{aligned} \quad (3.13)$$

finally leading to the following update rules for moving the control points in a gradient descent manner when introducing an artificial discrete evolution time  $k$  with step  $\tau \in \mathbb{R}^+$ :

$$c_{j,d}^{a,k+1} = c_{j,d}^{a,k} - \tau \frac{\partial}{\partial c_{j,d}^a} E(\mathbf{a}, t) \quad \text{and} \quad c_j^{t,k+1} = c_j^{t,k} - \tau \frac{\partial}{\partial c_j^t} E(\mathbf{a}, t). \quad (3.14)$$

Since all dimensions come into play during the control point updates in each iteration, first the derivatives are computed for each control point, then the update is applied and finally the  $u_i$  for each point in the point cloud are recomputed.

For computing the closest axis position  $u_i$  for sample  $\mathbf{x}_i$  we must solve

$$u_i = \arg \min_u \|\mathbf{a}(u) - \mathbf{x}_i\|. \quad (3.15)$$

Only orthogonal projections of  $\mathbf{x}_i$  onto the axis tangent  $\frac{d}{du} \mathbf{a}(u)$  are possible candidates for  $u_i$ , which reduces the continuous search space to the discrete set of axis positions which fulfil

$$\left(\frac{d}{du} \mathbf{a}(u)\right)^\top (\mathbf{a}(u) - \mathbf{x}_i) = 0.$$

When plugging in the spline definition we obtain

$$\left(\frac{d}{du} \mathbf{a}(u)\right)^\top (\mathbf{a}(u) - \mathbf{x}_i) = \sum_{k=1}^D \left( \sum_{j=0}^{m-1} \sum_{j'=0}^{m-1} c_{j,k}^a c_{j',k}^a \left(\frac{d}{du} b_{j,p,s}(u)\right) b_{j',p,s}(u) - \sum_{j=0}^{m-1} c_{j,k}^a \frac{d}{du} b_{j,p,s}(u) x_{i,k} \right)$$

which is a degree  $2d - 1$  polynomial in  $u$  for each spline segment  $S_i$ , where  $i = p, \dots, m + p$ . Then  $u_i$  is the root minimizing (3.15) from this discrete set.

### 3. The *intrinsic Root Coordinate System (iRoCS)*

```

Input : Point set  $X$ , Initial cylinder  $(\mathbf{q}_1, \mathbf{q}_2, t_{\text{init}})$ , parameters  $\lambda, \mu, \tau$ , spline degree  $p$ 
Output : Nodes and control points of coupled B-Spline model  $(\mathbf{a}(u), t(u))$ 

// Initialize tube model
 $k \leftarrow 2(p + 1), m \leftarrow p + 1, \epsilon \leftarrow 10^{-7}$ ; //  $k = \text{\#knots}, m = \text{\#control points}$ 
 $s_1, \dots, s_{p+1} \leftarrow 0, s_{p+2}, \dots, s_k \leftarrow \|\mathbf{q}_2 - \mathbf{q}_1\|$ ;
for  $j \leftarrow 1$  to  $m$  do
     $\mathbf{c}_j^a \leftarrow \mathbf{q}_1 + \frac{j-1}{p} \cdot (\mathbf{q}_2 - \mathbf{q}_1)$ ; // equidistant control points on cylinder axis
     $\mathbf{c}_j^t \leftarrow t_{\text{init}}$ ;
end
repeat
     $E_{\text{outer}} \leftarrow E(\mathbf{a}, t)$ ; // (3.11)
    repeat
        // Compute orthogonal projections of points to current axis
        for  $i \leftarrow 1$  to  $n$  do
             $u_i \leftarrow \arg \min_u \|\mathbf{x}_i - \mathbf{a}(u)\|$ ;
        end
         $E_{\text{old}} \leftarrow E(\mathbf{a}, t)$ ; // (3.11)
        // Do gradient descent step
        for  $j \leftarrow 1$  to  $m$  do
            for  $d \leftarrow 1$  to  $D$  do
                 $c_{j,d}^a \leftarrow c_{j,d}^a - \tau \frac{\partial}{\partial c_{j,d}^a} E(\mathbf{a}, t)$ ; // (3.12) in (3.14)
            end
             $c_j^t \leftarrow c_j^t - \tau \frac{\partial}{\partial c_j^t} E(\mathbf{a}, t)$ ; // (3.13) in (3.14)
        end
         $E_{\text{new}} \leftarrow E(\mathbf{a}, t)$ ; // (3.11)
    until  $|E_{\text{old}} - E_{\text{new}}| < \epsilon \cdot |E_{\text{new}}|$ ;
    Insert knot and reparametrize model;
     $m \leftarrow m + 1$ ;
until  $E_{\text{outer}} - E_{\text{new}} < \epsilon \cdot |E_{\text{new}}|$ ;

```

**Algorithm 2** : The Coupled B-Spline fitting algorithm

#### Tube tracing

Up to now we mainly concentrated on the case, when the model is already close to the solution and all points are more or less well explained by the tube model. But in practice we will start from a local initialization and want the model to grow along the tube. To stay close to the curve length parametrization while allowing local growth of the tube, we want to restrict the influence of points on the model evolution to the local surrounding of the current tube model and define the

outlier-robust loss function

$$\psi(s^2) := \begin{cases} s^2 & s < \eta \\ \eta^2 & s \geq \eta \end{cases} \quad (3.16)$$

with user-defined threshold  $\eta \in \mathbb{R}$ . Its derivative with respect to  $s^2$  is

$$\psi'(s^2) = \begin{cases} 1 & s < \eta \\ 0 & s \geq \eta \end{cases} \quad (3.17)$$

therefore only points within a certain distance range defined by  $\eta$  will contribute to the derivatives which allows to adapt the model fitting to surface point density and data noise. We additionally linearly decrease  $\lambda$  and  $\mu$  with increasing arc length of the current axis estimate to avoid a bias towards short curves and update the thickness function only with points mapping orthogonally onto the axis to avoid a thickness over- and length under-estimation at the tube end points.

For the upcoming evaluation we initialize the fit with a manually chosen short cylinder segment represented by its end points  $\mathbf{q}_1$  and  $\mathbf{q}_2$  and radius  $t_{\text{init}}$ . To initialize the tube model, the corresponding B-spline with  $2(p+1)$  knots is generated. Its  $p+1$  control points are equidistantly placed on the cylinder main axis, and the control points for the thickness spline all set to the initial thickness. During the optimization the number of control points remains constant. The model will evolve until no more data points can be described by one single degree  $p$  polynomial. To also allow for more complex tube shapes, we alternate between fitting the model using a fixed number of control points till convergence and a re-gridding step in which an additional knot is inserted. In the re-gridding step we re-distribute the knots equidistantly along the curve leading to an intermediate curve length parametrization. The whole fitting process is summarized in Alg. 2.

In the iRoCS pipelines we use the central 20% of the main axis of the point distribution obtained from the nucleus detector to automatically initialize the model (see section 3.3.1). The initial thickness is chosen as the average point distance to the straight axis estimate in that root section.

### Extension to multiple tubes

To simultaneously trace multiple tubes, for each a seeding cylinder can be placed. In each iteration the point set is partitioned into subsets, so that the points in subset  $X_i$  are best described by the  $i$ th tube model according to the data term of the energy. The evolution of tube  $i$  is computed on its corresponding subset  $X_i$  only. The overall energy then becomes the sum over all tube energies.

### Results on synthetic data

We compared the proposed model to axis estimates obtained through Gaussian point cloud kernel smoothing (PKS) as presented in section 3.3.1, which resembles the drawbacks of averaging techniques for curve fitting. For this we synthetically generated data sets consisting of point clouds highlighting specific cases. We used trigonometric functions to model the axis and thickness functions and generated 1000 equally distributed tube surface points around the axis. The point positions

### 3. The *intrinsic Root Coordinate System (iRoCS)*

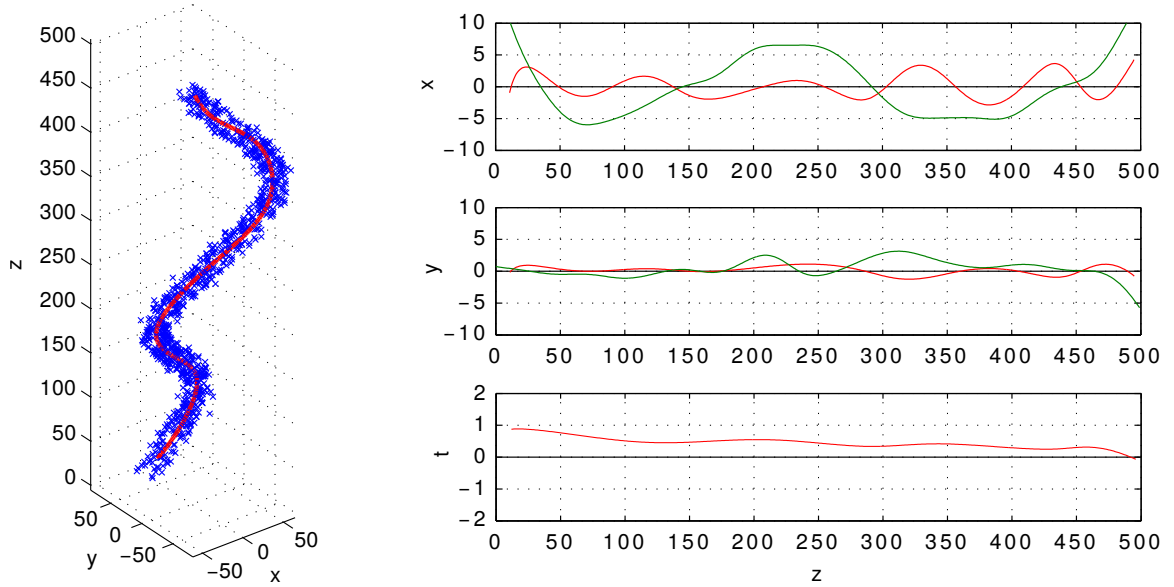


**Figure 3.10.:** Sample fit to synthetically generated noisy surface points of a curved tube with constant thickness. Synthesis parameters:  $\mathbf{a}(u) = (50 \sin(2\pi u/300), 70 \sin(2\pi u/800), u)^\top$ ,  $t(u) = 10$ , noise  $\sigma = 4$ . Left: point cloud (blue) and estimated axis using coupled curves (red); right: error of fit for each model dimension of point based kernel smoothing (PKS, green) and coupled curves model (CCM, red).

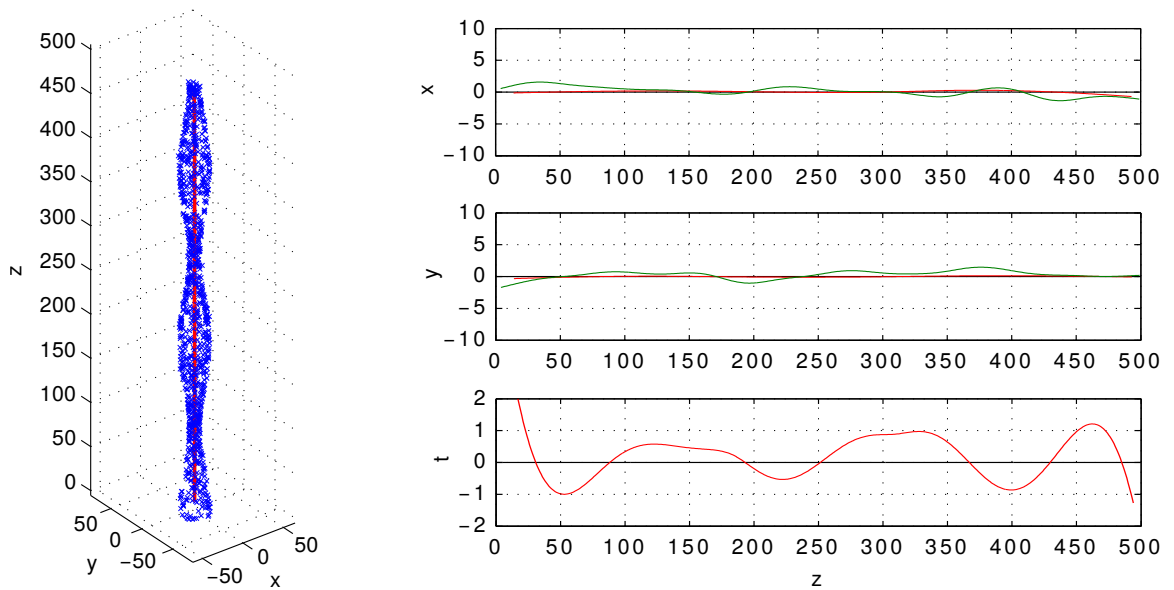


**Figure 3.11.:** Sample fit to synthetically generated noisy surface points of a straight tube with variable thickness. Synthesis parameters:  $\mathbf{a}(u) = (0, 0, u)^\top$ ,  $t(u) = 20 + 10 \sin(2\pi u/200)$ , noise  $\sigma = 1$ . Left: point cloud (blue) and estimated axis using coupled curves (red); right: error of fit for each model dimension of point based kernel smoothing (PKS, green) and coupled curves model (CCM, red).

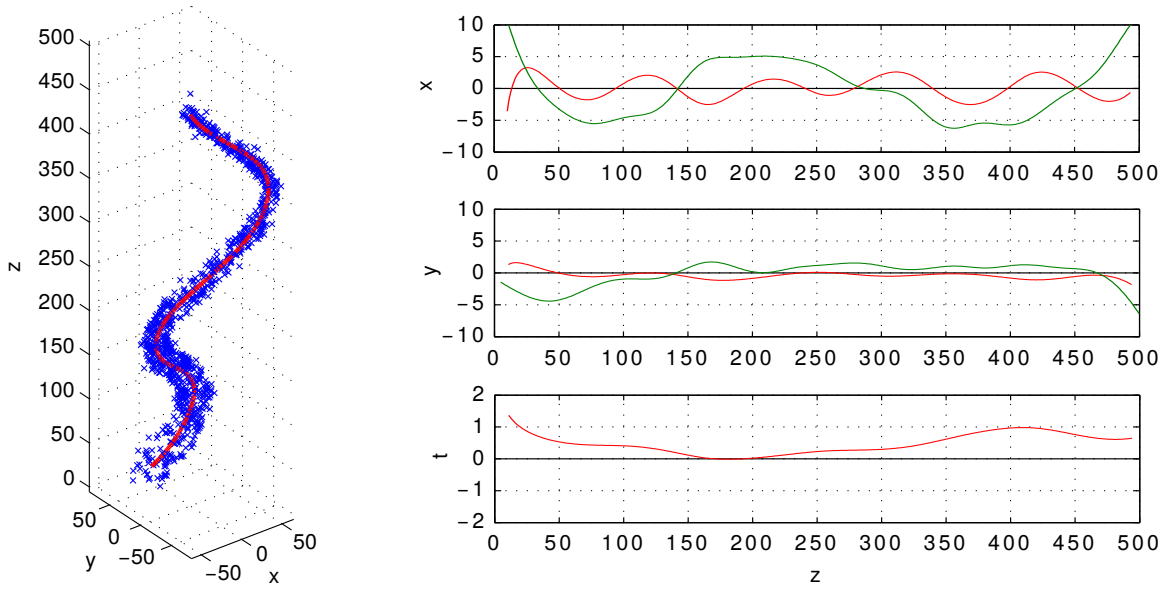


**Figure 3.12.:** Sample fit to synthetically generated noisy surface points of a curved tube with variable thickness. Synthesis parameters:  $\mathbf{a}(u) = (50 \sin(2\pi u/300), 70 \sin(2\pi u/800), u)^\top$ ,  $t(u) = 10 + 5 \sin(2\pi u/1000)$ , noise  $\sigma = 4$ . Left: point cloud (blue) and estimated axis using coupled curves (red); right: error of fit for each model dimension of point based kernel smoothing (PKS, green) and coupled curves model (CCM, red).

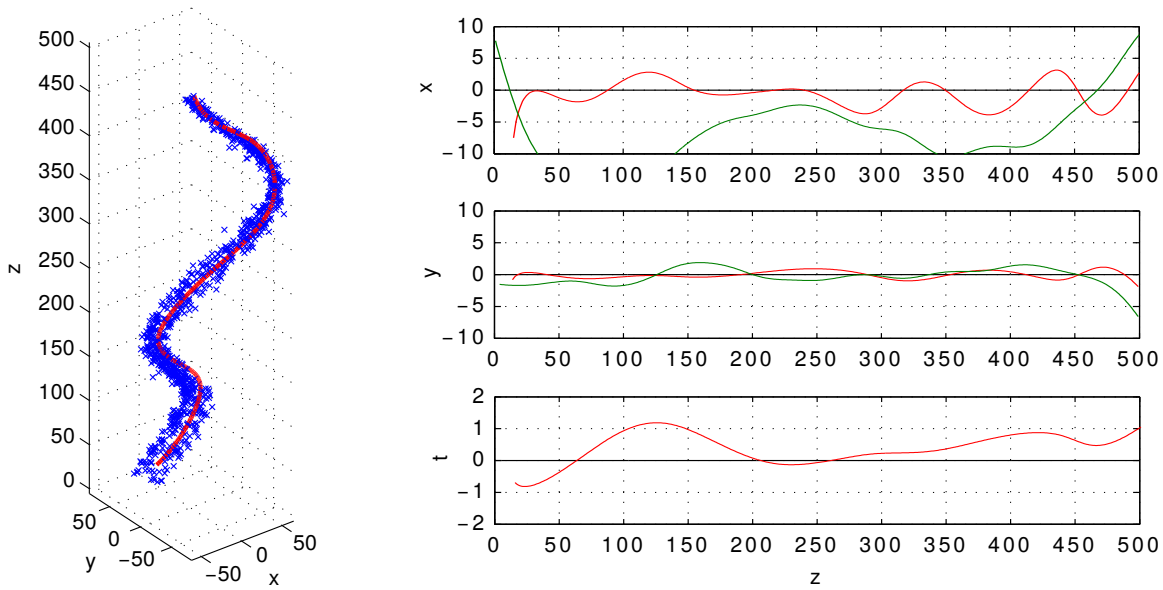


**Figure 3.13.:** Sample fit to synthetically generated noisy surface points of a curved tube with variable thickness and simulated self-occlusion. Synthesis parameters:  $\mathbf{a}(u) = (50 \sin(2\pi u/300), 70 \sin(2\pi u/800), u)^\top$ ,  $t(u) = 10 + 5 \sin(2\pi u/1000)$ , noise  $\sigma = 4$ . Left: point cloud (blue) and estimated axis using coupled curves (red); right: error of fit for each model dimension of point based kernel smoothing (PKS, green) and coupled curves model (CCM, red).

### 3. The *intrinsic Root Coordinate System (iRoCS)*

---

were then randomly displaced. The displacement was drawn from an isotropic Gaussian distribution with standard deviation  $\sigma$  leading to the synthetic ground truth (Fig. 3.10 – 3.13 left panels). The kernel width of the kernel smoothing approach was empirically chosen to minimize the fitting error. The errors of fit of PKS and the proposed coupled curve model (CCM) with cubic splines ( $p = 3$ ) are shown in the right panels. For constant tube thickness (Fig. 3.10) the axis error of CCM in each direction stays below 20% of the tube thickness whereas the smoothing in PKS already leads to undershoots. The thickness is over-estimated by on average 5%. Pure thickness variations as in Fig. 3.11 do not influence the axis localization accuracy, but they are reflected in the thickness error, because the model favors constant thickness. However, the error stays below 10% for low noise and small  $\mu$  (here  $\mu = 0$ ). Moderate thickness variations on a bent model as shown in Fig. 3.12 affect the quality of fit only marginally. Finally, the robustness to biased point cloud distributions on the tube surface is highlighted in Fig. 3.13. For this all sample points from Fig. 3.12 which are occluded when assuming a solid tube and a fixed view angle were removed from the set. This resulted in an axis position bias for PKS, whereas CCM still reliably estimates tube localization and thickness.

#### Results on the Arabidopsis root tip

Finally we show the applicability and robustness of our approach on our original problem of tracing Arabidopsis root tips based on detected epidermis nuclei. Orthogonal views of three sample roots with super-imposed axis fits are shown in Fig. 3.14(a-c) (panels 2 and 3). Despite an applied gamma correction, the signal attenuation in  $z$  direction is clearly visible.

To evaluate the accuracy of the axis fits, two experts manually annotated axis points of ten root tips. For this the data sets were first rotated to roughly align the root axis with the Euclidean  $x$ -axis, This avoids elliptic distortions of the visible root cross-sections during annotation. Both experts picked the root center at every 100th  $x$ -section of the data set guided by a circle of appropriate diameter. The average annotation difference between the experts is  $3\mu\text{m}$ , which is in the order of an average nucleus radius.

We again compared CCM to Gaussian kernel smoothing approaches, this time incorporating either the gray values directly (GKS) or the positions of the nuclei (PKS) that are also used in the CCM. We chose a kernel width of  $40\mu\text{m}$  to obtain smooth curves, that show good localization properties. The estimated axes on sample roots are shown in Fig. 3.14. Especially in Fig. 3.14(a) the bias of GKS towards regions with higher gray values is clearly visible. As already seen in the synthetic results PKS relies on homogeneously distributed points, and therefore on the detector quality. In Fig. 3.14(a) and (b) the detector reported many false positives in parts of the recordings with low SNR, leading to extreme deformations of the axis towards these points. CCM was also affected by the large proportion of false positives in the root volume (Fig. 3.14(b) (xz panel)) which results in a shift of the model axis in  $z$  direction, but the effect is less severe compared to PKS.

A quantitative comparison of all approaches on the manually annotated root axis points is given in table 3.3.

The described model is not restricted to axis tracing using sparse nucleus positions. We also applied it to the dense outer boundaries of the cellular segmentation. To obtain high performance we reduced

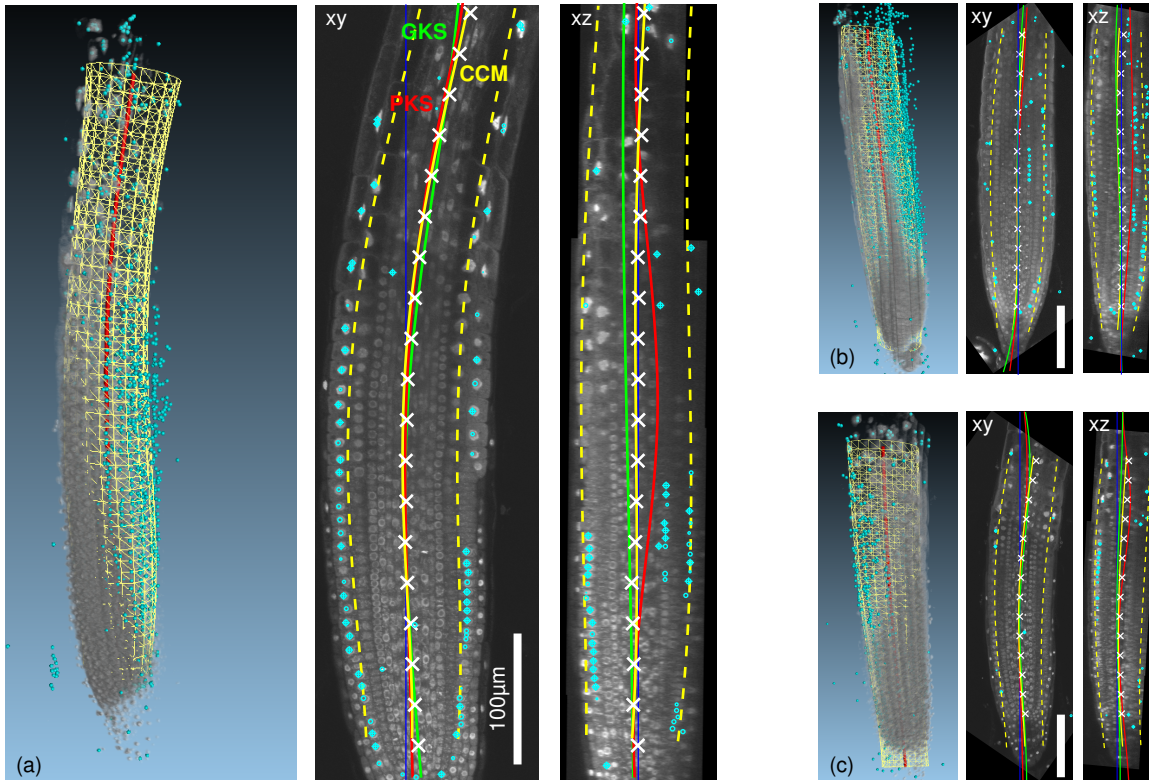


**Figure 3.14.:** The coupled curves model fit to sample root tip data sets. Gray: gamma corrected DAPI signal; red line (left panels): estimated root axis; yellow mesh: estimated center of the epidermal cell layer; cyan spheres: noisy epidermis nucleus positions. Right panel: Orthogonal cuts through the data sets and axis fits using gray value-based kernel smoothing (GKS), point-based kernel smoothing (PKS) and the proposed coupled curves model (CCM); White crosses: expert annotation.

**Table 3.3.:** Minimum/Maximum/Average root mean squared axis fitting errors between expert annotations and the fitting approaches on ten sample roots. (GKS = gray value-based kernel smoothing, PKS = point-based kernel smoothing, CCM = the proposed coupled curves model)

	Expert 2	GKS	PKS	CCM
	min/max/avg [ $\mu\text{m}$ ]			
Expert 1	1.78/5.32/3.09	5.52/17.30/10.68	3.69/16.94/8.46	<b>3.18/11.22/6.07</b>
Expert 2	N/A	6.38/14.66/11.38	<b>3.37/17.36/8.65</b>	<b>4.55/12.65/7.32</b>

the number of root surface points by factor four, in practice further reduction is easily possible without changing the resulting axis fit. Sample results for long root tip samples for either nucleus marker or cell boundary marker are given in figure 3.15.

### 3. The *intrinsic Root Coordinate System (iRoCS)*

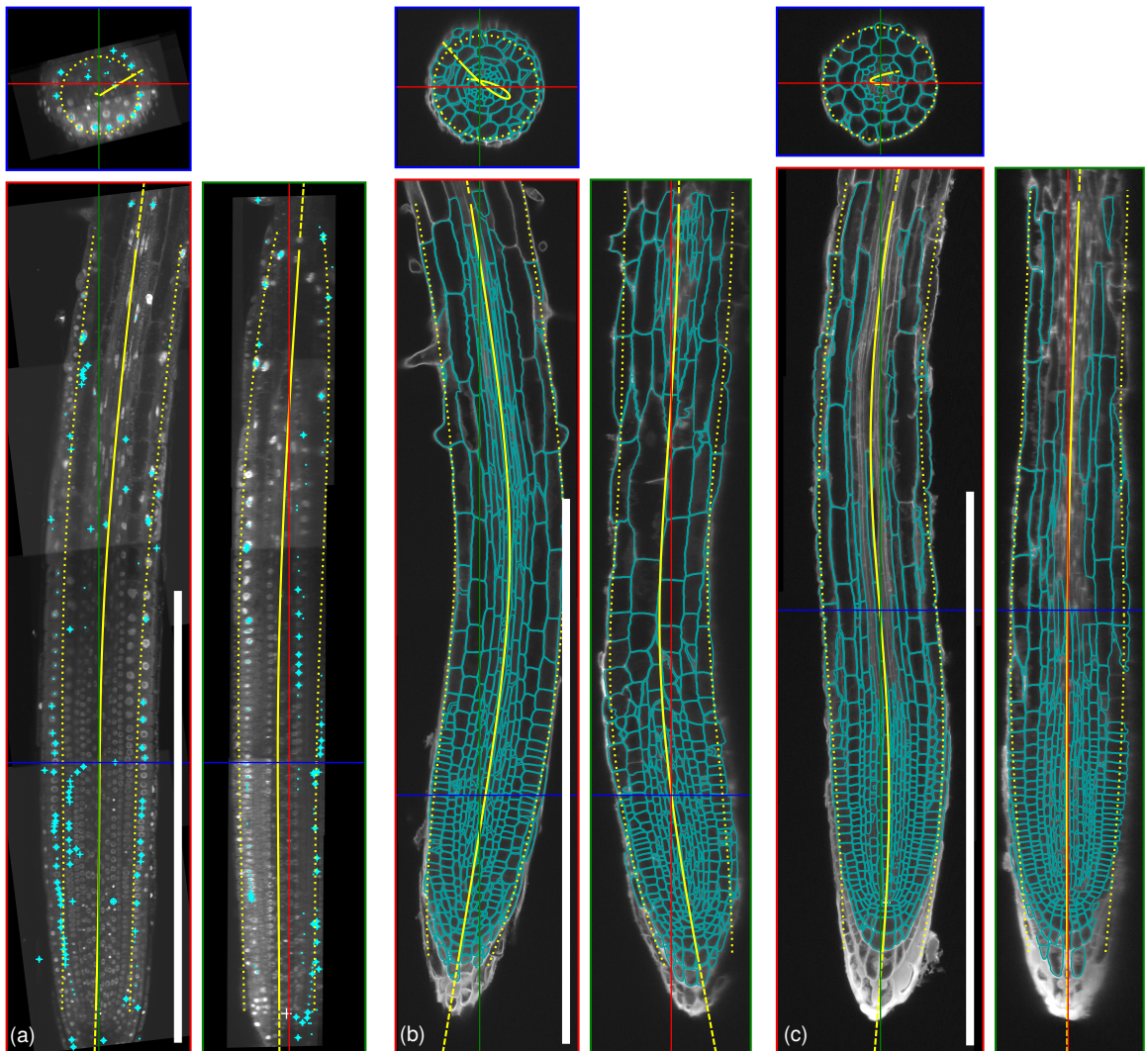


**Figure 3.15.:** The coupled curves model fit to up to 1mm long root tips. Gray: DAPI signal; Cyan: (a) Detected epidermis nuclei; (b-c) Cell segmentation; solid yellow lines: estimated root axis; dotted yellow lines: (a) estimated epidermis layer; (b-c) estimated root surface. Scale bars: 500 $\mu$ m.

### 3.4. Layer label assignment

Continuous description of the root geometry and the possibility to map any recorded marker pattern to a unique absolute bent cylinder coordinate within a normalized reference coordinate system is already a valuable tool in itself. However, this mapping does not yet allow to relate events to tissue layers or cell files which is the basis for a descriptive atlas.

**Table 3.4.:** Classification accuracy of the layer assignment. The confusion matrix shows the number of nucleus candidates classified as either root cap, epidermis, cortex, endodermis, pericycle, vasculature (either in interphase or in mitosis) or background. Rows indicate the real label (manually annotated), whereas columns show the label predicted by a soft-margin SVM with RBF kernel. The overall precision excluding the background class is given in the lower right corner.

		True label											$\Sigma$	Precision [%]		
		Background	Root Cap	Epidermis	Cortex	Endodermis	Pericycle	Vasculature	Root Cap (M)	Epidermis (M)	Cortex (M)	Endodermis (M)			Pericycle (M)	Vasculature (M)
Classified as	Background	2619	38	95	22	18	53	164	2	1	1	3013	86.9			
	Root Cap	97	1546	31	5	21	5	4	10	4		1723	89.7			
	Epidermis	113	32	1611	80	8	3		3	2		1852	87.0			
	Cortex	34	9	4	605	210	4			2		868	69.7			
	Endodermis	56			5	605	99	2			1	768	78.8			
	Pericycle	35	1			56	710	118				925	76.8			
	Vasculature	253	2	5	5	8	26	833				1141	73.0			
	Root Cap (M)	5	19						5	14		43	11.6			
	Epidermis (M)									14	7	21	66.7			
	Cortex (M)										14	14	100.0			
	Endodermis (M)										1	18	2	21	85.2	
	Pericycle (M)											1	15	1	17	88.2
	Vasculature (M)	3						10						24	37	64.9
	$\Sigma$	3215	1647	1746	722	926	900	1131	15	37	27	21	22	34		
Recall [%]	81.5	93.9	92.3	83.8	65.3	78.9	73.7	33.3	37.8	51.9	85.7	68.2	70.6	<b>80.8</b>		

### 3.4.1. Nucleus classification

In section 3.3.1, we already showed a layer classification based on our feature set that successfully distinguished nuclei of different cell layers with an accuracy of approx. 62% (3.1). With the continuous cylinder coordinates we now have a new strong cue for the cell layer label which can be easily incorporated by appending the coordinates  $z$  and  $r$  to the feature vector. The angle  $\varphi$  around the root axis can be left out because it does not give extra information for the layer labeling. As already mentioned in the previous section the radial component of the coordinates could be normalized to the root thickness. This normalization is only meaningful if the thicknesses of all layers are proportionally reduced or increased which would allow to define the different cell layers independent of global root thickness. However, this model fails if the change in root thickness is induced by a change in the number of cells in the inner root tissues. We therefore decided to trust in the ability of the classifier to distinguish nuclei based on their appearance and do not include root thickness normalization. As shown in table 3.4 we could achieve good results with the raw micrometer radius.

### 3. The *intrinsic Root Coordinate System (iRoCS)*

---

Classification errors now concentrate around the diagonal of the matrix, indicating that the residual errors are mainly due to an erroneous one-layer shift. The spurious second diagonal in the upper-right quadrant shows that some interphase nuclei were classified as mitoses, whereas especially for the root cap many mitoses were missed by the classification. The high error rate in the root cap class can be explained by the nuclear morphology of the differentiated root cap nuclei that show similarly dense DNA as mitoses trapped in metaphase by colchicine.

Due to the direct use of the bent cylinder coordinates the layer assignment only works accurately for mild phenotypes, and needs to be re-trained for more severe phenotypes. However, one can use the initial output as starting-point and manually correct erroneous layer assignments instead of doing a full annotation. The corrected samples can then be directly used for re-training if more roots of that specific phenotype have to be analyzed which is very likely in the case of population studies. All roots used for the statistical evaluations presented in section 3.5 were classified using only a single model trained on the wild type.

Even with a model trained on the correct phenotype some manual post-processing is required to achieve expert-level data quality. For the detection of subtle differences as *e.g.* in the upcoming analysis of mitosis distributions, the fully automatic classification result must be manually corrected. But manual annotation time is drastically reduced with the achieved halving of the number of misclassifications when incorporating the cylinder coordinates in the classification.

#### 3.4.2. Cell classification

The final assignment of cells to their layer is also done using a discriminative classifier. Instead of gray value-based invariants we extract cell shape features from the segmentation masks. The features consist of the cell extents in 26 directions starting from the cell's center of gravity. Directions are computed relative to the roots axis orientation and angle  $\varphi$ . The approach is thus a normalization approach in contrast to the invariant approach used in the nucleus classification. As in the nuclear layer assignment, the features are augmented by the cylinder coordinates of the cell's center of gravity with radial normalization to the [0, 1] range. Due to the available dense root surface we could use elliptical cross-sections in the iRoCS fit making the radial normalization very accurate even in elongation zone.

We trained a random forest with 200 trees on three manually annotated roots on the classes background, root cap, epidermis, cortex, endodermis, pericycle, vasculature and quiescent center. The final layer assignment accuracy of a leave-one-root out cross-validation experiment is shown in table 3.5.

As in the nucleus-based layer assignment, the outer tissues are easily assigned to the correct layer. Especially in stele the distinction of pericycle and vasculature is less accurate. There are several reasons for this: first, the pericycle layer is comparably thin and cells have very similar appearance to the adjacent pro-vascular tissue, and secondly pericycle is furthest away from any clear reference (axis, root surface). An expert could only distinguish pericycle from adjacent cell layers by counting the layers. This could also be implemented but has not been done so far.

### 3.5. The effect of *PIN2/4* knockout on proliferation in the *Arabidopsis thaliana* root tip

**Table 3.5.:** Layer assignment accuracy on the cell segmentation. The confusion matrix shows the number of cell candidates classified as either quiescent center, root cap, epidermis, cortex, endodermis, pericycle, vasculature or background. Columns indicate the real label (manually annotated), rows show the label predicted by a random forest classifier with 200 trees. The overall precision excluding the background class is given in the lower right corner.

		True label								Σ	Precision [%]
		Background	Root Cap	Epidermis	Cortex	Endodermis	Pericycle	Vasculature	QC		
Classified as	Background	<b>3535</b>	155	35	14	16	76	499		4330	81.6
	Root Cap	190	<b>1309</b>	23					1	1523	85.9
	Epidermis	18	9	<b>1773</b>	7				1	1808	98.1
	Cortex	7	1	1	<b>701</b>	1			2	713	98.3
	Endodermis	20			5	<b>861</b>	2			888	97.0
	Pericycle	147				12	<b>1039</b>	37	1	1236	84.1
	Vasculature	490				1	24	<b>1279</b>		1794	71.3
	QC				4				<b>23</b>	27	85.2
Σ	4407	1474	1832	731	891	1141	1815	28			
Recall [%]	80.2	88.8	96.8	95.9	96.6	91.1	70.5	82.1		<b>87.4</b>	

The overall classification with a precision of 87.4% is very good. However data were generated on PI stained roots with pseudo-Schiff staining that requires to rinse the root multiple times. Besides the cell walls this rinsing severely damages the cell content and is therefore not suited for studies that require intact cell content. When instead marking the cell membranes with an antibody stain the signal to noise ratio of the images is visibly worse. The image pre-processing using coherence-enhancing diffusion helps, but we could not achieve perfect segmentations on cell-membrane data even after attenuation correction and fusion of two views.

### 3.5. The effect of *PIN2/4* knockout on proliferation in the *Arabidopsis thaliana* root tip

Cell divisions are rare events in the *Arabidopsis* root (only 1-3% of root tip cells are in a mitotic phase of the cell cycle at any time point) and are restricted to the RAM (exception: lateral root initiation). To draw statistically significant conclusions on differences in the mitosis distributions among different populations large sample sizes have to be fully recorded and analyzed in 3D.

We applied the iRoCS pipeline to samples from three populations: a wildtype control, *pin4* and *pin2*. For each group we recorded at least ten samples, marked their QC positions and manually corrected classification errors of a random subset of 10 samples of each population with respect to

### 3. The *intrinsic Root Coordinate System* (iRoCS)

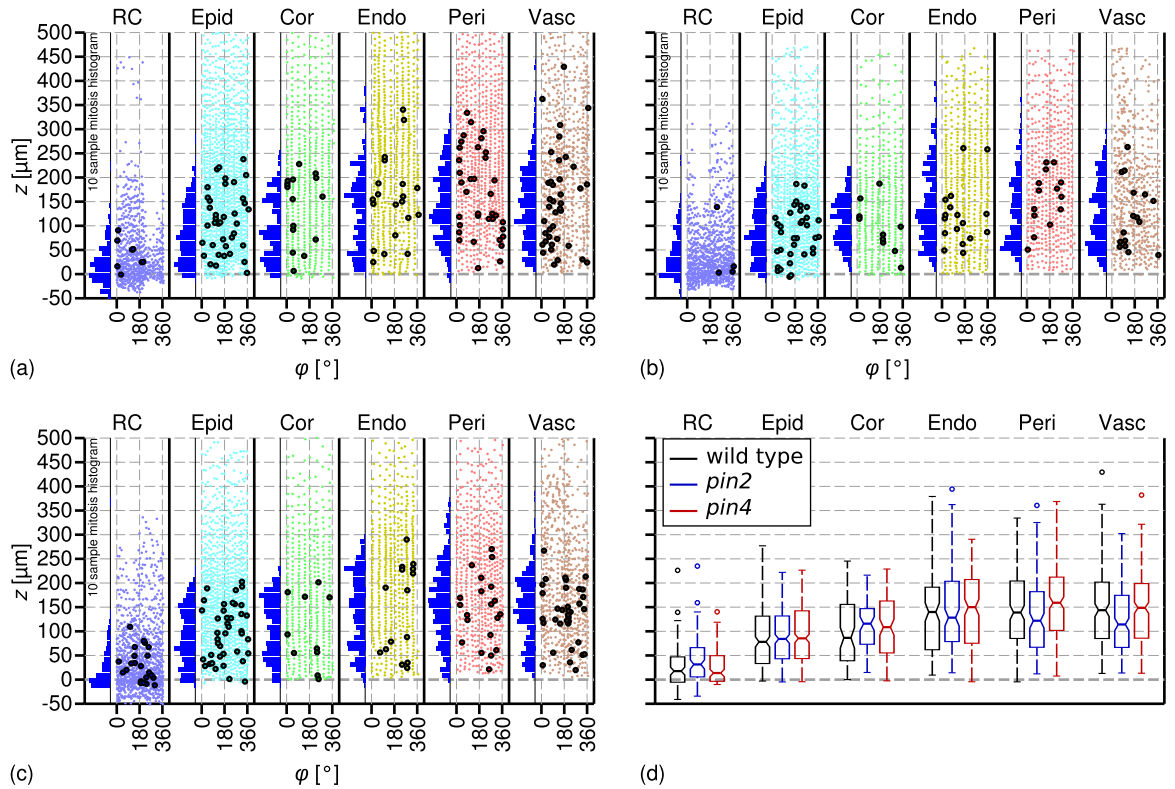


**Figure 3.16.:** Example nucleus maps and mitosis distribution histograms from semi-automatic analysis. Dots = nucleus positions; encircled dots = mitosis positions; RC = root cap; Epid = epidermis; Cor = cortex; Endo = endodermis; Peri = pericycle; Vasc = vasculature. (a) wild type ( $n = 10$ ); (b) *pin2* ( $n = 10$ ); (c) *pin4* ( $n = 10$ ); (d) Non-parametric statistical comparison of the obtained mitosis distributions. Median values (bar), interquartile range (IQR) (box), lowest and highest data within 1.5 IQR of lower and upper quartiles (lines) and outliers (open circles). Notches indicate significance of differences of the distribution medians using the non-parametric Kruskal-Wallis test. Non-overlapping notch-intervals indicate significantly different medians with a p-value of 0.95.

tissue layer and mitotic state to ensure maximum quality results. Since the auxin flux controlled by the PIN proteins affects the different layers differently we estimated the mitosis distributions along the root axis for each layer independently leading to the box plots shown in Fig. 3.16d. iRoCS allows to “virtually unroll” the roots and depict the nucleus positions for each individual layer in nucleus maps. Fig. 3.16a-c shows such nucleus maps of typical sample roots for each population. The histograms on the left in each layer panel show the cumulated mitosis distribution of all ten sample roots per population.

As expected *pin4* shows no significant differences in the distribution of mitoses compared to the wildtype. This is attributed to the high redundancy of the PIN network in the stele. However, our detailed analysis reveals significant differences in the mitosis distributions in vasculature for the *pin2* mutant. Its mitosis distributions in stele are shifted towards the quiescent centre, whereas the outer layers show no significant changes. However, one can also observe a slight distribution shift in

### 3.5. The effect of PIN2/4 knockout on proliferation in the *Arabidopsis thaliana* root tip

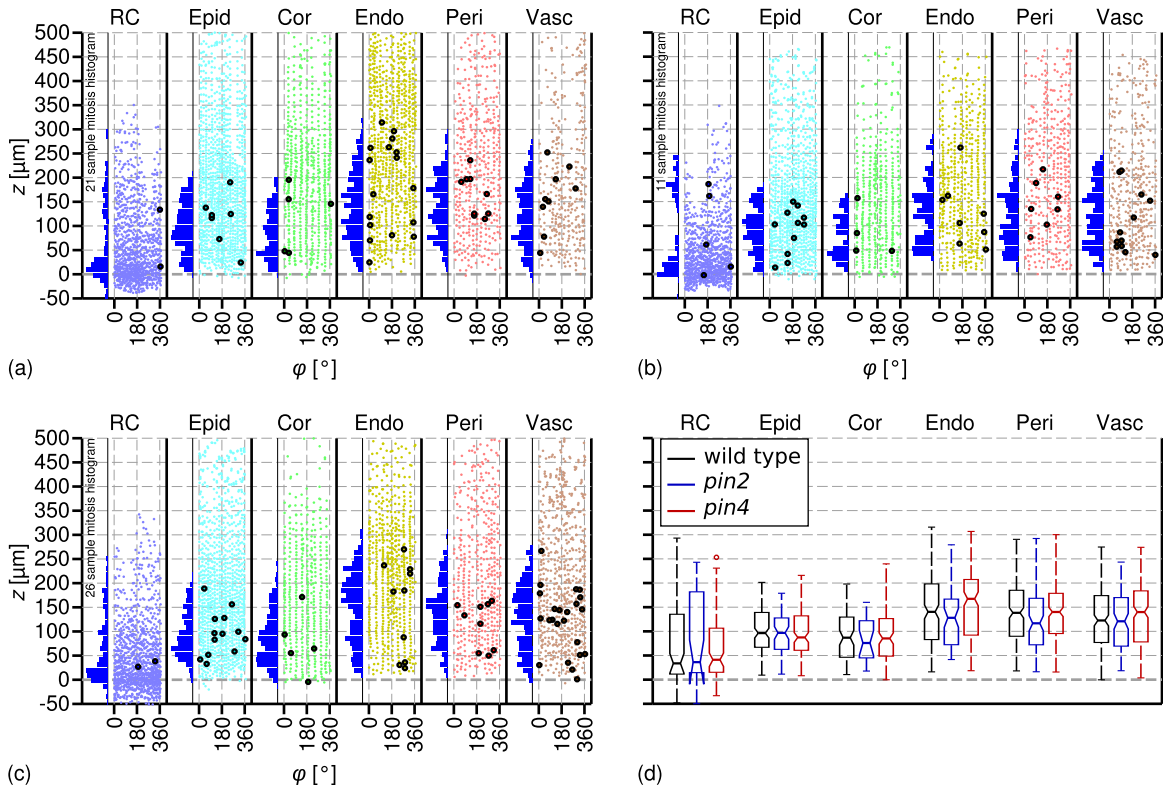


**Figure 3.17.:** Fully automatic mitosis distributions analysis. RC = root cap; Epid = epidermis; Cor = cortex; Endo = endodermis; Peri = pericycle; Vasc = vasculature. (a) wild type ( $n = 21$ ); (b) *pin2* ( $n = 11$ ); (c) *pin4* ( $n = 26$ ); (d) Axial mitosis distributions for the different cell layers. Median values (bar), interquartile range (IQR) (box), lowest and highest data within 1.5 IQR of lower and upper quartiles (lines) and outliers (open circles).

the cortex layer in basal direction. The reasons for these differences have to be further analyzed, but the reduced auxin efflux in the epidermis of the *pin2* mutant seems to significantly alter the auxin gradient in the stele.

As shown in section 3.4 the fully automatic pipeline has an approximate classification accuracy of approximately 80% for interphase and 60% for mitoses from raw data to final model (Table 3.4). To analyze, whether the classification accuracy is sufficient to still see the subtle differences without manual corrections of classification errors, we produced the same nucleus maps and distributions without manual corrections. The results are shown in Figure 3.17, where we included all recorded root samples (numbers given in the corresponding panels).

As already seen in the manually post-processed smaller populations the *pin2* mitosis distribution median in pericycle and vasculature is closer to the QC than in the wild type and *pin4* populations. The noise induced by wrong mitosis classifications damps the effect and significant differences cannot be detected, but the trend remains visible, showing that no systematic bias is introduced by the pipeline.

### 3. The *intrinsic Root Coordinate System (iRoCS)*

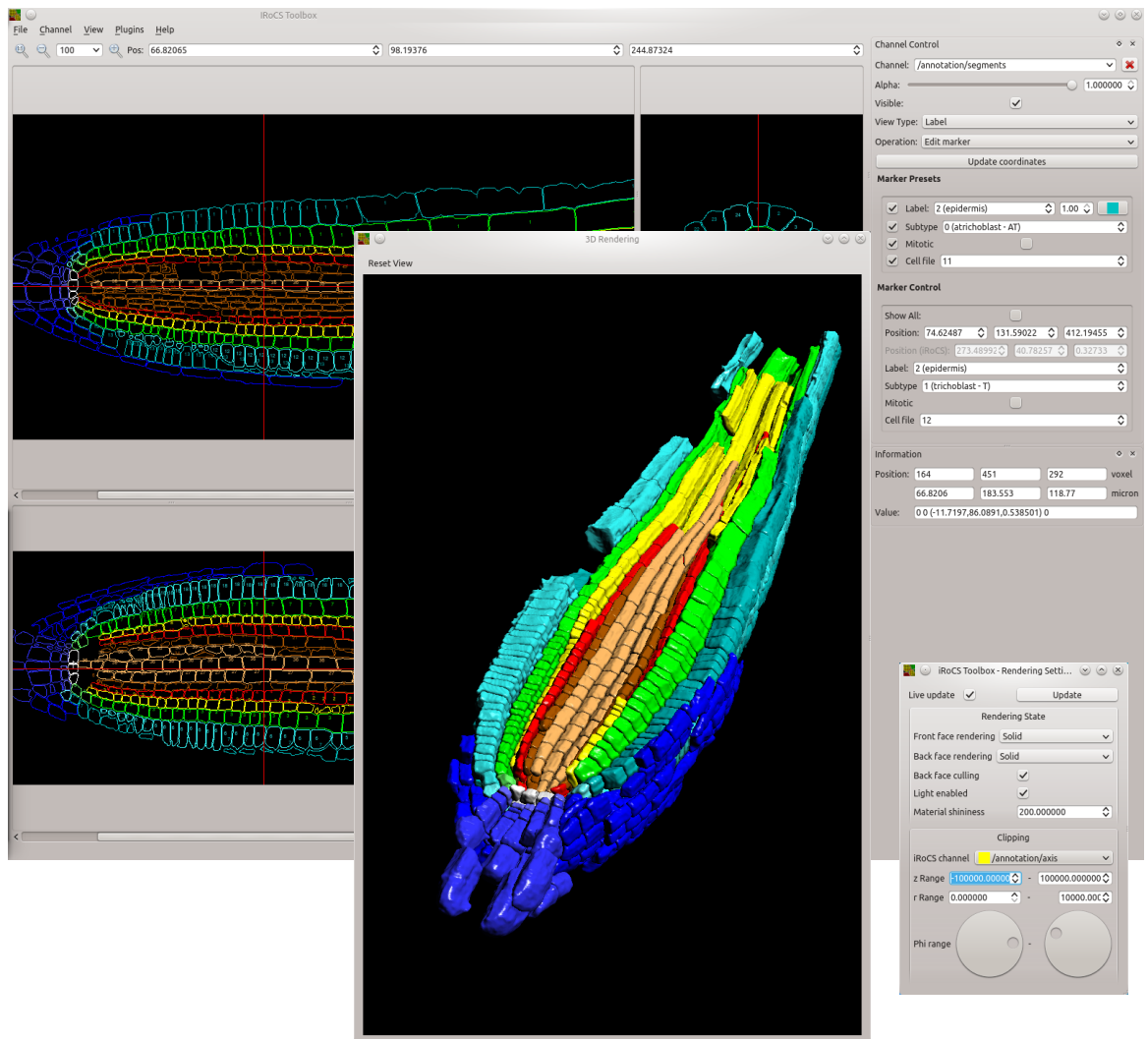


**Figure 3.18.:** The iRoCS Toolbox labelling GUI. Background: Cell/Nucleus editor based on three orthogonal views of the 3-D dataset. Foreground: 3D surface rendering for visual control. The shown cell segmentation was virtually cut along the root axis revealing the cells of different tissues.

## 3.6. Implementation: The iRoCS Toolbox

We provide all approaches discussed in this chapter to the scientific community as open source software in the iRoCS toolbox<sup>1</sup>. The toolbox is implemented in C++ based on the QT4 framework<sup>2</sup> (The Qt Company Ltd., Valimotie 21, FI-00380 Helsinki, Finland), which in principle allows to build it on Linux, Windows and Mac platforms without code adaptations. It is licensed under the

<sup>1</sup><http://lmb.informatik.uni-freiburg.de/lmbsoft/iRoCS/>

<sup>2</sup><http://www.qt.io/>

GNU general public license (GPL)<sup>3</sup> permitting free use, distribution, extension and modification. For 64Bit Linux we also provide pre-built binaries. It consists of a set of libraries that can be easily included to use the proposed methods in other projects. Additionally it consists of a set of command line tools and the graphical user interface `labelling` (Fig. 3.18) that allows to control the individual root analysis steps including manual annotation, error correction and training of new detector and layer assignment models for the nuclear pipeline. The toolbox is designed in a modular fashion separating algorithms from visualization and actual tools for data processing. This allows to implement command line tools and plugins for `labelling` on the same code base. When following this model the toolbox can be easily extended and adapted to a wide range of applications.

---

<sup>3</sup><http://www.gnu.org/>



## 4. Summary

Different approaches to extract quantitative data out of confocal microscopic recordings on different abstraction levels were described and their utility discussed. Despite the fact that the measured intensities are by no means quantitative we developed ways to extract relevant quantitative information from that data source.

With our variational attenuation correction framework we presented a physically motivated approach to pre-process microscopic images mapping the raw intensities to approximate attenuation-free intensities well suited for further processing. We presented a realistic image formation model that allows to simulate a confocal microscope including wavelength-dependent attenuations, photo bleaching and Poisson-Gaussian distributed noise as it occurs in photon counting processes. The attenuation problem was formulated in a Bayesian framework leading to a well-motivated variational energy minimization formulation. Especially the modeling of bleaching, although up-to-now only implemented as zero-order approximation, improves the reconstructions significantly on simulated and real world data. The edge-preserving TV prior on the attenuation fields allows to obtain crisp sample boundaries and is especially well-suited for the description of samples consisting of large homogeneous tissues at lower imaging resolutions. As a positive side-effect, it keeps the attenuation fields compact leading to less boundary artifacts. In combination with the presented sparsity prior the algorithm overcomes limitations of the approximative model, leading to stable results at convergence of the optimization.

With the presented iRoCS pipeline we could show that quantification on the abstract model level is not precluded by imperfect measurements, although the correction of degradations during imaging or in a pre-processing step helps to extract relevant structures. iRoCS allows to describe the Arabidopsis root tip in a standardized way and provides a basic cellular atlas of that plant organ in which localized discrete events can be quantified and related to the cellular root context.

We employed Gauß-Laguerre features to encode local appearance and global positional cues within the organ context for nucleus detection and classification. They are embedded in an intuitive learning-by-example approach which allows to extend its application to other detection tasks in 3-D volumetric data.

The variational approach to tube tracing is also not restricted to the modeling of plant roots. It can in principle be equally well applied to laser-range scan data of tubular structures or for vesicle tracking in MRT images (not shown). The intrinsic smoothness of the underlying four-dimensional B-Spline allows to trace tubes based on very few surface points only. The model automatically adapts its complexity to the available data by automatic addition of further spline control points. This allows to describe arbitrarily complex tubes with circular cross-sections and simple topology (*i.e.* without branches). Additional smoothness and thickness constancy priors further constrain the solution space if required.

### Future work

In the attenuation correction problem, next steps involve a validation of the multi-view model with structured illumination on real biological samples and a rigorous analysis of the two-view model including fluorescence-induced attenuations on synthetic data.

In future research the image formation model should be extended to also include light scatter and refraction. Combining attenuation correction with multiview fusion and deconvolution techniques is another interesting direction of research. Ideally the ray model is replaced by a model for wave optics in this course.

A draw-back of the variational tube tracing approach is its restriction to circular tube cross-sections. Although it makes the approach extremely robust to noise and outliers, it restricts its applicability. In the cell boundary-based root modeling we could exploit the dense almost noise-free surface of the segmentation to allow for elliptic cross-sections. A combination of both approaches that embeds fitting of bent elliptic cylinders into a well-motivated variational energy minimization framework with robust data term is an interesting extension for the near future. Another very interesting extension would be to allow for topological changes, *e.g.* branching which is very important to analyze complex vascular structures or whole root systems.

Especially in the cell-boundary based root modeling only basic cues were exploited. The direct availability of cell adjacency and the area of cell interfaces allows to refine the model beyond the cell layer dimension to also model cell files and possible partners in cell-to-cell signaling.

Another orthogonal approach is to build parametric or example-based generative models of root architecture and growth that can be matched against real root samples. Mai et al. (2014) recently presented a promising first approach for simultaneous cell detection and segmentation from learnt cell geometries.

# A. Variational attenuation correction

## A.1. Energy derivatives

### A.1.1. General framework

The general energy formulation is given by

$$E(\alpha^{\text{ex}}, \alpha^{\text{em}}, \hat{I}, \theta) = \sum_{i=1}^k \int_{\Omega} \left( \frac{f(I_i(\mathbf{x})) - f(F_i(\mathbf{x}))}{g(F_i(\mathbf{x}))} \right)^2 + \ln(g(F_i(\mathbf{x}))) \, d\mathbf{x} + E_{\text{prior}}$$

where we define  $D_i(\mathbf{x}) := \frac{f(I_i(\mathbf{x})) - f(F_i(\mathbf{x}))}{g(F_i(\mathbf{x}))}$ .

Its first derivative with respect to an arbitrary variable  $\theta$  is

$$\begin{aligned} & \frac{\partial E(\alpha^{\text{ex}}, \alpha^{\text{em}}, \hat{I}, \theta)}{\partial \theta} \\ &= \sum_{i=1}^k \int_{\Omega} \frac{\partial}{\partial \theta} \left( \frac{f(I_i(\mathbf{x})) - f(F_i(\mathbf{x}))}{g(F_i(\mathbf{x}))} \right)^2 + \frac{\partial}{\partial \theta} \ln(g(F_i(\mathbf{x}))) \, d\mathbf{x} + \frac{\partial E_{\text{prior}}}{\partial \theta} \\ &= \sum_{i=1}^k \int_{\Omega} 2D_i(\mathbf{x}) \frac{\partial}{\partial \theta} \left( \frac{f(I_i(\mathbf{x})) - f(F_i(\mathbf{x}))}{g(F_i(\mathbf{x}))} \right) + \frac{\frac{\partial g(F_i(\mathbf{x}))}{\partial \theta}}{g(F_i(\mathbf{x}))} \, d\mathbf{x} + \frac{\partial E_{\text{prior}}}{\partial \theta} \\ &= \sum_{i=1}^k \int_{\Omega} 2D_i(\mathbf{x}) \left( -\frac{\frac{\partial f(F_i(\mathbf{x}))}{\partial \theta}}{g(F_i(\mathbf{x}))} - \frac{D_i(\mathbf{x}) \frac{\partial g(F_i(\mathbf{x}))}{\partial \theta}}{g(F_i(\mathbf{x}))} \right) + \frac{\frac{\partial g(F_i(\mathbf{x}))}{\partial \theta}}{g(F_i(\mathbf{x}))} \, d\mathbf{x} + \frac{\partial E_{\text{prior}}}{\partial \theta} \\ &= -\sum_{i=1}^k \int_{\Omega} \frac{2D_i(\mathbf{x}) f'(F_i(\mathbf{x})) + (2D_i^2(\mathbf{x}) - 1) g'(F_i(\mathbf{x})) \frac{\partial F_i(\mathbf{x})}{\partial \theta}}{g(F_i(\mathbf{x}))} \, d\mathbf{x} + \frac{\partial E_{\text{prior}}}{\partial \theta}. \end{aligned}$$

and the second derivative is

$$\begin{aligned}
& \frac{\partial^2 E(\alpha^{\text{ex}}, \alpha^{\text{em}}, \hat{I}, \theta)}{\partial \theta^2} \\
&= - \sum_{i=1}^k \int_{\Omega} \frac{\partial}{\partial \theta} \left( \frac{2D_i f'(F_i) + (2D_i^2 - 1) g'(F_i)}{g(F_i)} \cdot \frac{\partial F_i}{\partial \theta} \right) \mathbf{d}\mathbf{x} + \frac{\partial^2 E_{\text{prior}}}{\partial \theta^2} \\
&= - \sum_{i=1}^k \int_{\Omega} \frac{\partial}{\partial \theta} \left( \frac{2D_i f'(F_i) + (2D_i^2 - 1) g'(F_i)}{g(F_i)} \right) \frac{\partial F_i}{\partial \theta} + \frac{2D_i f'(F_i) + (2D_i^2 - 1) g'(F_i)}{g(F_i)} \frac{\partial^2 F_i}{\partial \theta^2} \mathbf{d}\mathbf{x} + \frac{\partial^2 E_{\text{prior}}}{\partial \theta^2} \\
&= - \sum_{i=1}^k \int_{\Omega} \left( \frac{\frac{\partial}{\partial \theta} (2D_i f'(F_i) + (2D_i^2 - 1) g'(F_i))}{g(F_i)} - \frac{(2D_i f'(F_i) + (2D_i^2 - 1) g'(F_i)) \frac{\partial}{\partial \theta} g(F_i)}{g^2(F_i)} \right) \frac{\partial F_i}{\partial \theta} \\
&\quad + \frac{2D_i f'(F_i) + (2D_i^2 - 1) g'(F_i)}{g(F_i)} \frac{\partial^2 F_i}{\partial \theta^2} \mathbf{d}\mathbf{x} + \frac{\partial^2 E_{\text{prior}}}{\partial \theta^2} \\
&= - \sum_{i=1}^k \int_{\Omega} \frac{\frac{\partial}{\partial \theta} (2D_i f'(F_i) + (2D_i^2 - 1) g'(F_i))}{g(F_i)} \frac{\partial F_i}{\partial \theta} - \frac{2D_i f'(F_i) + (2D_i^2 - 1) g'(F_i)}{g^2(F_i)} g'(F_i) \left( \frac{\partial F_i}{\partial \theta} \right)^2 \\
&\quad + \frac{2D_i f'(F_i) + (2D_i^2 - 1) g'(F_i)}{g(F_i)} \frac{\partial^2 F_i}{\partial \theta^2} \mathbf{d}\mathbf{x} + \frac{\partial^2 E_{\text{prior}}}{\partial \theta^2} \\
&= - \sum_{i=1}^k \int_{\Omega} \frac{2f'(F_i) + 4D_i g'(F_i)}{g(F_i)} \frac{\partial}{\partial \theta} D_i \frac{\partial F_i}{\partial \theta} \\
&\quad + \left( \frac{2D_i f''(F_i) + (2D_i^2 - 1) g''(F_i)}{g(F_i)} - \frac{2D_i f'(F_i) + (2D_i^2 - 1) g'(F_i)}{g^2(F_i)} g'(F_i) \right) \left( \frac{\partial F_i}{\partial \theta} \right)^2 \\
&\quad + \frac{2D_i f'(F_i) + (2D_i^2 - 1) g'(F_i)}{g(F_i)} \frac{\partial^2 F_i}{\partial \theta^2} \mathbf{d}\mathbf{x} + \frac{\partial^2 E_{\text{prior}}}{\partial \theta^2} \\
&= - \sum_{i=1}^k \int_{\Omega} \frac{2f'(F_i) + 4D_i g'(F_i)}{g(F_i)} \left( \frac{\frac{\partial}{\partial \theta} (f(I_i) - f(F_i))}{g(F_i)} - \frac{(f(I_i) - f(F_i)) \frac{\partial}{\partial \theta} g(F_i)}{g^2(F_i)} \right) \frac{\partial F_i}{\partial \theta} \\
&\quad + \left( \frac{2D_i f''(F_i) + (2D_i^2 - 1) g''(F_i)}{g(F_i)} - \frac{2D_i f'(F_i) + (2D_i^2 - 1) g'(F_i)}{g^2(F_i)} g'(F_i) \right) \left( \frac{\partial F_i}{\partial \theta} \right)^2 \\
&\quad + \frac{2D_i f'(F_i) + (2D_i^2 - 1) g'(F_i)}{g(F_i)} \frac{\partial^2 F_i}{\partial \theta^2} \mathbf{d}\mathbf{x} + \frac{\partial^2 E_{\text{prior}}}{\partial \theta^2} \\
&= - \sum_{i=1}^k \int_{\Omega} \frac{2f'(F_i) + 4D_i g'(F_i)}{g^2(F_i)} \left( -\frac{\partial f(F_i)}{\partial \theta} - D_i \frac{\partial g(F_i)}{\partial \theta} \right) \frac{\partial F_i}{\partial \theta} \\
&\quad + \left( \frac{2D_i f''(F_i) + (2D_i^2 - 1) g''(F_i)}{g(F_i)} - \frac{2D_i f'(F_i) + (2D_i^2 - 1) g'(F_i)}{g^2(F_i)} g'(F_i) \right) \left( \frac{\partial F_i}{\partial \theta} \right)^2 \\
&\quad + \frac{2D_i f'(F_i) + (2D_i^2 - 1) g'(F_i)}{g(F_i)} \frac{\partial^2 F_i}{\partial \theta^2} \mathbf{d}\mathbf{x} + \frac{\partial^2 E_{\text{prior}}}{\partial \theta^2}
\end{aligned}$$

$$\begin{aligned}
&= \sum_{i=1}^k \int_{\Omega} \frac{2f'(F_i) + 4D_i g'(F_i)}{g^2(F_i)} (f'(F_i) + D_i g'(F_i)) \left( \frac{\partial F_i}{\partial \theta} \right)^2 \\
&\quad + \left( -\frac{2D_i f''(F_i) + (2D_i^2 - 1) g''(F_i)}{g(F_i)} + \frac{2D_i f'(F_i) + (2D_i^2 - 1) g'(F_i)}{g^2(F_i)} g'(F_i) \right) \left( \frac{\partial F_i}{\partial \theta} \right)^2 \\
&\quad - \frac{2D_i f'(F_i) + (2D_i^2 - 1) g'(F_i)}{g(F_i)} \frac{\partial^2 F_i}{\partial \theta^2} \, d\mathbf{x} + \frac{\partial^2 E_{\text{prior}}}{\partial \theta^2} \\
&= \sum_{i=1}^k \int_{\Omega} \left( \frac{(2f'(F_i) + 4D_i g'(F_i))(f'(F_i) + D_i g'(F_i)) + 2D_i f'(F_i) g'(F_i) + (2D_i^2 - 1) g'^2(F_i)}{g^2(F_i)} \right) \left( \frac{\partial F_i}{\partial \theta} \right)^2 \\
&\quad - \frac{2D_i f''(F_i) + (2D_i^2 - 1) g''(F_i)}{g(F_i)} \left( \frac{\partial F_i}{\partial \theta} \right)^2 - \frac{2D_i f'(F_i) + (2D_i^2 - 1) g'(F_i)}{g(F_i)} \frac{\partial^2 F_i}{\partial \theta^2} \, d\mathbf{x} + \frac{\partial^2 E_{\text{prior}}}{\partial \theta^2} \\
&= \sum_{i=1}^k \int_{\Omega} \left( \frac{2f'^2(F_i) + 8D_i f'(F_i) g'(F_i) + 4D_i^2 g'^2(F_i) + 2D_i^2 g'^2(F_i) - g'^2(F_i)}{g^2(F_i)} \right) \left( \frac{\partial F_i}{\partial \theta} \right)^2 \\
&\quad - \frac{2D_i f''(F_i) + (2D_i^2 - 1) g''(F_i)}{g(F_i)} \left( \frac{\partial F_i}{\partial \theta} \right)^2 - \frac{2D_i f'(F_i) + (2D_i^2 - 1) g'(F_i)}{g(F_i)} \frac{\partial^2 F_i}{\partial \theta^2} \, d\mathbf{x} + \frac{\partial^2 E_{\text{prior}}}{\partial \theta^2} \\
&= \sum_{i=1}^k \int_{\Omega} \left( \frac{2(f'^2(F_i) + 4D_i f'(F_i) g'(F_i) + 4D_i^2 g'^2(F_i)) - 2D_i^2 g'^2(F_i) - g'^2(F_i)}{g^2(F_i)} \right) \left( \frac{\partial F_i}{\partial \theta} \right)^2 \\
&\quad - \frac{2D_i f''(F_i) + (2D_i^2 - 1) g''(F_i)}{g(F_i)} \left( \frac{\partial F_i}{\partial \theta} \right)^2 - \frac{2D_i f'(F_i) + (2D_i^2 - 1) g'(F_i)}{g(F_i)} \frac{\partial^2 F_i}{\partial \theta^2} \, d\mathbf{x} + \frac{\partial^2 E_{\text{prior}}}{\partial \theta^2} \\
&= \sum_{i=1}^k \int_{\Omega} \left( \frac{2(f'(F_i) + 2D_i g'(F_i))^2 - (2D_i^2 + 1) g'^2(F_i) - 2D_i f''(F_i) + (2D_i^2 - 1) g''(F_i)}{g^2(F_i)} \right) \left( \frac{\partial F_i}{\partial \theta} \right)^2 \\
&\quad - \frac{2D_i f'(F_i) + (2D_i^2 - 1) g'(F_i)}{g(F_i)} \frac{\partial^2 F_i}{\partial \theta^2} \, d\mathbf{x} + \frac{\partial^2 E_{\text{prior}}}{\partial \theta^2}.
\end{aligned}$$

### A.1.2. Gâteaux derivatives of the basic simulation equation

The Gâteaux derivatives of the basic image formation equation are given by

$$\left. \frac{d}{d\epsilon} \left( (\hat{I} + \epsilon h) \cdot C^{[\alpha_{\text{ex}}]}(\mathbf{x}) \cdot C^{[\alpha_{\text{em}}]}(\mathbf{x}) \right) \right|_{\epsilon=0} = (C^{[\alpha_{\text{ex}}]} \cdot C^{[\alpha_{\text{em}}]} \cdot h)(\mathbf{x})$$

$$\begin{aligned} \left. \frac{d}{d\epsilon} \left( \hat{I} \cdot C^{[\alpha_{\text{ex}} + \epsilon h]} \cdot C^{[\alpha_{\text{em}}]}(\mathbf{x}) \right) \right|_{\epsilon=0} &= \\ & -2 \int_S s_i(\mathbf{r}) \int_0^\infty \left( \hat{I} \cdot T_{\mathbf{r}}^{[\alpha_{\text{ex}}]} \cdot C_i^{[\alpha_{\text{em}}]} \right)(\mathbf{x}) \cdot h(\mathbf{x} + \ell \mathbf{r}) \, d\ell \, d\mathbf{r} \end{aligned}$$

$$\begin{aligned} \left. \frac{d}{d\epsilon} \left( \hat{I} \cdot C^{[\alpha_{\text{ex}}]} \cdot C^{[\alpha_{\text{em}} + \epsilon h]}(\mathbf{x}) \right) \right|_{\epsilon=0} &= \\ & -2 \int_S s_i(\mathbf{r}) \int_0^\infty \left( \hat{I} \cdot C_i^{[\alpha_{\text{ex}}]} \cdot T_{\mathbf{r}}^{[\alpha_{\text{em}}]} \right)(\mathbf{x}) \cdot h(\mathbf{x} + \ell \mathbf{r}) \, d\ell \, d\mathbf{r} \end{aligned}$$

### A.1.3. Explicit polynomial solution of the approximate Poisson noise model

The analytic solution for  $\hat{I}$  given  $\alpha$  and  $\beta_2$  is given by one solution of the quartic function

$$\begin{aligned} 0 &= -4 \sum_{i=1}^2 \frac{D_i C_i^2}{\sqrt{\beta_i F_i + \frac{3}{8}}} \\ \Leftrightarrow 0 &= - \left( (C_1^2 + C_2^2)^2 \left( \hat{I} C_1^2 + \frac{3}{8} \right) \left( \beta_2 \hat{I} C_2^2 + \frac{3}{8} \right) - \mathcal{A}_1^2 C_1^4 \left( \beta_2 \hat{I} C_2^2 + \frac{3}{8} \right) - \mathcal{A}_2^2 C_2^4 \left( \hat{I} C_1^2 + \frac{3}{8} \right) \right)^2 \\ &\quad + 4 \mathcal{A}_1^2 \mathcal{A}_2^2 C_1^4 C_2^4 \left( \hat{I} C_1^2 + \frac{3}{8} \right) \left( \beta_2 \hat{I} C_2^2 + \frac{3}{8} \right) \\ \Leftrightarrow 0 &= -\hat{I}^4 \cdot \beta_2^2 C_1^4 C_2^4 (C_1^2 + C_2^2)^4 \\ &\quad + \hat{I}^3 \cdot 2\beta_2 C_1^2 C_2^2 (C_1^2 + C_2^2)^2 \left( C_1^2 C_2^2 (\beta_2 \mathcal{A}_1^2 C_1^2 + \mathcal{A}_2^2 C_2^2) - \frac{3}{8} (C_1^2 + C_2^2)^2 (C_1^2 + \beta_2 C_2^2) \right) \\ &\quad + \hat{I}^2 \cdot \left( \frac{3}{4} C_1^2 C_2^2 (C_1^2 + C_2^2)^2 (C_1^2 C_2^2 (\beta_2^2 \mathcal{A}_1^2 + \mathcal{A}_2^2) + 2 \cdot \beta_2 (\mathcal{A}_1^2 C_1^4 + \mathcal{A}_2^2 C_2^4)) \right. \\ &\quad \quad \left. - \left( \frac{3}{8} \right)^2 (C_1^2 + C_2^2)^4 \left( (C_1^2 + \beta_2 C_2^2)^2 + 2\beta_2 C_1^2 C_2^2 \right) - C_1^4 C_2^4 (\mathcal{A}_2^2 C_2^2 - \beta_2 \mathcal{A}_1^2 C_1^2)^2 \right) \\ &\quad + \hat{I} \cdot \frac{3}{4} \left( \frac{3}{8} (C_1^2 + C_2^2)^2 (2C_1^2 C_2^2 (\beta_2 \mathcal{A}_1^2 C_1^2 + \mathcal{A}_2^2 C_2^2) + \mathcal{A}_1^2 C_1^6 + \beta_2 \mathcal{A}_2^2 C_2^6) \right. \\ &\quad \quad \left. - \left( \frac{3}{8} \right)^2 (C_1^2 + C_2^2)^4 (C_1^2 + \beta_2 C_2^2) \right. \\ &\quad \quad \left. - C_1^2 C_2^2 (\mathcal{A}_2^4 C_2^6 + \beta_2 \mathcal{A}_1^4 C_1^6 - \mathcal{A}_1^2 \mathcal{A}_2^2 C_1^2 C_2^2 (C_1^2 + \beta_2 C_2^2)) \right) \\ &\quad + \left( \frac{3}{8} \right)^2 \left( \frac{3}{4} (C_1^2 + C_2^2)^2 (\mathcal{A}_1^2 C_1^4 + \mathcal{A}_2^2 C_2^4) - (\mathcal{A}_1^2 C_1^4 - \mathcal{A}_2^2 C_2^4)^2 - \left( \frac{3}{8} \right)^2 (C_1^2 + C_2^2)^4 \right) \end{aligned}$$

where we omitted the “of  $\mathbf{x}$ ” and introduced the shorthand  $\mathcal{A}_i := \sqrt{I_i + \frac{3}{8}}$  to shorten the notation.

### A.1.4. Regularization

#### Tikhonov Regularizer

Given a scalar field  $u : \Omega \subset \mathbb{R}^d \rightarrow \mathbb{R}$ . During a variational optimization, the field can be forced to be smooth using the Tikhonov regularizer

$$E_{\text{TM}}(u) := \frac{\lambda}{2} \int_{\Omega} \psi(\|\nabla u(\mathbf{x})\|^2) \, d\mathbf{x}$$

with quadratic loss function

$$\psi(s^2) := s^2 \quad \text{with derivative} \quad \psi'(s^2) = 1$$

and regularization parameter  $\lambda$ .

We compute its functional derivative using the calculus of variations to

$$\begin{aligned} \left. \frac{d}{d\epsilon} E_{\text{TM}}(u(\mathbf{x}) + \epsilon h(\mathbf{x})) \right|_{\epsilon=0} &= \left. \frac{d}{d\epsilon} \frac{\lambda}{2} \int_{\Omega} \psi(\|\nabla(u(\mathbf{x}) + \epsilon h(\mathbf{x}))\|^2) \, d\mathbf{x} \right|_{\epsilon=0} \\ &= \frac{\lambda}{2} \int_{\Omega} \psi'(\|\nabla u(\mathbf{x})\|^2) \sum_{d=1}^D \frac{d}{d\epsilon} \left( \frac{\partial(u(\mathbf{x}) + \epsilon h(\mathbf{x}))}{\partial x_d} \right)^2 \, d\mathbf{x} \Big|_{\epsilon=0} \\ &= \lambda \int_{\Omega} \psi'(\|\nabla u(\mathbf{x})\|^2) \sum_{d=1}^D \frac{\partial u(\mathbf{x})}{\partial x_d} \frac{\partial h(\mathbf{x})}{\partial x_d} \, d\mathbf{x} \\ &= -\lambda \int_{\Omega} \text{div}(\psi'(\|\nabla u(\mathbf{x})\|^2) \nabla u(\mathbf{x})) h(\mathbf{x}) \, d\mathbf{x} \\ &\quad + \lambda \sum_{d=1}^D \left[ \psi'(\|\nabla u(\mathbf{x})\|^2) \frac{\partial u(\mathbf{x})}{\partial x_d} h(\mathbf{x}) \right]_{\partial\Omega_{x_d}} \\ &\stackrel{\text{TM}}{=} -\lambda \int_{\Omega} \Delta u(\mathbf{x}) h(\mathbf{x}) \, d\mathbf{x} + \lambda [\mathbf{n}^{\top}(\mathbf{x}) \nabla u(\mathbf{x}) h(\mathbf{x})]_{\partial\Omega} \end{aligned}$$

where  $\Delta u$  is the Laplacian of  $u$ .

With Neumann boundary conditions (boundary derivative is zero) we obtain the Euler-Lagrange equation

$$\frac{\delta E_{\text{TM}}(u)}{\delta u(\mathbf{x})} = -\lambda \Delta u(\mathbf{x}) .$$

### Total variation relaxation

Given a scalar field  $u : \Omega \subset \mathbb{R}^d \rightarrow \mathbb{R}$ . During a variational optimization, the field can be forced to be locally constant using a total variation regularizer with loss function

$$\psi(s^2) := \sqrt{s^2} \quad \text{with derivative} \quad \psi'(s^2) = \frac{1}{2\sqrt{s^2}}.$$

The derivative is not defined at 0, therefore we relax the strict TV regularization according to Charbonnier et al. (1997) using the differentiable loss function

$$\psi(s^2) := \sqrt{s^2 + \epsilon^2} \quad \text{with derivative} \quad \psi'(s^2) = \frac{1}{2\sqrt{s^2 + \epsilon^2}}$$

where  $\epsilon \in \mathbb{R}^+$  is a small constant.

The last step of the Gâteaux derivation from above changes to

$$\begin{aligned} \left. \frac{d}{d\epsilon} E_{\text{TV}}(u(\mathbf{x}) + \epsilon h(\mathbf{x})) \right|_{\epsilon=0} &= -\frac{\lambda}{2} \int_{\Omega} \operatorname{div} \left( \frac{\nabla u(\mathbf{x})}{\sqrt{\|\nabla u(\mathbf{x})\|^2 + \epsilon^2}} \right) h(\mathbf{x}) \, d\mathbf{x} \\ &\quad + \frac{\lambda}{2} \left[ \mathbf{n}^{\top}(\mathbf{x}) \frac{\nabla u(\mathbf{x})}{\sqrt{\|\nabla u(\mathbf{x})\|^2 + \epsilon^2}} h(\mathbf{x}) \right]_{\partial\Omega} \end{aligned}$$

With Neumann boundary conditions we obtain the Euler-Lagrange equation

$$\frac{\delta E_{\text{TM}}(u)}{\delta u(\mathbf{x})} = -\frac{\lambda}{2} \operatorname{div} \left( \frac{\nabla u(\mathbf{x})}{\sqrt{\|\nabla u(\mathbf{x})\|^2 + \epsilon^2}} \right).$$

## A.2. Numerical integration

We use the trapezoidal rule between adjacent image planes

$$\int_a^b f(x) \, dx \approx (b-a) \frac{f(a) + f(b)}{2}$$

to estimate the continuous derivative along each ray.

Assume we want to compute the line integral along the ray with direction  $\mathbf{r} \in S$ . The main cone direction is the optical axis, *i.e.* the  $z$ -direction of the recorded volume. We only have measurements at discrete  $z$ -planes, therefore we rescale  $\mathbf{r}' := c\mathbf{r} = (x', y', h_z)^{\top}$  so that its  $z$ -component equals the distance  $h_z$  between two adjacent recording planes to avoid unnecessary inter-plane interpolation. The approximation for the integral up to plane  $z$  then becomes

$$\int_0^z f(\mathbf{x} + \ell \mathbf{r}') \, d\ell \approx \|\mathbf{r}'\| \sum_{\ell=1}^z \frac{f(\mathbf{x} + (\ell-1) \cdot \mathbf{r}') + f(\mathbf{x} + \ell \cdot \mathbf{r}')}{2}.$$

We formulate two different integration strategies, first a scheme for thin rays, and secondly a scheme with conic rays obtained through incremental interpolation during the integration. To obtain efficient algorithms, the schemes must be able to compute all line integrals for direction  $\mathbf{r}$  simultaneously for all voxels in the recording volume. We assume that values outside the recorded volume do not contribute to the integral (zero-padding).

### A.2.1. Integration along thin rays

Within this scheme the recording volume is first sheared according to the plane-offset  $-(x', y')^\top$  using a backwarp transformation and bilinear interpolation to obtain values at sub-pixel positions. The integration direction becomes the  $z$ -direction of the sheared volume. Then the line integration is performed along  $(0, 0, h_z)^\top$ . To obtain the integral for the original voxel positions, the integral volume is sheared by  $(x', y')^\top$  to the original coordinate system requiring a second backwarp transform with bilinear interpolation.

### A.2.2. Interpolation along conic rays

In this alternative scheme both the previous integral and the previous plane are sheared according to the plane-offset  $(x', y')^\top$  using a backwarp transformation and bilinear interpolation. After the shearing they match the discrete positions of the voxels in the current plane and are simply added according to the trapezoidal rule. The incremental interpolation of the previous plane integral leads to a natural widening of the rays. This scheme was proposed by Ronneberger et al. (2012) in the ViBE-Z zerfish atlas.

## A.3. Numerical differentiation

We define the 2nd order central differences of a discrete function  $f : \mathbb{Z}^3 \rightarrow \mathbb{R}$  as

$$\Delta_x^c f_{x,y,z} := \frac{f_{x+h_x,y,z} - f_{x-h_x,y,z}}{2h_x}, \quad \Delta_y^c f_{x,y,z} := \frac{f_{x,y+h_y,z} - f_{x,y-h_y,z}}{2h_y}, \quad \Delta_z^c f_{x,y,z} := \frac{f_{x,y,z+h_z} - f_{x,y,z-h_z}}{2h_z},$$

the first order forward differences as

$$\Delta_x^f f_{x,y,z} := \frac{f_{x+h_x,y,z} - f_{x,y,z}}{h_x}, \quad \Delta_y^f f_{x,y,z} := \frac{f_{x,y+h_y,z} - f_{x,y,z}}{h_y}, \quad \Delta_z^f f_{x,y,z} := \frac{f_{x,y,z+h_z} - f_{x,y,z}}{h_z},$$

and the first order backward differences as

$$\Delta_x^b f_{x,y,z} := \frac{f_{x,y,z} - f_{x-h_x,y,z}}{h_x}, \quad \Delta_y^b f_{x,y,z} := \frac{f_{x,y,z} - f_{x,y-h_y,z}}{h_y}, \quad \Delta_z^b f_{x,y,z} := \frac{f_{x,y,z} - f_{x,y,z-h_z}}{h_z}.$$

The gradient norms for the faces of the voxel at position  $\mathbf{x} = (x, y, z)^\top$  are then given by

$$\begin{aligned} \left\| \nabla \alpha_{x+\frac{h_x}{2}, y, z} \right\| &\approx \sqrt{\left( \Delta_x^f \alpha_{x,y,z} \right)^2 + \left( \frac{1}{2} \left( \Delta_y^c \alpha_{x+h_x, y, z} + \Delta_y^c \alpha_{x, y, z} \right) \right)^2 + \left( \frac{1}{2} \left( \Delta_z^c \alpha_{x+h_x, y, z} + \Delta_z^c \alpha_{x, y, z} \right) \right)^2} \\ \left\| \nabla \alpha_{x-\frac{h_x}{2}, y, z} \right\| &\approx \sqrt{\left( \Delta_x^b \alpha_{x,y,z} \right)^2 + \left( \frac{1}{2} \left( \Delta_y^c \alpha_{x, y, z} + \Delta_y^c \alpha_{x-h_x, y, z} \right) \right)^2 + \left( \frac{1}{2} \left( \Delta_z^c \alpha_{x, y, z} + \Delta_z^c \alpha_{x-h_x, y, z} \right) \right)^2} \\ \left\| \nabla \alpha_{x, y+\frac{h_y}{2}, z} \right\| &\approx \sqrt{\left( \Delta_y^f \alpha_{x,y,z} \right)^2 + \left( \frac{1}{2} \left( \Delta_x^c \alpha_{x, y+h_y, z} + \Delta_x^c \alpha_{x, y, z} \right) \right)^2 + \left( \frac{1}{2} \left( \Delta_z^c \alpha_{x, y+h_y, z} + \Delta_z^c \alpha_{x, y, z} \right) \right)^2} \\ \left\| \nabla \alpha_{x, y-\frac{h_y}{2}, z} \right\| &\approx \sqrt{\left( \Delta_y^b \alpha_{x,y,z} \right)^2 + \left( \frac{1}{2} \left( \Delta_x^c \alpha_{x, y, z} + \Delta_x^c \alpha_{x, y-h_y, z} \right) \right)^2 + \left( \frac{1}{2} \left( \Delta_z^c \alpha_{x, y, z} + \Delta_z^c \alpha_{x, y-h_y, z} \right) \right)^2} \\ \left\| \nabla \alpha_{x, y, z+\frac{h_z}{2}} \right\| &\approx \sqrt{\left( \Delta_z^f \alpha_{x,y,z} \right)^2 + \left( \frac{1}{2} \left( \Delta_x^c \alpha_{x, y, z+h_z} + \Delta_x^c \alpha_{x, y, z} \right) \right)^2 + \left( \frac{1}{2} \left( \Delta_y^c \alpha_{x, y, z+h_z} + \Delta_y^c \alpha_{x, y, z} \right) \right)^2} \\ \left\| \nabla \alpha_{x, y, z-\frac{h_z}{2}} \right\| &\approx \sqrt{\left( \Delta_z^b \alpha_{x,y,z} \right)^2 + \left( \frac{1}{2} \left( \Delta_x^c \alpha_{x, y, z} + \Delta_x^c \alpha_{x, y, z-h_z} \right) \right)^2 + \left( \frac{1}{2} \left( \Delta_y^c \alpha_{x, y, z} + \Delta_y^c \alpha_{x, y, z-h_z} \right) \right)^2} \end{aligned}$$

and the divergence can be computed to

$$\begin{aligned} \operatorname{div} \left( \psi' \left( \left\| \nabla \alpha_{x,y,z} \right\|^2 \right) \nabla \alpha_{x,y,z} \right) &= \psi' \left( \left\| \nabla \alpha_{x+\frac{h_x}{2}, y, z} \right\|^2 \right) \Delta_x^f \alpha_{x,y,z} - \psi' \left( \left\| \nabla \alpha_{x-\frac{h_x}{2}, y, z} \right\|^2 \right) \Delta_x^b \alpha_{x,y,z} \\ &+ \psi' \left( \left\| \nabla \alpha_{x, y+\frac{h_y}{2}, z} \right\|^2 \right) \Delta_y^f \alpha_{x,y,z} - \psi' \left( \left\| \nabla \alpha_{x, y-\frac{h_y}{2}, z} \right\|^2 \right) \Delta_y^b \alpha_{x,y,z} \\ &+ \psi' \left( \left\| \nabla \alpha_{x, y, z+\frac{h_z}{2}} \right\|^2 \right) \Delta_z^f \alpha_{x,y,z} - \psi' \left( \left\| \nabla \alpha_{x, y, z-\frac{h_z}{2}} \right\|^2 \right) \Delta_z^b \alpha_{x,y,z}. \end{aligned}$$

#### A.4. Data conditioning for direct L-BFGS-B optimization

If direct optimization of the intensities is not possible as in the case of fluorescence-induced absorption, we have to condition the optimization problem to allow direct optimization of intensities and attenuations using L-BFGS-B. Without reconditioning the gradient along the  $\alpha$ -dimensions is extremely steep compared to a very shallow gradient along the  $\hat{I}$ -dimensions. This leads to severe problems in the numerical optimization due to a very narrow ridge-like energy function. Changes in the attenuation field are over-emphasized leading to strong oscillation along those dimensions while at the same time the intensities do not change at all. The attenuations may not be changed without severely affecting the resulting model but the intensities can be easily scaled. A suitable scaling factor  $\nu \in \mathbb{R}^+$  that rescales the dynamic range of the intensities to match the dynamic range of the attenuations makes the problem more well-behaved.

We insert the scaled estimated intensity  $\hat{I}'(\mathbf{x}) := \frac{1}{\nu} \hat{I}(\mathbf{x})$  into the simulation equation with fluores-

cence absorption and obtain

$$F_i^{[\alpha, \hat{\Gamma}', \beta_i, \gamma]}(\mathbf{x}) := \beta_i \nu \hat{\Gamma}'(\mathbf{x}) \cdot \underbrace{\int_S s_i(\mathbf{r}) e^{-\int_0^\infty (\alpha + \gamma \nu \hat{\Gamma}')(\mathbf{x} + \ell \mathbf{r}) d\ell} d\mathbf{r}}_{=: C_i^{[\alpha, \hat{\Gamma}', \gamma]}(\mathbf{x})} \cdot \underbrace{\int_S s_i(\mathbf{r}) e^{-\int_0^\infty \alpha(\mathbf{x} + \ell \mathbf{r}) d\ell} d\mathbf{r}}_{=: C_i^{[\alpha]}(\mathbf{x})}$$

with Gâteaux/partial derivatives

$$\begin{aligned} \left. \frac{d}{d\epsilon} F_i^{[\alpha + \epsilon h, \hat{\Gamma}', \beta_i, \gamma]}(\mathbf{x}) \right|_{\epsilon=0} &= -\beta_i \nu \hat{\Gamma}'(\mathbf{x}) \cdot \int_S s_i(\mathbf{r}) \left( T_{\mathbf{r}}^{[\alpha, \hat{\Gamma}', \gamma]} \cdot C_i^{[\alpha]} + C_i^{[\alpha, \hat{\Gamma}', \gamma]} \cdot T_{\mathbf{r}}^{[\alpha]} \right)(\mathbf{x}) \int_0^\infty h(\mathbf{x} + \ell \mathbf{r}) d\ell d\mathbf{r} \\ \left. \frac{d}{d\epsilon} F_i^{[\alpha, \hat{\Gamma}' + \epsilon h, \beta_i, \gamma]}(\mathbf{x}) \right|_{\epsilon=0} &= \beta_i \nu \left( C_i^{[\alpha, \hat{\Gamma}', \gamma]} \cdot C_i^{[\alpha]} \right)(\mathbf{x}) \cdot h(\mathbf{x}) \\ &\quad - \beta_i \gamma \nu^2 \hat{\Gamma}'(\mathbf{x}) \cdot \int_S s_i(\mathbf{r}) \left( T_{\mathbf{r}}^{[\alpha, \hat{\Gamma}', \gamma]} \cdot C_i^{[\alpha]} \right)(\mathbf{x}) \int_0^\infty h(\mathbf{x} + \ell \mathbf{r}) d\ell d\mathbf{r} \\ \frac{\partial}{\partial \beta_i} F_i^{[\alpha, \hat{\Gamma}', \beta_i, \gamma]}(\mathbf{x}) &= \nu \left( \hat{\Gamma}' \cdot C_i^{[\alpha, \hat{\Gamma}', \gamma]} \cdot C_i^{[\alpha]} \right)(\mathbf{x}) \\ \frac{\partial}{\partial \gamma} F_i^{[\alpha, \hat{\Gamma}', \beta_i, \gamma]}(\mathbf{x}) &= -\beta_i \nu^2 \hat{\Gamma}'(\mathbf{x}) \cdot \int_S s_i(\mathbf{r}) \left( T_{\mathbf{r}}^{[\alpha, \hat{\Gamma}', \gamma]} \cdot C_i^{[\alpha]} \right)(\mathbf{x}) \int_0^\infty \hat{\Gamma}'(\mathbf{x} + \ell \mathbf{r}) d\ell d\mathbf{r}. \end{aligned}$$

Finally we plug the new simulation equation and its derivative into the Poisson-Gaussian models. For the generalized Anscombe model we obtain

$$E_{\text{data}}^{\mathcal{A}\mathcal{P}\mathcal{G}}(\alpha, \hat{\Gamma}', \beta_2, \gamma) := \sum_{i=1}^k \int_{\Omega} \left( \mathcal{A}\mathcal{P}\mathcal{G} \left( \frac{I_i(\mathbf{x})}{a} \right) - \mathcal{A}\mathcal{P}\mathcal{G} \left( \frac{F^{[\alpha, \hat{\Gamma}', \beta_i, \gamma]}(\mathbf{x})}{a} \right) \right)^2 d\mathbf{x}$$

with derivatives

$$\begin{aligned}
\frac{\delta E_{\text{data}}^{\mathcal{A}p\mathcal{G}}(\alpha, \hat{\Gamma}', \beta_2, \gamma)}{\delta \alpha(\mathbf{x})} &= \\
& \nu \sum_{i=1}^k \beta_i \int_S s_i(\mathbf{r}) \int_0^\infty \left( \mathcal{D}_i^{[\alpha, \hat{\Gamma}', \beta_i, \gamma]} \cdot \hat{\Gamma}' \cdot \left( T_{\mathbf{r}}^{[\alpha, \hat{\Gamma}', \gamma]} \cdot C_i^{[\alpha]} + C_i^{[\alpha, \hat{\Gamma}', \gamma]} \cdot T_{\mathbf{r}}^{[\alpha]} \right) \right) (\mathbf{x} - \ell \mathbf{r}) \, d\ell \, d\mathbf{r} \\
\frac{\delta E_{\text{data}}^{\mathcal{A}p\mathcal{G}}(\alpha, \hat{\Gamma}', \beta_2, \gamma)}{\delta \hat{\Gamma}'(\mathbf{x})} &= -\nu \sum_{i=1}^k \beta_i \left( \mathcal{D}_i^{[\alpha, \hat{\Gamma}', \beta_2, \gamma]} \cdot C_i^{[\alpha, \hat{\Gamma}', \gamma]} \cdot C_i^{[\alpha]} \right) (\mathbf{x}) \\
& \quad + \gamma \nu^2 \sum_{i=1}^k \beta_i \int_S s_i(\mathbf{r}) \int_0^\infty \left( \mathcal{D}_i^{[\alpha, \hat{\Gamma}', \beta_2, \gamma]} \cdot \hat{\Gamma}' \cdot T^{[\alpha, \hat{\Gamma}', \gamma]} \cdot C_i^{[\alpha]} \right) (\mathbf{x} - \ell \mathbf{r}) \, d\ell \, d\mathbf{r} \\
\frac{\delta E_{\text{data}}^{\mathcal{A}p\mathcal{G}}(\alpha, \hat{\Gamma}', \beta_2, \gamma)}{\partial \beta_2} &= -\nu \int_{\Omega} \left( \mathcal{D}_2^{[\alpha, \hat{\Gamma}', \beta_2, \gamma]} \cdot \hat{\Gamma}' \cdot C_2^{[\alpha, \hat{\Gamma}', \gamma]} \cdot C_2^{[\alpha]} \right) (\mathbf{x}) \, d\mathbf{x} \\
\frac{\delta E_{\text{data}}^{\mathcal{A}p\mathcal{G}}(\alpha, \hat{\Gamma}', \beta_2, \gamma)}{\partial \gamma} &= \\
& \nu^2 \sum_{i=1}^k \beta_i \int_{\Omega} \left( \mathcal{D}_i^{[\alpha, \hat{\Gamma}', \beta_i, \gamma]} \cdot \hat{\Gamma}' \cdot T_{\mathbf{r}}^{[\alpha, \hat{\Gamma}', \gamma]} \cdot C_i^{[\alpha]} \right) (\mathbf{x}) \int_S s_i(\mathbf{r}) \int_0^\infty \hat{\Gamma}'(\mathbf{x} + \ell \mathbf{r}) \, d\ell \, d\mathbf{r} \, d\mathbf{x}
\end{aligned}$$

## B. Arabidopsis sample preparation

All root samples were prepared and recorded by our colleagues from the Biology II department Taras Pasternak, Dorothée Aubry-Hivet, Thomas Blein and Jasmin Dürr following this protocol.

### B.1. Nucleus-based analysis

Seeds were surface-sterilized and sown on square Petri dishes of 1/2 Murashige and Skoog (MS) medium containing vitamins, 0.5% saccharose and 1% (w/v) agar (Sigma). The dishes were kept at room temperature for four hours before transfer to 4°C for 12 hours. Dishes were then transferred to 22°C under long days (16h) of white light for the next 60 hours. To avoid an impact from the circadian cycle, all operations were performed in identical day-time periods. After scanning the dishes with a Canon F950 scanner, the primary root length was measured with Scion Image (Scion Corporation). To ensure a comparable developmental age, all seedlings showing a root length difference greater than 10% from the average (8mm) were not kept for the following steps. The remaining seedlings were transferred to a 12-well plate containing liquid 1/2 MS medium (containing vitamins, and 0.5% saccharose) for 12 hours. Colchicine was then added (final concentration 0.1% (w/v)) and plants were incubated for either 30, 60 or 90 minutes. After incubation the plants were fixed under vacuum in 2% (w/v) paraformaldehyde in MTSB for 30 minutes. Then, the plants were washed twice with distilled water for 10 minutes, incubated in DAPI (20µg/l) for 20 minutes, washed again with distilled water and mounted on slides using a 120 µm spacer and FluoromountG (Southern Biotechnology Inc.) as embedding medium.

The DAPI-stained root tips were recorded using a confocal laser scanning microscope (LSM 510 Duo Live) at an excitation wavelength of 405nm with a C-Apochromat 40x/1.2 W corrected UV-VIS-IR objective. Serial optical sections were reconstituted into 3D image stacks to a depth of 100 µm, with an in-plane sampling of 0.15 µm and a section spacing of 1µm. Two or three partially overlapping image stacks were recorded for each root.

### B.2. Cell boundary-based analysis

The cell wall propidium staining was adapted from that of Truernit et al. (2008) as following. Plants were fixed in (50% methanol and 10% acetic acid) and stored at 4°C until use. After a progressive rehydration, an overnight amylase treatment at 37°C (phosphate buffer 20mM pH7 with NaCl 2mM, CaCl<sub>2</sub> 0.25mM, 0.01% amylase) was done as previously described (Wuyts et al., 2010). After rinsing in water the roots were incubated for 40 minutes in 1% periodic acid at room temperature.

## *B. Arabidopsis sample preparation*

---

After another rinse in water the seedlings were incubated in Schiff reagent with propidium iodide (100 mM sodium metabisulphite and 0.15 N HCl; propidium iodide to a final concentration of 0.1 mM was freshly added) for 15 minutes. The samples were then rinsed in water before incubation for 1h in 10% glycerol and then 1h in mounting solution (80g of chloral hydrate in 27ml H<sub>2</sub>O, 3ml of glycerol). After an overnight incubation in new mounting solution, the samples were mounted on slides with a 120 $\mu$ m spacer.

The PI-stained roots were recorded using a confocal laser scanning microscope (LSM 510) at an excitation wavelength of 488nm with a Plan-Neofluar 40 $\times$ /1.3 oil objective. Serial optical sections were reconstituted into 3D image stacks to a depth of 100 $\mu$ m, with an in-plane sampling of 0.4 $\mu$ m and a section spacing of 0.4 $\mu$ m.

### **B.3. Pre-processing**

Consecutive images were stitched to a total length of 500  $\mu$ m from the quiescent centre (QC) using xuvTools (Emmenlauer et al., 2009). The liquid embedding may induce small root rotations that cannot be resolved with the strict translational model of xuvTools; therefore datasets with errors exceeding 10  $\mu$ m at the stitching boundary were discarded. The stitching error does not influence the mitosis distributions, because the proliferation zone was fully included in the first tile. The goal of the stitching was to ensure that no mitoses in the distal part from QC were missed. For the description of more distal events the root should be mechanically fixed to the cover-slip.

For all recordings the microscope was setup to optimally use the available dynamic range of 12 bit (Gray values: [0, 4096]).

## References

- F. J. Anscombe. The Transformation of Poisson, Binomial and Negative-Binomial Data. *Biometrika*, **35(3–4)**, 1948, 246–254. doi:10.1093/biomet/35.3-4.246.
- D. H. Ballard. Generalizing the Hough Transform to Detect Arbitrary Shapes. *Pattern Recognition*, **13(2)**, 1981, 111–122.
- U. Bauer and K. Polthier. Generating Parametric Models of Tubes from Laser Scans. *Computer-Aided Design*, **41(10)**, 2009, 719–729. doi:10.1016/j.cad.2009.01.002.
- M. Booth, M. Neil and T. Wilson. Aberration correction for confocal imaging in refractive-index-mismatched media. *Journal of Microscopy*, **192(2)**, 1998, 99–98. doi:10.1111/j.1365-2818.1998.99999.x.
- T. Brox. *Von Pixeln zu Regionen: Partielle Differenzialgleichungen in der Bildanalyse*. Ph.D. thesis, Universität des Saarlandes, Mathematische Bildverarbeitungsgruppe, Fakultät für Mathematik und Informatik Universität des Saarlandes, 66041 Saarbrücken, 2005.
- A. Can, O. Al-kofahi, S. Lasek, D. H. Szarowski, J. N. Turner and B. Roysam. Attenuation Correction in Confocal Laser Microscopes: A Novel Two-View Approach. *Journal of Microscopy*, **211**, 2003, 67–79. doi:10.1046/j.1365-2818.2003.01195.x.
- H. M. Cederholm, A. S. Iyer-Pascuzzi and P. N. Benfey. Patterning the primary root in Arabidopsis. *Wiley Interdisciplinary Reviews: Developmental Biology*, 2012. doi:10.1002/wdev.49.
- P. Charbonnier, L. Blanc-Feraud, G. Aubert and M. Barlaud. Deterministic edge-preserving regularization in computed imaging. *IEEE Transactions on Image Processing*, **6(2)**, 1997, 298–311. doi:10.1109/83.551699.
- L.-Y. C. Chiu and M. Moharezzadeh. Fourier transform of spherical Laguerre Gaussian functions and its application in molecular integrals. *International Journal of Quantum Chemistry*, **73(3)**, 1999, 265–273. doi:10.1002/(SICI)1097-461X(1999)73:3<265::AID-QUA1>3.0.CO;2-7.
- R. W. Cole, T. Jinadasa and C. M. Brown. Measuring and interpreting point spread functions to determine confocal microscope resolution and ensure quality control. *Nature Protocols*, **6(12)**, 2011, 1929–1941. doi:10.1038/nprot.2011.407.
- P. Davidovits and M. D. Egger. Scanning Laser Microscope. *Nature*, **223**, 1969, 831. doi:10.1038/223831a0.

- C. de Boor. *A practical guide to splines, Applied Mathematical Sciences*, volume 27. Springer-Verlag, 3 edition, 1978.
- A. E. Dorr, J. Lerch, S. Spring, N. Kabania and R. M. Henkelman. High resolution three-dimensional brain atlas using an average magnetic resonance image of 40 adult C57Bl/6J mice. *NeuroImage*, **42(1)**, 2008, 60–69. doi:10.1016/j.neuroimage.2008.03.037.
- A. R. Edmonds. *Angular Momentum in Quantum Mechanics*. Princeton University Press, 1957.
- A. Egner and S. W. Hell. Aberrations in Confocal and Multi-Photon Fluorescence Microscopy Induced by Refractive Index Mismatch. In J. B. Pawley (ed.), *Handbook of Biological Confocal Microscopy*, chapter 20. Springer, 3rd edition, 2006, pp. 404–413.
- M. Emmenlauer, O. Ronneberger, A. Ponti, P. Schwarb, A. Griffa, A. Filippi, R. Nitschke, W. Driever and H. Burkhardt. XuvTools: free, fast and reliable stitching of large 3D datasets. *Journal of Microscopy*, **233(1)**, 2009, 42–60. doi:10.1111/j.1365-2818.2008.03094.x.
- M. Emmenlauer, O. Ronneberger, M. Temerinac, H. Burkhardt, A. Filippi, R. Nitschke and W. Driever. Fast Automatic Recombination of Multiple 3D Datasets for Large Volumes and High Dynamic Range (HDR). In *49th Symposium of the Society for Histochemistry*. 2007.
- F. Federici, L. Dupuy, L. Laplaze, M. Heisler and J. Haseloff. Integrated genetic and computation methods for in planta cytometry. *Nature Methods*, **9(5)**, 2012, 483–485. doi:10.1038/nmeth.1940.
- A. W. Fitzgibbon. A Buyer’s Guide to Conic Fitting. In *Proceedings of the British Machine Vision Conference*. 1995, pp. 513–522. doi:10.5244/C.9.51.
- A. Foi, M. Trimeche, V. Katkovnik and K. Egiazarian. Practical Poissonian-Gaussian Noise Modeling and Fitting for Single-Image Raw-Data. *Transactions on Image Processing*, **17(10)**, 2008, 1737–1754. doi:10.1109/TIP.2008.2001399.
- C. C. Fowlkes, C. L. L. Hendriks, S. V. Keränen, G. H. Weber, O. Rübél, M.-Y. Huang, S. Chatoor, A. H. DePace, L. Simirenko, C. Henriquez, A. Beaton, R. Weiszmann, S. Celniker, B. Hamann, D. W. Knowles, M. D. Biggin, M. B. Eisen and J. Malik. A Quantitative Spatiotemporal Atlas of Gene Expression in the Drosophila Blastoderm. *Cell*, **133**, 2008, 364–374. doi:10.1016/j.cell.2008.01.053.
- O. Friman, M. Hindennach, C. Kühnel and H.-O. Peitgen. Multiple hypothesis template tracking of small 3D vessel structures. *Medical Image Analysis*, **14**, 2010, 160–171. doi:10.1016/j.media.2009.12.003.
- J. Friml, E. Benková, I. Blilou, J. Wisniewska, T. Hamann, K. Ljung, S. Woody, G. Sandberg, B. Scheres, G. Jürgens and K. Palme. AtPIN4 Mediates Sink-Driven Auxin Gradients and Root Patterning in Arabidopsis. *Cell*, **108(5)**, 2002, 661–673. doi:10.1016/S0092-8674(02)00656-6.
- Y. Q. Guan, Y. Y. Cai, X. Zhang, Y. T. Lee and M. Opas. Adaptive correction technique for 3D reconstruction of fluorescence microscopy images. *Microscopy Research and Technique*, **71(2)**, 2008, 146–157. doi:10.1002/jemt.20536.

- J. Kapuscinski. DAPI: a DNA-specific fluorescent probe. *Biotechnic and Histochemistry*, **70(5)**, 1995, 220–233.
- P. J. Keller and E. H. K. Stelzer. Lichtscheiben-Mikroskopie in der molekularen Zellbiophysik. *Laborwelt*, **7(5)**, 2006, 18–21.
- M. Keuper, T. Schmidt, M. Temerinac-Ott, J. Padeken, P. Heun, O. Ronneberger and T. Brox. Blind deconvolution of widefield fluorescence microscopic data by regularization of the optical transfer function (OTF). In *IEEE Conference on Computer Vision and Pattern Recognition (CVPR)*. 2013, pp. 2179 – 2186. doi:10.1109/CVPR.2013.283.
- C. Kirbas and F. Quek. A review of vessel extraction techniques and algorithms. *ACM Comput. Surv.*, **36(2)**, 2004, 81–121. doi:10.1145/1031120.1031121.
- A. Köhler. Ein neues Beleuchtungsverfahren für mikrophotographische Zwecke. *Zeitschrift für wissenschaftliche Mikroskopie und für mikroskopische Technik*, **10(4)**, 1893, 433–440.
- F. Laibach. Arabidopsis thaliana (L.) Heynh. als Objekt für genetische und entwicklungsphysiologische Untersuchungen. *Botanisches Archiv*, **44**, 1943, 439–455.
- I. Laptev, H. Mayer, T. Lindeberg, W. Eckstein, C. Steger and A. Baumgartner. Automatic extraction of roads from aerial images based on scale space and snakes. In *Machine Vision and Applications*, volume 12. Computational Vision and Active Perception Laboratory (CVAP), NADA, KTH, 100 44 Stockholm, Sweden SE, Springer Berlin / Heidelberg, 2000, pp. 23–31. doi:10.1007/s001380050121.
- I.-K. Lee. Curve reconstruction from unorganized points. *Computer Aided Geometric Design*, **17(2)**, 2000, 161–177. doi:10.1016/S0167-8396(99)00044-8.
- M. Leewenhoek and R. de Graaf. A Specimen of Some Observations Made by a Microscope. *Philosophical Transactions of the Royal Society of London*, **8**, 1673, 6037–6038.
- E. S. Lein, M. J. Hawrylycz, N. Ao, M. Ayres, A. Bensinger et al. Genome-wide atlas of gene expression in the adult mouse brain. *Nature*, **445**, 2007, 168–176. doi:10.1038/nature05453.
- K. Liu, T. Schmidt, T. Blein, J. Dürr, K. Palme and O. Ronneberger. Joint 3D Cell Segmentation and Classification in the Arabidopsis Root using Energy Minimization and Shape Priors. In *IEEE International Symposium on Biomedical Imaging (ISBI)*. 2013, pp. 422–425. doi:10.1109/ISBI.2013.6556502.
- K. Liu, H. Skibbe, T. Schmidt, T. Blein, K. Palme, T. Brox and O. Ronneberger. Rotation-Invariant HOG Descriptors using Fourier Analysis in Polar and Spherical Coordinates. *International Journal of Computer Vision*, **106(3)**, 2014, 342–364. doi:10.1007/s11263-013-0634-z.
- X. Liu, F. Long, H. Peng, S. J. Aerni, M. Jiang, A. Sánchez-Blanco, J. I. Murray, E. Preston, B. Mericle, S. Batzoglou, E. W. Myers and S. K. Kim. Analysis of Cell Fate from Single-Cell Gene Expression Profiles in *C. elegans*. *Cell*, **139(3)**, 2009, 623–633. doi:10.1016/j.cell.2009.08.044.

## References

---

- F. Long, H. Peng, X. Liu, S. K. Kim and E. Myers. A 3D digital atlas of *C. elegans* and its application to single-cell analyses. *Nature Methods*, **6**, 2009, 667–672. doi:10.1038/nmeth.1366.
- D. G. Lowe. Distinctive Image Features from Scale-Invariant Keypoints. *International Journal of Computer Vision*, **60**, 2004, 91–110.
- O. Lummer and F. Reiche. *Die Lehre von der Bildentstehung im Mikroskop von Ernst Abbe*. F. Vieweg, Braunschweig, Germany, 1910.
- D. Mai, J. Dürr, K. Palme and O. Ronneberger. Accurate Detection in Volumetric Images using Elastic Registration based Validation. In *German Conference on Pattern Recognition (GCPR)*. 2014, pp. 453–463. doi:10.1007/978-3-319-11752-2\_37.
- M. Mäkitalo and A. Foi. Optimal Inversion of the Generalized Anscombe Transformation for Poisson-Gaussian Noise. *IEEE Transactions on Image Processing*, **22(1)**, 2013, 91–103. doi:10.1109/TIP.2012.2202675.
- E. Meijering, M. Jacob, J.-C. Sarria, P. Steiner, H. Hirling and M. Unser. Design and validation of a tool for neurite tracing and analysis in fluorescence microscopy images. *Cytometry Part A*, **58A(2)**, 2004, 167–176. doi:10.1002/cyto.a.20022.
- F. Meyer. Topographic distance and watershed lines. *Signal Processing*, **38(1)**, 1994, 113–125. doi:10.1016/0165-1684(94)90060-4.
- M. Minsky. *Microscopy Apparatus*. 1957.
- A. Müller, C. Guan, L. Gälweiler, P. Tänzler, P. Huijser, A. Marchant, G. Parry, M. Bennett, E. Wisman and K. Palme. AtPIN2 defines a locus of Arabidopsis for root gravitropism control. *The EMBO Journal*, **17(23)**, 1998, 6903–6911. doi:10.1093/emboj/17.23.6903.
- J. Platt. Probabilistic outputs for support vector machines and comparisons to regularized likelihood methods. In A. Smola, P. Bartlett, B. Schoelkopf and D. Schuurmans (eds.), *Advances in Large Margin Classifiers*. 2000, pp. 61–74.
- T. Pock, R. Beichel and H. Bischof. A Novel Robust Tube Detection Filter for 3D Centerline Extraction. In *Proceedings of the 14th Scandinavian Conference on Image Analysis (SCIA), LNCS*, volume 3540. Springer, 2005, pp. 481–490. doi:10.1007/11499145\_49.
- Q. Wang, O. Ronneberger and H. Burkhardt. Using Lateral Coupled Snakes for Modeling the Contours of Worms. In *Pattern Recognition (Proc. DAGM), LNCS*, volume 10. DAGM, Springer, 2009, pp. 542–551.
- M. Reisert. *Group Integration Techniques in Pattern Analysis - A Kernel View*. Ph.D. thesis, Albert-Ludwigs-University, Freiburg, Germany, 2008.
- O. Ronneberger, K. Liu, M. Rath, D. Rueß, T. Mueller, H. Skibbe, B. Drayer, T. Schmidt, A. Filippi, R. Nitschke, T. Brox, H. Burkhardt and W. Driever. ViBE-Z: A Framework for 3D Virtual Colocalization Analysis in Zebrafish Larval Brains. *Nature Methods*, **9(7)**, 2012, 735–742. doi:10.1038/nmeth.2076.

- L. Santuari, E. Scacchi, A. Rodriguez-Villalon, P. Salinas, E. M. Dohmann, G. Brunoud, T. Vernoux, R. S. Smith and C. S. Hardtke. Positional Information by Differential Endocytosis Splits Auxin Response to Drive *Arabidopsis* Root Meristem Growth. *Current Biology*, **21**, 2011, 1918–1923. doi:10.1016/j.cub.2011.10.002.
- P. Sarder and A. Nehorai. Deconvolution methods for 3-D fluorescence microscopy images. *Signal Processing Magazine, IEEE*, **23(3)**, 2006, 32–45. doi:10.1109/MSP.2006.1628876.
- B. Scheres, P. Benfey and L. Dolan. Root Development. In *The Arabidopsis Book*, volume 1, chapter e0101. American Society of Plant Biologists, 2002. doi:10.1199/tab.0101.
- T. Schmidt, J. Dürr, M. Keuper, T. Blein, K. Palme and O. Ronneberger. Variational attenuation correction in two-view confocal microscopy. *BMC Bioinformatics*, **14**, 2013a, 366. doi:10.1186/1471-2105-14-366.
- T. Schmidt, J. Dürr, M. Keuper, T. Blein, K. Palme and O. Ronneberger. Variational Attenuation Correction of Two-View Confocal Microscopic Recordings. In *IEEE International Symposium on Biomedical Imaging (ISBI)*. 2013b, pp. 169–172.
- T. Schmidt, M. Keuper, T. Pasternak, K. Palme and O. Ronneberger. Modeling of Sparsely Sampled Tubular Surfaces Using Coupled Curves. In *Pattern Recognition (Proc. DAGM)*. 2012, pp. 83–92. doi:10.1007/978-3-642-32717-9\_9.
- T. Schmidt, T. Pasternak, K. Liu, T. Blein, D. Aubry-Hivet, A. Dovzhenko, J. Duerr, W. Teale, F. A. Ditungou, H. Burkhardt, O. Ronneberger and K. Palme. The iRoCS Toolbox – 3D analysis of the plant root apical meristem at cellular resolution. *The Plant Journal*, **77(5)**, 2014, 806–814. doi:10.1111/tpj.12429.
- R. Schnabel, R. Wahl and R. Klein. Efficient RANSAC for Point-Cloud Shape Detection. *Computer Graphics Forum*, **26(2)**, 2007, 214–226.
- B. Schölkopf and A. J. Smola. *Learning With Kernels*. MIT Press, 1998.
- J. Schulz, T. Schmidt, O. Ronneberger, H. Burkhardt, T. Pasternak, A. Dovzhenko and K. Palme. Fast Scalar and Vectorial Grayscale Based Invariant Features for 3D Cell Nuclei Localization and Classification. *Lecture Notes in Computer Science*, **4174/2006**, 2006, 182–191. doi:10.1007/11861898\_19.
- G. Sena, Z. Frentz, K. D. Birnbaum and S. Leibler. Quantitation of Cellular Dynamics in Growing *Arabidopsis* Roots with Light Sheet Microscopy. *PLoS ONE*, **6(6)**, 2011. doi:10.1371/journal.pone.0021303.
- L. A. Shepp and B. F. Logan. The Fourier Reconstruction of a Head Section. *IEEE Trans Nuclear Science*, **21(3)**, 1974, 21–43. doi:10.1109/TNS.1974.6499235.
- O. Shimomura, F. H. Johnson and Y. Saiga. Extraction, Purification and Properties of Aequorin, a Bioluminescent Protein from the Luminous Hydromedusan, *Aequorea*. *Journal of Cellular and Comparative Physiology*, **59**, 1962, 223–239.

- H. Skibbe, M. Reiser, T. Schmidt, T. Brox, O. Ronneberger and H. Burkhardt. Fast Rotation Invariant 3D Feature Computation utilizing Efficient Local Neighborhood Operators. *IEEE Transactions on Pattern Analysis and Machine Intelligence*, **34(8)**, 2012, 1563–1575. doi:10.1109/TPAMI.2011.263.
- S. G. Stanciu, G. A. Stanciu and D. Coltuc. Automated Compensation of Light Attenuation in Confocal Microscopy by Exact Histogram Specification. *Microscopy Research and Technique*, **73**, 2010, 165–175. doi:10.1002/jemt.20767.
- J.-L. Starck, F. Murtagh and A. Bijaoui. *Image Processing and Data Analysis: The Multiscale Approach*. Cambridge University Press, New York, NY, USA, 1998. Isbn: 0-521-59914-8.
- W. D. Teale, I. A. Paponov and K. Palme. Auxin in action: signalling, transport and the control of plant growth and development. *Nature Reviews: Molecular Cell Biology*, **7**, 2006, 847–859. doi:10.1038/nrm2020.
- M. Temerinac-Ott, O. Ronneberger, P. Ochs, W. Driever, T. Brox and H. Burkhardt. Multiview deblurring for 3-D images from light sheet based fluorescence microscopy. *IEEE Transactions on Image Processing*, **21(4)**, 2012, 1863–1873. doi:10.1109/TIP.2011.2181528.
- A. Tikhonov. Solution of incorrectly formulated problems and the regularization method. *Soviet Math. Doklady*, **4**, 1963, 1035–1038.
- E. Truernit, H. Bauby, B. Dubreucq, O. Grandjean, J. Runions, J. Barthélémy and J.-C. Palauqui. High-resolution whole-mount imaging of three-dimensional tissue organization and gene expression enables the study of Phloem development and structure in Arabidopsis. *Plant Cell*, **20(6)**, 2008, 1494–1503. doi:10.1105/tpc.107.056069.
- V. N. Vapnik. *Statistical Learning Theory*. Wiley-Interscience, 1998. ISBN 471030031.
- M. Čapek, J. Janáček and L. Kubínová. Methods for compensation of the light attenuation with depth of images captured by a confocal microscope. *Microscopy Research And Technique*, **69(8)**, 2006, 624–635. doi:10.1002/jemt.20330.
- T. Visser, F. Groen and G. Brakenhoff. Absorption and scattering correction in fluorescence confocal microscopy. *Journal of Microscopy*, **163(2)**, 1991, 189–200. doi:10.1111/j.1365-2818.1991.tb03171.x.
- J. Weickert. *Anisotropic Diffusion In Image Processing*. B.G. Teubner Stuttgart, 1998.
- N. Wuyts, J.-C. Palauqui, G. Conejero, J.-L. Verdeil, C. Granier and C. Massonnet. High-contrast three-dimensional imaging of the Arabidopsis leaf enables the analysis of cell dimensions in the epidermis and mesophyll. *Plant Methods*, **6**, 2010, 17. doi:10.1186/1746-4811-6-17.
- B. Zhang, J. Zerubia and J.-C. Olivo-Marin. Gaussian approximations of fluorescence microscope point-spread function models. *Applied Optics*, **46(10)**, 2007, 1819–1829. doi:10.1364/AO.46.001819.

- C. Zhu, R. H. Byrd, P. Lu and J. Nocedal. Algorithm 778: L-BFGS-B: Fortran subroutines for large-scale bound-constrained optimization. *ACM Trans. Math. Softw.*, **23(4)**, 1997, 550–560. doi:10.1145/279232.279236.